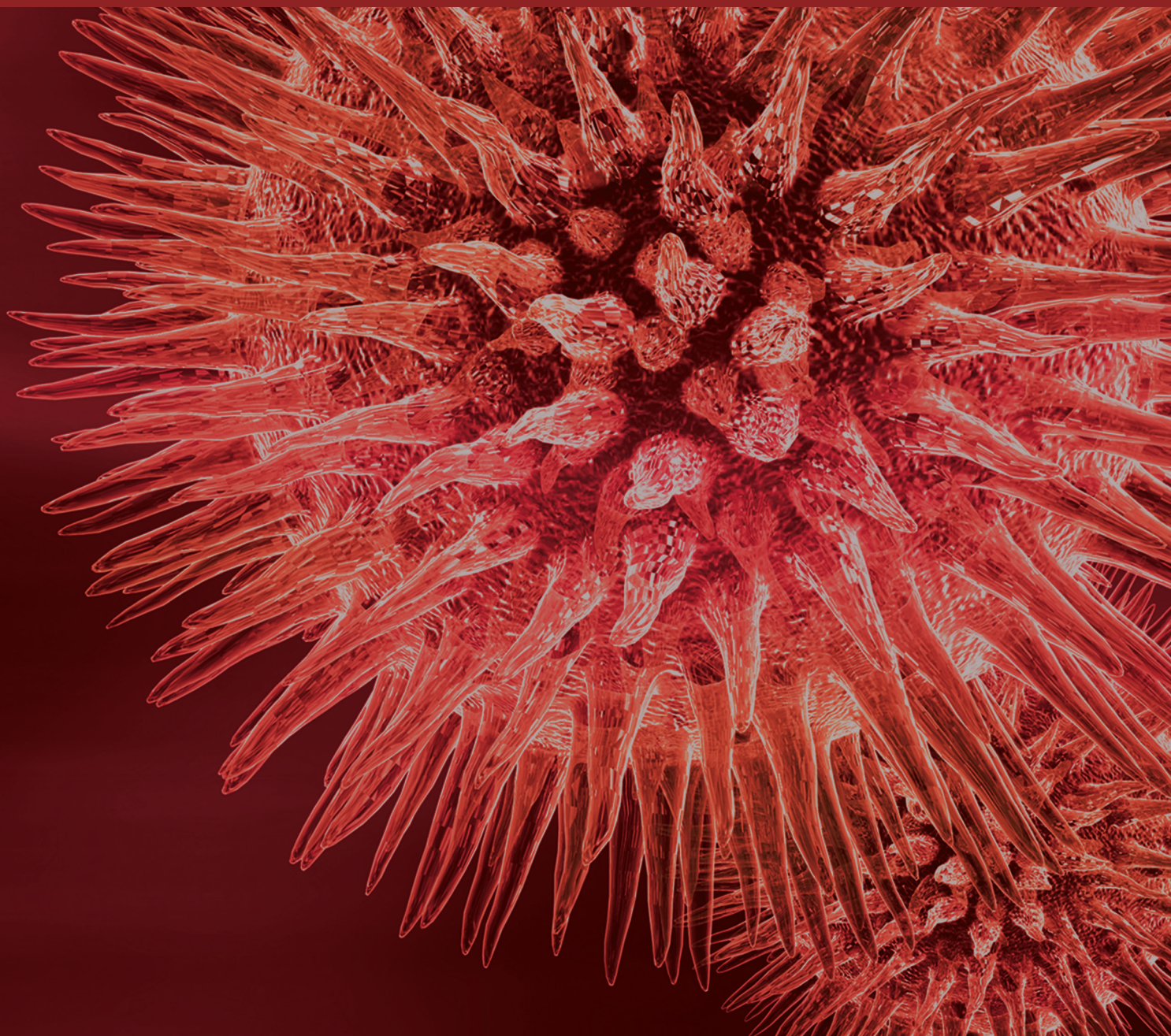


BioMed Research International

Advances in Translational Cancer Imaging: Opportunities and Challenges

Guest Editors: Yi-Xiang Wang, Yong E. Chung, Weibo Cai, and Kenji Suzuki





Advances in Translational Cancer Imaging: Opportunities and Challenges

BioMed Research International

Advances in Translational Cancer Imaging: Opportunities and Challenges

Guest Editors: Yi-Xiang Wang, Yong E. Chung, Weibo Cai,
and Kenji Suzuki



Copyright © 2016 Hindawi Publishing Corporation. All rights reserved.

This is a special issue published in “BioMed Research International.” All articles are open access articles distributed under the Creative Commons Attribution License, which permits unrestricted use, distribution, and reproduction in any medium, provided the original work is properly cited.

Contents

A Novel Two-Step Technique for Retrieving Fractured Peripherally Inserted Central Catheter Segments Migrating into the Heart or the Pulmonary Artery

Juan Peng, Xiao-Ming Zhang, Lin Yang, Hao Xu, Nan-Dong Miao, Yong-Jun Ren, Kang Liu, Xu-Li Min, Ke Yang, Shi Yang, and Cheng Yang
Volume 2016, Article ID 7814529, 5 pages

Fuzzy Clustering Applied to ROI Detection in Helical Thoracic CT Scans with a New Proposal and Variants

Alfonso Castro, Alberto Rey, Carmen Boveda, Bernardino Arcay, and Pedro Sanjurjo
Volume 2016, Article ID 8058245, 15 pages

Intraoperative Contrast Enhanced Ultrasound Evaluates the Grade of Glioma

Ling-Gang Cheng, Wen He, Hong-Xia Zhang, Qian Song, Bin Ning, Hui-Zhan Li, Yan He, and Song Lin
Volume 2016, Article ID 2643862, 9 pages

Diffusion-Weighted Imaging of Small Peritoneal Implants in “Potentially” Early-Stage Ovarian Cancer

Laretta Grabowska-Derlatka, Pawel Derlatka, Wojciech Szeszkowski, and Andrzej Cieszanowski
Volume 2016, Article ID 9254742, 5 pages

Diffusion-Weighted Imaging with Two Different *b*-Values in Detection of Solid Focal Liver Lesions

Da-wei Yang, Ke-yang Wang, Xun Yao, Hui-yi Ye, Tao Jiang, Yuan Liu, Jia-yin Gao, Min Chen, Cheng Zhou, and Zheng-han Yang
Volume 2016, Article ID 8128207, 9 pages

Analysis of Residual DSBs in Ataxia-Telangiectasia Lymphoblast Cells Initiating Apoptosis

Teresa Anglada, Mariona Terradas, Laia Hernández, Anna Genescà, and Marta Martín
Volume 2016, Article ID 8279560, 12 pages

Improvement in the Detection of Cystic Metastatic Papillary Thyroid Carcinoma by Measurement of Thyroglobulin in Aspirated Fluid

Yong Wang, Huan Zhao, Yi-Xiang J. Wang, Min-Jie Wang, Zhi-Hui Zhang, Li Zhang, Bin Zhang, Anil T. Ahuja, Chun-Wu Zhou, Yu-Xin Jiang, and Hui-Qin Guo
Volume 2016, Article ID 8905916, 6 pages

Dynamic Contrast-Enhanced CT Characterization of Xp11.2 Translocation/TFE3 Gene Fusions versus Papillary Renal Cell Carcinomas

Jian He, Kefeng Zhou, Bin Zhu, Gutian Zhang, Xiaogong Li, Hongqian Guo, Weidong Gan, Zhengyang Zhou, and Tian Liu
Volume 2015, Article ID 298679, 8 pages

Molecular Imaging with MRI: Potential Application in Pancreatic Cancer

Chen Chen, Chang Qiang Wu, Tian Wu Chen, Meng Yue Tang, and Xiao Ming Zhang
Volume 2015, Article ID 624074, 10 pages

Research Article

A Novel Two-Step Technique for Retrieving Fractured Peripherally Inserted Central Catheter Segments Migrating into the Heart or the Pulmonary Artery

Juan Peng, Xiao-Ming Zhang, Lin Yang, Hao Xu, Nan-Dong Miao, Yong-Jun Ren, Kang Liu, Xu-Li Min, Ke Yang, Shi Yang, and Cheng Yang

Sichuan Key Laboratory of Medical Imaging, Department of Radiology, Affiliated Hospital of North Sichuan Medical College, Nanchong, Sichuan 637000, China

Correspondence should be addressed to Lin Yang; linyngmd@163.com

Received 19 October 2015; Revised 14 November 2015; Accepted 13 July 2016

Academic Editor: Kenji Suzuki

Copyright © 2016 Juan Peng et al. This is an open access article distributed under the Creative Commons Attribution License, which permits unrestricted use, distribution, and reproduction in any medium, provided the original work is properly cited.

Objective. To report the experience of a percutaneous technique for retrieving fractured peripherally inserted central catheter (PICC) segments migrating into the heart or the pulmonary artery. **Method.** From April 2013 to July 2015, we performed percutaneous retrieval of fractured PICC segments migrating into the heart or the pulmonary artery in five cancer patients who had undergone chemotherapy via PICC. The fractures were diagnosed with chest plain radiography. The patients included three cases of breast cancer, one case of rectal cancer, and one case of lower limb Ewing's tumor. The fractures were retained in the vessels of the patients for 1 to 3 days. All the fractures were retrieved by using a novel two-step technique in the digital subtraction angiography (DSA) suite. This two-step technique involves inserting a pigtail catheter to the heart or the pulmonary artery to grasp the fractured catheter fragment and bring it to the lower segment of the inferior vena cava, followed by grasping and removing the catheter fragment with a retrieval loop system of the vena cava filter retrieval set. **Result.** The fractured PICC segments were removed successfully in all five patients via unilateral (four patients) or bilateral (one patient) femoral vein access. No complications occurred during the interventional procedure. **Conclusion.** Percutaneous retrieval can be a safe, convenient, and minimally invasive method for the removal of fractured PICC segments. The technique reported in this paper will be applicable for the retrieval of fractured PICC segments and other catheter fragments migrating into the heart or the pulmonary artery.

1. Introduction

Peripherally inserted central catheters (PICCs) are widely used to provide central venous access in chronically ill patients with long-term intravenous access requirements, such as those related to chemotherapy, parenteral alimentation, irritant drug infusion, and so forth. Multiple substantial complications of PICC, including catheter malposition, migration, obstruction, infection, thrombosis, and catheter fracture, have been reported in the literature [1–5]. Fractured catheter fragments should be retrieved to prevent further complications. Percutaneous retrieval of intravascular foreign bodies is considered the gold standard treatment because it is a minimally invasive, relatively simple, safe procedure, with low complication rates compared to conventional

surgical treatment [6, 7]. However, it can be difficult to retrieve the fractured catheter segments migrating into the heart or the pulmonary artery [8], so advanced techniques are required. In this report, we described our experience of 5 patients with fractured PICC segments in the heart or the pulmonary arteries which were successfully retrieved with a novel two-step method.

2. Materials and Methods

2.1. Patients. This is a retrospective report based on the medical records of 5 consecutive patients treated from April 2013 to July 2015. Of the 5 patients, 2 were males and 3 were females, with an average age of 39.4 ± 17.2 years (range: 10 to 55 years). The patients included three cases of breast

TABLE 1: Summary of patient details.

Case number	Sex	Age	Diagnosis	Access
1	Female	44 years old	Breast cancer	Right femoral vein
2	Female	41 years old	Breast cancer	Right femoral vein
3	Female	47 years old	Breast cancer	Right femoral vein
4	Male	55 years old	Rectal cancer	Bilateral femoral vein
5	Male	10 years old	Lower limb Ewing's tumor	Right femoral vein

cancer, one case of rectal cancer, and one case of lower limb Ewing's tumor (Table 1). One patient presented cardiac symptoms (frequent ventricular premature beat), and the other four patients were asymptomatic with the fractured PICC segments. The fractured PICC segments were retained in the vessels of the patients for 1 to 3 days. The fracture was diagnosed with chest plain film.

2.2. Techniques. Through percutaneous right femoral venous access, the 11 Fr. coaxial retrieval sheath system of a vena cava filter retrieval set (William Cook Europe Aps, Sandet 6, DK-4632, Bjaeverskov, Denmark) was advanced to the inferior vena cava over the wire guide (guide wire 0.035, 180 cm; Terumo Corporation, 44-1, 2-Chome, Hatagaya, Shibuya-ku, Tokyo 151-0072, Japan), and then the inner coaxial catheter and wire guide were removed. The position of the coaxial retrieval sheath system was verified by injecting contrast medium. A 5 Fr. pigtail catheter (straight pigtail 0.038, 110 cm; Terumo Corporation, 44-1, 2-Chome, Hatagaya, Shibuya-ku, Tokyo 151-0072, Japan) was placed at the fractured catheter body over the same wire guide. At the moment when the wire was removed, the fractured catheter body was grasped by the pigtail catheter. After the pigtail catheter and the fractured catheter coiled each other by rotating the pigtail catheter, the fractured catheter was brought to the lower segment of the inferior vena cava to be removed by pulling the pigtail catheter. After the pigtail catheter was removed, the retrieval loop system of the vena cava filter retrieval set was introduced through the coaxial retrieval sheath system to the inferior vena cava, until it was placed at the anterior end of the fractured catheter. At this moment, the fractured catheter was grasped by the device and taken to the sheath to be removed. A follow-up chest radiograph excluded residual fragments in the heart and the pulmonary artery, as well as the inferior vena cava. All the procedures should be performed under ECG guidance systematically.

3. Result

In this group of consecutive patients, the location of the fractured catheters was confirmed by an X-ray examination. The proximal and distal end of the fracture were located in the left and right branches of the pulmonary artery trunk, respectively, in two patients, and the proximal end was located in the superior vena cava and the distal end in the trunk of the pulmonary artery in two patients. The proximal end was located in the right atrium and the distal end in the right ventricle in one patient. All the fractured catheters were

removed successfully without complications (Figure 1). In all the cases, the right femoral access was used in 4 cases, and both the right femoral access and the left femoral access were used in 1 case. The median of duration time of the procedure is 9 min with a range of 7 to 69 min.

4. Discussion

If a catheter fracture occurs, the broken catheter will migrate distally along the blood stream and finally lodge in the superior vena cava, the right atrium, the right ventricle, the main pulmonary artery or its branches. Surov et al. [8] studied a total of 215 cases of intravenous catheter embolization. In their group, sites of catheter fragments were the superior vena cava or peripheral veins (15.4%), the right atrium (27.6%), right ventricle (22.0%), and pulmonary arteries (35.0%). The most common site for fragments was the pulmonary artery (35.0%). In this group, the proximal end and the distal end of the fracture were located in the left and right branches of the pulmonary artery trunk, respectively, in two patients; the proximal end was located in the superior vena cava and the distal end in the trunk of the pulmonary artery in two patients; and the proximal end was located in the right atrium and the distal end in the right ventricle in one patient.

The majority of patients have no or modest symptoms but substantial sequelae may develop. The clinical presentation of catheter embolization varies considerably. A systematic review [8] reported that the clinical signs included catheter malfunction (56.3%), arrhythmia (13.0%), pulmonary symptoms (4.7%), and septic syndromes (1.8%). In this study, only 1 patient presented frequent ventricular premature beat, and the other 4 patients were asymptomatic. Intravascular foreign bodies should be removed to prevent potentially lethal complications. When there are symptoms or the risk of infection is high, the foreign body should be removed promptly. If the catheter adheres to the wall of the right heart system, leading to incessant arrhythmia, or the catheter goes through the unclosed foramen ovale into the left heart system, leading to serious artery embolism, it needs to be removed urgently. Usually, transient arrhythmia (premature beat and tachycardia) related to endocardial catheter maneuvers may occur but disappears quickly after exiting the catheter.

Several percutaneous transcatheter retrieval techniques including a loop snare, a guide wire, a balloon, a forceps, and a basket catheter have been applied to remove cardiovascular catheter fragments and other foreign bodies [9–27]. The loop snare method is relatively safe with reliable effects, so it is currently widely used [9–11, 15–18]. However, when using a

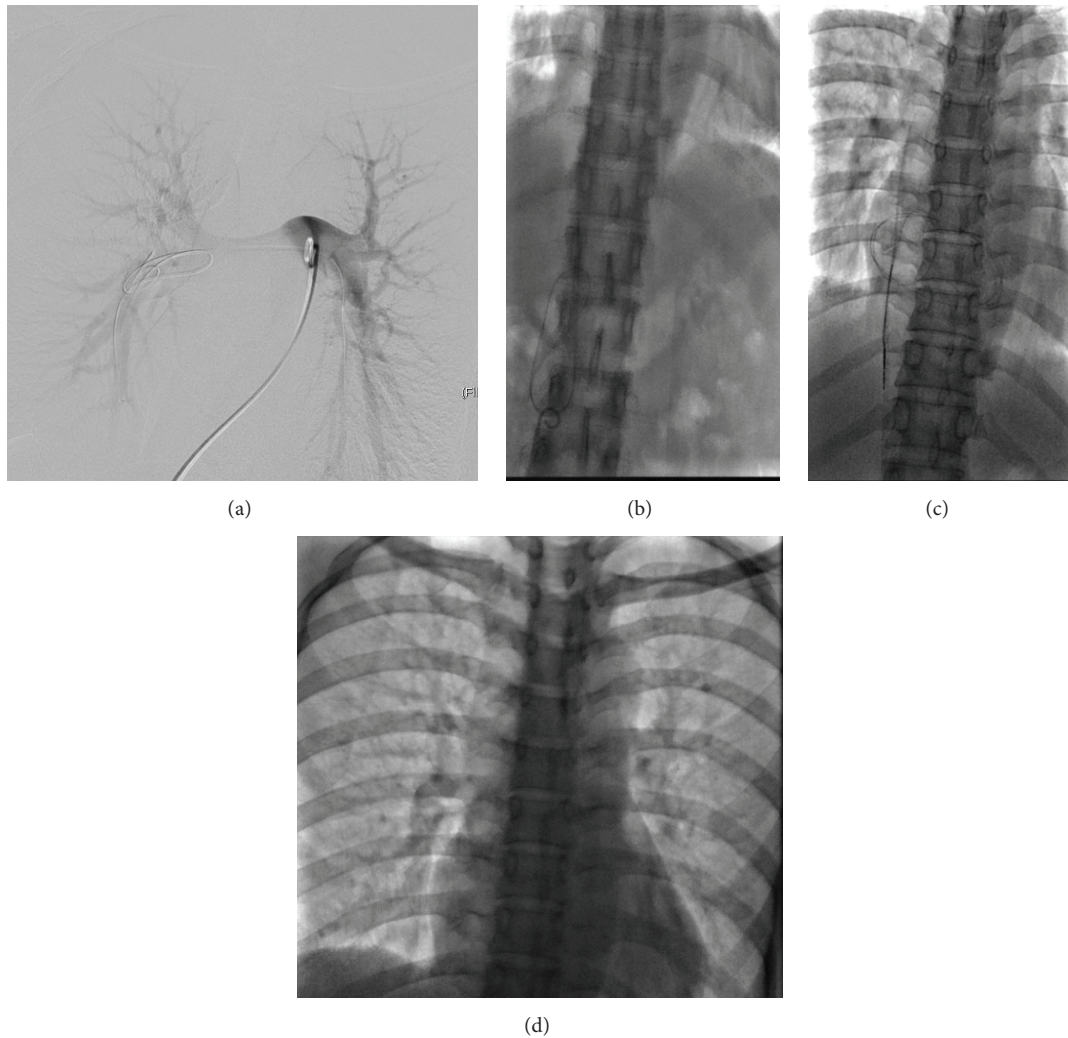


FIGURE 1: (a) The proximal and distal ends of the fractured catheter were located in the left and right branches of the pulmonary artery trunk, respectively, and the fractured catheter body was grasped by a pigtail catheter. (b) The fractured catheter was brought to the lower segment of the inferior vena cava to be removed. (c) The fractured catheter was grasped by the loop system of the vena cava filter retrieval set to be removed. (d) Chest radiograph after percutaneous retrieval of the fractured catheter, demonstrating the absence of any residual fragments.

loop snare to remove PICC fractures, the loop snare must be placed at the end of the catheter to grasp it. If the end of the catheter is lodged in the vessel wall or in a difficult plane, it will be difficult to grasp it successfully [19]. If the fractured catheter is located in the pulmonary artery, especially in the pulmonary artery branches, it will also be difficult to successfully grasp the end of the fractured catheter, because the movement of the loop cannot be easily controlled in the pulmonary artery and its branches. Teragawa et al. [9] reported a successful endovascular technique using a snare with a suture to retrieve a migrated broken PICC in the pulmonary artery of a chemotherapy patient. Although their technique is interesting and a useful method to control catheter movement, it may be associated with a risk of vascular injury and other unresolved problems, such as those relating to the thickness and type of suture used. Kawata et al. [10] experienced three cases of retrieval of silicone port catheters migrating into the cardiac ventricle or pulmonary

artery. Several devices, including a snare wire, an ablation catheter, and a basket catheter, in combination with an interventional guiding catheter were applied to retrieve them. Yen et al. [11] reported 13 patients who had an embolization caused by central venous catheter fragments including 4 PICCs, and they utilized the “goose-neck” snare to retrieve a catheter fragment with its free end floating in the pulmonary trunk. If the fractured catheter fragment was engaged in the trabecula of the right ventricle and could not be grasped by the loop snare, a floppy guide wire was inserted through the other vein to cross the fragment and grasp its tip using the loop snare. As discussed previously, a guide wire can be used with a catheter to construct a homemade loop snare. The technique of the balloon is useful in the recovery of stents; it requires a guide wire passing through the intravascular foreign body (IFB) or a portion of it. It is important to choose an appropriate retrieval balloon. If the balloon is too large, it will not pass the IFB; if the balloon is too small, it will not

capture the IFB [22, 28]. The grasping power of the forceps is advantageous in removing a foreign body strongly adhering to the vessel wall; however, in this case, to control the catheter head is difficult. The catheter material is stiff, and there is a danger of causing damage to vessels [22, 28, 29]. The basket is a well-known device that is often used in the biliary system. This catheter is capable of withdrawing relatively large foreign bodies and is preferred in situations where a foreign body is attached to the vessel wall without a free edge [29]. As it is made of stiff material with less flexibility, it can sometimes damage the vessel wall [22, 28, 29]. Another disadvantage of basket is its poor navigation capability [28].

In the present study, the fractured PICC segments located in the heart or the pulmonary artery were removed successfully using a pigtail catheter in combination with a vena cava filter retrieval set. However, there is a drawback of losing the retrieved catheter during the moment in between the two steps. If the fractured catheter fragment returns to the heart from the inferior vena cava, a pigtail catheter is inserted through the other femoral vein to bring the fractured catheter fragment to the lower segment of the inferior vena cava, and then it can be grasped and removed by the retrieval loop through the coaxial retrieval sheath system successfully. These procedures will increase the duration of the procedure. In this study, both the right femoral access and the left femoral access were used in 1 case; the duration of the procedure is 69 min.

Our experience is that the fractured catheter bodies in the heart or the pulmonary artery can be easily grasped using a pigtail catheter, and when the fractured catheters are brought to the inferior vena cava, they can also be easily grasped and removed using a vena cava filter retrieval set.

In conclusion, a two-step method of retrieving fractured PICC segments migrating into the heart or the pulmonary artery is described in this study. It adds a valuable technical option to the existing percutaneous techniques for retrieving cardiovascular foreign bodies.

Competing Interests

The authors declare that they have no competing interests.

References

- [1] V. Chopra, S. Anand, S. L. Krein, C. Chenoweth, and S. Saint, "Bloodstream infection, venous thrombosis, and peripherally inserted central catheters: reappraising the evidence," *American Journal of Medicine*, vol. 125, no. 8, pp. 733–741, 2012.
- [2] S. S. Amerasekera, C. M. Jones, R. Patel, and M. J. Cleasby, "Imaging of the complications of peripherally inserted central venous catheters," *Clinical Radiology*, vol. 64, no. 8, pp. 832–840, 2009.
- [3] C. Dupont, H. Gouya, R. Panzo et al., "Complications of peripherally inserted central catheters in adults with cystic fibrosis or bronchiectasis," *Journal of Vascular Access*, vol. 16, no. 3, pp. 245–249, 2015.
- [4] P. J. Carr and J. C. Rippey, "Upper extremity deep vein thrombosis: a complication of an indwelling peripherally inserted central venous catheter," *Clinical Case Reports*, vol. 3, no. 3, pp. 170–174, 2015.
- [5] P. Cotogni, C. Barbero, C. Garrino et al., "Peripherally inserted central catheters in non-hospitalized cancer patients: 5-year results of a prospective study," *Supportive Care in Cancer*, vol. 23, no. 2, pp. 403–409, 2014.
- [6] J. M. Motta Leal Filho, F. C. Carnevale, F. Nasser et al., "Endovascular techniques and procedures, methods for removal of intravascular foreign bodies," *A Revista Brasileira de Cirurgia Cardiovascular*, vol. 25, no. 2, pp. 202–208, 2010.
- [7] R. Sheth, V. Someshwar, and G. Warawdekar, "Percutaneous retrieval of misplaced intravascular foreign objects with the Dormia basket: an effective solution," *CardioVascular and Interventional Radiology*, vol. 30, no. 1, pp. 48–53, 2007.
- [8] A. Surov, A. Wienke, J. M. Carter et al., "Intravascular embolization of venous catheter causes, clinical signs, and management: a systematic review," *Journal of Parenteral and Enteral Nutrition*, vol. 33, no. 6, pp. 677–685, 2009.
- [9] H. Teragawa, T. Sueda, Y. Fujii et al., "Endovascular technique using a snare and suture for retrieving a migrated peripherally inserted central catheter in the left pulmonary artery," *World Journal of Cardiology*, vol. 5, no. 9, pp. 369–372, 2013.
- [10] M. Kawata, K. Ozawa, T. Matsuura et al., "Percutaneous interventional techniques to remove embolized silicone port catheters from heart and great vessels," *Cardiovascular Intervention and Therapeutics*, vol. 27, no. 3, pp. 196–200, 2012.
- [11] H.-J. Yen, B. Hwang, P.-C. Lee, and C. C. Meng, "Transcatheter retrieval of different types of central venous catheter fragment: experience in 13 cases," *Angiology*, vol. 57, no. 3, pp. 347–353, 2006.
- [12] M. Ootaki, S. Kuribayashi, and S. Matsuyama, "Percutaneous retrieval of intravascular foreign body from the pulmonary artery," *Nippon Igaku Hoshasen Gakkai Zasshi. Nippon Acta Radiologica*, vol. 53, no. 12, pp. 1374–1379, 1993.
- [13] F.-S. Yang, I. Ohta, H.-J. Chiang, J. C.-T. Lin, S.-L. Shih, and Y.-C. Ma, "Non-surgical retrieval of intravascular foreign body: experience of 12 cases," *European Journal of Radiology*, vol. 18, no. 1, pp. 1–5, 1994.
- [14] O. K. Kim, S. H. Kim, J. B. Kim et al., "Transluminal removal of a fractured and embolized indwelling central venous catheter in the pulmonary artery," *Korean Journal of Internal Medicine*, vol. 21, no. 3, pp. 187–190, 2006.
- [15] S. Cekirge, J. P. Weiss, R. G. Foster, H. L. Neiman, and G. K. McLean, "Percutaneous retrieval of foreign bodies: experience with the nitinol Goose Neck snare," *Journal of Vascular and Interventional Radiology*, vol. 4, no. 6, pp. 805–810, 1993.
- [16] J.-H. Jang, S.-I. Woo, D.-H. Yang, S.-D. Park, D.-H. Kim, and S.-H. Shin, "Successful coronary stent retrieval from the ascending aorta using a gooseneck snare kit," *Korean Journal of Internal Medicine*, vol. 28, no. 4, pp. 481–485, 2013.
- [17] M. Ghaderian, M. R. Sabri, and A. R. Ahmadi, "Percutaneous retrieval of an intracardiac central venous port fragment using snare with triple loops," *Journal of Research in Medical Sciences*, vol. 20, no. 1, pp. 97–99, 2015.
- [18] M. Bostan, M. Durakoğlugil, Ö. Satiroğlu, B. Erdivanli, and G. Tufan, "Retrieval of embolized tip of port catheter from branch of right pulmonary artery using a macro snare catheter," *Interventional Medicine and Applied Science*, vol. 6, no. 2, pp. 93–95, 2014.
- [19] A. K. Gupta, S. Purkayastha, and T. Krishnamoorthy, "Percutaneous retrieval of intravascular broken catheter fragments. A

- novel technique using a balloon,” *Interventional Neuroradiology*, vol. 11, no. 2, pp. 149–154, 2005.
- [20] A. A. Schricker, G. K. Feld, and S. Tsimikas, “Retrieval of a detached transseptal sheath tip from a right pulmonary artery branch following catheter ablation,” *Catheterization and Cardiovascular Interventions*, vol. 86, no. 6, pp. 1131–1135, 2015.
- [21] A. B. Ramondo, L. Favero, and R. Chioin, “Percutaneous retrieval of a broken catheter from the left atrium in an adult,” *Journal of Interventional Cardiology*, vol. 15, no. 5, pp. 417–419, 2002.
- [22] J. B. Woodhouse and R. Uberoi, “Techniques for intravascular foreign body retrieval,” *CardioVascular and Interventional Radiology*, vol. 36, no. 4, pp. 888–897, 2013.
- [23] H. Zamani, K. Babazadeh, R. Ghaffari, H. Karami, S. Fattahi, and F. M. Esbuie, “The successful withdrawal of a migrated central venous catheter,” *Caspian Journal of Internal Medicine*, vol. 3, no. 4, pp. 550–553, 2012.
- [24] M. Funami, T. Kashima, M. Aiba et al., “Technic of nonsurgical removal of iatrogenic catheter fragment from the heart with a modified basket grasping forceps,” *Kyobu Geka*, vol. 41, no. 7, pp. 566–567, 1988.
- [25] P.-C. Wang, H.-L. Liang, T.-H. Wu et al., “Percutaneous retrieval of dislodged central venous port catheter: experience of 25 patients in a single institute,” *Acta Radiologica*, vol. 50, no. 1, pp. 15–20, 2009.
- [26] J. B. Selby, C. J. Tegtmeier, and G. M. Bittner, “Experience with new retrieval forceps for foreign body removal in the vascular, urinary, and biliary systems,” *Radiology*, vol. 176, no. 2, pp. 535–538, 1990.
- [27] T. K. Egglin, K. W. Dickey, M. Rosenblatt, and J. S. Pollak, “Retrieval of intravascular foreign bodies: experience in 32 cases,” *American Journal of Roentgenology*, vol. 164, no. 5, pp. 1259–1264, 1995.
- [28] C. Floridi, L. Nocchi-Cardim, M. De Chiara, A. M. Ierardi, and G. Carrafiello, “Intravascular foreign bodies: what the radiologist needs to know,” *Seminars in Ultrasound, CT and MRI*, vol. 36, no. 1, pp. 73–79, 2015.
- [29] M. Tateishi and Y. Tomizawa, “Intravascular foreign bodies: danger of unretrieved fragmented medical devices,” *Journal of Artificial Organs*, vol. 12, no. 2, pp. 80–89, 2009.

Research Article

Fuzzy Clustering Applied to ROI Detection in Helical Thoracic CT Scans with a New Proposal and Variants

Alfonso Castro,¹ Alberto Rey,¹ Carmen Boveda,¹ Bernardino Arcay,¹ and Pedro Sanjurjo²

¹*Department of Information and Communication Technologies, Faculty of Computer Science, University of A Coruña, Campus de A Coruña, 15071 A Coruña, Spain*

²*Radiology Service, Meixoeiro Hospital, Camiño Meixoeiro, 36200 Vigo, Spain*

Correspondence should be addressed to Alberto Rey; alberto.rey@udc.es

Received 2 October 2015; Accepted 9 June 2016

Academic Editor: Kenji Suzuki

Copyright © 2016 Alfonso Castro et al. This is an open access article distributed under the Creative Commons Attribution License, which permits unrestricted use, distribution, and reproduction in any medium, provided the original work is properly cited.

The detection of pulmonary nodules is one of the most studied problems in the field of medical image analysis due to the great difficulty in the early detection of such nodules and their social impact. The traditional approach involves the development of a multistage CAD system capable of informing the radiologist of the presence or absence of nodules. One stage in such systems is the detection of ROI (regions of interest) that may be nodules in order to reduce the space of the problem. This paper evaluates fuzzy clustering algorithms that employ different classification strategies to achieve this goal. After characterising these algorithms, the authors propose a new algorithm and different variations to improve the results obtained initially. Finally it is shown as the most recent developments in fuzzy clustering are able to detect regions that may be nodules in CT studies. The algorithms were evaluated using helical thoracic CT scans obtained from the database of the LIDC (Lung Image Database Consortium).

1. Introduction

In the field of medical image analysis, the thorax area has been the object of extensive investigation [1] due to the complexity of the pulmonary structure itself, with approximately 23 generations of branching arteries, and the problems experienced in the detection of elements of interest within this structure (nodules, tumours, etc.) [2].

The most widely used images for diagnosis have traditionally been chest X-rays because of their low cost. However, images obtained using helical CTs are being used more and more since they enable high-definition observation of lung structures, allowing images to be acquired in intervals of time shorter than a breath and with resolutions of less 1 mm. It is becoming increasingly possible to find multislice CTs [3] which provide a more accurate image of the area under examination, although they are rather costly and still not very widespread.

Within this field, one of the problems that has received most attention is the detection of pulmonary nodules due to the high rates of lung cancer found in modern societies. This

disease has one of the highest mortality rates (Figure 1, [4]) and therefore early detection is fundamental [5].

The analysis of these types of studies is extremely time consuming for the radiologist because of the huge amount of data that has to be analyzed (more than 100 thin-section images) [6] and also due to the difficulty in distinguishing nodules in their initial phase because they are not clearly defined and due to their similarity to other elements present in the lungs. Clinically speaking, a solitary pulmonary nodule is considered to be any isolated and intrapulmonary lesion, rounded or oval in shape, surrounded by ventilated lung, whose diameter according to arbitrarily established criteria is less than 4 cm [7]. Furthermore, the contours of a nodule or mass must also be sufficiently defined and clear in order to be able to determine its approximate size with relative precision.

On the basis of the aforementioned information, multiple CAD (Computer Aided Diagnosis) systems have been developed to perform this task with a wide variety of techniques being used for this purpose: [8] proposed a multilevel thresholding technique designed to identify connected components of similar intensity and eliminate vessels present in the CT in

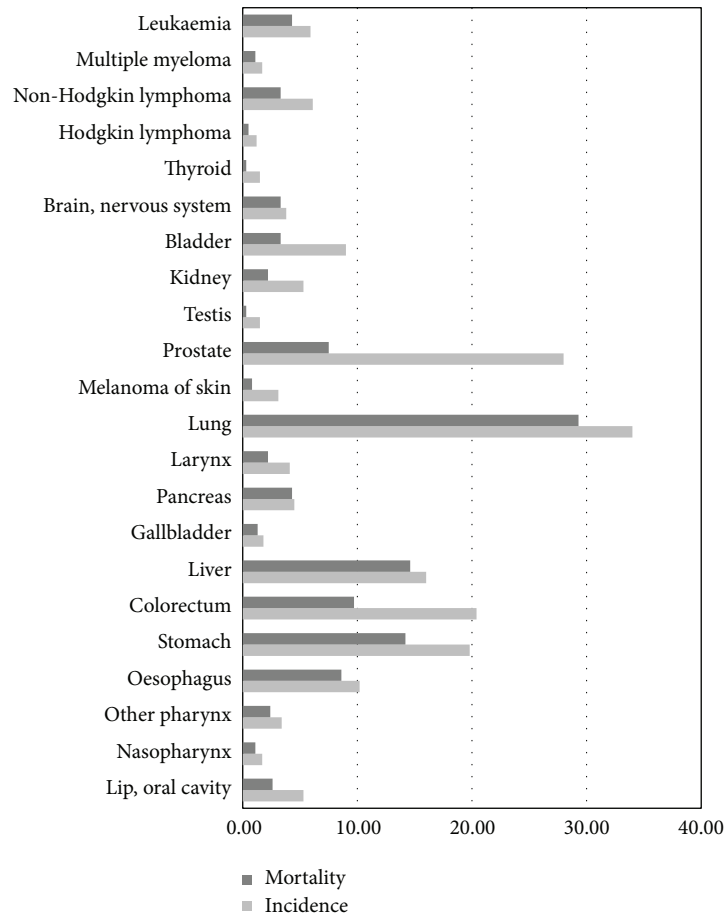


FIGURE 1: Incidence and mortality of different types of cancer in men.

order to detect nodules; [9] divided the CT into grids using a genetic algorithm that used a template to detect elements which could correspond with nodules; [10] proposed a new QCI filter as part of a CAD to detect nodules in CT; and [11] used thresholding and morphological operators to detect candidate nodules followed by the use of a Fisher Linear Discriminant classifier to reduce false positives. Other papers describing major systems within this area are [12–19].

Our research group is developing a CAD system to perform this task automatically. This system uses fuzzy logic as a basis for detecting lung nodule candidates and, in particular, fuzzy clustering algorithms.

In Figure 2 we can see the phases of a typical CAD system. The first task to be undertaken in pulmonary CAD systems is a preprocessing stage to isolate the pulmonary lobes, removing external elements that may affect classification. The system we are developing also includes an initial stage for this purpose [20, 21], Figure 3. In this process each of the unwanted elements (e.g., the diaphragm) is isolated and eliminated in a series of steps and when the only remaining elements are the lungs themselves, a range of morphological operations (opening, closing) are applied to eliminate any defects that might have arisen during the process, such as the recuperation of pixels previously eliminated from the juxta-pleural nodules.

This work focuses on the following phase, the purpose of which is to detect ROIs with a view to reducing the search area and obtaining the lowest possible number of candidate zones that may be nodules; the aim is to reduce the number of false positives and increase that of true positives. The objective is for this stage to be conducted automatically by the system given its advantages: a significant reduction in the workload of the specialist and the elimination of bias errors.

In this paper, we present and analyze the results of various fuzzy clustering algorithms that use different strategies to classify the pixels that make up an image. We also propose a new algorithm, formulated by merging two of the algorithms we have analyzed.

The FCM, KFCM, SFCM, and SKFCM algorithms were studied and the MSKFCM algorithm is proposed. The algorithms analyzed using spatial information were modified so that 3D neighborhoods could be used in the classification process (these algorithms were originally designed for use with 2D neighborhoods) which should allow for a better classification, working with further information, and offer a better reflection of the authentic anatomical structure.

Section 2 on material discusses the characteristics of the studies used in the tests and the tools employed to implement the algorithms. A description is then provided of each algorithm. Section 3 describes the methodology used in the tests.

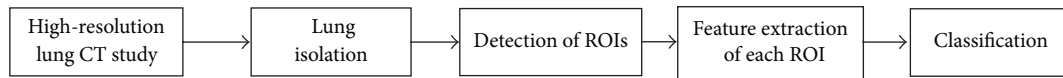


FIGURE 2: Phases of a CAD system.

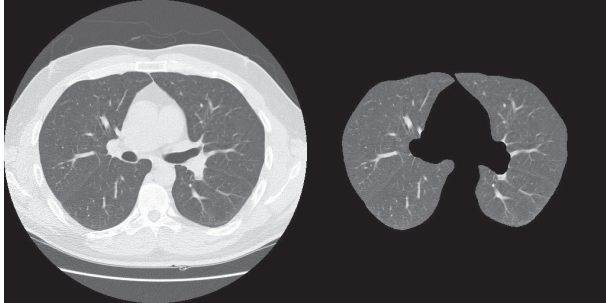


FIGURE 3: Original CT image and the result after applying the preprocessing stage to isolate the lungs.

In Section 4 we present and discuss the results obtained and the metrics used to take measurements. Finally, the conclusions will be considered.

2. Material and Methods

For the purposes of this analysis we used a set of helical thoracic CT scans from the LIDC (Lung Image Database Consortium) [22], which can be accessed from the National Biomedical Imaging Archive (NBIA).

The goal of this project is to develop a reference repository of CT lung images for the development and evaluation of CAD systems in the detection of lung nodules. Five North American institutions have collaborated in its construction: Cornell University; the University of California, Los Angeles; the University of Chicago; the University of Iowa; and the University of Michigan.

Each image was annotated by four experts, initially as a blind review, so that any discrepancies between annotations could then be forwarded to the corresponding experts, who could then make the appropriate amendments. The images are stored according to the DICOM standard, sized 512×512 , with a pixel size from 0.5 to 0.8 mm and a 12-bit grayscale of 12 bits in Hounsfield Units (HU). These CT scans were acquired from a wide range of scanner manufacturers and models under X-ray tube current ranging from 40 to 627 mA (mean: 221.1 mA) and tube voltage at either 120 or 140 kVp. The CT studies were reconstructed with pixel resolution ranging from 0.461 to 0.977 mm (mean: 0.688 mm) and slice thickness ranging from 0.45 to 5.0 mm (mean: 1.74 mm) [23].

Each analysis incorporates an XML file indicating the presence of one or more nodules (or their absence), their type, and their contour (specified by the coordinates of the constituent pixels).

Figure 4 shows some of the slices used in the study with the location of the nodule marked by a black rectangle.

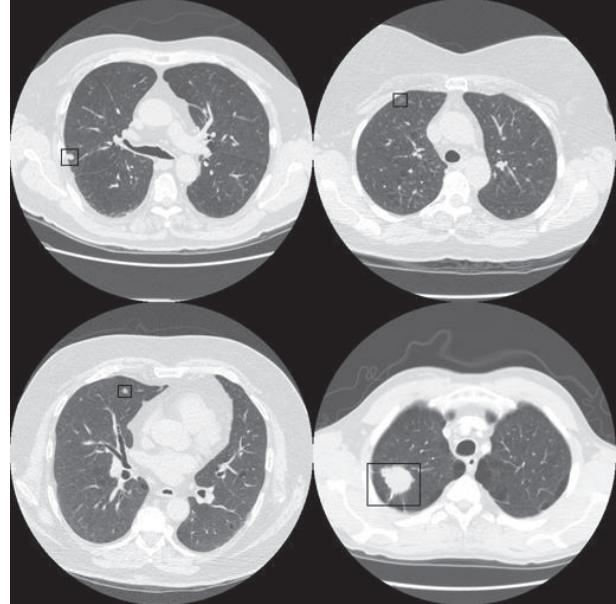


FIGURE 4: Different helical thoracic CT scans used in the tests with the nodule marked by a black rectangle.

Fuzzy clustering algorithms were used to detect ROIs due to their capacity for handling multidimensional information, making them easily adaptable for the classification of images, their low sensitivity to noise, which should make it easier to differentiate between nodules and other elements in images, and their capacity for handling ambiguous information, a common characteristic of medical images due to the low signal/noise ratio [24].

In the last years, new algorithms have been developed in order to resolve the problems associated with classical fuzzy algorithms and to provide better results [25–27]. In this paper, we selected some of the recent fuzzy algorithms that use kernel functions (KFCM) to simulate calculation in larger spaces or algorithms that use the pixel neighborhoods to calculate their membership (SFCM), increasing their insensitivity to noise. Moreover, those algorithms have been developed and tested within the medical image analysis field, being suitable to the problem described in this paper.

In this study, the two algorithms mentioned above were combined to obtain a new spatial kernelized algorithm and to determine whether the combination of these two techniques yielded better results than each technique individually for the problem addressed in this research. The SKFCM algorithm was analyzed to estimate the improvement that the new algorithm was expected to offer compared with the other algorithms using the same strategy. This has also been used for

medical imaging analysis and specifically for MRI (Magnetic Resonance Imaging) in brain scans [28].

To enhance the quality and increase the scope of the analysis, the spatial algorithms were modified so that 3D neighborhoods could be used. These neighborhoods enabled a better appreciation of the real structure of the element to be defined and used more information in the classification process. For this reason, we expected to obtain a better classification than by using 2D neighborhoods.

We also analyzed the FCM algorithm which was the first fuzzy clustering algorithm to be developed and is currently used as a reference in the literature.

The ITK toolkit was used to implement the algorithms. This is an open-source software toolkit for registering and segmenting medical images, developed in C++ using the generic programming paradigm. The algorithms were implemented using base classes since there was no support for fuzzy logic.

Details of the implementation of some algorithms used in this analysis were published in Insight Journal [29] and are freely available to any interested researchers to allow the scientific community to confirm that the algorithms were implemented correctly and facilitate their use.

2.1. FCM (Fuzzy C-Means). The FCM algorithm was developed by Bezdek et al. [30] and is the first fuzzy clustering algorithm. It is a method for the division of sets based on Picard iterations on the necessary conditions for calculating the minimum square error of the objective function:

$$J_m = \sum_{k=1}^n \sum_{i=1}^c (u_{ik})^m |x_k - v_i|^2. \quad (1)$$

In this algorithm, u_{ik} represents the membership value of pixel k to class i , x_k is the k th pixel, v_i the centroid for class i , c is the number of clusters, n is the number of pixels to classify, and m is a weight factor that must be bigger than 1. The FCM initially needs the number of clusters in which the image will be divided and a sample of each cluster.

The steps of this algorithm are as follows.

- (1) Calculation of the membership of each element to each cluster:

$$u_k(i, j) = \left(\frac{\sum_{j=1}^c \|y(i, j) - v_k\|^{2/(m-1)}}{\sum_{j=1}^c \|y(i, j) - v_j\|^{2/(m-1)}} \right)^{-1}, \quad (2)$$

$1 \leq k \leq c, 1 \leq i, j \leq n,$

where $y(i, j)$ represents each pixel of the initial image.

- (2) Calculation of the new centroids of the image:

$$v_k = \frac{\sum_{i,j} u_k(i, j)^m y(i, j)}{\sum_{i,j} u_k(i, j)^m}, \quad k = 1, \dots, c. \quad (3)$$

- (3) If the error stays below a certain threshold, stop. In the contrary case, return to step (1). The parameters that were varied in the analysis of the algorithm were the samples provided and the value of m .

2.2. KFCM (Kernelized Fuzzy C-Means). This algorithm was proposed in Chen and Zhang [31] and is based on FCM, integrated with a kernel function that allows the transfer of the data to a space with more dimensionality, which makes it easier to separate the clusters.

The purpose of the kernel function is to “simulate” the distances that would be obtained by transferring the points to a space with more dimensionality, which in most cases would imply exaggerated computational costs. The proposed objective function is

$$J_m = \sum_{i=1}^c \sum_{k=1}^n u_{ik}^m (1 - K(x_k, v_i)). \quad (4)$$

The kernel functions used most often are polynomial functions (5) and Gaussian radial basis functions (6). Consider

$$K(X, Y) = \varphi(X) \cdot \varphi(Y) = (X \cdot Y + b)^d, \quad (5)$$

$$K(X, Y) = \varphi(X) \cdot \varphi(Y) = \exp\left(-\frac{(X - Y)^2}{2\sigma^2}\right), \quad (6)$$

where σ is the sigma of the Gaussian function.

The algorithm consists of the following steps.

- (1) Calculation of the membership function:

$$u_{ik} = \frac{(1 - K(x_k, v_i))^{-1/(m-1)}}{\sum_{j=1}^c (1 - K(x_k, v_j))^{-1/(m-1)}}. \quad (7)$$

- (2) Calculation of the new kernel matrix $K(x_j, v_k)$ and $K(v_k, v_k)$:

$$v_i = \frac{\sum_{k=1}^n u_{ik}^m K(x_k, v_i) x_k}{\sum_{k=1}^n u_{ik}^m K(x_k, v_i)}. \quad (8)$$

- (3) If the error stays below a determined threshold, stop. In the contrary case, return to step (1).

The different parameters for the analysis of this algorithm were the initial samples and number of clusters.

2.3. SFCM (Spatial Fuzzy C-Means). This is a spatial fuzzy clustering algorithm [32] that uses a spatial function, which is the sum of the memberships of the pixels in the neighborhood of the pixel under consideration. The main advantages deriving from the use of a spatial function are the possibility of obtaining more homogeneous regions and less sensitivity to noise.

In the initial stage the algorithm applies the traditional FCM (Fuzzy C-Means) algorithm to obtain the initial memberships for each pixel, the iterative stage being omitted. It then calculates the spatial function value for each pixel in the image:

$$h_{ij} = \sum_{k \in \text{NB}(x_j)} u_{ik}, \quad (9)$$

where $NB(x_i)$ represents a square window centred around the pixel under consideration, its size being a configurable parameter of the algorithm. The greater the number of neighboring pixels that belong to the same cluster, the higher the value of the function.

The next step is to calculate the spatial membership function:

$$u'_{ij} = \frac{u_{ij}^p h_{ij}^q}{\sum_{k=1}^c u_{kj}^p h_{kj}^q}, \quad (10)$$

where p and q are control parameters for the importance of functions u_{ij} and h_{ij} . Finally, the new centroids are calculated:

$$c_j = \frac{\sum_{i=1}^N u'_{ij} x_i}{\sum_{i=1}^N u'_{ij}}. \quad (11)$$

The error is calculated. When this is below a determined threshold, the algorithm will stop; otherwise the FCM will be recalculated and a further iteration will commence.

2.4. SKFCM (Spatial Kernelized Fuzzy C-Means). This algorithm [28] introduces a penalty factor that contains spatial neighborhood information to the KFCM (Kernelized Fuzzy

C-Means) algorithm proposed in the same study. The paper only considers the Gaussian radial basis function kernel:

$$K(x, y) = \exp\left(-\frac{\|x - y\|^2}{\sigma^2}\right). \quad (12)$$

Therefore, modifying the objective function of the FCM in order to introduce the kernel function and add the penalty factor, we obtain the final objective function:

$$JS_m^\phi = \sum_{i=1}^c \sum_{k=1}^N u_{ik}^m (1 - K(x_k, v_i)) + \frac{\alpha}{N_R} \sum_{i=1}^c \sum_{k=1}^N u_{ik}^m \sum_{r \in N_k} (1 - K(x_r, v_i)), \quad (13)$$

where N_k represents the square window which includes the neighbors of pixel x_k (without considering it), N_R is the cardinality of N_k , and α ($0 < \alpha < 1$) is a parameter that controls the effect of the penalty term. Deriving the objective function (see (13)) with respect to u_{ik} and v_i , the authors obtained two conditions that minimize the objective function. Finally, an iterative algorithm can be derived from the above conditions.

When initialising the algorithm, the parameters c , that is, the number of clusters, the initial class centroids, and the threshold epsilon, must be determined.

In the first step of the iterative process, the memberships are calculated as follows:

$$u_{ik} = \frac{\left((1 - K(x_k, v_i)) + (\alpha/N_R) \sum_{r \in N_k} (1 - K(x_r, v_i))^m\right)^{-1/(m-1)}}{\sum_{j=1}^c \left(\left(1 - K(x_k, v_j)\right) + (\alpha/N_R) \sum_{r \in N_k} (1 - K(x_r, v_j))^m\right)^{-1/(m-1)}}. \quad (14)$$

Finally, the centroids are updated as follows:

$$v_i = \frac{\sum_{k=1}^n u_{ik}^m \left(K(x_k, v_i) x_k + (\alpha/N_R) \sum_{r \in N_k} K(x_r, v_i) x_r\right)}{\sum_{k=1}^n u_{ik}^m \left(K(x_k, v_i) + (\alpha/N_R) \sum_{r \in N_k} K(x_r, v_i)\right)}. \quad (15)$$

As in the other algorithms, repeat these steps until condition $\|v_{i-1} - v_i\| \leq \epsilon$ is satisfied, where epsilon is a determined threshold.

2.5. MSKFCM (Modified Spatial Kernelized Fuzzy C-Means). The modification proposed in this study ([29]) is a combination of the algorithms described previously (KFCM and SFCM) in order to combine their strengths. Thus, kernelized algorithms simulate the calculation of distances in a space of greater dimensionality, enabling better classification of elements. Spatial algorithms reduce sensitivity to noise and local variations by using the membership of all the pixels belonging to the neighborhood we wish to calculate.

The initial parameters required for the proposed modification are the number of clusters into which the image is to be divided, a sample of each cluster, and the values for the parameters p, q in order to calculate spatial membership.

The algorithm consists of the following steps.

(1) Calculation of the membership function:

$$u_{ik} = \frac{(1 - K(x_k, v_i))^{-1/(m-1)}}{\sum_{j=1}^c (1 - K(x_k, v_j))^{-1/(m-1)}}. \quad (16)$$

(2) Calculation of spatial memberships:

$$u'_{ik} = \frac{u_{ik}^p h_{ik}^q}{\sum_{j=1}^c u_{jk}^p h_{jk}^q} \quad (17)$$

with $h_{ik} = \sum_{z \in NB(x_k)} u_{iz}$, where NB is the neighborhood centred in x_k .

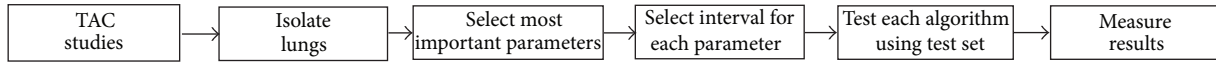


FIGURE 5: Flow chart followed to make the tests.

(3) Calculation of the new centroids:

$$v'_i = \frac{\sum_{k=1}^n u_{ik}^m K(x_k, v_i) x_k}{\sum_{k=1}^n u_{ik}^m K(x_k, v_i)}. \quad (18)$$

(4) If the error stays below a determined threshold $\|v_{i-1} - v_i\| \leq \epsilon$, stop. In the contrary case, return to step (1).

By combining what are currently the two most widely used techniques for developing fuzzy clustering algorithms, we aimed to improve the classification of the pixels forming the nodule, improve the detection of true positives using a kernel function to improve cluster separation, and reduce false positives using neighboring pixels to calculate membership. Consequently, it was determined that, with the exception of very fuzzy nodules, the pixels forming it had neighborhoods that allowed better differentiation from other areas of the image with similar values for each pixel.

3. Methodology

To carry out the analysis, a moderate number of studies were used to better determine the different features that influence the outcome and detect any possible problems that might arise. 1500 slices were used belonging to the nine studies which contain the different cases in this type of medical image: the initial stage, adherent to the pulmonary membrane, clearly consolidated, and located in the different thoracic zones: lower, middle, and upper.

In order to measure the success rate of the algorithms we decided to calculate the number of true positives (TP) and false positives (FP), sensitivity against sensibility, considering the true positive as those pixels that are part of the nodule and they are classified as nodule. Oppositely, false positives are pixels classified as nodule but really they are part of another element of the slice. An algorithm that correctly classifies the nodules must assign a high number of true positives and a low number of false positives. If other values were obtained, this would indicate that the algorithm performed a poor classification, either because the rate of success in terms of the classification of the nodule pixels was low or because the algorithm incorrectly classified a large number of pixels that were not nodule as nodule pixels.

The traditional method used to evaluate CAD systems is to use the outcome for a series of cases for which the results are known and to construct a ROC curve on the basis of TPF (True-Positive Fraction) and FPR (False-Positive Fraction) [33] so that the quality of the system can be observed as well as the outcome through the variation of different parameters. However, given the declared aim of this work, this is not the most adequate focus, given that the objective of this module is not to identify the ultimate outcome but to reduce the search space to localize those zones that may be nodules.

For this reason, we decided to use the approximation proposed by Bowyer [34] to evaluate edge detection algorithms. In this framework, each set of parameter values for each edge detector and image will produce a count of true-edge pixels and false-edge pixels. By sampling broadly enough in the parameter space for an edge detector, and at fine enough intervals, it is possible to produce a representative range of possible tradeoffs in true versus false positives. This results in a graphical representation of possible “true positive/false positives” tradeoffs similar to a receiver operating characteristic (ROC) curve. This provides a comparison of the behaviour of the algorithm for different parameters and the selection of the best combination, adapted and aligned to our aim.

Another factor that favored this solution for evaluating these results from fuzzy clustering algorithms was that the masks supplied by the LIDC for the different slices only contain information about the nodules indicating the points that constitute their edge and type, with no data on the other elements that may exist in each slice. The use of other measurements would involve creating masks with the correct classification for each pixel in each slice and for each study which is beyond the capacity of our group. Even so, we had to create an application using XML files that provides LIDC for each study with the data of the nodules for each slice and translates this information as a representation allowing for a rapid and efficient evaluation.

In Figure 5 the steps followed to make the tests can be seen. In first place, a preprocessing was applied to all the studies with the objective of isolating the lungs. In the next step, the relevant parameters were identified that influenced the results obtained for each algorithm. In the fourth step, we determine the test interval for each parameter of each algorithm, in order to reduce the search space. In this sense, different values were tested based on a fixed space covering the entire interval. Following that, we test each algorithm and the different combination of parameters over the data set. Finally, we evaluate the results obtained for each slice applying each algorithm with its combinations of parameters.

Table 1 shows the parameters analyzed for each algorithm and the ranges used for each parameter analyzed. The first parameter analyzed was the number of clusters into which the image was to be divided; the best results were obtained with three and four clusters; a different set of test images and different validity indices were used [35, 36]. The second parameters were the number and initial samples used for initialisation since these parameters could induce variations in algorithm convergence speed and results [37]. We decided to use samples that were obtained randomly and through an operator for each slice. Finally, it was observed that for parameters p and q of the SFCM and MKSFCM algorithms the best results were obtained in the interval $[0, 2]$.

To illustrate the results we will use graphs that allow us to see the conditions in which the best results were obtained

TABLE 1: Parameters analyzed and most relevant values identified for each parameter.

FCM	Number of clusters	[3, 4]
	Set of initial samples	Random Operator
KFCM	Number of clusters	[3, 4]
	Set of initial samples	Random Operator
	σ	[150, 750]
SFCM	Number of clusters	[3, 4]
	Set of initial samples	Random Operator
	p	[0, 2]
	q	[0, 2]
SKFCM	Number of clusters	[3, 4]
	Set of initial samples	Random Operator
	σ	[150, 750]
MSKFCM	Number of clusters	[3, 4]
	Set of initial samples	Random Operator
	p	[0, 2]
	q	[0, 2]
	σ	[150, 750]

for each algorithm. The aim is to estimate how stable they are and to visualize their behaviour for our studies. In order to improve the clarity in the presentation of the results, each algorithm will be presented using a different subsection.

4. Results

The first algorithm analyzed was the FCM due to its current status as a reference algorithm, as mentioned above.

4.1. *FCM*. Figure 6 shows the results obtained for this algorithm in one study; the algorithm is used with samples selected by an operator (a radiologist) with each result represented by a point. For this algorithm, it was decided to represent the TP against sensitivity to better observe its behaviour. It can be observed in the graph that variability is quite high for the different slices: there are cases where the success rate is very low (below 40%) or very high (close to 100%); in addition the number of false positives is also high increasing with the success rate. The behaviour of the algorithm in the rest of the studies was similar.

This result is due to the FCM algorithm classifying by means of hyperspheres (if the Euclidean distance is used in the calculation of the memberships); it is not possible to separate mixed classes that have different structures [38], as is the present case, which impedes the algorithm from calculating centroids of sufficient quality to produce a good partitioning of the image. Further evidence that corroborates this fact is the results obtained using random samples, in which the values for TP and FP measurements were similar to those

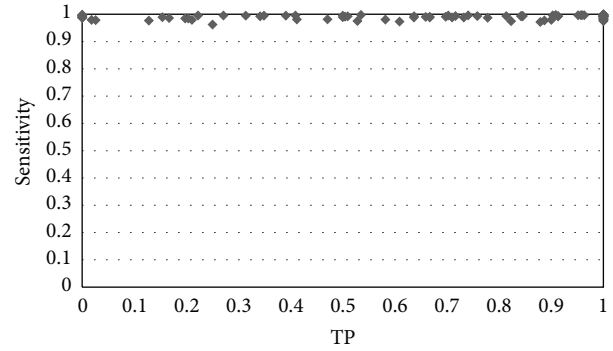


FIGURE 6: Results obtained for the FCM algorithm for one of the analyzed studies.

obtained using samples selected by an operator (the difference was less than 1%), which shows that the result principally depends on membership function used in the classification rather than the samples used.

Figure 7 shows the result for the FCM algorithm for one of the slices used in the tests in which it can be observed that while the algorithm is able to detect a part of the nodule, there are an elevated number of false positives. The same slice will be used in the remainder of the paper to illustrate the results of the different algorithms and to facilitate their comparison.

4.2. *KFCM*. A Gaussian kernel was used in the testing process for the KFCM algorithm. Figure 8 shows the results for this algorithm in all the analysis studies. In the graph, it can be observed that a high success rate for a significant number of slices was achieved. Nevertheless, the results indicate that this algorithm is not adequate for the automatic detection of ROIs, the aim of this paper. Although the success rate for the majority of slices is high (more than 65%), the noise level is very high (more than 30% in almost all). This can be clearly seen in the graph with the majority of points situated in the upper right corner making them very difficult to eliminate.

Figure 9 shows the results obtained for 23 slices selected from all the studies analyzed in order to obtain a clearer insight into these results. This combination of slices was also used to illustrate the behaviour of the rest of the algorithms to allow for the comparison of the results and the performance of each algorithm. The graph shows how false positives reach 70% in various slices and are not lower than 20–30% in almost all. This implies that, even with the construction of an efficient classifier for the following stage, it would be extremely difficult to eradicate these erroneous zones from the result. An elevated number shows features that are very similar to those of a nodule, such as midrange HU values, shape, and size, which makes it very difficult to establish criteria that allow for a good classification.

The kernelized function employed by this algorithm is not able to discriminate between the pixels that belong to each cluster because of the overlap existing between the pixels in different clusters given that the only information that the algorithm uses is the attenuation value, which for the majority of pixels is very close for the nodule and the lung tissue.

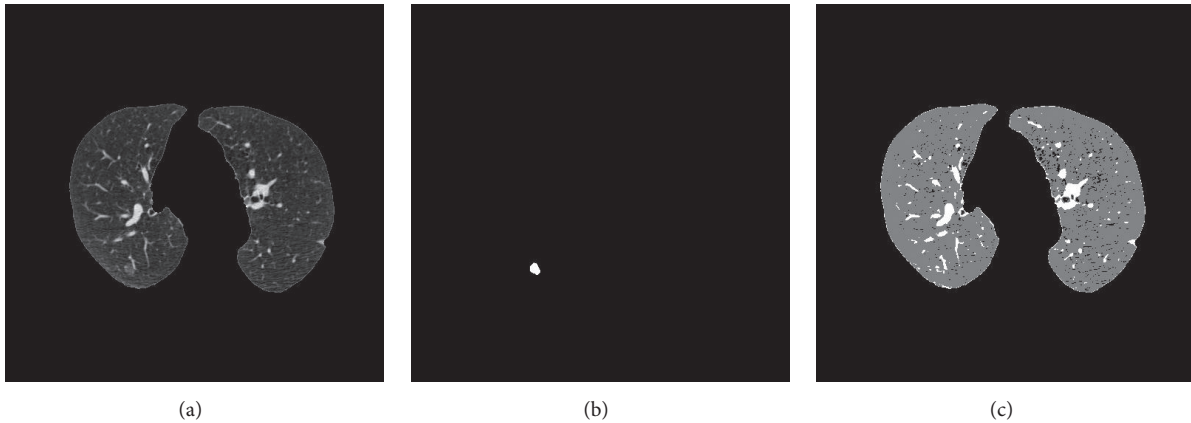


FIGURE 7: (a) Original image, (b) mask, and (c) result obtained for the FCM algorithm.

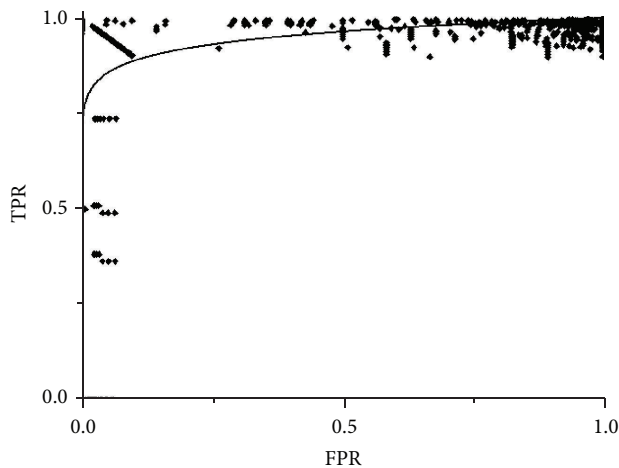


FIGURE 8: Results obtained for the KFCM algorithm for the different studies.

As such, this algorithm provides a good classification and a quality result for each slice or, if there are many serious errors, a low quality result. There is a substantial range in the success rate from 10 to 90%. Figure 10 shows a slice result typical of the majority of cases. It can be seen that the algorithm correctly classifies almost all the pixels of the nodule but the number of false positives is very high complicating, to a large extent, the analysis in subsequent stages.

4.3. SFCM. The next algorithm to be analyzed was SFCM and Figure 11 shows the results of its application to the pool of test studies. What is notable about this algorithm, and clearly visible in the previous graph, is the low number of false positives produced (10–15% in almost slices). The reason for this result is the spatial character of the algorithm which makes it easier to differentiate (compared with the previously analyzed algorithms) the pixels which make up the nodule and those pixels which are part of the tissue when using the neighboring space to calculate membership. However this algorithm is unable of achieving a high success rate in the detection of the nodule in the majority of slices. It was only

able to achieve an adequate level of success in about 30% of the slices which can be observed in Figure 12 in the distribution of points along the TP axis. This means that it is not a good option for the aim we have in mind in this paper, given that it cannot provide, with its high level of variability, a consistent rate of success for all the test studies.

Figure 12 shows the results obtained for the selected slices which are similar to those for the complete study: the number of false positives is low with a high success rate but clear variability depending on the slice. Selected samples were used in these tests. The slices with a low success rate were 2, 11, 18, and 7. The best results were obtained by partitioning the image in 3 clusters with the number of false positives less than if it was partitioned in 4 clusters without significantly reducing the true positives. However, the differences in the results were minimal when the only parameter varied was the samples: random or operator-selected.

This, in our view, does not indicate a limitation in this algorithm as it does in the FCM algorithm because, to obtain good results, it is necessary that the spatial function is the component with greater weight in the membership function. It is used as an additional characteristic to calculate the value of membership allowing the discrimination between pixels of different clusters based on neighborhood; so the more the importance it has, the less the number of false positives. This, however, causes the initial samples to have much less weight in the classification with the FCM membership much less valued and its influence on the final result much less. Figure 13 shows a result for one of the test slices.

4.4. SKFCM. The results obtained for the algorithm SKFCM show a low level of false positives using selected samples. The best results were obtained by dividing the image into three clusters and using a spatial window 3×3 ; the success rate was above 80% for the majority of slices with the false positives lower than 20% for most of the study. Figure 14 shows the results obtained for all the studies used in the analysis.

The figure of true positives, using random samples, is grouped within the range of 60%–100%, although values of below 20% can be observed in some slices as, for example, slice numbered 2 (15% with random samples) (Figure 15). In

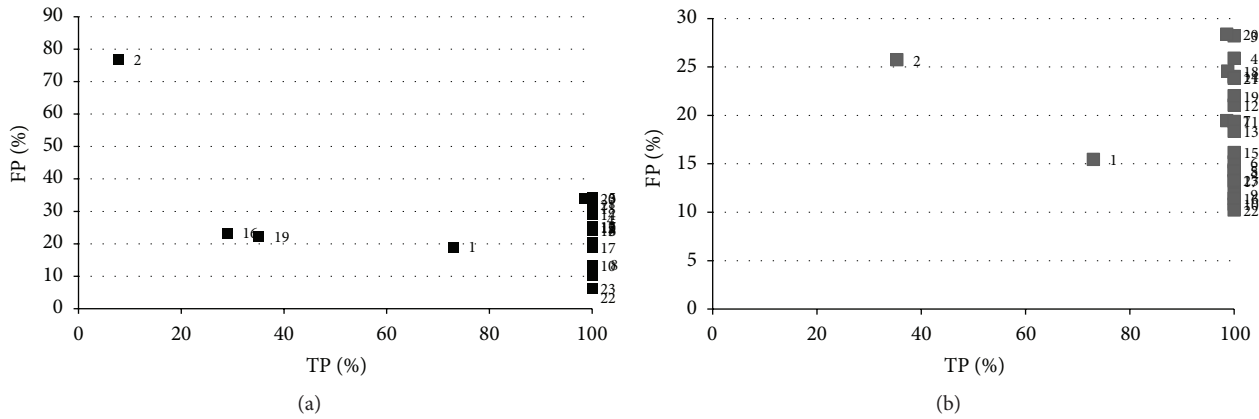


FIGURE 9: Results for a set of slices selected for the KFCM algorithm: (a) random samples, (b) operator samples.



FIGURE 10: Image result for the KFCM algorithm.

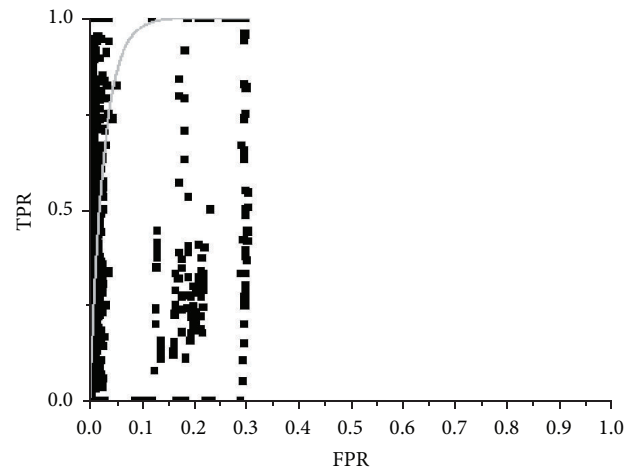


FIGURE 11: Results obtained for the SFCM algorithm.

the latter case, this results from the loss of pixels from the nodule during the preprocessing stage of the lungs and, above all, from the inability of the algorithm to divide the more complicated slices for classification.

The most critical entry parameter for this algorithm is the sigma selection (Figure 16), obtaining significant variations in the results for the false positives varying this parameter, creating associated problems in the ROI classification at the next stage, and making identification of nodules difficult (Figure 16(b)).

In Figure 15, the results, using random and selected samples, can be observed having good ratios of true positives of around 100% for the greater part of the study using operator samples, although they do present a greater number of false positives with respect to using random samples. In the latter case, it can be seen that the success rate decreases for some images, to a range of between 50 and 100%.

The size of the neighboring window has not produced significant variations with its best value as indicated previously. This is due to the membership function having a strong dependence on the kernel function, which is strongly influenced by the initially selected samples.

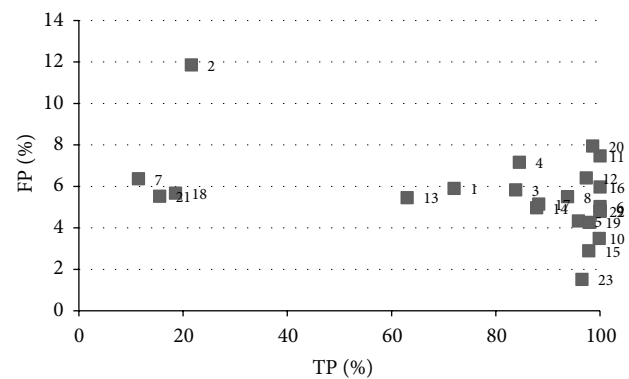


FIGURE 12: Results obtained for the SFCM algorithm.

4.5. *MSKFCM*. Finally, we will analyze the results of the new algorithm we are proposing which combines the two previous strategies, the objective of which is to improve classification using a kernelized function and to decrease the false positives taking into account the spatiality of each pixel. This is the trend that the most recent algorithms follow.



FIGURE 13: Resulting image for the SFCM algorithm.

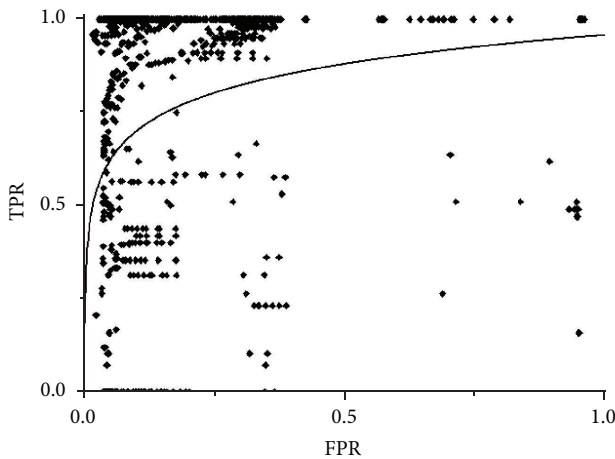


FIGURE 14: Results obtained for the SKFCM study set.

It can be observed in Figure 18 how the algorithm achieves a good success rate for almost all images with a low number of false positives (the worst result around 15%). This behaviour can also be seen in Figure 17 where the number of false positives has decreased substantially compared to other algorithms analyzed, maintaining a high success rate (>60%) for the majority of slices. It should be pointed out that although the curve is similar to that of SKFCM, this is due, not to the similar behaviour of the algorithm, but to the fitting function used.

By analyzing more in detail the results of the selected set of slices, the success rate deteriorated in the case of random samples ($\approx 10\%$); we can also see a low rate of false positives was maintained, and in some cases improved results were obtained (Figure 17). Individually examining each slice with a low rate success, it can be seen that the lost part of the nodule in the majority of the slices could later be recovered using other techniques. Figure 19 shows an example of a result applying this algorithm.

This algorithm also displays a more stable performance than the others (Table 2). A problem observed with the other

TABLE 2: Results (%) for a subset of slices displaying the greatest problems for the algorithms using spatial information.

	SFCM			SKFCM			MSKFCM			
	3×3	5×5	7×7	3×3	5×5	7×7	3×3	5×5	7×7	
1	TP	72.0	72.0	71.0	73.0	73.0	66.0	64.0	58.0	56.0
	FP	5.9	5.5	5.1	9.1	9.7	12.6	9.5	9.7	9.4
2	TP	21.6	19.6	19.6	31.4	33.3	33.3	29.4	29.4	29.4
	FP	11.9	11.7	11.6	14.3	17.3	18.5	21.2	21.3	21.1
7	TP	11.4	8.6	5.7	95.7	95.7	94.3	61.4	64.3	60.0
	FP	6.4	5.9	5.4	14.0	12.4	10.3	9.9	10.2	9.7
13	TP	62.9	59.3	55.6	96.3	100.0	96.3	96.3	100.0	92.6
	FP	5.5	4.9	4.6	11.8	11.2	10.2	8.9	10.1	8.9
17	TP	88.2	88.2	85.3	100.0	100.0	100.0	97.1	97.1	97.1
	FP	5.1	4.8	4.6	10.4	10.7	9.8	6.6	6.8	7.0
21	TP	15.5	8.4	5.6	100.0	100.0	100.0	69.0	81.7	81.7
	FP	5.5	4.9	4.5	14.4	11.3	9.0	8.5	9.9	9.4

algorithms is that when the sample set was modified in order to improve the results, there was also a variation in the cluster to which the nodule was assigned, depending on the initialisation and the number of clusters into which the slice had been divided. In the case of the new algorithm, however, when the number of clusters is set at 3, it consistently classifies the nodule in the same cluster, in addition to a good and stable performance with random samples, automated classification, which was the objective outlined at the beginning of this paper.

4.6. 3D Neighborhood. From the analysis of the results, it can be deduced that the algorithms which best address the problem presented in this paper are those which use spatial membership functions and, among these, those which combine this technique with a kernelized membership. To improve these results, we decided to modify the spatial kernelized algorithms to use 3D instead of 2D neighborhoods in the calculation of the memberships.

Helical thoracic CT scans allow for a 3D reconstruction of the target zone that is very similar to the original, given the high levels of resolution it is able to achieve. The use of the 3D structure instead of 2D provides more information when calculating memberships and avoids noise and loss of information associated with projecting a 3D structure in 2D.

This modification was applied to those algorithms which provided the best results and presented more stable behaviour during the analysis: SKFCM and MKSFCM. Figure 20 presents the scheme followed to obtain 3D neighborhood and the pixels that are used to calculate the spatial function for a $3 \times 3 \times 3$ neighborhood, formed by the slice that the pixel belongs to; the previous and following in the form of a rectangular prism. It should be noted that, in its implementation using ITK, any shape (spherical, rhomboid) can be used to obtain the neighborhood.

The methodology, described for the test process in Section 3, was applied and in order to allow a direct comparison of the results, which were obtained in the same way from the same set of images, the test unit was the study and not

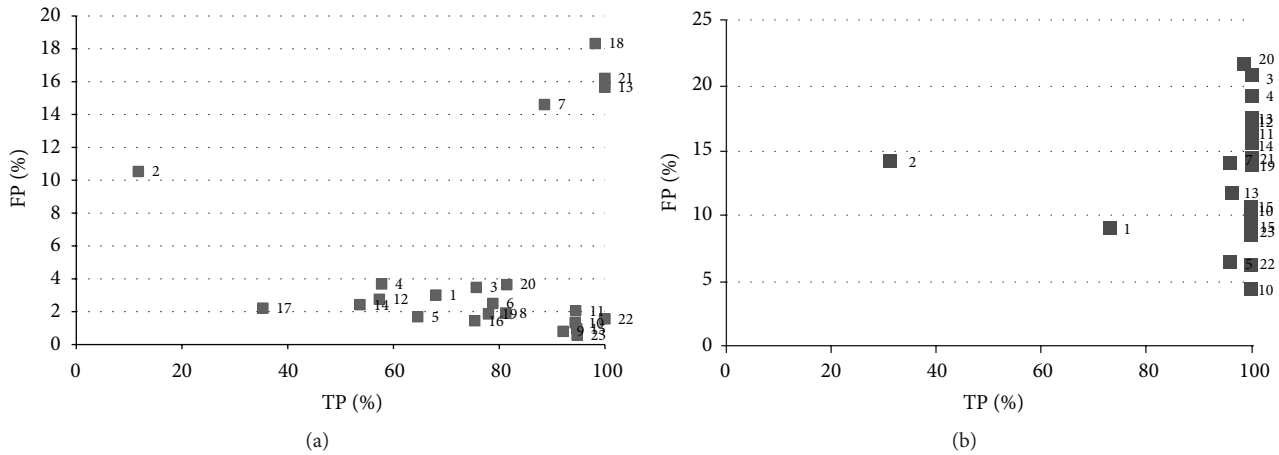


FIGURE 15: Results obtained for the SKFCM for the selected subset: (a) random samples, (b) operator samples.

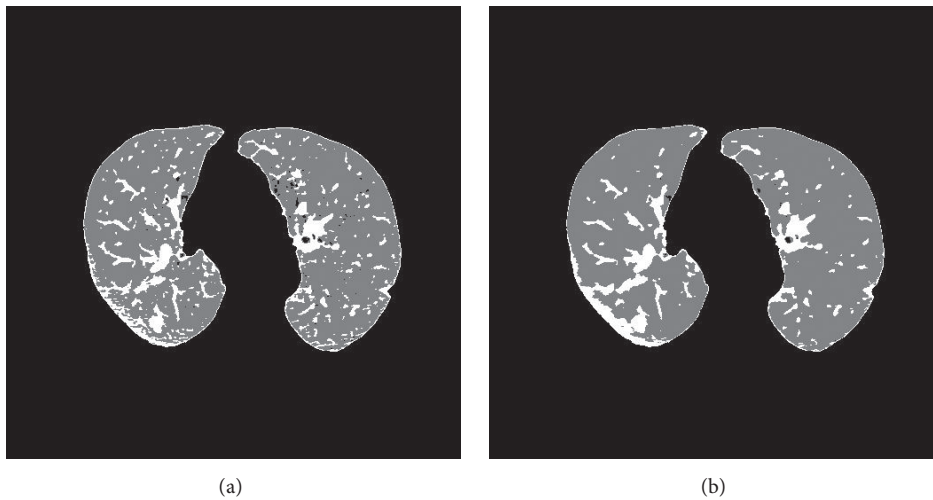


FIGURE 16: Results obtained for the algorithm SKFCM using different sigmas: (a) $\sigma = 250$, (b) $\sigma = 500$.

the slice. For the two algorithms, tridimensional neighborhoods sized 3, 5, and 7 were used in rectangular prism. The parameters modified for the MSKFCM algorithm were σ in [150, 700] and p and q in [1, 2]. For the SKFCM the modified parameters were σ in [150, 700] and α in [0.1, 0.2]. The analysis of the results was conducted by slice for direct comparison with those obtained in previous tests.

The success rate, in the results obtained for the 3D version of MSKFCM, was close to 100% in more than 90% of the slices analyzed and the false positives did not exceed 18% in any of the slices. The slices that had a low success rate were juxtapleural nodules with problems, at the initial preprocessing stage, in maintaining all the points that belong to the nodule and nodules marked with a single pixel and classified as having an indefinite nature in the database. As such, and not being able to identify them as a nodule or not, they were of no interest to the present study.

It is worth noting in the results that using larger neighborhoods reduced the number of TPs and FPs until, in extreme cases, the algorithm does not detect any pixel as belonging to the nodule. The best results for success rates and greater

stability were obtained using 3D neighborhoods sized $3 \times 3 \times 3$.

The success rate for 3D SKFCM was similar to the previous algorithm at around 100%. However, the FP figure was high exceeding 60% in the poorest results. In addition, stability was low with a lot of variabilities in the results for different slices and the same slice with different parameters. The best results were obtained using small α , reducing the weight of the spatial factor. The behaviour of this algorithm is opposite to that of 3D MSKFCM: the greater the size of the neighborhood, the more the TPs and FPs increased.

For both algorithms, it was proven that the greater the size of the neighborhood, the greater the tendency of the algorithms to classify all the points in one cluster; the 3D distribution of the points does not correspond with the anticipated shape by the membership function (the membership function of the algorithms is based on FCM) resulting in an accumulation of errors in the classification.

The SKFCM algorithm tends to group all the pixels in the cluster identified as a nodule, because, with most important factor being the initial samples or centroids (in this case,

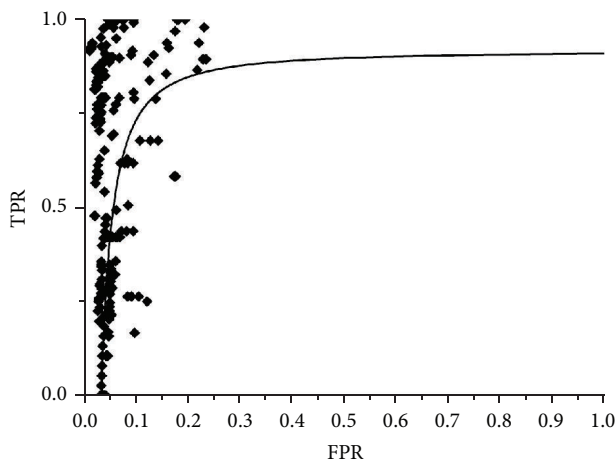


FIGURE 17: Results obtained in all studies for the MSKFCM algorithm.

the pixels which have been identified as belonging to the nodule are prioritized), the accumulation of errors means that more and more pixels associate with this cluster. MKFCM, for its part, groups all the pixels in one cluster, identified as a lung, giving more weight to those pixels which form part of the neighborhood than to the centroids in the calculation of memberships, as the majority of the pixels in the slice are lung owing to the preprocessing which seeks to eliminate all elements of no interest; therefore, all of the pixels end up being assigned to this cluster.

Table 3 shows the results for the two algorithms for a combination of slices (for this table, different slices have been used from those used in Tables 2 and 4), selected from the nine studies using 2D and 3D neighborhoods; those that best reflect the behaviour of all the set have been chosen. The most notable aspect of all the results obtained is that the two types of neighborhoods are similar for the majority of cases. This is due to the spatial functions having been designed for work with 2D neighborhoods, unable to benefit from the additional information provided with the use of 3D neighborhoods.

As such, the algorithm which provides the best results using 3D neighborhoods is MKSFCM, the results of which are similar to the 2D algorithm with an improvement in results in only some slices.

5. Discussion

The most complicated pixels to classify correctly are those which belong to less well defined nodules, still at a very initial stage or juxtapleural, which are very difficult to distinguish from other pulmonary elements.

This was confirmed using the first version of the masks for the studies provided by the LIDC. Each pixel in these masks was assigned a value between 0 and 1000, representing the level of consensus among radiologists that the pixel under consideration belonged to a nodule (1000 indicates that all radiologists are in agreement with the membership of the pixel to a nodule and 0 that all were in agreement that it did not belong to a nodule). For those pixels, where there was

TABLE 3: Results for slices from different studies using 2D and 3D neighborhoods.

		3 × 3		5 × 5		7 × 7		
		2D	3D	2D	3D	2D	3D	
1	MKSFCM	VP	61.8	61.8	43.6	60	41.8	50.9
		FP	6.9	7.3	3.8	6.3	3.6	5.9
	SKFCM	VP	49.1	63.6	49.1	63.6	60	63.6
		FP	5	34.2	5.2	29.4	5.8	31.3
2	MKSFCM	VP	30.9	49.4	27.2	45.7	23.5	42
		FP	3.3	5.7	3.1	5	2.9	4.4
	SKFCM	VP	34.6	51.9	34.6	51.9	35.8	53.1
		FP	3.7	26.3	3.7	29.6	3.70	31.1
3	MKSFCM	VP	100	95.7	65.2	30.4	47.8	21.7
		FP	4.8	3.6	3.8	1.9	1.8	1.7
	SKFCM	VP	95.7	100	100	100	100	100
		FP	3.5	10.1	8	19.2	14.9	23.4
4	MKSFCM	VP	100	95	95	95	90	95
		FP	9.4	6.3	6	5.5	5	5.3
	SKFCM	VP	100	100	100	100	100	100
		FP	30.8	23.8	32.8	26.6	34.3	41.7
5	MKSFCM	VP	78.9	78.9	78.9	78.9	0	76.3
		FP	13.6	13.7	9.5	13.9	3	14.5
	SKFCM	VP	89.5	89.5	89.5	89.5	89.5	92.1
		FP	20.9	35.2	26.1	38.5	28.7	40.1
6	MKSFCM	VP	96.9	90.70	93.8	88.7	85.6	67
		FP	17.4	6.7	15.8	4.3	15.7	3.7
	SKFCM	VP	97.9	97.3	99	97.9	99	97.9
		FP	31.1	21.3	33.5	27.5	35.3	30.2
7	MKSFCM	VP	43.8	43.8	42.2	42.2	42.2	32.8
		FP	7	6.8	6.2	5.5	5.3	4.7
	SKFCM	VP	43.8	43.8	43.8	43.8	43.8	43.8
		FP	9.7	8.4	15.3	15.9	21	21.2
8	MKSFCM	VP	98.8	97.6	97.6	84.5	100	84.5
		FP	4.6	3.8	3.6	2.6	4.4	2.4
	SKFCM	VP	100	100	100	100	100	100
		FP	6	5.2	8.6	10.1	11.7	14.2
9	MKSFCM	VP	97.8	95.1	92.2	92.1	91.6	91.6
		FP	5.5	1.7	1.1	1.1	0.9	0.9
	SKFCM	VP	97	97.8	100	100	100	100
		FP	2.4	5.9	13	14.7	17.1	19.2

strong agreement among the radiologists over membership to a nodule (with a punctuation equal to or above 800 points) both SKFCM and MSKFCM were capable of detecting them without any problems.

Figure 21 shows a section of a slice classified as a nodule by radiologists and the different results provided by the algorithms which have been considered in this study. The majority of classification errors correspond to pixels with a low punctuation (100–200) especially those at the edge of the nodule.

The best results and performance of the MKSFCM algorithm were obtained by dividing the slices into three clusters.

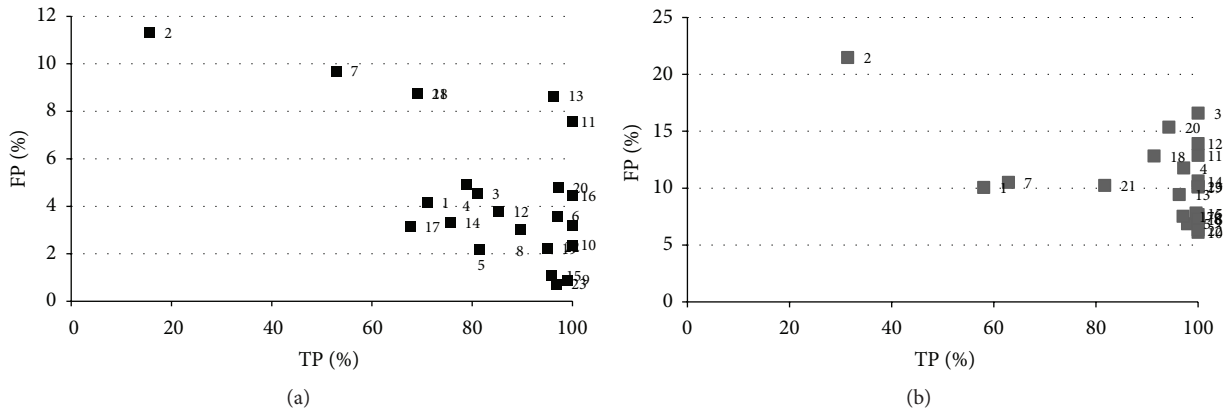


FIGURE 18: Results obtained for the MSKFCM for the selected subset: (a) random samples, (b) operator samples.



FIGURE 19: Results obtained for the algorithm MSKFCM for one of the slices using random samples.

TABLE 4: Results (%) for a subset of slices which present greater problems for the different algorithms.

		FCM	SFCM	KFCM	SKFCM	MKSFCM
1	TP	72	72	73	73	64
	FP	6.4	5.9	15.4	9.7	9.5
2	TP	23.5	21.6	35.3	33.3	29.4
	FP	12.2	11.9	25.7	17.3	21.2
7	TP	27.1	11.4	98.6	95.7	61.4
	FP	7.9	6.4	19.5	12.4	9.9
13	TP	77.8	62.9	100	100	96.3
	FP	7.1	5.5	18.4	11.2	8.9
17	TP	94.1	88.2	100	100	97.1
	FP	5.9	5.1	13.2	10.7	6.6
21	TP	38	15.5	100	100	69
	FP	7.5	5.5	23.9	11.3	8.5

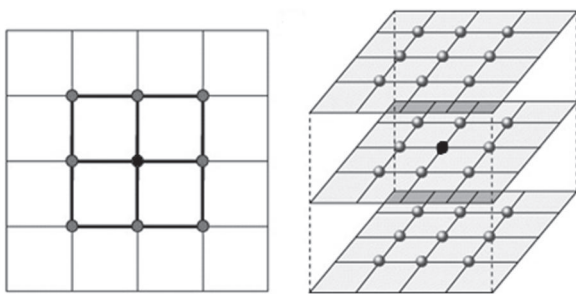


FIGURE 20: 2D and 3D neighborhoods.

This was because the membership function with a larger number of classes is unable to divide the space of the problem in which the nodule pixels are clearly separated from the pixels belonging to other clusters; the cluster to which they are assigned depends on the distribution of coefficients in the image and the number of clusters into which the image is to be divided. A much more powerful membership function, capable of performing a better classification, would be required to obtain better results with a larger number of clusters.

This conclusion is corroborated by the fact that when using 3D neighborhoods which use more information and better reflect the structure of the element, the results do not present an improvement (Table 3) and maintain their level of success and, in some cases, increase the false positives. The best results were also obtained by dividing the image into three clusters.

6. Conclusions

This paper presents an extensive and thorough analysis of the use of traditional and state-of-the-art (Table 4) fuzzy clustering algorithms for detecting ROIs in helical thoracic CT slices, with the aim of incorporating this method into a CAD system that will help professionals to detect pulmonary nodules, tested using a set of studies selected from a public database.

Traditional algorithms have been shown not to be the most appropriate solution due to the limitations of the membership functions they use; they are unable to achieve good quality results with large sets of slices.

0	17	111	176	213	175	68	11	0	0
5	73	278	32767	32767	32767	32767	68	6	0
11	134	32767	818	893	861	522	32767	23	0
11	32767	549	942	993	989	887	32767	85	6
11	32767	550	952	1000	1000	956	585	32767	16
5	94	32767	910	990	999	965	652	32767	17
0	29	32767	606	878	954	951	714	32767	12
0	7	83	32767	32767	605	724	622	32767	11
0	0	12	73	134	32767	32767	32767	109	11
0	0	0	5	11	13	27	27	46	5

(a)

3	3	3	2	2	2	2	2	3	3	3
3	2	2	2	2	2	2	2	2	3	3
3	2	2	2	2	2	2	2	2	2	3
3	2	2	2	2	2	2	2	2	2	3
3	2	2	2	2	2	2	2	2	2	3
3	2	2	2	2	2	2	2	2	2	3
3	2	2	2	2	2	2	2	2	2	2
3	3	2	2	2	2	2	2	2	2	2
3	3	3	2	2	2	2	2	2	2	2
3	3	3	3	3	3	3	2	2	2	2

(b)

2	2	2	2	2	2	2	2	2	2	2
2	2	3	3	3	3	3	2	2	2	2
2	2	3	4	4	4	4	3	2	2	2
2	3	4	4	4	4	4	4	3	2	2
2	2	4	4	4	4	4	4	3	2	2
2	2	3	4	4	4	4	4	3	2	2
2	2	3	4	4	4	4	4	3	2	2
2	2	2	3	4	4	4	4	3	3	2
2	2	2	2	3	3	3	3	3	3	2
2	2	2	2	2	2	2	2	3	3	3

(c)

2	2	2	2	2	2	2	2	2	2	2
2	2	2	2	2	3	3	2	2	2	2
2	2	3	3	3	3	3	3	2	2	2
2	2	3	3	3	3	3	3	3	2	2
2	2	3	3	3	3	3	3	3	2	2
2	2	2	3	3	3	3	3	3	3	2
2	2	2	2	3	3	3	3	3	3	2
2	2	2	2	2	3	3	3	3	3	2
2	2	2	2	2	2	2	3	3	3	2
2	2	2	2	2	2	2	2	2	2	2

(d)

FIGURE 21: The best classification obtained for one of the images analyzed: mask (a), KFCM ((b), value 2 represents the nodule), SFCM ((c), value 4 represents the nodule), and MKSFCM ((d), value 3 represents the nodule).

To resolve this limitation, algorithms which incorporate different modifications to the membership function were also analyzed: kernelized and spatial. The former improve the classification but continue to produce an elevated number of false positives, complicating the next stage of classification. Spatial algorithms also improve results but are very sensitive to noise (in the present case) and quite unstable given the significant variations, depending on the parameters and slice, in the results.

The next step was to analyze if by combining both techniques we could improve the results. We analyzed an algorithm which uses this strategy SKFCM and created a new algorithm combining two of the algorithms already analyzed: MSKFCM. Only by combining the two classification techniques (kernelized and spatial) was it possible to consistently classify the pixels as belonging to a nodule and therefore use it for the automatic detection of nodules in helical thoracic CT scans.

Both the SKFCM and MSKFCM algorithms provided an adequate rate of success for this task, with better results being obtained in some slices with the SKFCM algorithm. However, the MKSFCM algorithm presented more stable behaviour than the SKFCM algorithm with a much smaller number of false positives, allowing quality results to be obtained with a fixed set of input parameters and using samples not selected by an operator. This characteristic makes it more suitable for our objective: the automatic detection of ROIs that may be classified as a nodule.

Competing Interests

All authors declare that there is no conflict of interests regarding the publication of this paper.

Acknowledgments

This work was supported by project 09SIN006PR from the I+D Suma Call of the Galician Plan for Research, Development and Technological Innovation (INCITE) from Xunta de Galicia.

References

- [1] I. Sluimer, A. Schilham, M. Prokop, and B. van Ginneken, "Computer analysis of computed tomography scans of the lung: a survey," *IEEE Transactions on Medical Imaging*, vol. 25, no. 4, pp. 385–405, 2006.
- [2] A. Guyton, *Textbook of Medical Physiology*, W.B. Saunders Company, Harcourt Brace Jovanovic, Philadelphia, Pa, USA, 1991.
- [3] J. Hwang, M. J. Chung, Y. Bae, K. M. Shin, S. Y. Jeong, and K. S. Lee, "Computer-aided detection of lung nodules: influence of the image reconstruction kernel for computer-aided detection performance," *Journal of Computer Assisted Tomography*, vol. 34, no. 1, pp. 31–34, 2010.
- [4] World Health Organization, GLOBOCAN 2008, Cancer incidence and mortality worldwide in 2008, <http://globocan.iarc.fr>.
- [5] H. K. Weir, M. J. Thun, B. F. Hankey et al., "Annual report to the nation on the status of cancer, 1975–2000," *Journal of National Cancer Institute*, vol. 95, no. 17, pp. 1276–1299, 2003.
- [6] G. D. Rubin, "Data explosion: the challenge of multidetector-row CT," *European Journal of Radiology*, vol. 36, no. 2, pp. 74–80, 2000.
- [7] M. A. Matabuena, M. Jorquera, J. Hernández et al., "Diagnóstico por imagen del dolor torácico," *Medicine*, vol. 23, pp. 148–164, 1992.
- [8] M. L. Giger, K. T. Bae, and H. Macmahonr, "Computerized detection of pulmonary nodules in computed: tomography images," *Investigative Radiology*, vol. 29, no. 4, pp. 459–465, 1994.

- [9] Y. Lee, T. Hara, H. Fujita, S. Itoh, and T. Ishigaki, "Automated detection of pulmonary nodules in helical CT images based on an improved template-matching technique," *IEEE Transactions on Medical Imaging*, vol. 20, no. 7, pp. 595–604, 2001.
- [10] S. Matsumoto, H. L. Kundel, J. C. Gee, W. B. Geftter, and H. Hatabu, "Pulmonary nodule detection in CT images with quantized convergence index filter," *Medical Image Analysis*, vol. 10, no. 3, pp. 343–352, 2006.
- [11] T. Messay, R. C. Hardie, and S. K. Rogers, "A new computationally efficient CAD system for pulmonary nodule detection in CT imagery," *Medical Image Analysis*, vol. 14, no. 3, pp. 390–406, 2010.
- [12] S. G. Armato III, M. L. Giger, C. J. Moran, J. T. Blackburn, K. Doi, and H. MacMahon, "Computerized detection of pulmonary nodules on CT scans," *Radiographics*, vol. 19, no. 5, pp. 1303–1311, 1999.
- [13] B. Li and J. M. Reinhardt, "Automatic generation of object shape models and their application to tomographic image segmentation," in *Medical Imaging Image Processing*, Proceedings of SPIE, pp. 311–322, San Diego, Calif, USA, February 2001.
- [14] M. N. Gurcan, B. Sahiner, N. Petrick et al., "Lung nodule detection on thoracic computed tomography images: preliminary evaluation of a computer-aided diagnosis system," *Medical Physics*, vol. 29, no. 11, pp. 2552–2558, 2002.
- [15] D. S. Paik, C. F. Beaulieu, G. D. Rubin et al., "Surface normal overlap: a computer-aided detection algorithm with application to colonic polyps and lung nodules in helical CT," *IEEE Transactions on Medical Imaging*, vol. 23, no. 6, pp. 661–675, 2004.
- [16] M. Tan, R. Deklerck, B. Jansen, M. Bister, and J. Cornelis, "A novel computer-aided lung nodule detection system for CT images," *Medical Physics*, vol. 38, no. 10, pp. 5630–5645, 2011.
- [17] S.-C. B. Lo, M. T. Freedman, J.-S. Lin, and S. K. Mun, "Artificial convolution neural network techniques and applications for lung nodule detection," *IEEE Transactions on Medical Imaging*, vol. 14, no. 4, pp. 711–718, 1995.
- [18] M. S. Brown, M. F. McNitt-Gray, J. G. Goldin, R. D. Suh, J. W. Sayre, and D. R. Aberle, "Patient-specific models for lung nodule detection and surveillance in CT images," *IEEE Transactions on Medical Imaging*, vol. 20, no. 12, pp. 1242–1250, 2001.
- [19] S. Chen, K. Suzuki, and H. MacMahon, "Development and evaluation of a computer-aided diagnostic scheme for lung nodule detection in chest radiographs by means of two-stage nodule enhancement with support vector classification," *Medical Physics*, vol. 38, no. 4, pp. 1844–1858, 2011.
- [20] A. Castro and B. Arcay, "A new algorithm for automatic preprocessing of high resolution lung CT," in *Proceedings of the 2nd Workshop on Context-Aware Recommender Systems (CARS '10)*, September 2010.
- [21] A. Rey, A. Castro, and B. Arcay, "An improved algorithm for the automatic isolation of lungs in CT studies," in *Proceedings of the 10th International Workshop on Biomedical Engineering*, pp. 1–4, IEEE, October 2011.
- [22] S. G. Armato III, G. McLennan, M. F. McNitt-Gray et al., "Lung image database consortium: developing a resource for the medical imaging research community," *Radiology*, vol. 232, no. 3, pp. 739–748, 2004.
- [23] S. G. Armato III, G. McLennan, L. Bidaut et al., "The Lung Image Database Consortium (LIDC) and Image Database Resource Initiative (IDRI): a completed reference database of lung nodules on CT scans," *Medical Physics*, vol. 38, no. 2, pp. 915–931, 2011.
- [24] M. Sutton, J. Bezdek, and T. Cahoon, "Image segmentation by fuzzy clustering: methods and issues," in *Handbook of Medical Imaging: Processing and Analysis*, I. N. Bankman, Ed., pp. 87–126, 2000.
- [25] U. Kaymak and M. Setnes, "Fuzzy clustering with volume prototypes and adaptive cluster merging," *IEEE Transactions on Fuzzy Systems*, vol. 10, no. 6, pp. 705–712, 2002.
- [26] B. Tutmez, "Spatial dependence-based fuzzy regression clustering," *Applied Soft Computing Journal*, vol. 12, no. 1, pp. 1–13, 2012.
- [27] T. Hatoria and M. Sato-Ilic, "A Fuzzy clustering method using the relative structure of the belongingness of objects to clusters," *Procedia Computer Science*, vol. 35, pp. 994–1002, 2014.
- [28] D.-Q. Zhang and S.-C. Chen, "A novel kernelized fuzzy C-means algorithm with application in medical image segmentation," *Artificial Intelligence in Medicine*, vol. 32, no. 1, pp. 37–50, 2004.
- [29] A. Rey, A. Castro, and B. Arcay, "Fuzzy clustering algorithms for image segmentation," *Insight Journal*, 2011, <http://hdl.handle.net/10380/3331>.
- [30] J. C. Bezdek, R. Ehrlich, and W. Full, "FCM: the fuzzy c-means clustering algorithm," *Computers and Geosciences*, vol. 10, no. 2–3, pp. 191–203, 1984.
- [31] S. C. Chen and D. Q. Zhang, "Robust image segmentation using FCM with spatial constraints based on new kernel-induced distance measure," *IEEE Transactions on Systems, Man, and Cybernetics, Part B: Cybernetics*, vol. 34, no. 4, pp. 1907–1916, 2004.
- [32] K.-S. Chuang, H.-L. Tzeng, S. Chen, J. Wu, and T.-J. Chen, "Fuzzy c-means clustering with spatial information for image segmentation," *Computerized Medical Imaging and Graphics*, vol. 30, no. 1, pp. 9–15, 2006.
- [33] "Receiver operating characteristic analysis in medical imaging," *Journal of the ICRU*, vol. 8, no. 1, 2008.
- [34] K. W. Bowyer, "Validation of medical image analysis techniques," in *Handbook of Medical Imaging. Volume 2: Medical Image Processing and Analysis*, M. Sonka and J. M. Fitzpatrick, Eds., pp. 567–607, SPIE Press, 2000.
- [35] J. C. Bezdek, *Pattern Recognition with Fuzzy Objective Function Algorithms*, Plenum, New York, NY, USA, 1981.
- [36] X. L. Xie and G. A. Beni, "A validity measure for fuzzy clustering," *IEEE Transactions on Pattern Analysis and Machine Intelligence*, vol. 13, no. 8, pp. 841–847, 1991.
- [37] S. Z. Selim and M. A. Ismail, "K-means-type algorithms: a generalized convergence theorem and characterization of local optimality," *IEEE Transactions on Pattern Analysis and Machine Intelligence*, vol. 6, no. 1, pp. 81–87, 1984.
- [38] S. Z. Selim and M. S. Kamel, "On the mathematical and numerical properties of the fuzzy c-means algorithm," *Fuzzy Sets and Systems*, vol. 49, no. 2, pp. 181–191, 1992.

Clinical Study

Intraoperative Contrast Enhanced Ultrasound Evaluates the Grade of Glioma

Ling-Gang Cheng,¹ Wen He,¹ Hong-Xia Zhang,¹ Qian Song,¹ Bin Ning,¹
Hui-Zhan Li,¹ Yan He,¹ and Song Lin²

¹Department of Ultrasound, Beijing Tiantan Hospital, Capital Medical University, 6 Tiantan Xili, Dongcheng District, Beijing 100050, China

²Department of Neurosurgery, Beijing Tiantan Hospital, Capital Medical University, 6 Tiantan Xili, Dongcheng District, Beijing 100050, China

Correspondence should be addressed to Wen He; hewen168@sohu.com

Received 2 October 2015; Revised 5 December 2015; Accepted 16 February 2016

Academic Editor: Yi-Xiang Wang

Copyright © 2016 Ling-Gang Cheng et al. This is an open access article distributed under the Creative Commons Attribution License, which permits unrestricted use, distribution, and reproduction in any medium, provided the original work is properly cited.

Objective. The aim of our study was to investigate the value of intraoperative contrast enhanced ultrasound (CEUS) for evaluating the grade of glioma and the correlation between microvessel density (MVD) and vascular endothelial growth factor (VEGF). **Methods.** We performed intraoperative conventional ultrasound (CUS) and CEUS on 88 patients with gliomas. All of the patients have undergone surgery and obtained the results of pathology. All patients have undergone intraoperative CUS and CEUS to compare the characteristics of different grade gliomas and the results of CUS and CEUS were compared with pathological results. **Results.** The time to start (TTS) and time to peak (TTP) of low grade glioma (LGG) were similar to those of edema and normal brain surrounding glioma. The enhanced extent of LGG was higher than that of the normal brain and edema. The TTS and TTP of high grade glioma were earlier than those of the edema and normal brain surrounding glioma. The enhancement of HGG was higher than that of LGG. The absolute peak intensity (API) was correlated with MVD and VEGF. **Conclusion.** Intraoperative CEUS could help in determining boundary of peritumoral brain edema of glioma. Intraoperative CEUS parameters in cerebral gliomas could indirectly reflect the information of MVD and VEGF.

1. Introduction

Glioma is the most common primary neuroepithelial tumors, which accounts for 50% of intracranial tumors [1]. The grade of glioma is closely related to the prognosis. The growth, invasion, and metastasis of tumor depended on angiogenesis, and the degree of tumor angiogenesis is closely related to malignancy and prognosis of tumor. CT can accurately determine the location of the lesion and clearly show the glioma calcification, but the accuracy is not good. MRI could diagnose the glioma more accurately than CT preoperatively. The image of MRI could detect small tumors which could not be displayed by CT. The assessment of gliomas by MRI was more accurate than CT, but it has limited application in surgery [2–4]. However it is difficult to distinguish the grade of glioma by CT or MRI preoperatively [5].

Glioma is one of the malignant tumors which are rich in angiogenesis. Invasive growth is one of the most important biological behaviors of the malignant tumor. Angiogenesis was significantly correlated with invasion and growth of the glioma. Microvessel density (MVD) is a quantitative criterion for reflecting the situation of tumor angiogenesis, and it can reflect the proliferation of tumor cells, angiogenesis, and the degree of malignancy objectively. Angiogenesis of tumor is a process regulated by gene and a variety of growth factors, in which the vascular endothelial growth factor (VEGF) is the most important blood vessel growth stimulating factor. However, MVD and VEGF of tumors are limited in clinical applications due to the invasive and poor reproducibility [6–9].

CEUS is the technique which can significantly improve the resolution, sensitivity, and specificity of ultrasound

diagnostic. CEUS has become an important method of diagnosis, and it has been widely applied in the diagnosis of liver, kidney, and other organs but rarely used in the field of brain surgery. It could reflect and observe the blood perfusion of normal tissue and lesions [10, 11]. The residence time of contrast agents in intracranial benign and malignant tumor is different. It will certainly be helpful for the judgment of benign and malignant tumors according to the contrast agent development time-intensity curve [12–14].

Kanno et al. [15] did intraoperative CEUS in 37 patients with brain tumors; the results of vessels within the tumor had a good correlation between CEUS and digital subtraction angiography (DSA), but now the studies of distinguishing gliomas grading by CEUS were few. The purposes of this study were to explore the value of intraoperative CEUS in the evaluation of peritumoral edema and tumor grading, while evaluating relationship between contrast enhanced ultrasound parameters and MVD or VEGF in different pathologic grades of cerebral gliomas.

2. Materials and Methods

2.1. Patients. 88 patients were selected from April 2009 to December 2014 in the Beijing Tiantan Hospital neurosurgery. They were all diagnosed as having supratentorial gliomas by CT and/or MRI. They were 56 males and 32 females and aged from 18 to 69 years, with a mean age of 45.2 ± 12.8 years. Clinical manifestations were headache, limb weakness, limb twitching, blurred vision, aphasia, and so on. This study was approved by our local ethics committee, and written informed consent was obtained from each patient before the CEUS examination and biopsy procedures. The necessity and function of the ultrasonic imaging examination and the possible side effects were explained to patients or patients' families. "CEUS informed consents" were signed by the patients or their immediate family members.

2.2. Preoperative CT and/or MRI. All of the tumors whose diameters were from 2.1 to 5.4 cm were single. There were 33 cases of frontal gliomas, 19 cases of temporal gliomas, 2 cases of parietal gliomas, 4 cases of occipital gliomas, 15 cases of frontotemporal gliomas, 12 cases of temporal parietal gliomas, 1 case of thalamus glioma, and 2 cases of frontal and parietal gliomas.

2.3. Inclusion and Exclusion Criteria

2.3.1. Inclusion Criteria. The inclusion criteria are as follows: (1) all patients were suspected as glioma with preoperative CT and MRI; (2) the selected gliomas were those which had less clear border and supratentorial gliomas, especially those that had edema; (3) the diameter of gliomas is <5.5 cm; (4) all of the patients voluntarily join this study and are older than 18 years.

2.3.2. Exclusion Criteria. The exclusion criteria are as follows: (1) the patients who refused to participate in this study; (2) the patients who were allergic for contrast agent composition;

(3) the patients that were not suitable for participation in the study because of severe heart and lung disease; (4) the quality of conventional ultrasound image that was not satisfactory; (5) the patients who had received other treatment before surgery, such as radiotherapy and chemotherapy.

2.4. Instruments and Reagents. The ultrasound scanner is α -10 (Aloka, Japan), equipped with UST-9133 (transducer surface $3.0 \text{ cm} \times 1.0 \text{ cm}$), and the frequency of probes is 6–8 MHz, and its maximal depth is 18 cm. CEUS analysis software was installed into the ultrasound scanner. Ultrasound output mechanical index was 0.10–0.12.

Ultrasound contrast agents were SonoVue produced by Bracco Company, Italy. The agents were microbubbles of the phospholipids microencapsulated sulfur hexafluoride (SF_6). The average diameter of microbubbles was $2.5 \mu\text{m}$ and their pH values ranged from 4.5 to 7.5. 5 mL of 0.9% sodium chloride was injected into 59 mg of SonoVue before contrast and then thoroughly shaken. After 5 mL contrast agent was injected from femoral vein, 10 mL saline was injected immediately.

2.5. Inspection Method

2.5.1. Surgery. Under general anesthesia, the neurosurgeon shaved the hair and cleaned the skin in the surgical area. The neurosurgeon then made an incision through the scalp at the location of the glioma according to preoperative head CT/MRI. Brain surgery was performed through the bone flap after opening the skull.

The intraoperative ultrasound probe was placed into a sterile transducer cover (Surgical Sterile Protective Ship-Cover, 3L Medical Products Group Co., Ltd., Jiangxi, China) and was then inserted into the bone flap to observe the glioma after opening the calvarium and tenting the dura. The pressure on the brain was minimized as much as possible.

The doctor detects lesion directly on the brain surface that uses saline as a coupling agent after cutting the cerebral dura mater; multislice examination of the lesions was rowed within the range of bone window. We observed the location, relationship boundaries, shape, internal echo, peripheral edema brain tissue and normal brain tissue, tumor size, depth from the brain surface, blood flow characteristics, and the necrosis of glioma by using intraoperative CUS.

Ultrasound scanner setting was switched to CEUS after the best section of lesion displayed. The target was in the center of the screen and regulated the depth of scanner focus, and so forth. Five milliliters of contrast agent was bolus injected via the femoral vein and then 10 mL of saline was injected for washing. The timer on ultrasound scanner was started at the same time of contrast agent injection. The characteristics of enhancement in glioma and surrounding brain tissue during the administration of ultrasound contrast agents were observed in real time for 2 min. The characteristics of the glioma on real time CEUS were observed. The real time images of CEUS were stored on cine loops and static images.

Remove cotton sheets, tissue debris, and blood clot in residual cavity after surgery. The residual cavity was filled

with saline after repeated washing and observed whether the glioma was removed completely or not.

Intraoperative CUS and CEUS were done by the same doctor, and the injection of contrast agent was also by the same nurse.

2.5.2. Postoperative Image Handling. All raw data were stored in the instrument's hard drive and then analyzed by the time-intensity curve (TIC) software equipped in the machine. A plurality of regions of interest was analyzed and compared, in order to get the time to start (TTS), time to peak (TTP), the absolute peak intensity (API) of glioma, peritumoral edema, and surrounding normal brain tissue.

2.6. Image Analysis. Five values were obtained about every glioma, peritumoral edema, and normal brain tissue for TIC analysis. The regions of interest (ROI) were circularity whose diameter was 0.9 cm. ROI were selected avoiding the area of necrosis of lesion. The following parameters were obtained: the time to start (TTS), which means the time of interesting regions starts to be enhanced; the time to peak (TTP), which means the time of interest regions is enhanced to the peak; the absolute peak intensity (API), which is equal to peak intensity-baseline intensity. The average values of all the 5 were obtained as the TTS, TTP, and API of the ROI. The images were analyzed by two experienced sonographers and they reached an agreement about the results.

2.7. Immunohistochemical Detection of MVD and VEGF

2.7.1. Reagents of Pathology. They are biotinylated goat anti-human VEGF polyclonal antibody (CYB165004), mouse anti-human CD34 monoclonal antibody (SPM123), SABC immunohistochemistry kit (SA1020), and DAB substrate kit (PW017). Pathological images were received by image analysis system and radiography.

2.7.2. Quantification of MVD. There were two ways of treatment for postoperative specimens: (1) conventional sections after being fixed with formalin, and then embedded with paraffin, and HE staining and (2) 4 μ m thick paraffin sections that were stained by anti-CD34 monoclonal antibody peroxidase labeled avidin-linked enzyme. The result and statistics were got by two pathologists who had extensive clinical experience in double blind method.

The standards of MVD count were referring to count technique proposed by Yu et al. [16]. Microvessels which were counted contained single endothelial cells which were dyed brown single endothelial cells, endothelial cell clusters into the lumen, and even larger vessels, as long as it was separated from the neighboring capillaries, tumor cells, or other connective tissues. The number would be counted as two microvessels if the "head" and "tail" of the same vessel are displayed in the same plane; the vessel would be counted as a blood vessel if there were less than 8 caught red blood cells in the luminal diameter; if there were >8 red blood cells or smooth muscle wall, the vessels were not counted. First "hot spots" which were glioma cell infiltration and areas that

contain most microvessels were selected at low magnification. "Hot spots" were generally common in the edges of glioma. The MVD would be counted under high magnification vision after finding "hot spots"; every sample would count number of microvessels in five horizons (counting units: bar/HPF), the average of which was as the MVD of the glioma.

2.7.3. Expression of VEGF. Postoperative specimens were fixed in 10% formalin and embedded by paraffin and then biotinylated goat anti-human VEGF polyclonal antibody as an antibody. The positive staining of VEGF was that there was granular brown substance in the cytoplasm or nucleus. Each slide was counted five high power fields randomly. Each field counted 200 cells. The average positive rate = the number of positive cells/ the number of counted cells. The result was the average of five visions. Positive grading criteria are as follows: positive cell rate between 0% and 10% was (-); 11% to 40% was (+); 41% to 75% was (+); higher than 76% was (+++).

2.8. Statistical Analysis. SPSS19.0 statistical software was used to analyze the results. Normal measurement data were representing mean \pm standard deviation. Measurement data were compared by *t*-test or analysis of variance. Count data were compared by χ^2 test or rank sum test. *P* < 0.05 was considered statistically significant.

3. Results

3.1. The Basic Condition of the Patients. All patients obtained a clear image of CEUS, and all patients were well tolerated about CEUS. There were no adverse reactions such as dizziness, headache, abdominal pain, feeling strange, joint and muscle pain, and weakness during and after the examination.

All of 88 patients were glioma confirmed by pathology. Low grade gliomas (LGG) included levels I and II, and high grade glioma (HGG) mainly included levels III and IV referring to the WHO classification of glioma in 2000. There were 38 cases of low grade gliomas and 50 cases of high grade gliomas (Table 1), 56 males and 32 females, aged from 20 to 69 years, with a mean age of 47.9 ± 11.4 . The area of edema appeared in 7 cases in low grade glioma and 22 cases in high grade glioma.

3.2. The Intraoperative CUS and CEUS Performance of Gliomas. The CUS showed that the glioma is hyperechoic, the boundary is not clear, and the shape is irregular. The echo of peripheral edema was lower than that of glioma but still higher than that of normal brain tissue. The boundaries between glioma and edema were unclear. The area of intraleSIONAL necrosis presented as hypoechoic, which was lower than the surrounding brain parenchyma. CDFI showed that there was little blood flow in the glioma.

88 patients with glioma injected contrast agent via femoral venous. TTS of LGG was from 6 s to 18 s, TTP of which was from 12 s to 28 s; TTS of HGG was from 4 s to 14 s, and TTP of HGG was from 10 s to 24 s. CEUS features of LGG are as follows: the TTS and TTP of glioma and edema and normal brain surrounding glioma were similar.

TABLE 1: The comparison of CEUS about different grade gliomas.

Sampling sites	LGG			HGG		
	TTS	TTP	API	TTS	TTP	API
Cancer	11.11 ± 3.36	19.56 ± 4.27	147.48 ± 46.29	10.26 ± 2.82	17.34 ± 3.68	171.22 ± 29.34
Peritumoral normal tissue	11.21 ± 3.59	19.84 ± 4.68	81.88 ± 29.49	11.72 ± 2.76	19.36 ± 3.66	71.74 ± 24.23
<i>t</i> value	0.56	1.70	11.65	5.99	6.65	19.65
<i>P</i> value	0.58	0.09	0.000	0.000	0.000	0.000

TABLE 2: The comparison of brain edema about different grade gliomas.

Sampling sites	LGG			HGG		
	TTS	TTP	API	TTS	TTP	API
Cancer	11.19 ± 2.44	19.29 ± 3.80	154.64 ± 31.71	9.99 ± 3.12	17.29 ± 3.77	177.12 ± 31.79
Peritumoral edema	12.19 ± 2.30	19.49 ± 3.87	111.37 ± 29.42	11.51 ± 2.62	19.55 ± 3.08	107.88 ± 19.13
Peritumoral normal tissue	11.45 ± 3.44	19.39 ± 3.73	81.92 ± 29.71	11.99 ± 2.66	19.41 ± 3.20	63.25 ± 21.30
<i>F</i> value	0.24	0.01	10.20	3.03	3.11	111.62
<i>P</i> value	0.78	0.99	0.001	0.06	0.051	0.000

TABLE 3: Comparison of different grade gliomas and edema by CEUS.

Grade	Gliomas			Edma		
	TTS	TTP	API	TTS	TTP	API
LGG	11.11 ± 3.36	19.56 ± 4.27	147.48 ± 46.29	12.19 ± 2.30	19.49 ± 3.87	111.37 ± 29.42
HGG	10.26 ± 2.82	17.34 ± 3.68	171.22 ± 29.34	11.51 ± 2.62	19.55 ± 3.08	107.88 ± 19.13
<i>t</i> value	1.29	2.61	2.93	0.61	0.04	0.37
<i>P</i> value	0.20	0.01	0.004	0.55	0.97	0.72

The enhancement of glioma was uniform or nonuniform and higher than the normal brain and edema. Peritumoral edema showed equal enhancement approximately. The surrounding normal brain tissue showed equal enhancement (Figure 1). CEUS features of HGG are as follows: the TTS and TTP of glioma were earlier than the edema and normal brain surrounding glioma. The enhancement of glioma was uniform or nonuniform and higher. Peritumoral brain edema was highly enhanced. The boundary of glioma was clear with peritumoral edema brain tissue and surrounding normal brain tissue (Figure 2).

3.3. Time-Intensity Curve of Intraoperative CEUS (TIC). The API of LGG was higher than the surrounding normal brain tissue and peritumoral brain edema, and it was statistically significant between the two groups ($P < 0.05$). The difference of TTS and TTP between the glioma and the surrounding normal brain tissue was not statistically significant ($P > 0.05$) (Table 1, Figure 3). The API of HGG was higher than the surrounding normal brain tissue and peritumoral brain edema significantly. It was statistically significant between the two groups ($P < 0.05$). The difference of TTS and TTP between the glioma and the surrounding normal brain tissue was statistically significant ($P < 0.05$) (Table 1, Figure 4).

There was cerebral edema appearing in 7 cases of LGG. The difference of TTS and TTP among glioma, peritumoral edema, and the surrounding normal brain tissue was not statistically significant ($P > 0.05$) (Table 2). API of edema

had statistically significant difference compared with glioma ($P < 0.05$), and it had no statistically significant difference compared with the surrounding normal brain tissue ($P > 0.05$). There were 22 patients in HGG who could find cerebral edema around the glioma. The difference of TTS and TTP among glioma, peritumoral edema, and the surrounding normal brain tissue was not statistically significant ($P > 0.05$) (Table 2). API of edema had statistically significant difference compared with glioma and the surrounding normal brain tissue ($P < 0.05$).

There was no statistically significant difference about TTS in glioma and the surrounding normal brain tissue between LGG and HGG. The difference of TTP and API was statistically significant ($P < 0.05$) (Table 3). The TTS, TTP, and API of edema had no statistically significant difference between LGG and HGG (Table 3).

3.4. Relationship between Glioma of CEUS and MVD. All the microvessel endothelial cells of 38 cases showed that anti-CD34 antibody staining was positive. MVD of 42 cases is from 14.20 to 64.80. MVD of high grade (III, IV) glioma was significantly higher than the low ones. The difference between the two groups was statistically significant ($P < 0.05$) (Table 4). API of glioma showed a positive correlation with MVD ($r = 0.899$, $P = 0.000$; Figure 5).

3.5. Relations between Different Pathological Grade Gliomas with VEGF. The expression of VEGF about normal brain

TABLE 4: The comparison of MVD and VEGF about different pathological grade glioma.

Grade	Number (N)	MVD	VEGF			
			-	+	++	+++
Low grade glioma	18	23.02 ± 6.78	7	7	3	1
High grade glioma	24	51.37 ± 9.34	0	3	9	12

$P < 0.05$; the difference of MVD and VEGF was statistically significant.

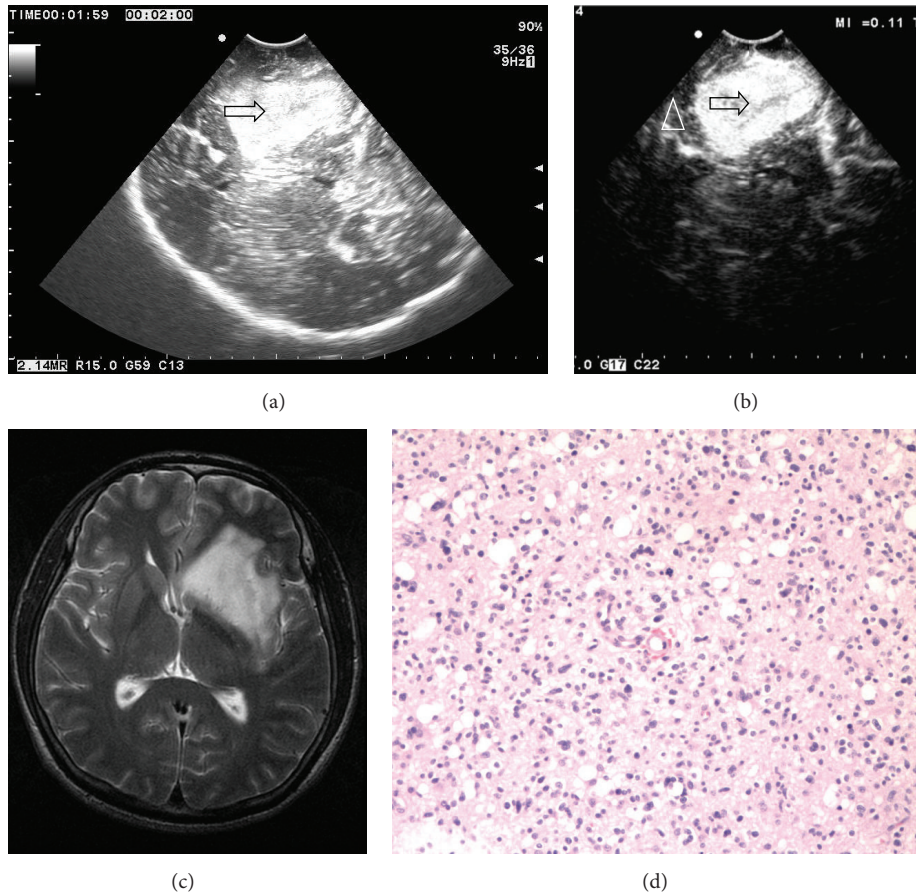


FIGURE 1: (a) Ultrasound image shows that the low grade glioma (II level) is partially hyperechoic, the boundary is not clear, internal echo is nonuniform, and edema is not obvious (arrow showed tumor). (b) CEUS shows that the echo of the glioma is enhanced significantly, the boundary is clear, and normal brain tissue is enhanced lower than the glioma (arrows show tumor; triangle shows normal brain tissue). (c) MRI T2W image shows that the glioma is hyperintense, irregular, and the boundary is not clear. (d) The pathological image of the same patient shows that the number of capillary vessels is less (HE ×100).

tissue was negative. The expression of VEGF staining positive was located in the cytoplasm of glioma tumor cells and endothelial cells. VEGF of HGG was higher than the LGG; the difference between groups was statistically significant ($P < 0.05$) (Table 4).

4. Discussion

Glioma is the most common malignant brain tumor, whose basic treatment is surgery combined with radiotherapy and chemotherapy. Whether the glioma is removed completely or not is directly related to the prognosis of patients. Radical tumor surgery is important for improving the clinical

outcome and keeping neurological function at the same time [17, 18]. At present, many advanced imaging techniques have been used in the field of neurosurgery surgery, such as nerve navigation, intraoperative CT, and MRI. These methods are not yet widely used in surgery limited by various conditions. Intraoperative CUS not only has the advantages of being cheap, convenience, and repeatability, but also can get real time imaging fully synchronized with surgical procedures [19]. However there was lack of clear boundary and capsule around the glioma due to the biological characteristics of the invasive growth of glioma. It is difficult for intraoperative CUS to distinguish the boundary of glioma, especially for distinguishing the boundary of residual glioma

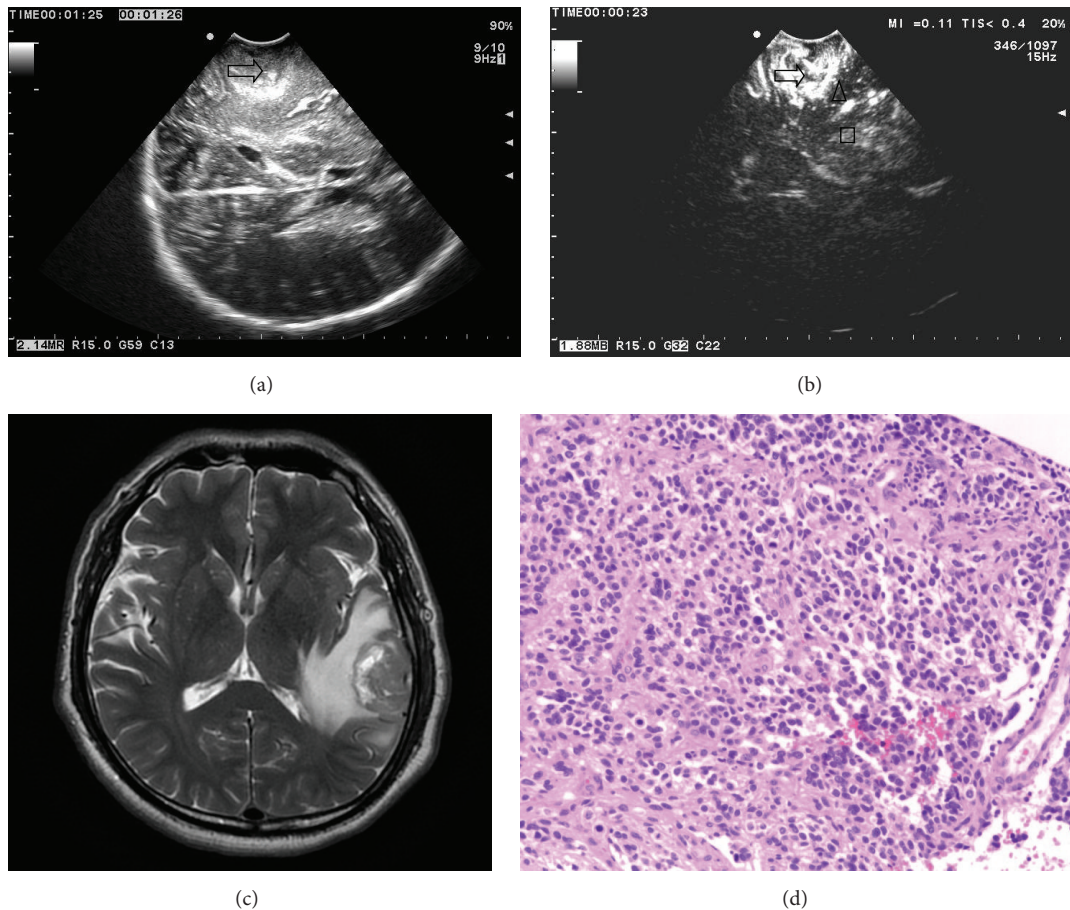


FIGURE 2: (a) Ultrasound image of high grade glioma shows that the tumor is hyperechoic, and the boundary is not clear and heterogeneous internal echo. The edema is obvious (arrow tumor). (b) CEUS shows that the echo of the glioma is enhanced significantly, brain edema is enhanced lower than the glioma, and brain tissue is enhanced lower than the glioma, brain edema (arrow showed the glioma, brain edema triangle shown, and the box showed normal brain tissue). (c) MRI T2W shows that the high grade glioma is mixed-signal, and there is edema around it. (d) The pathological image of the same patient shows that the microvessel is abundant (HE $\times 100$).

with peritumoral edema [20, 21]. It is difficult to reduce the residual tumors and increase tumor total resection rate just by using intraoperative CUS. In this study, CEUS was applied in glioma surgery. It not only improves the ability of intraoperative ultrasound to identify the glioma, residual glioma, and peritumoral edema, but also can judge the tumor pathological nature preliminary.

Because of the biological characteristics of the invasive growth of glioma, we found that it has varying degrees of edema around some tumor tissue. It is difficult to distinguish tumor boundary between peritumoral edema and normal brain tissue by intraoperative CUS. It may lead to unnecessary brain damage, if the edema brain tissue was removed mistakenly as tumor. At present, the formation mechanism of peritumoral edema is not yet clear. Some scholars [22, 23] noted that the most generation of edema is of vascular origin. Some scholars [24–26] believe that toxic tissue edema due to glioma cells produces abnormal capillaries leaking. Different pathological grade gliomas had different ultrasound contrast images. The results of this study show that the number of peritumoral edema cases of HGG was significantly more than

LGG. 22 cases of HGG have peritumoral edema, and only 7 cases of LGG have peritumoral edema. We found that the TTS and TTP of LGG, edema, and normal brain surrounding glioma were similar in CEUS. The enhancement of glioma was uniform or nonuniform, and it is higher than the normal brain and edema. Peritumoral edema showed equal enhancement approximately. The surrounding normal brain tissue showed equal enhancement. The TTS and TTP of HGG were earlier than the edema and normal brain surrounding glioma. The enhancement of glioma was higher. Peritumoral brain edema was highly enhanced. The boundaries of glioma were clear with peritumoral edema brain tissue and surrounding normal brain tissue. Thus we can distinguish tumor with peritumoral edema and the brain tissue by intraoperative CEUS of glioma, which could improve the diagnosis of the glioma and brain tissue edema compared to IOUS. The higher the malignancy degree of gliomas, the more abundant the blood vessels of gliomas [27–29].

Angiogenesis was significantly increased with the increase of the degree of malignancy, which could result in microvessel increase and the structure of abnormal new

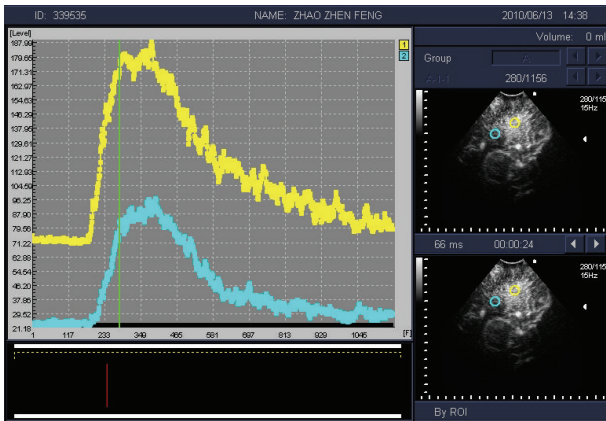


FIGURE 3: Time-intensity curve (TIC) of low grade glioma (yellow) shows that contrast peak intensity of glioma is significantly higher than the surrounding normal brain tissue (blue).

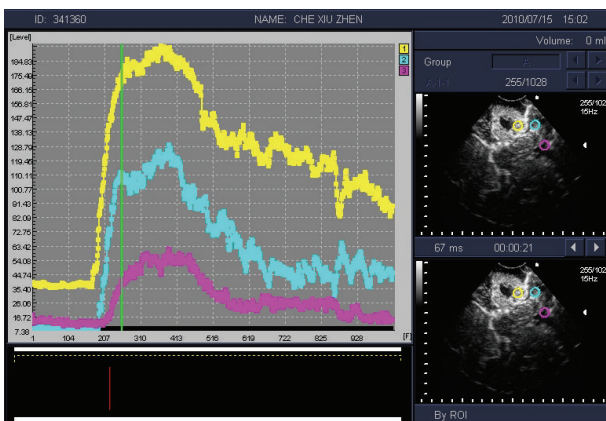


FIGURE 4: Time-intensity curve (TIC) of high grade glioma shows that tumor tissue (yellow) is significantly higher than the peak intensity of contrast peritumoral brain edema (blue) and the surrounding normal brain tissue (pink).

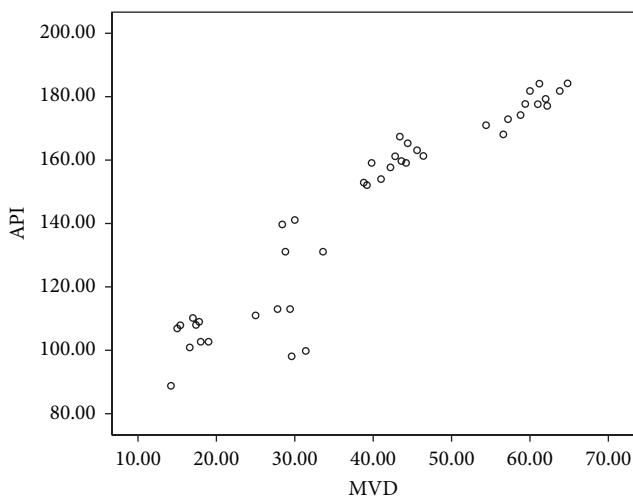


FIGURE 5: Correlation of absolute peak intensity (API) and microvessel density (MVD) about glioma tumor.

blood vessels. MVD was the gold standard to evaluate tumor angiogenesis, which can reflect tumor cell proliferation, angiogenesis, and the degree of malignancy, and so on objectively. It is an important indicator for evaluating brain tumor biological behavior and prognosis by the clinical and molecular pathology. CD34 is widely distributed in the tumor vascular endothelial cells in gliomas. Tiny tumor blood vessels can be identified by CD34 staining [25, 30]. However, MVD is limited in the clinical application due to the invasive and poor reproducibility. TIC of CEUS had rich quantitative information. It can reflect tumor blood perfusion, and it becomes the latest inspection methods of evaluation of tumor blood vessels [31, 32]. Tumor blood supply is more abundant; the amount of blood flow increased with the increase of the number of tumor angiogeneses. The degree of enhancement of tumor was more obvious. This study found that API was positively correlated with MVD. Thus, quantitative parameters of CEUS about glioma may indirectly reflect the hemodynamic characteristics and MVD of glioma, which can evaluate glioma angiogenesis reliably and noninvasively, and determine pathological level and provide valuable information for clinical treatment. Angiogenesis is the process regulated by gene and a variety of growth factors. Malignant glioma cells could secrete large amounts of VEGF, stimulate endothelial cell proliferation and migration, and then generate new tumor blood vessels. Nakada et al. [26] found that angiogenesis can be inhibited by inhibiting VEGF and matrix metalloproteinase activity. This study shows that VEGF expression in HGG group was significantly higher than the LGG group, suggesting that VEGF are closely related to the invasiveness and malignancy of glioma.

5. Study Limitations

(1) Only a small part of typical glioma was examined by CEUS intraoperative CEUS. This paper summarizes the CEUS characteristics of gliomas and is not comprehensive enough, and it needs to be supplemented. (2) It is only a preliminary judgment of pathological grade about glioma by CEUS, and we do not do the pathological grade. We hope that it could be further studied and solved by expanding the sample size and histological type.

6. Conclusion

Intraoperative CEUS can show the boundary of glioma clearly. TTS, TTP, and API of glioma, peritumoral brain edema, and normal brain tissue were quantitatively analyzed. API was positively correlated with MVD and VEGF.

Conflict of Interests

The authors declare that there is no conflict of interests regarding the publication of this paper.

Acknowledgment

This work was supported by the National Natural Science Foundation of China (no. 81071239).

References

- [1] M. Janson, K. Michael, J. Berg, and J. C. Anderson, "The role of intraoperative sonography in neurosurgery," *Journal of Diagnostic Medical Sonography*, vol. 21, no. 2, pp. 148–151, 2005.
- [2] P. Bargellini, R. Orlandi, C. Paloni et al., "Contrast-enhanced ultrasonographic characteristics of adrenal glands in dogs with pituitary-dependent hyperadrenocorticism," *Veterinary Radiology and Ultrasound*, vol. 54, no. 3, pp. 283–292, 2013.
- [3] D.-A. Clevert, A. Helck, P. M. Paprottka, M. F. Reiser, and E. M. Jung, "Contrast-enhanced ultrasound imaging of the carotid artery," *Radiologe*, vol. 51, no. 6, pp. 483–489, 2011.
- [4] C. De Lange, K. Brabrand, K. E. Emblem et al., "Cerebral perfusion in perinatal hypoxia and resuscitation assessed by transcranial contrast-enhanced ultrasound and 3 T MRI in newborn pigs," *Investigative Radiology*, vol. 46, no. 11, pp. 686–696, 2011.
- [5] D. Deng, G. Dan, J. Tao et al., "Conventional and contrast-enhanced ultrasound assessment of craniocerebral gunshot wounds," *Genetics and Molecular Research*, vol. 14, no. 2, pp. 3345–3354, 2015.
- [6] F. Prada, A. Perin, A. Martegani et al., "Intraoperative contrast-enhanced ultrasound for brain tumor surgery," *Neurosurgery*, vol. 74, no. 5, pp. 542–552, 2014.
- [7] E. Quaia, "Assessment of tissue perfusion by contrast-enhanced ultrasound," *European Radiology*, vol. 21, no. 3, pp. 604–615, 2011.
- [8] K. Ritschel, I. Pechlivanis, and S. Winter, "Brain tumor classification on intraoperative contrast-enhanced ultrasound," *International Journal of Computer Assisted Radiology and Surgery*, vol. 10, pp. 531–540, 2015.
- [9] X. Zhou, L. Chen, C. Feng et al., "Establishing an animal model of intracerebral hemorrhage under the guidance of ultrasound," *Ultrasound in Medicine and Biology*, vol. 39, no. 11, pp. 2116–2122, 2013.
- [10] O. F. Kaneko and J. K. Willmann, "Ultrasound for molecular imaging and therapy in cancer," *Quantitative Imaging in Medicine and Surgery*, vol. 2, no. 2, pp. 87–97, 2012.
- [11] M. A. Pysz, I. Guracar, L. Tian et al., "Fast microbubble dwell-time based ultrasonic molecular imaging approach for quantification and monitoring of angiogenesis in cancer," *Quantitative Imaging in Medicine and Surgery*, vol. 2, pp. 68–80, 2012.
- [12] Y. Wang, L. Li, Y.-X. J. Wang et al., "Time-intensity curve parameters in rectal cancer measured using endorectal ultrasonography with sterile coupling gels filling the rectum: correlations with tumor angiogenesis and clinicopathological features," *BioMed Research International*, vol. 2014, Article ID 587806, 7 pages, 2014.
- [13] X. Xu, L. Luo, J. Chen et al., "Acoustic radiation force impulse elastography for efficacy evaluation after hepatocellular carcinoma radiofrequency ablation: a comparative study with contrast-enhanced ultrasound," *BioMed Research International*, vol. 2014, Article ID 901642, 7 pages, 2014.
- [14] Y.-X. J. Wang, Y. Choi, Z. Chen, S. Laurent, and S. L. Gibbs, "Molecular imaging: from bench to clinic," *BioMed Research International*, vol. 2014, Article ID 357258, 3 pages, 2014.
- [15] H. Kanno, Y. Ozawa, K. Sakata et al., "Intraoperative power Doppler ultrasonography with a contrast-enhancing agent for intracranial tumors," *Journal of Neurosurgery*, vol. 102, no. 2, pp. 295–301, 2005.
- [16] S. Q. Yu, J. S. Wang, S. Y. Chen et al., "Diagnostic significance of intraoperative ultrasound contrast in evaluating the resection degree of brain glioma by transmission electron microscopic examination," *Chinese Medical Journal*, vol. 128, no. 2, pp. 186–190, 2015.
- [17] P. L. Gildenberg and S. Y. Woo, "Multimodality program involving stereotactic surgery in brain tumor management," *Stereotactic and Functional Neurosurgery*, vol. 75, no. 2-3, pp. 147–152, 2000.
- [18] H. Duffau, "New concepts in surgery of WHO grade II gliomas: Functional brain mapping, connectionism and plasticity—a review," *Journal of Neuro-Oncology*, vol. 79, no. 1, pp. 77–115, 2006.
- [19] M. Principi, M. Italiani, A. Guiducci et al., "Perfusion MRI in the evaluation of the relationship between tumour growth, necrosis and angiogenesis in glioblastomas and grade 1 meningiomas," *Neuroradiology*, vol. 45, no. 5, pp. 205–211, 2003.
- [20] N. Erdoan, B. Tucer, E. Mavl, A. Menkü, and A. Kurtsoy, "Ultrasound guidance in intracranial tumor resection: correlation with postoperative magnetic resonance findings," *Acta Radiologica*, vol. 46, no. 7, pp. 743–749, 2005.
- [21] N. Y. Cui, Y. Wang, R. Zhang et al., "Contrast enhanced ultrasound demonstration of a proliferative mass in rectum wall in a patient after rectal cancer surgery," *Quantitative Imaging in Medicine and Surgery*, vol. 2, no. 2, pp. 130–132, 2012.
- [22] W. He, L.-S. Wang, H.-Z. Li, L.-G. Cheng, M. Zhang, and C. G. Wladyka, "Intraoperative contrast-enhanced ultrasound in traumatic brain surgery," *Clinical Imaging*, vol. 37, no. 6, pp. 983–988, 2013.
- [23] D. N. Louis, "Molecular pathology of malignant gliomas," *Annual Review of Pathology*, vol. 1, no. 3, pp. 97–117, 2006.
- [24] P. Martin, B. Bender, and N. K. Focke, "Post-processing of structural MRI for individualized diagnostics," *Quantitative Imaging in Medicine and Surgery*, vol. 5, no. 2, pp. 188–203, 2015.
- [25] Y. Yao, T. Kubota, K. Sato, R. Kitai, H. Takeuchi, and H. Arishima, "Prognostic value of vascular endothelial growth factor and its receptors Flt-1 and Flk-1 in astrocytic tumours," *Acta Neurochirurgica*, vol. 143, no. 2, pp. 159–166, 2001.
- [26] M. Nakada, D. Kita, K. Futami et al., "Roles of membrane type 1 matrix metalloproteinase and tissue inhibitor of metalloproteinases 2 in invasion and dissemination of human malignant glioma," *Journal of Neurosurgery*, vol. 94, no. 3, pp. 464–473, 2001.
- [27] L. Bonilha and S. S. Keller, "Quantitative MRI in refractory temporal lobe epilepsy: relationship with surgical outcomes," *Quantitative Imaging in Medicine and Surgery*, vol. 5, no. 2, pp. 204–224, 2015.
- [28] P. Wachsberger, R. Burd, and A. P. Dicker, "Tumor response to ionizing radiation combined with antiangiogenesis or vascular targeting agents: exploring mechanisms of interaction," *Clinical Cancer Research*, vol. 9, no. 6, pp. 1957–1971, 2003.
- [29] T. Hölscher, B. Ozgur, S. Singel, W. G. Wilkening, R. F. Mattrey, and H. Sang, "Intraoperative ultrasound using phase inversion harmonic imaging: first experiences," *Neurosurgery*, vol. 60, supplement 2, no. 4, pp. 382–387, 2007.
- [30] W. He, X.-Q. Jiang, S. Wang et al., "Intraoperative contrast-enhanced ultrasound for brain tumors," *Clinical Imaging*, vol. 32, no. 6, pp. 419–424, 2008.

- [31] K. Ritschel, I. Pechlivanis, and S. Winter, "Brain tumor classification on intraoperative contrast-enhanced ultrasound," *International Journal of Computer Assisted Radiology and Surgery*, vol. 10, no. 5, pp. 531–540, 2015.
- [32] R. Rodriguez-Cruces and L. Concha, "White matter in temporal lobe epilepsy: clinico-pathological correlates of water diffusion abnormalities," *Quantitative Imaging in Medicine and Surgery*, vol. 5, no. 2, pp. 264–278, 2015.

Research Article

Diffusion-Weighted Imaging of Small Peritoneal Implants in “Potentially” Early-Stage Ovarian Cancer

Laretta Grabowska-Derlatka,¹ Pawel Derlatka,²
Wojciech Szeszkowski,¹ and Andrzej Cieszanowski^{1,3}

¹2nd Department of Clinical Radiology, Medical University of Warsaw, Banacha 1a Street, 02-097 Warsaw, Poland

²2nd Department of Obstetrics and Gynecology, Medical University of Warsaw, Karowa 2 Street, 00-315 Warsaw, Poland

³Department of Radiology I, Maria Skłodowska-Curie Memorial Cancer Center, Institute of Oncology, Roentgena 5 Street, 02-781 Warsaw, Poland

Correspondence should be addressed to Pawel Derlatka; derlatek@gmail.com

Received 4 December 2015; Accepted 4 February 2016

Academic Editor: Yi-Xiang Wang

Copyright © 2016 Laretta Grabowska-Derlatka et al. This is an open access article distributed under the Creative Commons Attribution License, which permits unrestricted use, distribution, and reproduction in any medium, provided the original work is properly cited.

Introduction. MRI is established modality for the diagnosis of ovarian malignancies. Advances in MRI technology, including DW imaging, could lead to the further increase in the sensitivity of MRI for the detection of peritoneal metastases. The aim of this study was to assess the accuracy of DW imaging for detection of peritoneal metastatic disease in patients suspected of having potentially early ovarian cancer and secondly to evaluate ADC values of peritoneal implants. **Materials and Methods.** The prospective study group consisted of 26 women with sonographic or/and CT diagnosis of suspected ovarian tumor. Based on the results of the above imaging, in none of them was extraovarian spread of disease or ascites recognized. All patients underwent MRI with DW imaging. **Results.** Overall, 18 extraovarian peritoneal lesions were found on DW images in 10 from 26 examined patients. All implants had diameter ≤ 10 mm. The presence of all lesions diagnosed by MRI was confirmed intraoperatively. Histopathologic findings in 17 proofs confirmed ovarian cancer. PPV was 94%. On all DW images (with b values of 0, 50, 100, 150, 200, 400, 800, and 1200 s/mm²) the mean signal intensities of peritoneal lesions were significantly higher than the mean signal intensities of normal adjacent tissue ($p = 0.000001$).

1. Introduction

About 3300 new cases of ovarian cancer are annually diagnosed in Poland of which 70% are advanced (stages III and IV) [1]. Currently, the standard treatment for early-stage ovarian cancer is primarily surgical management (with or without chemotherapy). According to the International Federation of Gynecology and Obstetrics (FIGO) guidelines, the optimal staging procedures for early ovarian cancer are abdominal hysterectomy, bilateral salpingo-oophorectomy, peritoneal biopsy, omentectomy, diaphragmatic scraping, bilateral pelvic, and para-aortic lymph node dissection [2].

The treatment of patients with advanced-stage ovarian cancer is based on debulking surgery and adjuvant chemotherapy. The surgeon aims at achieving a maximal possible cytoreduction [3]. Numerous studies have shown

that the patients in whom the removal of all macroscopic lesions was possible have the best prognosis [4–6].

When the disease has spread intra-abdominally, complete surgical tumor debulking is increasingly difficult. In patients with massive peritoneal spread, the method of choice is neoadjuvant chemotherapy, followed by interval surgery [7]. The interpretation of peritoneal findings at preoperative imaging requires detailed knowledge of the complex peritoneal anatomic configuration and the directionality of peritoneal fluid flow [8].

Magnetic resonance imaging (MRI) is established modality for the diagnosis of ovarian malignancies. This technique may be also utilized to determine the extension of disease, including detection of peritoneal metastatic disease in these patients. Advances in MRI technology, including

TABLE 1: Parameters of applied MR sequences.

Parameter	T2 TSE	T2 TSE Fat-Sat	DW EPI	T2 TIRM	3D T1 GRE
Repetition time (ms)	4250	2110	3800	6100	3,05
Echo time (ms)	117	123	73	39	1,13
Flip angle (deg.)	137	150	90	150	10
Turbo factor	51	51	—	9	—
EPI factor	—	—	96	—	—
iPAT factor	—	2	2	—	2
Plane	Axial	Axial	Axial	Axial	Axial
Number of signal averages	1	1	4	1	1
Field of view, FOV (mm)	360	360	360	360	360
Rectangular FOV (%)	75	100	75	75	75
Matrix	384 × 512	256 × 256	96 × 128	288 × 384	156 × 288
Slice thickness (mm)	5	5	6	5	3
Respiratory triggering	No	Yes	No	No	No
Breath-hold	No	Yes	No	No	No

improvement of DW imaging technique, could lead to the further increase in the sensitivity of MRI for the detection of peritoneal metastases. Studies have recently investigated the efficacy of DW images to detect peritoneal implants in different pelvic and abdominal malignancies [9]. The results were for the most part promising; however there are still important issues which need to be addressed and resolved, including the lack of standardization of DW images acquisition (choice of different b values) and various methods of calculation of apparent diffusion coefficient (ADC).

The aim of this study was twofold: firstly, to assess the accuracy of DW imaging for detection of peritoneal metastatic disease in patients suspected of having potentially early ovarian cancer and secondly to evaluate ADC values of peritoneal implants.

2. Materials and Methods

2.1. Patient Population. The prospective study group consisted of 26 women aged from 34 to 67 years with transvaginal and transabdominal sonographic diagnosis of suspected ovarian tumor. All patients had elevated serum levels of CA 125 or CA 19-9. In eight patients additional computed tomography (CT) of abdomen and pelvis was performed. Based on the results of the above imaging, in none of them was extraovarian spread of disease or ascites recognized.

2.2. MR Imaging. All patients underwent MR imaging of the abdomen and pelvis at our institution. MR imaging examinations were performed in all 26 patients using a 1.5 T clinical whole-body MR system (MAGNETOM Avanto; Siemens AG, Erlangen, Germany) with the Spine Matrix coil and combined two Body Matrix coils for larger coverage.

MRI protocol for the detection of the abdominal and pelvic lesions contained turbo spin-echo (tse) T2-weighted

images, fat-suppressed T2-weighted, T2-TIRM, DW EPI, and pre- and postcontrast dynamic 3D T1 GRE in transverse orientation. The details of the applied parameters of MR imaging are presented in Table 1.

Axial DWI images were acquired using the same multislice EPI sequence for all patients: 34 × 6 mm slices (abdominal part) and 30 × 6 mm slices (pelvic part); 380 × 380 mm FoV; 128 × 96 matrix; TR = 3800 ms; TE = 73 ms; with diffusion weightings of 0, 50, 100, 150, 200, 400, 800, and 1200 s/mm².

In all patients Gadobutrol (Gadovist, Bayer Schering, Berlin, Germany) was administered, at a dose of 0.1 mL/kg bodyweight, immediately followed by a bolus of 20 mL of physiological saline (NaCl 0.9%).

2.3. Image Analysis. Regions of interest were outlined in Multimodality Workplace Station (Siemens Medical Solution, Erlangen, Germany) by a genitourinary radiologist (with experience in pelvic MR imaging), who documented the number and location of peritoneal metastases on DW images and ADC maps. The number and location of metastatic peritoneal implants were confirmed intraoperatively and compared with MRI findings.

Subsequently, freehand regions of interest (ROI) were drawn on the ADC and all b values DWI images by using the T2-weighted images for guidance. ROI included largest possible part of the lesion, avoiding partial volume effect, areas of necrosis, and artifacts. Then ROI was copied and pasted from DWI image to corresponding ADC map and the measurement on ADC map was recorded. ADC was measured twice for each lesion and these measurements were averaged. Separate ADC measurements were performed for adjacent, normal tissues (e.g., liver, small bowel).

ADC values were calculated by monoexponential regression with the following formula: $S = S_0 \cdot \exp(-b \cdot \text{ADC})$,

TABLE 2: Locations of the extraovarian lesions.

Location	N—total 18
Hilus of the liver	2 (one false positive)
Cecum	2
Omental sac	1
Omentum	4
Douglas pouch	4
Diaphragm	2
Capsule of the liver	1
Transverse colon	1
Mesentery	1

where S is the signal intensity after application of the diffusion gradient and S_0 is the signal intensity at $b = 0 \text{ s/mm}^2$. Eight b values were applied for ADC calculation.

The number and location of metastatic peritoneal implants were confirmed intraoperatively and compared with MRI findings.

The reference standard for the diagnosis was histopathologic proof obtained intraoperatively.

2.4. Statistical Analysis. All statistical analyses were performed using the STATISTICA ver.12 (Statsoft) software package. Comparisons of mean ADC and mean b values images (b 50, 100, 150, 200, 400, 800, and 1200 s/mm^2) between peritoneal implants and normal surrounding tissue were analyzed using an unpaired t -test; ROC curve analysis $p < 0.05$ indicated a statistically significant difference.

3. Results

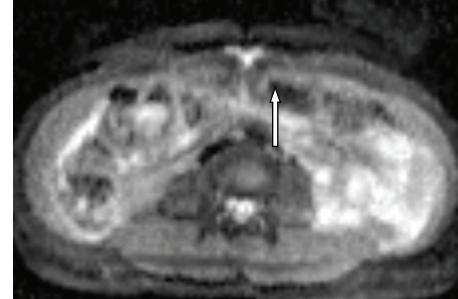
Overall, 18 extraovarian peritoneal lesions were found on DW images in 10 from 26 examined patients. The location of these lesions is presented in Table 2. All implants had diameter of 10 mm or less. The presence of all lesions diagnosed by MRI was confirmed intraoperatively. Histopathologic findings in 17 proofs confirmed ovarian cancer (13 serous, 3 mucinous, 1 endometrioid). One proof confirmed chronic inflammatory lymph node of hilus of the liver. No additional peritoneal implants were identified during surgical exploration; therefore positive predictive value (PPV) and negative predictive value (NPV) of DW imaging for the detection of metastatic peritoneal disease were, respectively, 94% and 100%.

On all DW images (with b values of 0, 50, 100, 150, 200, 400, 800, and 1200 s/mm^2) the mean signal intensities of peritoneal lesions were significantly higher than the mean signal intensities of normal adjacent tissue ($p = 0.000001$). Mean ADC values of peritoneal lesions were significantly lower than those of adjacent tissues ($p = 0.0005$) (Figures 1(a), 1(b), 2(a), and 2(b)).

The ROC curve analysis proved very high sensitivity and specificity of DW methods: from 89% (sensitivity) and 85% (specificity) for ADC to 100% (sensitivity) and 100% (specificity) for b value 1200, respectively (Figure 3).



(a)



(b)

FIGURE 1: (a) DW image ($b = 800 \text{ s/mm}^2$) shows the small implant with high signal intensity (arrow) on transverse colon serosa. (b) On an ADC map, the implant demonstrates restricted diffusion (arrow).

4. Discussion

Magnetic resonance imaging is regarded as an accurate technique for the detection and characterization of peritoneal spread of abdominal and pelvic malignancies. Advances in MRI technology, such as introduction of high-performance gradient systems, parallel imaging, or increased field homogeneity, resulted in improvement of quality of several MR techniques, including diffusion-weighted imaging. According to published reports this method could be also implemented for the detection of metastatic peritoneal disease in patients with malignant ovarian lesions [10].

At present, CT is the method of choice in preoperative evaluation of ovarian cancer and has been proved an accurate technique for predicting the results of cytoreduction in bulky disease [8]. In cases of “probably” early-stage ovarian cancer, limited only to ovarian mass, peritoneal implants are small and single, making the preoperative diagnosis challenging. CT is often not capable of reliably identifying small implants (with maximum diameter less than 5 mm) on the mesentery, bowel serosa, or peritoneum, especially in the absence of ascites [8, 11]. When diagnosed by MRI, these small lesions are usually better seen on DW images than on standard T1 and T2-weighted images [12].

Sala et al. in 2012 described the group of 22 ovarian cancer patients in which the mean ADC for peritoneal metastases was lower than that of omental ($p = 0.006$) and ovarian mass ($p = 0.015$) [10].

DW imaging, especially when quantitative analysis is performed, has several limitations. The acquisition as well

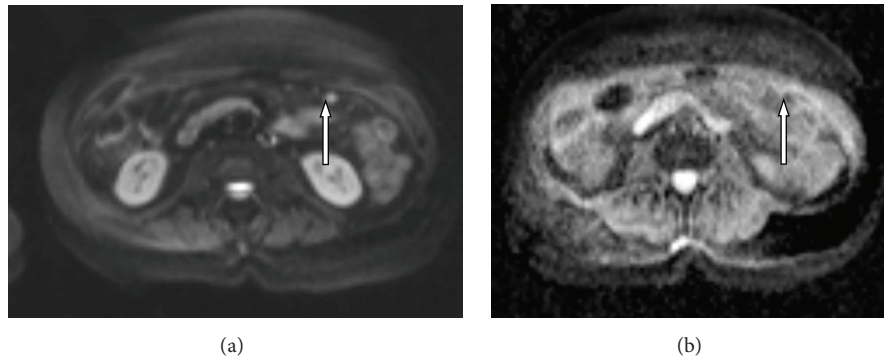


FIGURE 2: (a) DW image ($b = 800 \text{ s/mm}^2$) shows the small implant with high signal intensity (arrow) in omentum. (b) An ADC map, the implant demonstrates restricted diffusion (arrow).

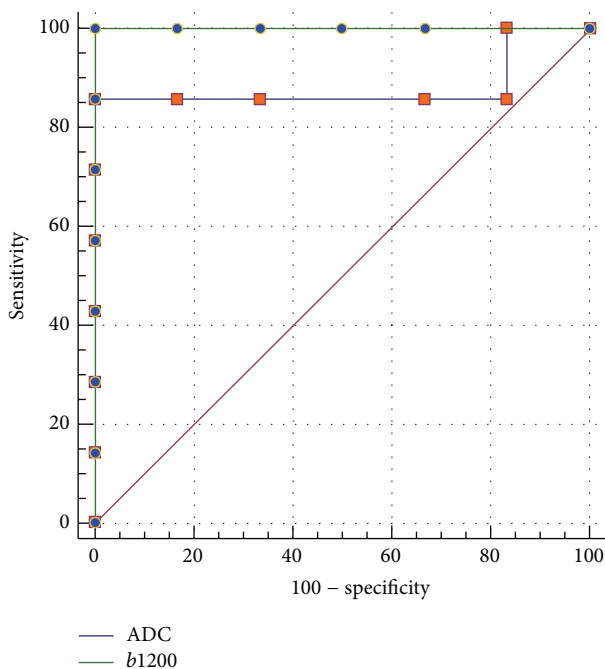


FIGURE 3: The ROC curve analysis of DW imaging for b value 1200 and ADC.

as analysis of DW images is not standardized. The choice of b values (number, range, and the first b value) and the method for ADC calculation (monoexponential versus biexponential model) have important implications for calculated ADC values of analyzed lesions. On the expense of prolonged imaging time, we implemented 8 b values (0, 50, 100, 150, 200, 400, 800, and 1200 s/mm^2) aiming to obtain more reliable ADC values than with the use of less b values. However, alternatively, we cannot exclude that monoexponential model applied in this study for ADC calculation could be less accurate than biexponential model [13].

One of the important limitations of this study is small number of patients. Therefore our results have to be regarded as preliminary in terms of sensitivity and specificity of DW

imaging for the detection of small peritoneal implants and should be confirmed on larger group of patients.

5. Conclusions

The results of this preliminary study confirmed that implementation of DW imaging has potential for the detection of small peritoneal metastatic implants, which is very important especially in patients with potentially early malignant ovarian masses. We presume that implementation of DW imaging of the abdomen and pelvis may provide important, supplementary information regarding extension of neoplastic disease and influence patient's treatment.

Conflict of Interests

The authors declare that there is no conflict of interests regarding the publication of this paper.

References

- [1] J. Didkowska, U. Wojciechowska, and W. Zatonski, *Cancer in Poland 2011*, Polish National Cancer Registry, Warsaw, Poland, 2013.
- [2] J. L. Benedet, H. Bender, H. Jones III, H. Y. Ngan, and S. Pecorelli, "FIGO staging classifications and clinical practice guidelines in the management of gynecologic cancers. FIGO Committee on Gynecologic Oncology," *International Journal of Gynecology and Obstetrics*, vol. 70, no. 2, pp. 209–262, 2000.
- [3] L. Verleye, P. B. Ottevanger, W. van der Graaf, N. S. Reed, and I. Vergote, "EORTC–GCG process quality indicators for ovarian cancer surgery," *European Journal of Cancer*, vol. 45, no. 4, pp. 517–526, 2009.
- [4] P. Wimberger, N. Lehmann, R. Kimmig, A. Burges, W. Meier, and A. Du Bois, "Prognostic factors for complete debulking in advanced ovarian cancer and its impact on survival. An exploratory analysis of a prospectively randomized phase III study of the Arbeitsgemeinschaft Gynaekologische Onkologie Ovarian Cancer Study Group (AGO-OVAR)," *Gynecologic Oncology*, vol. 106, no. 1, pp. 69–74, 2007.
- [5] E. L. Eisenhauer, N. R. Abu-Rustum, Y. Sonoda, C. Aghajanian, R. R. Barakat, and D. S. Chi, "The effect of maximal surgical cytoreduction on sensitivity to platinum-taxane chemotherapy

- and subsequent survival in patients with advanced ovarian cancer,” *Gynecologic Oncology*, vol. 108, no. 2, pp. 276–281, 2008.
- [6] R. E. Bristow, A. Santillan, T. P. Diaz-Montes et al., “Centralization of care for patients with advanced-stage ovarian cancer: a cost-effectiveness analysis,” *Cancer*, vol. 109, no. 8, pp. 1513–1522, 2007.
- [7] P. Morice, E. Leblanc, F. Narducci et al., “Initial or interval debulking surgery for advanced stage ovarian cancer: state-of-the-art. How to select patients?” *Gynecologie Obstetrique Fertilité*, vol. 33, no. 1-2, pp. 55–63, 2005.
- [8] S. Nougaret, H. C. Addley, P. E. Colombo et al., “Ovarian carcinomatosis: how the radiologist can help plan the surgical approach,” *RadioGraphics*, vol. 32, no. 6, pp. 1775–1800, 2012.
- [9] S. Kyriazi, D. J. Collins, V. A. Morgan, S. L. Giles, and N. M. deSouza, “Diffusion-weighted imaging of peritoneal disease for noninvasive staging of advanced ovarian cancer,” *Radiographics*, vol. 30, no. 5, pp. 1269–1285, 2010.
- [10] E. Sala, M. Y. Kataoka, A. N. Priest et al., “Advanced ovarian cancer: multiparametric MR imaging demonstrates response- and metastasis-specific effects,” *Radiology*, vol. 263, no. 1, pp. 149–159, 2012.
- [11] F. V. Coakley, P. H. Choi, C. A. Gougoutas et al., “Peritoneal metastases: detection with spiral CT in patients with ovarian cancer,” *Radiology*, vol. 223, no. 2, pp. 495–499, 2002.
- [12] R. N. Low, C. P. Sebrechts, R. M. Barone, and W. Muller, “Diffusion-weighted MRI of peritoneal tumors: comparison with conventional MRI and surgical and histopathologic findings—a feasibility study,” *American Journal of Roentgenology*, vol. 193, no. 2, pp. 461–470, 2009.
- [13] E. Sala, A. N. Priest, M. Kataoka et al., “Apparent diffusion coefficient and vascular signal fraction measurements with magnetic resonance imaging: feasibility in metastatic ovarian cancer at 3 Tesla,” *European Radiology*, vol. 20, no. 2, pp. 491–496, 2010.

Research Article

Diffusion-Weighted Imaging with Two Different b -Values in Detection of Solid Focal Liver Lesions

Da-wei Yang,^{1,2} Ke-yang Wang,¹ Xun Yao,³ Hui-yi Ye,⁴ Tao Jiang,⁵ Yuan Liu,⁶ Jia-yin Gao,⁷ Min Chen,⁷ Cheng Zhou,⁷ and Zheng-han Yang^{1,2}

¹Department of Radiology, Beijing Friendship Hospital, Capital Medical University, Beijing 100050, China

²National Clinical Research Center for Digestive Diseases, Beijing 100050, China

³Department of Radiology, Peking University People's Hospital, Beijing 100044, China

⁴Department of Radiology, PLA General Hospital, Beijing 100853, China

⁵Department of Radiology, Beijing Chaoyang Hospital, Capital Medical University, Beijing 100020, China

⁶Department of Ultrasound, Beijing Hospital, Beijing 100730, China

⁷Department of Radiology, Beijing Hospital, Beijing 100730, China

Correspondence should be addressed to Zheng-han Yang; zhenghanyang@263.net

Received 22 September 2015; Revised 19 November 2015; Accepted 29 November 2015

Academic Editor: Yi-Xiang Wang

Copyright © 2016 Da-wei Yang et al. This is an open access article distributed under the Creative Commons Attribution License, which permits unrestricted use, distribution, and reproduction in any medium, provided the original work is properly cited.

One hundred and eighty-two consecutive patients with suspected liver disease were recruited to receive diffusion-weighted imaging (DWI) with two different b -values, in comparison with T2-weighted imaging (T2WI). The detection rate of three MR sequences in solid focal liver lesions (FLLs) and subgroup analyses were performed. Our prospective study found that DWI600 was equivalent to DWI100 and T2WI for the detection of solid FLLs overall but was significantly more accurate in the detection of malignant solid FLLs and lesions larger than 10 mm.

1. Introduction

Early detection and diagnosis of hepatic tumor are an important step in clinical work, which would allow effective surgical or mini-invasive therapy [1–6]. With the advances in magnetic resonance imaging (MR) technology, diffusion-weighted magnetic resonance imaging (DWI) is now widely used as a standard imaging sequence in clinical work and shows its potential benefit in evaluation of the focal hepatic tumor [7–11]. DWI with small b -values less than 100–150 sec/mm² can suppress the intrahepatic vascular signal, creating the so-called black blood effect, which improves the detection of small focal liver lesions (FLLs) especially localized near small hepatic vessels. Meanwhile, DWI with low b -value has higher imaging quality compared with single shot fast spin-echo sequences [11–13], due to the fact that it is less affected by artifacts such as eddy currents or blurring.

A substantial number of studies [14–17] have compared low b -value DWI with T2-weighted imaging (T2WI) for image quality and detection of FLLs. These studies generally

showed better performance of DWI with low b -value in terms of lesion detection and conspicuity compared with T2WI. However, most previous studies mainly focused on the detection of metastases or just included cysts and hemangiomas as benign lesions, lacking of common solid FLLs such as focal nodular hyperplasias (FNHs), or other less common solid FLLs such as inflammatory pseudotumors (IPTs). Furthermore, DWI with low b -value could not simultaneously improve the detection as well as characterization of lesion, which is usually performed with DWI with higher b -value ($b > 500$ sec/mm²) and/or other conventional sequences.

DWI with higher b -value mainly reflects diffusion information of water molecules motion within the lesions, which help to improve the characterization of solid FLLs [8]. Meanwhile, we found in practice that DWI with higher b -value also enables a better detection of lesions in liver or pancreas compared with T2WI or other conventional sequences. For example, solid FLLs such as FNHs and hepatocellular carcinomas (HCCs) sometime can be difficult to be detected on T2WI or even DWI with low b -value due to either iso- or

TABLE 1: Parameters of three evaluation MR sequences.

Parameters	DWI600	DWI100	T2WI
Acquisition mode	Respiratory-triggered	Breath-hold	Respiratory-triggered
Repetition time (TR)	2-3 respiratory cycles	2400 ms	2-3 respiratory cycles
Echo time (TE)	Minimum	Minimum	80 ± 10 ms
<i>b</i> -value (s/mm ²)	0 and 600	0 and 100	/
Section thickness (mm)	6	6	6
Intersection gap (mm)	1.5	1.5	1.5
Field of view (mm)	320–380	320–380	320–380
Rectangle FOV	90%–100%	90%–100%	75%
Matrix	128 × 128	128 × 128	224 × 320
Number of signal averages	4	2	2
Parallel acceleration factor	2	2	/
Echo train length	64	64	<20
Acquisition time	2-3 min	19 s	3–5 min

DWI600: diffusion-weighted imaging with *b*-value of 0, 600 sec/mm²; DWI100: diffusion-weighted imaging with *b*-value of 0, 100 sec/mm²; T2WI: T2-weighted imaging.

slightly hypersignal intensity to liver parenchyma [18–20]; however, those lesions could be more conspicuous on DWI with higher *b*-value. Although some studies [16, 21–23] have investigated DWI with higher *b*-value in FLL detection, none of the studies has discussed the role of DWI with higher *b*-value in detection of solid FLLs covering the topic of common disease. Therefore, the purpose of this multicenter clinical study was to prospectively investigate the DWI with low *b*-values of 0, 100 sec/mm² (DWI100), DWI with higher *b*-value of 0, 600 sec/mm² (DWI600) in detection of solid FLLs in a large number of patients with a wide spectrum of lesions, in comparison with T2WI.

2. Methods and Materials

2.1. Patients. This prospective, multicenter study was approved by Institutional Human Ethics Board and registered in <http://www.chictr.org.cn/> numbering ChiCTR-DDT-11001587. Written informed consent was obtained from all patients. From June 2011 to December 2012, 182 patients were recruited in 6 hospitals (Beijing Friendship Hospital, Beijing Hospital, PLA General Hospital, Beijing Chaoyang Hospital, Nantong Third People's Hospital, and Ningbo Lihuili Hospital). The inclusion criteria were patients who have (1) focal liver lesions (FLLs) found on ultrasound or CT, (2) chronic liver disease or cirrhosis or viral hepatitis B/hepatitis C infection, (3) extrahepatic malignancy, and (4) no contraindication to MR contrast agents. 85 patients were excluded according to at least one of the following exclusion criteria: (1) undergoing antineoplastic treatment before MR scanning ($n = 8$), (2) no definite diagnosis ($n = 6$), (3) incomplete DW imaging ($n = 3$), (4) no lesion detected ($n = 37$), and (5) only cystic lesion detected ($n = 31$). Those without histologic diagnosis as well as typical MR findings finally were defined as patients with no definite diagnosis, who were then strongly suggested to take follow-up under the guidance of doctor considering other useful clinical tests. Patients with incomplete DW imaging were excluded

from the study population; however, the lack of several DW images did not hamper making diagnosis.

2.2. MR Imaging. A 1.5 T MRI whole-body scanner (Signa Twin-speed HD, GE Healthcare, Milwaukee, WI) with an eight-element phased array coil was used for signal reception in all study sites. Gradient strengths were 23/40 mT/m. Gradient slew rate were 80/150 mT/m/ms. Diffusion-weighted MR imaging with low and higher *b*-value sequences and respiratory-triggered T2-weighted fast spin-echo imaging were performed as study MR sequences. The spectrally selective fat suppression technique was used at all three MR sequences. The detailed parameters for three MR sequences are shown in Table 1. We choose the *b*-value of 100 s/mm² and 600 s/mm² to represent the low and higher *b*-value, respectively, because both of them were used routinely in our clinical work and proven to be a good option.

Other MR sequences including in- and opposed-phase spoiled gradient-recalled echo T1-weighted imaging and contrast-enhanced fat-suppressed three-dimensional spoiled gradient-recalled echo imaging were performed.

2.3. Reference Standard. Standard of reference for FLL detection was established by the consensus reading of the two observers (Ye Tan and Jie Zhu, with 15 and 10 years of experience in abdominal imaging, resp.), using all available MR sequences including precontrast T1-weighted sequence, in- and opposed-phase gradient-recalled-echo T1-weighted sequence, and dynamic contrast-enhanced MR sequence. A lesion was considered as present if it could be detected on at least one sequence and also was confirmed by histopathologic analysis or follow-up MR imaging.

FLLs characterization was established optimally by histopathologic findings. For cases without available histopathologic findings, the clinical diagnosis was made by the combination of clinical history, typical MR imaging findings, and follow-up MR imaging with a minimum interval of 6 months. The clinical diagnosis of benign lesions

including FNH, IPT, solitary necrotic nodule (SNN), and hepatic pseudolipoma was made by using validated criteria [24–27] and by their stable appearance at follow-up MR imaging with a minimum interval of 6 months. HCCs were diagnosed clinically from a complicated consideration of cirrhosis background, typical imaging findings [28, 29], the American Association for the Study of Liver Disease (AASLD) criteria for HCC [30], elevated tumor markers (e.g., α -fetoprotein), and progressively enlargement in follow-up. Metastases were diagnosed on the basis of presence of a known primary malignancy, MR imaging findings [31, 32], and follow-up imaging results showing interval progression.

2.4. Qualitative Evaluation. All MR images were independently interpreted by two observers (Yue Guo and Chen Zhang, with 8 and 7 years of experience in abdominal imaging, resp.) who were blinded to clinical history and imaging reports. DWI600, DWI100, and T2WI were randomly analyzed in three sessions separated by at least 3 weeks to minimize a recall bias. All the cases in each session were interpreted in a random manner. For each patient, the number, size, location (with Couinaud segments delineated), and image number of FLLs were recorded. A maximum of 5 largest lesions were recorded per patient, if multiple FLLs were present. Evaluation was done at GE ADW 4.4 workstation. Each sequence for lesion conspicuity was subjectively rated by using a four-point scale, as follows: score 1, definitely not present; score 2, probably not present; score 3, probably present; score 4, definitely present. Positive detection was calculated based on lesions assigned more than or equal to score 3.

2.5. Statistical Analysis. The diagnostic accuracy of DWI600, DWI100, and T2WI for solid FLLs detection was evaluated by comparing the detection rate between each two MR sequences. A statistical analysis was done by using a binary logistic regression model in which the detection accuracy was included as a dependent variable. Subgroup analyses based on the type (benign and malignant), size (≤ 10 mm, > 10 mm), and location (right lobe and left lobe) were also performed. The cut-point of 10 mm selected was based on the average diameter of intrahepatic vessels we measured.

k statistic was used to assess interobserver agreement for lesion detection, defined as poor (< 0.2), fair (0.21–0.40), moderate (0.41–0.60), good (0.61–0.80), and excellent (0.81–1.00) agreement. All statistical analyses were performed using SPSS 17.0 software (Windows, SPSS, Chicago, IL). A *P* value of less than 0.05 was considered to be statistically significant.

3. Results

3.1. Consensus Reading. Ninety-seven patients had a total of 137 solid FLLs (size range, 5.5–75 mm; mean, 21.9 mm) (Table 2). Sixty patients had 96 malignant solid FLLs, including 73 HCCs, 20 metastases, two cholangiocarcinomas, and one hemangioendothelioma. Histopathologic diagnosis was used for 52 HCCs, one metastatic lesion, two cholangiocarcinomas, and one hemangioendothelioma. Clinical diagnosis was used for 21 HCCs and 19 metastases. Thirty-seven

TABLE 2: Clinical information of the 97 patients and characteristics of 137 solid FLLs.

Age range (mean age)	25–77 years (52.2 years)
Sex (M/F)	65/32
Background liver	30 chronic hepatitis
	25 liver cirrhosis
	20 steatosis
	22 normal liver
Diagnosis of the lesions (<i>n</i> = 137)	
Benign (<i>n</i> = 41)	14 FNHs
	10 IPTs
	9 SNNs
	5 hepatic pseudolipomas
	1 angiomyolipoma
	1 hepatic adenoma
	1 ectopic adrenal adenoma
Malignant (<i>n</i> = 96)	73 HCCs
	20 metastases
	2 cholangiocarcinomas
	1 hemangioendothelioma
Location of the lesions	41 left lobes and 96 right lobes
Primary site of malignancy Patients (<i>n</i> = 5)	3 rectal-colons
	1 breast
	1 pancreas

FNH: focal nodular hyperplasia; IPT: inflammatory pseudotumor; SNN: solitary necrotic nodule; HCC: hepatocellular carcinoma.

patients had 41 benign solid FLLs, including 14 FNHs, 10 IPTs, nine SNNs, five hepatic pseudolipomas, one angiomyolipoma, one hepatic adenoma, and one ectopic adrenal adenoma. Among those benign solid FLLs, one angiomyolipoma, two FNHs, one adenoma, one ectopic adrenal adenoma, two IPTs, and one hepatic pseudolipoma were diagnosed pathologically. The diagnosis of remaining benign solid FLLs was made clinically according to the standard of reference.

3.2. Qualitative Evaluation. The detection rates using different MR sequences by each observer were shown in Table 4. Interobserver agreement for the FLLs detection using DWI600, DWI100, and T2WI was excellent, given the *k* values of 0.982, 0.900, and 0.861, respectively.

The subgroup analysis by lesion size showed that three MR sequences were more accurate in detection of lesions (> 10 mm) than of lesions smaller than 10 mm ($P < 0.001$, for all MR sequences) (Table 5). However, there were no significant differences between each two MR sequences in detection of lesion no matter larger or smaller than 10 mm.

The subgroup analysis by lesion location showed there were no significant differences between each two MR sequences in detection of lesions in left lobe or in right lobe (Table 5). However, T2WI was significantly better in detection of FLLs in the left lobe than in the right lobe (76.8% versus 56.3%, $P < 0.05$).

3.3. Missed FLLs. The missed FLLs by both observers at DWI600 included 13 HCCs, eight FNHs, five pseudolipomas, six IPTs, two metastases, four SNNs, and one hepatic adenoma.

TABLE 3: Detection rate of solid FLLs with each sequence in all, benign, and malignant lesions.

Sequence	All lesions ($n = 137$)	Benign lesions ($n = 41$)	Malignant lesions ($n = 96$)
DWI600	71.1 (97.5/137)	40.2 (16.5/41)	84.4 (81/96)
DWI100	67.9 (93/137)	57.3 (23.5/41)	72.4 (69.5/96)
T2WI	62.4 (85.5/137)	42.7 (17.5/41)	70.8 (68/96)
	DWI100 versus DWI600	0.573	0.127
<i>P</i> value	DWI100 versus T2WI	0.333	0.190
	DWI600 versus T2WI	0.125	0.825

Data are averaged for two independent observers. Unless otherwise indicated, numbers are percentages, with raw data in parentheses. DWI600: diffusion-weighted imaging with b -value of 0, 600 sec/mm²; DWI100: diffusion-weighted imaging with b -value of 0, 100 sec/mm²; T2WI: T2-weighted imaging.

TABLE 4: Detection rate of solid FLLs with each sequence by the two readers in all, benign, and malignant lesions.

	Sequence	All lesions ($n = 137$)	Benign lesions ($n = 41$)	Malignant lesions ($n = 96$)
Observer 1	DWI600	71.5 (98/137)	41.4 (17/41)	84.4 (81/96)
	DWI100	69.3 (95/137)	60.9 (25/41)	72.9 (70/96)
	T2WI	59.1 (81/137)	36.6 (15/41)	68.8 (66/96)
Observer 2	DWI600	70.8 (97/137)	39.0 (16/41)	84.4 (81/96)
	DWI100	66.4 (91/137)	53.7 (22/41)	71.9 (69/96)
	T2WI	65.7 (90/137)	48.8 (20/41)	72.9 (70/96)

Unless otherwise indicated, numbers are percentages, with raw data in parentheses. DWI600: diffusion-weighted imaging with b -value of 0, 600 sec/mm²; DWI100: diffusion-weighted imaging with b -value of 0, 100 sec/mm²; T2WI: T2-weighted imaging.

TABLE 5: Detection rate of solid FLLs with each sequence stratified by location and size.

Sequence	Lesion location		Lesion size		
	Left lobe ($n = 41$)	Right lobe ($n = 96$)	≤10 mm	>10 mm	
DWI600	79.3 (32.5/41)	67.7 (65/96)	31.2 (75/24)	79.6 (90/113)	
DWI100	70.7 (29/41)	66.7 (64/96)	25 (6/24)	77.0 (87/113)	
T2WI	76.8 (31.5/41)	56.3 (54/96)	16.7 (4/24)	72.1 (81.5/113)	
	DWI100 versus DWI600	0.411	0.878	0.588	0.628
<i>P</i> value	DWI100 versus T2WI	0.573	0.138	0.477	0.382
	DWI600 versus T2WI	0.794	0.102	0.212	0.175

Data are averaged for two independent observers. Unless otherwise indicated, numbers are percentages, with raw data in parentheses. DWI600: diffusion-weighted imaging with b -value of 0, 600 sec/mm²; DWI100: diffusion-weighted imaging with b -value of 0, 100 sec/mm²; T2WI: T2-weighted imaging.

The missed FLLs by both observers at DWI100 included 20 HCCs, five FNHs, five pseudolipomas, four IPTs, four metastases, one SNN, one hepatic adenoma, and one cholangiocarcinoma.

The detection rates using different MR sequences in all, benign, and malignant solid FLLs were shown in Table 3. The overall detection rate in all solid FLLs with DWI600, DWI100, and T2WI were 71.1%, 67.9%, and 62.4%, respectively. There were no significant differences between each two MR sequences. For malignant solid FLLs, DWI600 allowed identification of more FLLs (84.4%) than DWI100 (versus 72.4%, $P < 0.05$) and T2WI (versus 70.8%, $P < 0.05$) (Figures 1 and 2). The subgroup analysis in benign solid FLLs showed that the detection rate of DWI100 (57.3%) was higher than DWI600 (40.2%) and T2WI (42.7%) without significant difference (Figure 3). Meanwhile, DWI600 and T2WI were more accurate in the detection of malignant solid FLLs than of benign lesions (84.4% versus 40.2%, $P < 0.001$; 70.8% versus 42.7%, $P < 0.05$, resp.). However, no significant difference was observed for DWI100 in the detection of

malignant solid FLLs in comparison of benign lesions ($P = 0.082$).

The missed FLLs by both observers at T2WI included 22 HCCs, seven FNHs, four pseudolipomas, four IPTs, four metastases, five SNNs, and one hepatic adenoma.

4. Discussion

Our study showed that there were no significant differences among DWI600 (71.1%), DWI100 (67.9%), and T2WI (62.4%) in detection of solid FLLs overall. However, DWI600 (84.4%) was significantly better than DWI100 (versus 72.4%, $P < 0.05$) and T2WI (versus 70.8%, $P < 0.05$) in detection of malignant solid FLLs. It is well known that DWI with low b -value of approximately 100–150 sec/mm² is hypothesized to attenuate signal from microcirculatory perfusion, while DWI with higher b -value ($b > 500$ s/mm²) is thought to reveal restriction of water molecular diffusion in lesions [11–13]. With the highly cellular tissue, the tortuosity of the extracellular space, and the high density of cell membranes,

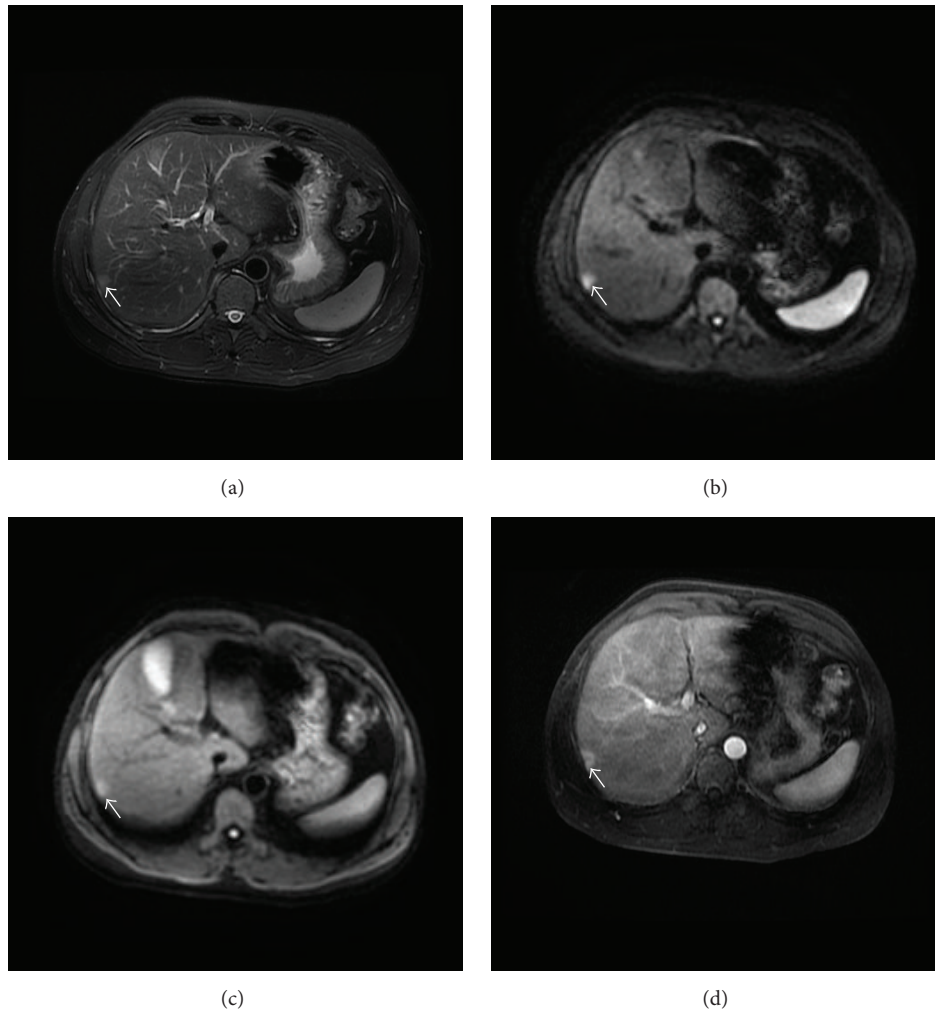


FIGURE 1: Transverse images in 49-year-old man with HCC. (a) Fat-suppressed T2-weighted fast spin-echo image shows that lesion is slightly hyperintense to the liver. (b) DW image with higher b -value shows that lesion is strongly hyperintense to the liver. (c) DW image with low b -value shows that lesion is slightly hyperintense to the liver with ill-defined margin. (d) Contrast-enhanced T1-weighted image in arterial phase demonstrates strong enhancement of lesion.

malignant FLLs can be more easily detected on DWI600 than on DWI100. In addition, T2WI was poorly reliable in detection of malignant solid FLLs when it showed iso- or slightly hypersignal intensity to liver parenchyma. Several studies [18, 33] have shown the limitation of T2WI in the detection of HCC in cirrhosis, mostly related to HCC signal intensity on T2WI images with appearing iso- or hypointense in 42.1%–53% of HCC. Results of our studies were in line with the findings of previous reports with lower rate of 32.2% (23.5/73, average between two observers) HCCs defined as undetectable (score < 3) according to the subjective rate system on T2WI, in comparison with 17.8% (13/73, average between two observers) HCCs undetectable on DWI600.

In addition, our study showed that DWI600 (40.2%) and T2WI (42.7%) were inferior in detecting benign solid FLLs in comparison with DWI100 (57.3%), although the differences did not reach significance. In our study, four FNHs, three SNNs, and two IPTs by observer 1 and three FNHs, three SNNs, and one IPT by observer 2 were visible on DWI100

but not on DWI600. The difference between DWI100 and DWI600 in detection of benign lesions is possibly attributed to three factors. First, over half of benign solid FLLs in our study did not show diffusion restriction. Second, although some benign solid lesions showed high signal intensity on DWI600 due to restricted water molecular diffusion, the lesion-to-liver contrast of those lesions on DWI600 was not as high as malignant lesions such as HCC [34]. Third, black blood effect, better imaging quality, and better contrast-to-noise ratio with DWI100 result in the better lesion conspicuity [12, 13]. Unfortunately, not enough benign solid FLLs as much as malignant lesions were included in our study; the potential benefit of DWI100 in detection of benign solid FLLs needs more studies to be investigated.

Of interest, our study found DWI600 had the higher detection rate of FLLs on left lobe than on right lobe. Several studies [21, 35] reported the poor visibility of the left lobe on DWI due to cardiac-motion induced signal loss; DWI was thought to be less sensitive in the left lobe. However, one must

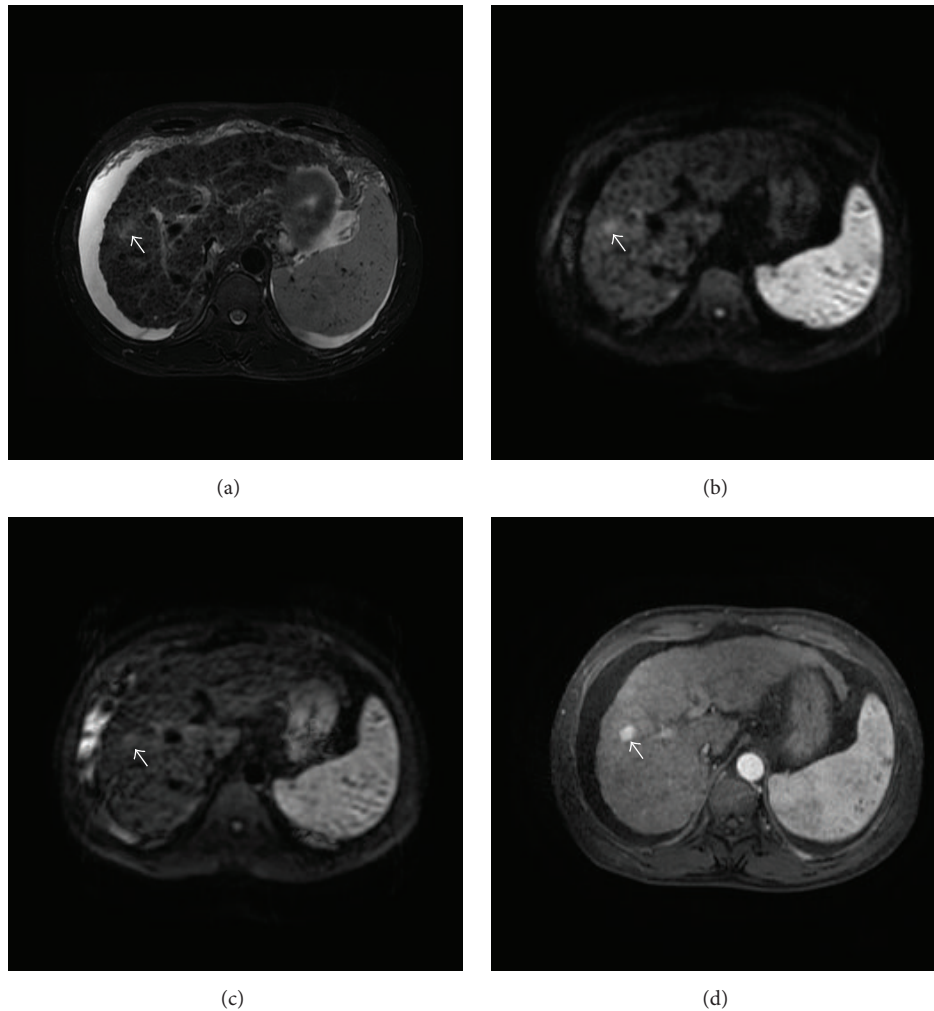


FIGURE 2: Transverse images in 62-year-old man with HCC. (a) Fat-suppressed T2-weighted fast spin-echo image shows that lesion is difficult to be detected. (b) DW image with higher b -value shows that lesion is strongly hyperintense to the liver. (c) DW image with low b -value shows that lesion is obscure. (d) Contrast-enhanced T1-weighted image in arterial phase demonstrates strong enhancement of lesion.

note that lesions with definite diffusion restriction can also be detected on DWI600 in left lobe. Meanwhile, results from our subgroup analysis on lesion size suggested that the detection rate was significantly influenced by the lesion size. The larger the lesion was, the easier it could be detected on all three MR sequences.

Our results were in disagreement with previous studies [14, 17] that DWI with a low b -value can significantly improve detection rate of both malignant and benign FLLs, comparing with T2-weighted imaging. For example, our study found that the detection rate of T2WI (70.8%) in malignant solid FLLs was as much as of DWI100 (72.4%). There is no doubt that the suppression of intrahepatic vessels with DWI100 considerably improves the detectability of perivascular lesions. However, T2WI is still helpful in detecting perivascular lesions when the size of lesion is much larger than adjacent vessel or when the lesion-to-vessel contrast is obvious. In addition, one potential explanation is that lacking the susceptibility artifact and image distortion, T2WI is helpful in detection of FLLs in the periphery of the liver and in the subphrenic hepatic areas.

There are several limitations of the study. First, the low and higher b -value DW images were acquired using different techniques for respiratory motion suppression and different numbers of signal averages. The results of this study may be confounded by the differences in acquisition between breath-hold and respiratory-triggered study and differences in the number of signal averages. The reason is that the MR scanners used in our study could not obtain two b -values DWI in one acquisition. The breath-hold acquisition mode for the DWI100 was selected to achieve a short acquisition time and few motion artifacts. In addition, the superiority of respiratory-triggered DW imaging over breath-hold DW imaging for lesion detection has been suggested by previous report [14]. Second, not all FLLs were confirmed pathologically. However, clinical diagnosis can be firmly established based on careful consensus reading by experienced abdominal radiologists and follow-up data. Third, we did not make analysis of apparent diffusion coefficient (ADC) maps, because analysis of ADC values was not within the scope of this work. Fourth, we did not investigate contrast-enhanced

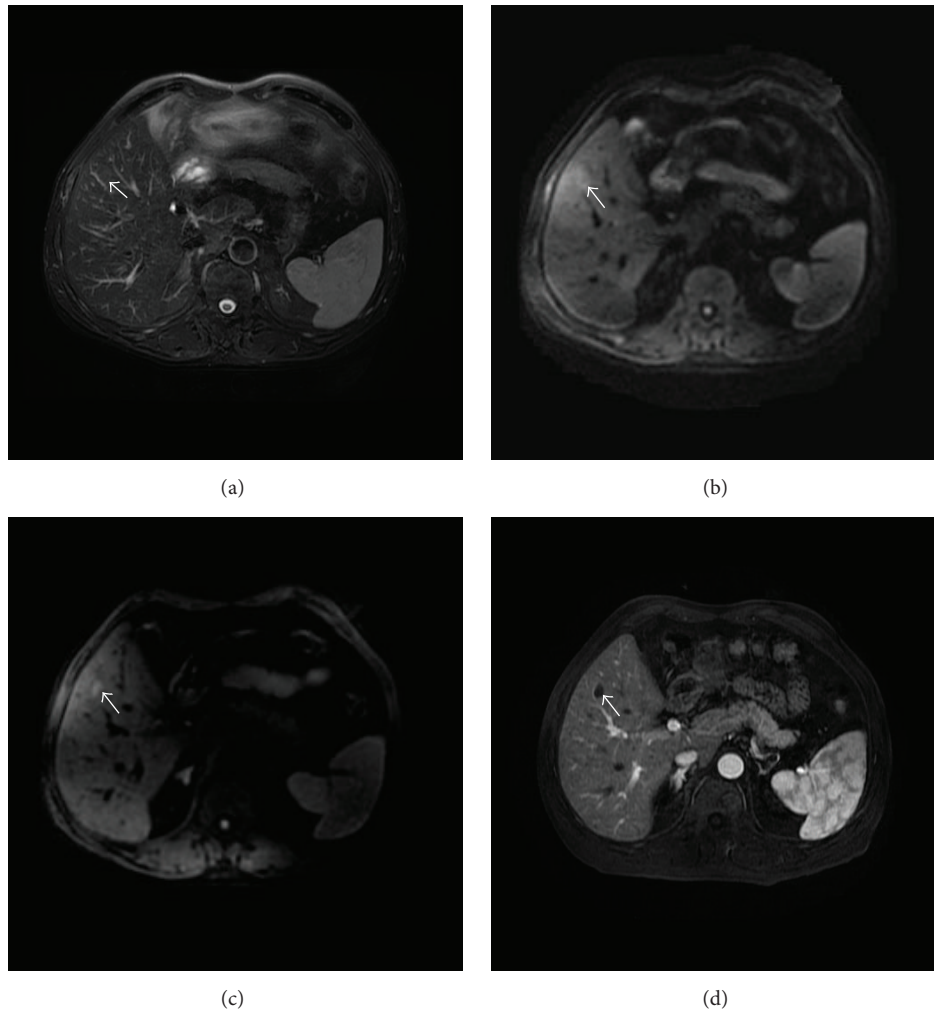


FIGURE 3: Transverse images in 56-year-old man with solitary necrotic nodule. (a) Fat-suppressed T2-weighted fast spin-echo image shows that lesion is isointense to the liver. (b) DW image with higher b -value shows that lesion is difficult to be identified. (c) DW image with low b -value shows lesion of hyperintensity could easily be detected. (d) Contrast-enhanced T1-weighted image in arterial phase demonstrates nonenhancement of lesion.

MR sequence in our study. Contrast-enhanced MR sequence is better than unenhanced MR sequences in the detection of FLLs [36]. Nevertheless, DWI and T2WI play an irreplaceable role in the detection of FLLs in patients having contrast agent allergy or renal dysfunction. Fifth, the number of benign FLLs and small FLLs (<10 mm) was relatively small. However, we believe our results are valid because we included a consecutive series of patients during a relatively long period and covered topic of common disease.

In conclusion, DWI600 was equivalent to DWI100 and T2WI for the detection of solid FLLs in all lesions but was significantly more accurate in detection of malignant solid FLLs and lesions larger than 10 mm. The results of our study show the superiority of DWI600 in the detection of malignant solid FLLs, but also the disadvantage of DWI600 for the depiction of benign solid FLLs such as FNHs and IPTs and tiny lesions. Both low and higher b -value diffusion-weighted imaging should be recommended as supplementary MR sequences in clinical practice.

Conflict of Interests

The authors declare that there is no conflict of interests regarding the publication of this paper.

Authors' Contribution

Da-wei Yang and Ke-yang Wang contributed equally to this study.

Acknowledgments

Editorial support was provided by Xiao-zheng Wang, M.D. The authors would like to express their enormous appreciation and gratitude to all participating sites. This study was supported by (1) Beijing Municipal Science & Technology Commission, Contract Grant no. D101100050010056, and (2) National Key Technology R&D Program, Contract Grant no. 2015BAI13B09.

References

- [1] T. Yau, V. Y. F. Tang, T.-J. Yao, S.-T. Fan, C.-M. Lo, and R. T. P. Poon, "Development of Hong Kong liver cancer staging system with treatment stratification for patients with hepatocellular carcinoma," *Gastroenterology*, vol. 146, no. 7, pp. 1691–1700.e3, 2014.
- [2] Y.-X. J. Wáng, T. De Baere, J.-M. Idée, and S. Ballet, "Transcatheter embolization therapy in liver cancer: an update of clinical evidences," *Chinese Journal of Cancer Research*, vol. 27, no. 2, pp. 96–121, 2015.
- [3] Y.-X. J. Wáng, Y. Choi, Z. Chen, S. Laurent, and S. L. Gibbs, "Molecular imaging: from bench to clinic," *BioMed Research International*, vol. 2014, Article ID 357258, 3 pages, 2014.
- [4] X. Xu, L. Luo, J. Chen et al., "Acoustic radiation force impulse elastography for efficacy evaluation after hepatocellular carcinoma radiofrequency ablation: a comparative study with contrast-enhanced ultrasound," *BioMed Research International*, vol. 2014, Article ID 901642, 7 pages, 2014.
- [5] R. Loffroy, S. Favelier, V. Cherblanc, and L. Estivalet, "C-arm dual-phase cone-beam CT: a revolutionary real-time imaging modality to assess drug-eluting beads TACE success in liver cancer patients," *Quantitative Imaging in Medicine and Surgery*, vol. 3, no. 4, pp. 196–199, 2013.
- [6] R. Loffroy, S. Favelier, O. Chevallier et al., "Preoperative portal vein embolization in liver cancer: indications, techniques and outcomes," *Quantitative Imaging in Medicine and Surgery*, vol. 5, no. 5, pp. 730–739, 2015.
- [7] G.-H. Kwon, K. A. Kim, S. S. Hwang et al., "Efficiency of non-contrast-enhanced liver imaging sequences added to initial rectal MRI in rectal cancer patients," *PLoS ONE*, vol. 10, no. 9, Article ID e0137320, 2015.
- [8] T. Namimoto, M. Nakagawa, Y. Kizaki et al., "Characterization of liver tumors by diffusion-weighted imaging: comparison of diagnostic performance using the mean and minimum apparent diffusion coefficient," *Journal of Computer Assisted Tomography*, vol. 39, no. 4, pp. 453–461, 2015.
- [9] S. E. Bouchaibi, K. Coenegrachts, M. A. Bali, J. Absil, T. Metens, and C. Matos, "Focal liver lesions detection: comparison of respiratory-triggering, triggering and tracking navigator and tracking-only navigator in diffusion-weighted imaging," *European Journal of Radiology*, vol. 84, no. 10, pp. 1857–1865, 2015.
- [10] S. Lewis, A. Kamath, M. Chatterji et al., "Diffusion-weighted imaging of the liver in patients with chronic liver disease: comparison of monopolar and bipolar diffusion gradients for image quality and lesion detection," *American Journal of Roentgenology*, vol. 204, no. 1, pp. 59–68, 2015.
- [11] N. Galea, V. Cantisani, and B. Taouli, "Liver lesion detection and characterization: role of diffusion-weighted imaging," *Journal of Magnetic Resonance Imaging*, vol. 37, no. 6, pp. 1260–1276, 2013.
- [12] N. Bharwani and D. M. Koh, "Diffusion-weighted imaging of the liver: an update," *Cancer Imaging*, vol. 13, no. 2, pp. 171–185, 2013.
- [13] T. Takahara and T. C. Kwee, "Low b-value diffusion-weighted imaging: emerging applications in the body," *Journal of Magnetic Resonance Imaging*, vol. 35, no. 6, pp. 1266–1273, 2012.
- [14] T. Parikh, S. J. Drew, V. S. Lee et al., "Focal liver lesion detection and characterization with diffusion-weighted MR imaging: comparison with standard breath-hold T2-weighted imaging," *Radiology*, vol. 246, no. 3, pp. 812–822, 2008.
- [15] H. Wang, X.-Y. Wang, X.-X. Jiang, and Z.-X. Ye, "Comparison of diffusion-weighted with T2-weighted Imaging for detection of small hepatocellular carcinoma in cirrhosis: preliminary quantitative study at 3-T," *Academic Radiology*, vol. 17, no. 2, pp. 239–243, 2010.
- [16] K. Coenegrachts, J. Delanote, L. Ter Beek et al., "Improved focal liver lesion detection: comparison of single-shot diffusion-weighted echoplanar and single-shot T₂ weighted turbo spin echo techniques," *British Journal of Radiology*, vol. 80, no. 955, pp. 524–531, 2007.
- [17] C. J. Zech, K. A. Herrmann, O. Dietrich, W. Horger, M. F. Reiser, and S. O. Schoenberg, "Black-blood diffusion-weighted EPI acquisition of the liver with parallel imaging: comparison with a standard T2-weighted sequence for detection of focal liver lesions," *Investigative Radiology*, vol. 43, no. 4, pp. 261–266, 2008.
- [18] H. K. Hussain, I. Syed, H. V. Nghiem et al., "T2-weighted MR imaging in the assessment of cirrhotic liver," *Radiology*, vol. 230, no. 3, pp. 637–644, 2004.
- [19] J. Chen, M. Wu, R. Liu, S. Li, R. Gao, and B. Song, "Preoperative evaluation of the histological grade of hepatocellular carcinoma with diffusion-weighted imaging: a meta-analysis," *PLoS ONE*, vol. 10, no. 2, Article ID e0117661, 2015.
- [20] S. M. Hussain, T. Terkivatan, P. E. Zondervan et al., "Focal nodular hyperplasia: findings at state-of-the-art MR imaging, US, CT, and pathologic analysis," *Radiographics*, vol. 24, no. 1, pp. 3–17, 2004.
- [21] S. Goshima, M. Kanematsu, H. Kondo et al., "Diffusion-weighted imaging of the liver: optimizing b value for the detection and characterization of benign and malignant hepatic lesions," *Journal of Magnetic Resonance Imaging*, vol. 28, no. 3, pp. 691–697, 2008.
- [22] M. Bruegel, J. Gaa, S. Waldt et al., "Diagnosis of hepatic metastasis: comparison of respiration-triggered diffusion-weighted echo-planar MRI and five T2-weighted turbo spin-echo sequences," *American Journal of Roentgenology*, vol. 191, no. 5, pp. 1421–1429, 2008.
- [23] X.-Y. Cui and H.-W. Chen, "Role of diffusion-weighted magnetic resonance imaging in the diagnosis of extrahepatic cholangiocarcinoma," *World Journal of Gastroenterology*, vol. 16, no. 25, pp. 3196–3201, 2010.
- [24] M. Ronot and V. Vilgrain, "Imaging of benign hepatocellular lesions: current concepts and recent updates," *Clinics and Research in Hepatology and Gastroenterology*, vol. 38, no. 6, pp. 681–688, 2014.
- [25] J. Y. Park, M. S. Choi, Y.-S. Lim et al., "Clinical features, image findings, and prognosis of inflammatory pseudotumor of the liver: a multicenter experience of 45 cases," *Gut and liver*, vol. 8, no. 1, pp. 58–63, 2014.
- [26] L. X. Wang, K. Liu, G. W. Lin, and R. Y. Zhai, "Solitary necrotic nodules of the liver: histology and diagnosis with CT and MRI," *Hepatitis Monthly*, vol. 12, no. 8, Article ID e6212, 2012.
- [27] S. R. Prasad, H. Wang, H. Rosas et al., "Fat-containing lesions of the liver: radiologic-pathologic correlation," *Radiographics*, vol. 25, no. 2, pp. 321–331, 2005.
- [28] R. F. Sheng, M. S. Zeng, Y. Ji, L. Yang, C. Z. Chen, and S. X. Rao, "MR features of small hepatocellular carcinoma in normal, fibrotic, and cirrhotic livers: a comparative study," *Abdominal Imaging*, vol. 40, no. 8, pp. 3062–3069, 2015.
- [29] M. A. Fischer, D. A. Raptis, O. F. Donati et al., "MR imaging features for improved diagnosis of hepatocellular carcinoma in the non-cirrhotic liver: multi-center evaluation," *European Journal of Radiology*, vol. 84, no. 10, pp. 1879–1887, 2015.

- [30] J. Bruix and M. Sherman, "Management of hepatocellular carcinoma," *Hepatology*, vol. 42, pp. 1208–1236, 2005.
- [31] A. D. Hardie, M. Naik, E. M. Hecht et al., "Diagnosis of liver metastases: value of diffusion-weighted MRI compared with gadolinium-enhanced MRI," *European Radiology*, vol. 20, no. 6, pp. 1431–1441, 2010.
- [32] I.-M. Danet, R. C. Semelka, P. Leonardou et al., "Spectrum of MRI appearances of untreated metastases of the liver," *American Journal of Roentgenology*, vol. 181, no. 3, pp. 809–817, 2003.
- [33] G. A. Krinsky, V. S. Lee, N. D. Theise et al., "Hepatocellular carcinoma and dysplastic nodules in patients with cirrhosis: prospective diagnosis with MR imaging and explantation correlation," *Radiology*, vol. 219, no. 2, pp. 445–454, 2001.
- [34] F. Agnello, M. Ronot, D. C. Valla, R. Sinkus, B. E. Van Beers, and V. Vilgrain, "High-b-value diffusion-weighted MR imaging of benign hepatocellular lesions: quantitative and qualitative analysis," *Radiology*, vol. 262, no. 2, pp. 511–519, 2012.
- [35] S. M. Hussain, J. De Becker, W. C. J. Hop, S. Dwarkasing, and P. A. Wielopolski, "Can a single-shot black-blood T2-weighted spin-echo echo-planar imaging sequence with sensitivity encoding replace the respiratory-triggered turbo spin-echo sequence for the liver? An optimization and feasibility study," *Journal of Magnetic Resonance Imaging*, vol. 21, no. 3, pp. 219–229, 2005.
- [36] P. Soyer, M. Boudiaf, V. Placé et al., "Preoperative detection of hepatic metastases: comparison of diffusion-weighted, T2-weighted fast spin echo and gadolinium-enhanced MR imaging using surgical and histopathologic findings as standard of reference," *European Journal of Radiology*, vol. 80, no. 2, pp. 245–252, 2011.

Research Article

Analysis of Residual DSBs in Ataxia-Telangiectasia Lymphoblast Cells Initiating Apoptosis

Teresa Anglada, Mariona Terradas, Laia Hernández, Anna Genescà, and Marta Martín

Departament de Biologia Cel·lular, Fisiologia i Immunologia, Universitat Autònoma de Barcelona, Edifici C, Bellaterra, 08193 Cerdanyola del Vallès, Spain

Correspondence should be addressed to Marta Martín; marta.martin@uab.cat

Received 2 September 2015; Accepted 1 December 2015

Academic Editor: Yi-Xiang Wang

Copyright © 2016 Teresa Anglada et al. This is an open access article distributed under the Creative Commons Attribution License, which permits unrestricted use, distribution, and reproduction in any medium, provided the original work is properly cited.

In order to examine the relationship between accumulation of residual DNA double-strand breaks (DSBs) and cell death, we have used a control and an ATM (Ataxia-Telangiectasia Mutated) defective cell line, as Ataxia-Telangiectasia (AT) cells tend to accumulate residual DSBs at long times after damage infliction. After irradiation, AT cells showed checkpoint impairment and a fraction of cells displayed an abnormal centrosome number and tetraploid DNA content, and this fraction increased along with apoptosis rates. At all times analyzed, AT cells displayed a significantly higher rate of radiation-induced apoptosis than normal cells. Besides apoptosis, 70–85% of the AT viable cells (TUNEL-negative) carried ≥ 10 γ H2AX foci/cell, while only 12–27% of normal cells did. The fraction of AT and normal cells undergoing early and late apoptosis were isolated by flow cytometry and residual DSBs were concretely scored in these populations. Half of the γ H2AX-positive AT cells undergoing early apoptosis carried ≥ 10 γ H2AX foci/cell and this fraction increased to 75% in late apoptosis. The results suggest that retention of DNA damage-induced γ H2AX foci is an indicative of lethal DNA damage, as cells undergoing apoptosis are those accumulating more DSBs. Scoring of residual γ H2AX foci might function as a predictive tool to assess radiation-induced apoptosis.

1. Introduction

Following DNA double-strand breaks (DSBs) generation by ionizing radiation (IR), the cell undergoes an Ataxia-Telangiectasia Mutated (ATM) dependent p53 activation of the DNA damage response (DDR) cascade to activate the cell checkpoints in order to gain time for DNA repair [1–3]. If the DNA damage cannot be repaired during checkpoint arrest, cells are driven to undergo an irreversible fate by apoptosis or senescence [4, 5]. Sensing of the DNA damage involves the extensive phosphorylation of histone H2AX molecules at both sides of the DNA break [6]. Phosphorylated H2AX forms foci immediately after DNA damage induction by IR. These γ H2AX IRIF (Ionizing Radiation-Induced Foci) are detectable with immunostaining or cytometry techniques as soon as 3 minutes afterwards, and the maximum number of foci is detected 30–60 minutes after irradiation [7]. The number of γ H2AX foci has been found to closely correlate with the number of radiation-induced DSBs [8, 9]. Very soon after irradiation, γ H2AX foci are numerous and small and

they disappear along with resolution of DNA damage [8]. Nonetheless, several results have shown that radiosensitive cell lines retain γ H2AX foci longer than radioresistant cell lines after exposure to radiation [10–12]. The fraction of tumor cells that retain γ H2AX foci 24 hours after irradiation has been correlated with the fraction of cells that fail to divide and form colonies [13, 14], suggesting that the H2AX assay can be used as an indicator of cell death. However, there are also negative studies that found no correlation between γ H2AX and clonogenic cell survival [15, 16], demonstrating that it is yet unclear whether residual DSBs are ultimately related with apoptosis triggering.

Recently, apoptosis and mitotic catastrophe (MC) have been functionally linked [17, 18]. MC has been defined as an oncosuppressive mechanism resulting from a combination of deficient cell cycle checkpoints, persistence of DNA damage and mitotic failure, which can ultimately lead to cell death during mitosis or alternatively by apoptosis or senescence. This mechanism mainly operates in a cell-cycle-specific kinases-dependent and p53-dependent way to avoid

accumulation of genomic instability and is prevalent in cancer cells that exhibit genomic instability and are devoid of proper checkpoint control [17, 19, 20].

The goal of this study was to examine the relationship between DNA damage accumulation and apoptosis. In radiosensitive ATM deficient cells, the defects in triggering the whole DDR following IR lead to checkpoint failure and to the accumulation of unresolved DSBs [1, 3], thus being an ideal model to study this relationship. Our results show that AT and normal lymphoblastoid cell lines undergoing apoptosis accumulate a higher number of γ H2AX foci than those belonging to the viable fraction. Specifically, AT lymphoblasts accumulate a higher fraction of residual DSBs and undergo significantly higher levels of IR-induced apoptosis at all postirradiation (pIR) times analyzed. Also AT lymphoblasts display a strong G2/M arrest and tetraploidization, suggesting that MC contributes to apoptosis in ATM deficient cells.

2. Results and Discussion

2.1. AT Lymphoblasts Efficiently Trigger a p53-Dependent Apoptotic Response and Undergo High Levels of Radiation-Induced Apoptosis. In order to determine a relationship between persistent radiation-induced DSBs and apoptosis, we had to first determine the ability to undergo apoptosis in AT and normal lymphoblastoid cell lines (LCLs). To this end, Annexin-V (An) and propidium iodide (PI) incorporation in cells was measured by flow cytometry, and cells were analyzed at 0, 24, 48, and 72 hours after 5 Gy irradiation. Loss of plasma membrane asymmetry by exposing phosphatidylserine in the outer leaflet is an early event in the apoptotic process, previous to loss of membrane integrity and to DNA fragmentation. Thereby, cells positive for Annexin-V and negative for PI staining (An+/PI-) are considered to be undergoing early stages of apoptosis (EA) [21–23]. Later in this process, cells lose membrane integrity, allowing PI staining. Therefore, cells that are An+/PI+ are considered to be in late apoptosis (LA), although necrotic cells can also be found in this fraction [21, 24].

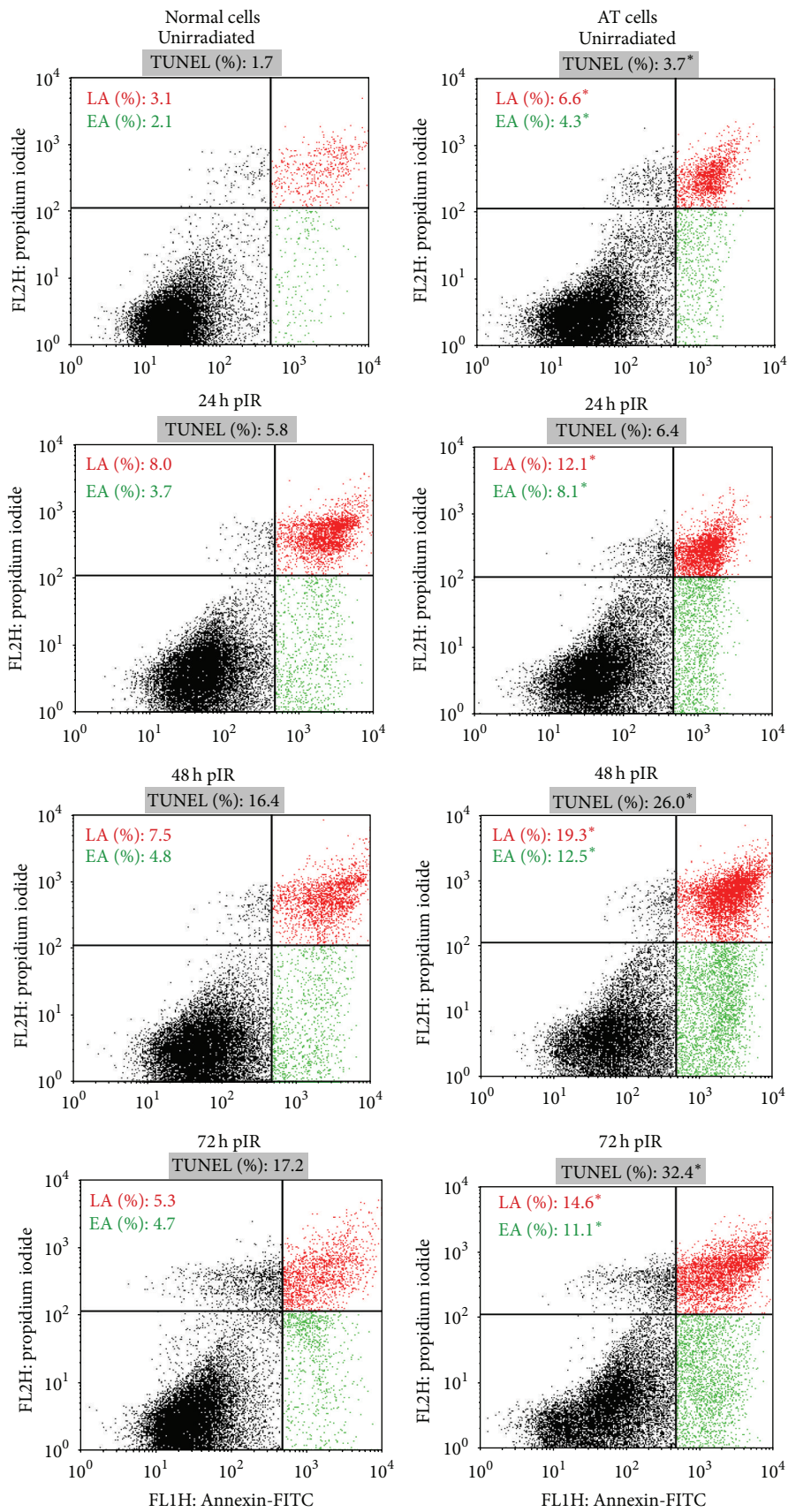
As shown in Figure 1(a), the fraction of An+/PI- cells is higher in AT LCL at all times analyzed, even before irradiation. AT cells undergoing early apoptosis reach 8.0% and 12.5% at 24 hours and 48 hours pIR, respectively, while the fraction of normal cells An+/PI- during these time points is always lower than 5%. The overall fraction of Annexin-positive cells (sum of An+/PI- and An+/PI+ cells) reaches its maximum at 48 hours after irradiation, being 12.3% in normal LCL and 31.8% in AT LCL. At later time points, An+/PI- and An+/PI+ cells start to slowly decline, although they are still significantly higher in AT cells and far from the basal levels in both cell lines. These results demonstrate that this AT LCL not only efficiently triggers apoptosis, but also undergoes higher rates of radiation-induced apoptosis than its normal counterpart.

Because several works have reported contradictory results regarding apoptosis induction in AT cells [25–31], we aimed to confirm the previous results obtained with Annexin-V/PI by analyzing radiation-induced apoptosis

using TUNEL methodology. One characteristic feature of the later stages of apoptosis is the internucleosomal fragmentation of DNA into ~180 bp repeats often referred to as DNA laddering [32]. TUNEL allows the detection of these DNA fragments by labeling their 3'-OH end with a fluorescent molecule. AT and normal lymphoblasts were irradiated at the same dose of γ -rays (5 Gy), and apoptosis levels were analyzed at the same time points previously described. TUNEL was performed on slides and quantitation of TUNEL-positive cells was performed with an epifluorescence microscope. The majority of TUNEL-positive cells also displayed characteristic morphological features of apoptosis, such as nuclei shrinkage, DNA compaction, and nuclear fragmentation. All these features combined with TUNEL staining allowed certain detection of apoptotic cells (Figure 1(b)).

As shown in Figure 1(a), the levels of spontaneous apoptosis measured with TUNEL were higher in AT than in normal cells. Higher rates of spontaneous apoptosis in AT lymphoblasts have been described before [33] and are confirmed by the results obtained in the present study with both apoptotic cell detection assays (total Annexin-V-positive cells before irradiation: 5.2% in normal cells versus 10.9% in AT cells; χ^2 test, $p < 0.0001$; TUNEL: 3.7% in AT cells versus 1.7% in normal cells; χ^2 test, $p < 0.0072$). At early postirradiation times, the fraction of TUNEL-positive cells remains low in both cell lines, but they increase at 48 hours pIR and reach maximum levels at 72 hours pIR, being of 17.2% in normal and 32.4% in AT cells (χ^2 test, $p < 0.0001$). Although both Annexin-V/PI and TUNEL methodologies measure apoptosis, they seem to detect correlative stages of this process. At twenty-four hours after irradiation, there has been an increase of cells undergoing EA and evolving to a LA stage compared to unirradiated cells, while yet very few cells are positive for TUNEL staining. EA and LA fractions reach a plateau level at 48 hours pIR, while at this time there is an increasing frequency of TUNEL-positive events. Because TUNEL methodology detects extensive DNA fragmentation, TUNEL-positive cells might undergo a later apoptotic stage than those signaled with Annexin. In this way, the combination of the results obtained with the Annexin-V/PI and the TUNEL procedures renders a dynamic picture of the apoptotic process in the lymphoblast cells analyzed.

Lymphocytes are removed, both physiologically and after irradiation, by a p53- and caspase-dependent apoptotic pathway that leads to DNA cleavage [19, 34, 35]. The role of the ATM protein in triggering this IR-induced apoptotic response has been examined using different experimental systems in AT lymphoblasts, AT lymphoblastoid cell lines (LCLs), and *Atm*^{-/-} mouse thymocytes with conflicting results. Lymphocytes from AT patients were found to have an increased spontaneous apoptotic level [33]. Also, a normal apoptotic response after IR was demonstrated in *Atm*^{-/-} mouse cells [26] and in lymphocytes from AT patients [27]. Variable results have been described in AT LCLs, although most of them displayed a normal apoptotic response to IR [28, 36]. To ultimately determine p53 status, we analyzed p53 presence and its activation after IR. Levels of p21, a p53 effector involved in cell cycle arrest at G1 and S phases



(a)

FIGURE I: Continued.

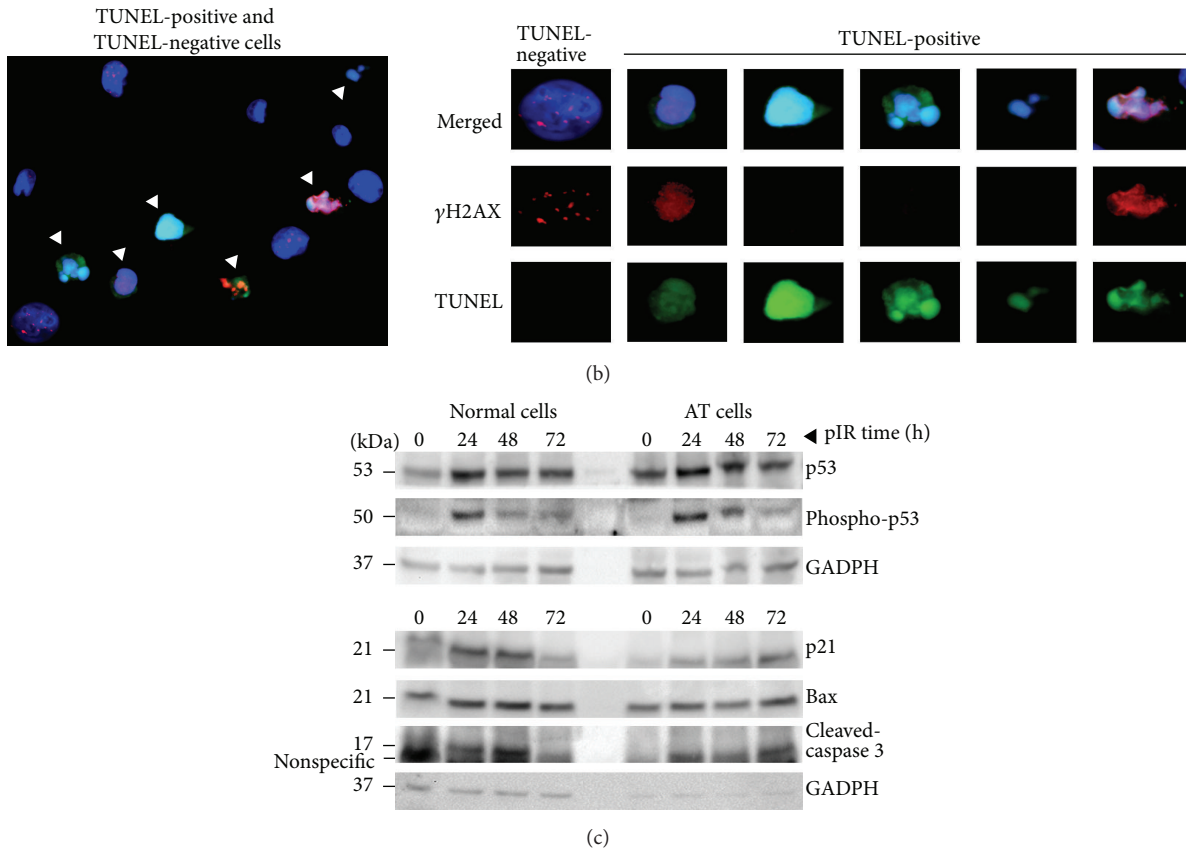


FIGURE 1: (a) Radiation-induced apoptosis measured by means of Annexin-V/PI and TUNEL methodologies. Cytometry plots were used for gating cells stained using Annexin-V (An) and propidium iodide (PI) before and after irradiation. In all plots, the lower left quadrant corresponds to the viable, nonapoptotic cell population (An-/PI-). The lower right quadrant corresponds to the cell population An+PI-, which is undergoing early apoptosis (EA) and is shown in green. The upper right quadrant corresponds to the cell population An+PI+, which is undergoing late apoptosis (LA) and is shown in red. Frequencies of EA and LA are shown in each graph at 0, 24, 48, and 72 hours after irradiation in normal and AT cells and they correspond to the mean of 3 different experiments with two replicas each. A minimal number of 10000 cells were analyzed in each experiment. The asterisks indicate statistical differences in the apoptotic levels between AT and normal cells when comparing the EA fraction, the LA fraction, and the sum of Annexin-V-positive cells (EA + LA). In all cases, χ^2 test was applied and the p values were <0.005 . Frequencies of TUNEL-positive cells for each cell type at 0, 24, 48, and 72 hours pIR are shown over each cytometry plot. The asterisks indicate statistical differences between AT and normal cells (χ^2 test; p values < 0.007). The values for TUNEL were obtained after scoring 1000 cells for each time point and each cell line using an epifluorescence microscope. (b) Scoring of TUNEL-positive cells. On the left, a general view under the microscope (40x) showing irradiated cells in which a combination of TUNEL staining (green) and γ H2AX immunofluorescence (red) has been applied. DNA is stained with DAPI (blue). TUNEL-positive cells (white arrowheads) depict intense TUNEL staining and they show the morphological features of apoptotic cells (right panel): smaller nuclei with highly condensed chromatin—intensely stained with blue—undergoing variable levels of nuclear fragmentation. Also, TUNEL-positive cells could depict a pan-nuclear γ H2AX staining but never had γ H2AX foci. (c) Western blot detection of apoptotic markers. Normal and AT cells were irradiated with 5 Gy of γ -rays and expression of p53, its activated form phospho-p53 (Ser15), and other p53 targets such as p21, Bax, and the cleaved fraction of caspase 3 were analyzed at 0, 24, 48, and 72 hours after irradiation. Proteins were detected in two different experiments and GADPH was used as the housekeeping gene.

after DNA damage induction [37], have also been analyzed. As shown in Figure 1(c), despite ATM absence, p53 was effectively induced in normal and AT cells at 24 hours pIR, when the fraction of apoptotic cells starts to increase. Consistent with greater apoptotic induction, levels of activated p53 are still high in AT cells at 48 hours pIR. Induction of p21 is observed in both cell lines although higher expression is observed in normal than in AT cells. In this regard, it has been suggested that ATM regulates distinct p53-dependent pathways that selectively trigger checkpoint arrest

or apoptosis. For example, effective p53 induction coupled with checkpoint failure and a normal apoptotic response after IR has been described in ATM deficient cells [26, 28, 38, 39]. In agreement with these works, normal cells efficiently arrest at G1 after irradiation while the AT lymphoblastoid cell line tested in this study undergoes high apoptosis rates along with G1 checkpoint failure (see Section 2). Bax, another p53 target involved in activation of caspases, shows a similar expression in both LCLs. The cleaved fragment of caspase 3 is detected only after irradiation in both cell lines but in

AT cells its expression is still visible at 72 hours, consistent with higher frequency of apoptotic AT cells at this time point. Altogether, our results are in agreement with a role for ATM selectively activating p53 to regulate cell-cycle checkpoint but not apoptosis. In this regard, ATM- and Rad3-related (ATR), Chk2 and DNA-PKcs have been proposed as candidates to regulate IR-induced apoptosis in AT cells [38–40].

2.2. Radiation-Induced Mitotic Catastrophe Is a More Relevant Cell Death Process in AT Lymphoblasts Than in Its Normal Counterparts. We proceeded by analyzing cell cycle progression after irradiation. As shown in Figure 2(a), normal lymphoblasts are efficiently arrested at G1, as demonstrated by a diminution of the S fraction at 24 h pIR that prevails up to 72 h. As expected, impairment of proper G1 arrest in the AT LCL was demonstrated by no noticeable decrease in the S fraction at 24 hours pIR, and later decreases were low when compared to normal cells. These results are consistent with the Western blot results showing a weak induction of p21 in AT cells after irradiation (Figure 1(c)) and are in agreement with the ATM deficiency cell phenotype, which is characterized by impairment of G1 and intra-S checkpoint activation upon DNA damage infliction. This leads to cell cycle progression of cells bearing unresolved DNA damage [3, 41]. These cells are efficiently arrested in G2 [42] unless the DNA damage has been inflicted during G2 phase, in which case ATM deficient cells proceed into mitosis [43]. In any case, damaged cells that surpass G1 and/or G2 checkpoints become later arrested in mitosis (M) because of spindle anaphase checkpoint (SAC). In this work, cells were irradiated during their exponential growth, implying that many AT cells will surpass G1 and intra-S checkpoints and will be arrested at G2, while those AT cells irradiated during G2 phase will surpass the G2 checkpoint and arrest in M by SAC. Remarkably, our results show that AT lymphoblasts significantly accumulate at G2/M after irradiation at all times analyzed (Figure 2(a)), suggesting that, besides cells arrested at G2 checkpoint, some of them might remain in M phase.

Persistent arrest at G2/M boundaries after DNA damage infliction is a first indicator of mitotic catastrophe (MC), so we aimed to analyze the possibility that MC contributes to cell death in AT cells. MC has been described as an onc suppressive mechanism that, in order to avoid accumulation of genomic instability, senses this mitotic failure and responds to it by driving the cell to death during mitosis [20]. Sometimes, some of these cells do not die during mitosis and eventually overcome SAC signaling and “slip” into the next interphase without dividing. These cells may reenter the cell cycle and reduplicate its DNA content, turning into the accumulation of tetraploid cells within the population. Indeed, AT lymphoblasts showed an increasing frequency of cells with a 4N DNA content that reached 5.6% at 72 hours after irradiation (Figures 2(a) and 2(b)). Although small, this fraction was higher than in normal lymphoblasts, whose tetraploid population was lower than 0.7% at all times analyzed. To further confirm these results, we quantified the centrosome number, as cells that skip mitosis and reenter the cell cycle will reduplicate their centrosomes along with DNA.

Centrosomes were scored by means of immunofluorescent pericentrin detection and cells were classified into those having a normal number of centrosomes (1 centrosome in interphase and 2 centrosomes in S, G2, and M phases) or an aberrant number of centrosomes (more than 2). As shown in Figure 2(b), the basal frequency of AT cells with >2 centrosomes was very low, but it strikingly increased at 48 hours after irradiation, when it reached almost 3% of the cell population and correlated with the appearance of a 4N cell population (Figure 2(b)). In contrast, the fraction of normal lymphoblasts with an abnormal number of centrosomes did not reach 1% of the population during the 48 h analyzed (χ^2 test, $p < 0.002$). Thus, some AT cells are able to reach mitosis despite defective repair. Eventually, some of them skip M phase, giving raise to the appearance of a tetraploid population together with an increasing population of cells with an abnormal centrosome number. Polyploid cells with extra centrosomes are prone to form transient multipolar mitotic spindles, which can either directly trigger mitotic death or result in the generation of aneuploid daughter cells. A small fraction of these cells might survive and enter a mitotic round that is also likely to be catastrophic [20]. Because the MC mechanism can ultimately culminate in apoptotic cell death [20], we propose that this mechanism contributes to the radiation-induced apoptotic levels detected in AT lymphoblasts.

2.3. Viable AT Lymphoblasts Display Higher Levels of Radiation-Induced DNA Damage and Delayed DSB Repair at Long Times after Irradiation. We next aimed to examine the levels of radiation-induced DNA damage in both lymphoblast cell lines. To this end, we analyzed γ H2AX foci corresponding to radiation-induced DSBs in viable cells—those negative for TUNEL (Figure 3(a)). Figure 3(b) shows that, 24 h after irradiation, 64.1% of the normal lymphoblasts have γ H2AX foci, a 3.2-fold increase compared to unirradiated cells. Within the same time interval, viable AT lymphoblasts displayed a 7-fold increase, as 87% of them showed γ H2AX foci (χ^2 test, $p = 0.0135$). At 72 h pIR normal cells have repaired most of their DSBs and only 22.2% of them have γ H2AX foci, while this fraction is still around 50% in AT lymphoblasts (χ^2 test, $p < 0.0001$). All together, these results reflect the DNA repair impairment of AT cells, which repair most of the DSBs in a fast and efficient way, while a subset of breaks remains unrepaired for long times, even days, after DNA damage infliction [3, 10–12, 44]. In agreement with that, our results show that AT cells, despite showing an initial decline in the fraction of cells displaying γ H2AX foci, are unable to efficiently proceed to further diminish this population and accumulate high numbers of residual DSBs, even at very long times after DNA damage has been induced.

After that, we scored the number of γ H2AX foci in the TUNEL-negative cells and classify them into two groups: cells with less than 10 γ H2AX foci and cells with 10 or more γ H2AX foci (Figure 3(b)). Only a small fraction of the normal cells accumulated 10 or more γ H2AX foci, reaching a peak of ~18% at 24 hours pIR and declining thereafter. On the contrary, most of the irradiated AT cells accumulated 10 or

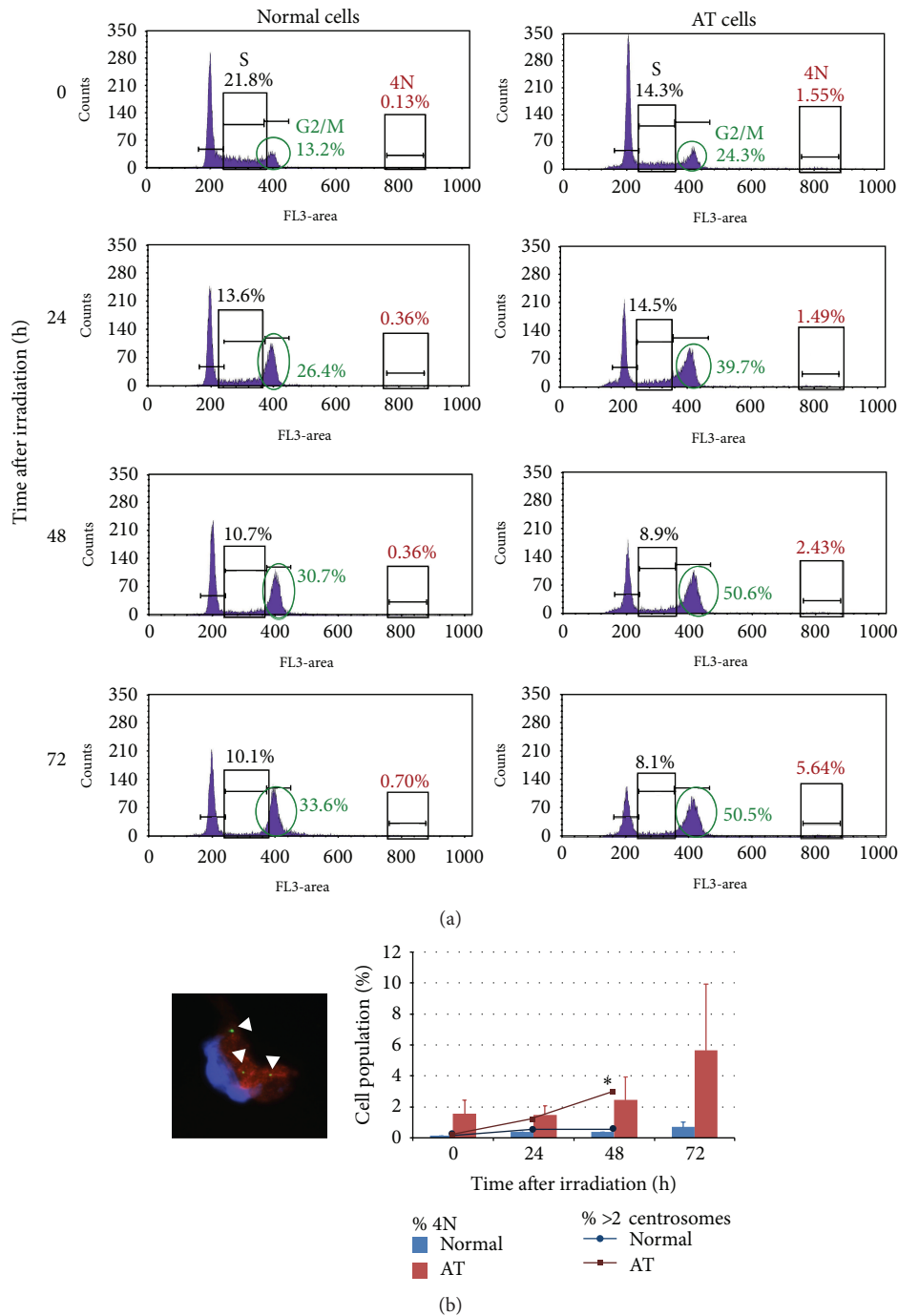


FIGURE 2: (a) Cell cycle analysis. The histograms show the cell cycle distribution of normal and AT cells before irradiation and at 24, 48, and 72 hours after irradiation. Cell cycle distribution was obtained by means of PI staining, which measures DNA content. The frequency of cells entering in S-phase for each cell type and each time point is shown, evidencing lack of IR-induced G1 checkpoint arrest in AT cells. The fraction of cells arrested in G2/M after irradiation and the tetraploid population (4N) arising after irradiation have also been highlighted. The frequencies displayed are the mean of two independent experiments in which a minimum number of 10000 cells were analyzed. (b) Tetraploidization and centrosome number. The image shows an AT lymphoblast (probably a metaphase) with 3 pericentrin signals (green; white arrowheads). The DNA is stained with DAPI and the red staining corresponds to α -tubulin. The bars in the graph show the fraction of tetraploid cells scored in AT and normal lymphoblasts before and after irradiation. The values are the mean of two experiments, and the error bars show the standard deviation. The lines in the graph depict the fraction of cells with an abnormal centrosome number (>2) within the same time points. The values for centrosome number were obtained after analyzing a minimal number of 400 cells for each cell type and each time point. The asterisk indicates statistical differences between normal and AT lymphoblasts in the frequency of cells with more than 2 centrosomes (χ^2 test; p values < 0.002).

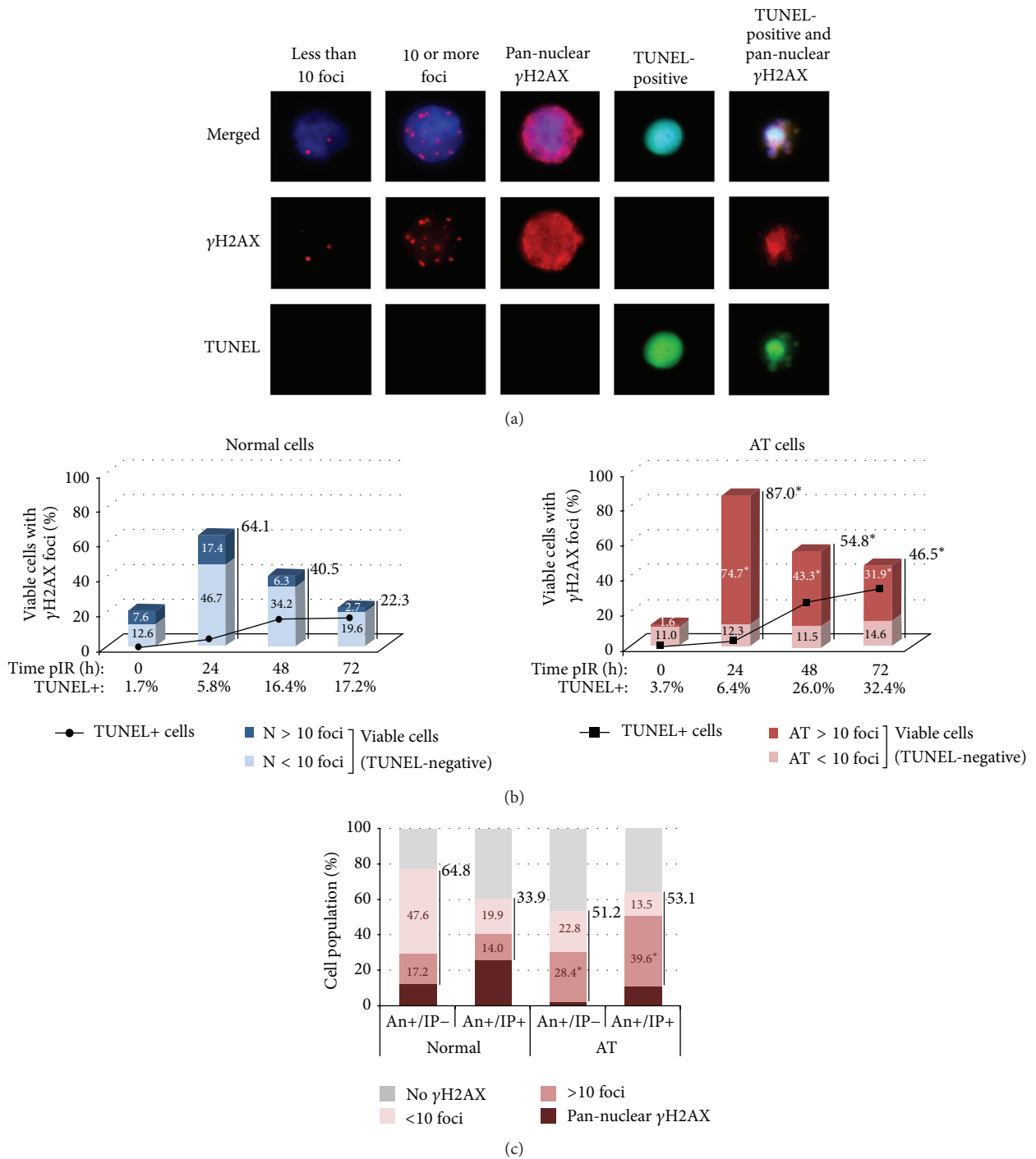


FIGURE 3: (a) Immunodetection of γ H2AX in lymphoblasts. DSBs were scored by γ H2AX foci detection in TUNEL-negative, An+/PI-, and An+/PI+ cells. Pan-nuclear γ H2AX staining was scored in TUNEL-negative, An+/PI-, and An+/PI+ and in TUNEL-positive cells. (b) γ H2AX-labeling in viable (TUNEL-negative) cells. The number and frequency of viable cells with γ H2AX foci are reflected in the bars. Within this fraction, the frequency of cells with <10 foci or with ≥ 10 foci is shown inside the bars. The asterisks indicate statistical differences between normal and AT lymphoblasts in the fraction of cells with γ H2AX foci or in the fraction of cells with ≥ 10 γ H2AX foci (χ^2 test; p values from $p = 0.0270$ to $p < 0.0001$). The frequencies for each category are calculated over the total number of TUNEL-negative scored cells. A minimal number of 350 TUNEL-negative cells were analyzed for each cell type and each time point. The apoptotic rate measured with TUNEL is depicted in the graph as a continuous line. Values for TUNEL-positive cells are given under the x-axis and are those corresponding to Figure 1(a). (c) γ H2AX-labeling in Annexin-positive cells. AT and normal cells were irradiated and fractions corresponding to EA and LA were isolated by cell sorting. An+/PI- and An+/PI+ cells were classified into those with or without γ H2AX foci and those with pan-nuclear γ H2AX staining. The frequency of cells with γ H2AX foci is depicted next to the bar. Within this fraction, the frequency of cells with less than 10 foci (light pink) or with 10 or more foci (pink) is shown inside the bars. The asterisks indicate statistical differences between normal and AT lymphoblasts in the frequency of cells with ≥ 10 γ H2AX foci (χ^2 test; p values from $p = 0.0020$ to $p < 0.0001$). The frequencies are calculated over the total number of An+/PI- and An+/PI+ sorted cells. A minimal number of 400 cells were analyzed for each cell type and each time point.

more γ H2AX foci, reaching a maximum of around 75% at 24 hours pIR (χ^2 test, $p < 0.0001$). From 24 to 72 hours after irradiation, 85 to 70% of the γ H2AX-positive AT cells carry 10 or more DSBs while this frequency is much lower in normal cells (27 to 12%). Thus, after irradiation, AT cells accumulate more cells with DSBs and more DSBs/cell than their normal counterparts.

The results presented here suggest that DSB repair might be inversely correlated with apoptosis induction. Indeed, at 48 hours pIR, the percentage of normal cells with ≥ 10 γ H2AX foci is low (6.3%) and it coincides with the stabilization of the TUNEL-positive rate (around 17%). On the other hand, at 48 hours pIR, still most of AT cells have ≥ 10 γ H2AX foci (43.3%) and TUNEL rates continue to increase at 72 hours pIR (from 26 to 32%; Figure 3(b)). In agreement with that, recent studies have revealed that some residual 53BP1, Rad51, and γ H2AX foci remain in cells for a relatively long time after irradiation and have indicated an inverse correlation between the number of residual foci and the surviving fraction of cells [45–49]. Similarly, a correlation between a higher rate of foci loss and a higher clonogenic surviving fraction in ten different cancer cell lines has been described [50]. Finally, it is worth noting that the fraction of AT cells with less than 10 γ H2AX foci remains stable before and after irradiation and is hardly changed along with the apoptotic rate (Figure 3(b)), thus discarding this subpopulation of cells as that with more probabilities of undergoing IR-induced apoptosis. This result is in agreement with other studies describing that low background levels of foci (< 3 foci per cell) scored at 24 hours after irradiation were correlated with cell survival [14, 51].

2.4. Apoptotic AT Cells Accumulate More Residual DSBs Than Normal Lymphoblasts. To further analyze this possibility, we proceeded to analyze radiation-induced DSBs in normal and AT lymphoblasts undergoing apoptosis. The characteristic DSB-signaling processes of the DDR, such as phosphorylation of histone H2AX forming visible foci, are eventually abolished in cells undergoing last stages of apoptosis, probably due to DNA condensation [52]. Consequently, no γ H2AX foci were scored in TUNEL-positive cells (Figure 3(a)). We reasoned that earlier apoptotic stages, such as those detected with Annexin-V/PI methodology, would better allow the detection of radiation-induced DSBs. To this end, AT and normal lymphoblasts were irradiated and enriched populations of early apoptotic (An+/PI-) and late apoptotic/necrotic (An+/PI+) cells were obtained by flow sorting at 48 hours after irradiation. Immediately after sorting, cells were fixed on slides and γ H2AX immunofluorescence was performed. This procedure resulted in the loss of Annexin-V and PI staining, allowing for reliable identification of γ H2AX signaling. In all the populations analyzed we found a fraction of cells displaying a pan-nuclear γ H2AX staining (Figure 3(a)). This kind of staining has been related to apoptosis induced by several DNA damaging agents and is concurrent with the initiation of DNA fragmentation resulting from the apoptotic process [53, 54]. This fraction of cells was taken into account when calculating the percentages shown in the figures. At the time point selected after

irradiation (48 hours), the fraction of cells undergoing early and late apoptosis was at its maximum in both cell lines. Cells undergoing early apoptosis (An+/PI-) were 4.8% in normal and 12.5% in AT cells, while those undergoing late apoptosis (An+/PI+) were 7.5% and 19.3% in normal and AT LCL, respectively (Figure 1(a)).

Within the above mentioned fraction of cells undergoing early apoptosis (An+/PI-), most of them had γ H2AX foci—64.8% of the normal lymphoblasts and 51.2% of the AT cells (Figure 3(c)). Nonetheless, most of the cells undergoing early apoptosis had less than 10 γ H2AX foci/cell in normal cells (47.6%) but ≥ 10 γ H2AX foci/cell in AT cells (28.4%), demonstrating that also the AT cells that initiate apoptosis (An+/PI-) accumulate a significantly higher number of DSBs than normal cells (χ^2 test; $p < 0.0001$). As normal lymphoblasts enter in later apoptotic/necrotic stages (An+/PI+), the frequency of cells with less than 10 γ H2AX foci is sharply reduced (from 47.6% to 19.9%; 2.4-fold reduction), while the fraction of cells with ≥ 10 γ H2AX foci is more or less maintained (14%). Similarly, the frequency of AT lymphoblasts undergoing later apoptotic stages (An+/PI+) that present less than 10 γ H2AX foci is reduced, while the population of cells with ≥ 10 γ H2AX foci is increased with respect to early apoptosis and to normal cells (75% of the γ H2AX-positive AT lymphoblasts). Thus, AT lymphoblasts accumulate more DSBs/cell than their normal counterparts, also while undergoing apoptosis (χ^2 test; $p = 0.0020$).

It is important to note that An+/PI- cells might be considered viable, as early apoptosis is believed to be reversible if the conditions inducing apoptosis are removed [55–57]. Moreover, it has been suggested that DNA repair is involved in this reversibility [58]. Thus, while undergoing early apoptosis, cells might be able to perform some degree of DSB repair that leads to reduction of γ H2AX foci-positive cells in later apoptotic stages. Most probably, cells that carry a larger amount of DSBs have a lower probability of eventually performing successful repair; thus cells with ≥ 10 γ H2AX foci accumulate at later stages of apoptosis. In this work, cells undergoing late apoptosis are those accumulating more DSBs, and the cell line with impaired repair activity is the one carrying more residual DSBs and displaying higher rates of cell death. Similar results have been very recently described in which cells carrying Rad51 foci at 24 hours pIR are the ones more likely to die [44]. It cannot be concluded that accumulation of ≥ 10 γ H2AX foci signals cells to undergo apoptosis, as γ H2AX foci dose-response may depend on cell type, time allowed after irradiation, and the cell cycle phase in the moment of irradiation among other factors. Nonetheless, these results support the notion that persistence of residual DSBs signals those cells that are more likely to undergo cell death.

3. Conclusions

Annexin-V/PI and TUNEL methodologies have been used to analyze IR-induced apoptosis. These methodologies seem to detect subtle differences in apoptotic frequencies that might correspond to progressive apoptotic stages, as maximum

levels of Annexin-V-positive cells are reached earlier than maximum levels of TUNEL-positive cells. Annexin-V/PI allows discrimination between cells undergoing early and late apoptosis as well as fast scoring of more cells. TUNEL detection on slides and subsequent microscope analysis allows the combination of TUNEL and protein immunodetection—like γ H2AX—and the analysis of these events in the apoptotic and the healthy fraction at the same time.

The results in this work show that AT LCL efficiently undergoes IR-induced apoptosis to a higher level than its normal counterpart at all times analyzed. Along with accumulation of residual DSBs, indicators of mitotic catastrophe such as prolonged G2/M arrest and DNA and centrosomes reduplication are found in irradiated AT cells, which also contribute to the apoptotic levels scored. In these cells, apoptosis is accompanied with p53 induction and cleavage of caspase 3, while they show low levels of p21 induction that correlate with impairment of G1 and intra-S checkpoint activation after irradiation. These results agree with a role for ATM selectively activating p53 to regulate apoptosis and not cell cycle checkpoint. Accumulation of radiation-induced unrepaired DSBs contributes to cell death. For this reason, viable cells that are undergoing apoptosis (Annexin-positive) have been isolated in both cell lines and γ H2AX foci have been scored. The results show that these are the cells accumulating more DSBs per cell. As cells progress from EA to LA, the fraction of cells with fewer γ H2AX foci decreases in both AT and normal cells, while cells with more than 10 γ H2AX foci accumulate in LA, especially in AT cells—consistent with their DNA repair defect. These results support the notion that persistence of residual DSBs signals those cells that are more likely to undergo cell death and that scoring of γ H2AX foci might function as a predictive tool to assess radiation-induced apoptosis.

4. Material and Methods

4.1. Cell Culture and γ -Irradiation. EBV-transformed human lymphoblastoid cell lines (LCLs) GM08436A (derived from a child suffering from Ataxia-Telangiectasia) and GM09622 (derived from a sex and age matched control) were obtained from the Coriell Cell Culture Repositories. Cells were grown in suspension in RPMI 1640 medium with GlutaMAX-I (Life Technologies, CA, USA) supplemented with 15% fetal bovine serum and kept in the incubator at 37°C and 5% CO₂ atmosphere. When indicated, cells were irradiated with 5 Gy γ -rays using an IBL-437C R-137 Cs irradiator, with a dose rate of 5.10 Gy/min.

4.2. Apoptosis Detection

4.2.1. Annexin-V-Fluorescein Assay. The Annexin-V/propidium iodide (PI) assay was performed following the manufacturer's instructions (Annexin-V-FLUOS Staining Kit, Roche, Switzerland). Briefly, lymphoblast cells were collected, centrifuged, and washed in 1xPBS. The cell pellet was resuspended in freshly prepared Annexin-V-FLUOS labeling solution with PI and incubated for 15 minutes (min) at

room temperature, in the dark. Cells were analyzed on a FACSCalibur flow cytometer (Becton-Dickinson, CA, USA) using 488 nm excitation and 530/30 nm band pass filter for fluorescein detection and a FL2 photomultiplier and band pass filter 585/42 nm for PI detection after electronic compensation. Flow cytometry analysis was done with the CellQuest software (Becton-Dickinson, CA, USA). Cells were classified into the following fractions: (a) viable cells (An-/PI-) were impermeable for PI and also did not bind Annexin-V (An); (b) early apoptotic cells (An+/PI-) bound An and were PI impermeable; (c) late apoptotic or, also called, secondary necrotic cells (An+/PI+) bound An and were PI permeable; (d) primary necrotic cells (An-/PI+) only displayed PI staining. When indicated, cell sorting of enriched populations of An+/PI- and An+/PI+ cells was performed with a FACS Aria SORP sorting cytometer (Becton-Dickinson Biosciences, CA, USA) using a 488 nm excitation laser and 525 nm band pass filter for fluorescein detection and a 350 nm excitation UV laser and 660/400 nm band pass filter for PI detection. Cells obtained after sorting were dropped on poly-L-lysine coated slides and allowed to attach for 3 min before proceeding with immunofluorescence.

4.2.2. TUNEL Assay. The TUNEL assay was performed following the manufacturer's instructions (In Situ Cell Death Detection Kit, Fluorescein, Roche, Switzerland). Briefly, lymphoblasts were centrifuged, washed with 1xPBS, and dropped on poly-L-lysine coated slides. Cells were then fixed with 2% paraformaldehyde for 20 min at room temperature and permeabilized with 0.1% Triton-X100 and 0.1% sodium citrate in 1xPBS for 5 min in ice. The TUNEL mix was applied to the cells following the manufacturer's instructions and allowed to be incubated at 37°C for 40 minutes. Before analysis, Vectashield Mounting Medium for fluorescence (Vector Laboratories Inc., CA, USA) supplemented with 4',6-diamino-2-phenylindole (DAPI) was applied. TUNEL analysis was performed with an Olympus BX41TF epifluorescence microscope equipped with an Olympus U-TVIX digital camera using the Isis v5.4.9 software (MetaSystems, Germany).

4.3. Cell Cycle Analysis. Lymphoblasts were washed in 1xPBS, centrifuged, and kept in 70% ethanol at -20°C until analysis. Cells were then centrifuged, washed with 1xPBS, and resuspended in 1 mL of freshly prepared PI/Triton/RNase solution: 0.1% Triton-X100, 2 mg RNase A (DNase free), and 200 μ L of 1 mg/mL PI. After 15 min incubation at 37°C, DNA content was measured on a FACSCalibur flow cytometer (Becton-Dickinson, CA, USA). Red fluorescence of PI-stained nuclei was excited at 488 nm with an argon laser and was collected through a 670 nm long pass filter detection into the FL3 photomultiplier tube on a linear scale, at a flow rate of 12 mL/min (low). Cell cycle analysis of the DNA histograms of integrated red fluorescence was performed with CellQuest software (Becton-Dickinson, CA, USA).

4.4. Immunofluorescence. Immunodetection of γ H2AX was performed on the same samples previously analyzed for

TUNEL or sorted after Annexin-V/PI staining. Pericentrin detection was performed on newly obtained samples of irradiated lymphoblasts allowed to attach onto poly-L-lysine slides. Cells were fixed for 15 min in 4% paraformaldehyde and permeabilized in 1xPBS-0.5% Triton-X100 solution for 15 min. After 30 minutes of blocking with 0.1% Tween20 and 5% FBS, mouse anti- γ H2AX (Ser139) (Upstate/Millipore, MA, USA) or rabbit anti-pericentrin (Abcam, UK) was applied at a 1:1000 concentration and allowed to incubate for 1 hour at room temperature. Anti-mouse Cy3 (Amersham Biosciences/GE Healthcare, NJ, USA) and anti-rabbit A488 (Invitrogen/Molecular Probes, OR, USA) secondary antibodies were applied at 1:1000 final concentration for 45 minutes at room temperature, followed by extensive washing. Before analysis, Vectashield Mounting Medium for fluorescence (Vector Laboratories Inc., CA, USA) supplemented with DAPI was applied. Slides were analyzed using an Olympus BX41TF epifluorescence microscope equipped with an Olympus U-TVIX digital camera using the Isis v5.4.9 software (MetaSystems, Germany).

4.5. Western Blotting. Cells were collected by centrifugation, washed with PBS, treated with RIPA lysis buffer, and sonicated. Whole-cell extracts were loaded onto a 10% SDS-polyacrylamide gel that was run at 150 V for 50 minutes in a Bio-Rad mini-gel system. Proteins were transferred to a nitrocellulose membrane (30 V, 90 minutes) and blocked for 1 h at room temperature in 5% BSA brought to 37°C or with nonfat milk at 4°C. Primary antibodies used were mouse monoclonal anti-p53 (Santa Cruz Biotechnology, Inc., TX, USA), rabbit monoclonal anti-phospho-p53 (Ser15) (Thermo Fisher Scientific, MA, USA), rabbit monoclonal anti-p21 (Abcam, UK), rabbit monoclonal anti-Bax (Abcam, UK), rabbit polyclonal anti-active caspase 3 (Abcam, UK), and mouse anti-GAPDH (Abcam, UK). Membranes were washed with TTBS (Tris 10 mM, NaCl 150 mM, and 0.005% Tween20) and incubated for 1 hour at room temperature with secondary antibody, goat anti-rabbit or goat anti-mouse, conjugated to horseradish peroxidase (Upstate/Millipore, MA, USA). Proteins were visualized using Immobilion Western kit (Upstate/Millipore, MA, USA) and the signal was captured with ChemiDoc XRS (Bio-Rad, CA, USA).

4.6. Statistical Analysis. The statistical analysis was performed using GraphPad InStat version 3.05 (GraphPad Software Inc., CA, USA).

Disclosure

The funders had no role in study design, data collection and analysis, decision to publish, or preparation of the paper.

Conflict of Interests

The authors declare that they have no competing financial interests.

Authors' Contribution

Marta Martín and Anna Genescà developed the study concept and design. Testing and data collection and analysis were performed by Teresa Anglada, Marta Martín, Mariona Terradas, and Laia Hernández. Marta Martín and Anna Genescà wrote the paper and approved its final version for submission.

Acknowledgments

This work was funded by grants from Consejo de Seguridad Nuclear (CSN 2012-0001) and EURATOM (Dark.Risk GA 323216). Anna Genescà Laboratory is supported by Generalitat de Catalunya (2009SGR-282). Laia Hernández is supported by the Universitat Autònoma de Barcelona Ph.D. programme fellowship. The authors would like to thank Dr. Dik van Gent and Dr. Humberto Sánchez for their valuable comments. They also thank the Radiological Protection Unit at Universitat Autònoma de Barcelona for sample irradiation and the Cytometry Service from the Centres Científics i Tecnològics (CCiT), Universitat de Barcelona (UB), for cell sorting.

References

- [1] C. J. Bakkenist and M. B. Kastan, "Initiating cellular stress responses," *Cell*, vol. 118, no. 1, pp. 9–17, 2004.
- [2] E. U. Kurz and S. P. Lees-Miller, "DNA damage-induced activation of ATM and ATM-dependent signaling pathways," *DNA Repair*, vol. 3, no. 8-9, pp. 889–900, 2004.
- [3] Y. Shiloh, "ATM and related protein kinases: safeguarding genome integrity," *Nature Reviews Cancer*, vol. 3, no. 3, pp. 155–168, 2003.
- [4] A. Di Leonardo, S. P. Linke, K. Clarkin, and G. M. Wahl, "DNA damage triggers a prolonged p53-dependent G1 arrest and long-term induction of Cip1 in normal human fibroblasts," *Genes & Development*, vol. 8, no. 21, pp. 2540–2551, 1994.
- [5] M. B. Kastan, O. Onyekwere, D. Sidransky, B. Vogelstein, and R. W. Craig, "Participation of p53 protein in the cellular response to DNA damage," *Cancer Research*, vol. 51, no. 23, pp. 6304–6311, 1991.
- [6] E. P. Rogakou, D. R. Pilch, A. H. Orr, V. S. Ivanova, and W. M. Bonner, "DNA double-stranded breaks induce histone H2AX phosphorylation on serine 139," *The Journal of Biological Chemistry*, vol. 273, no. 10, pp. 5858–5868, 1998.
- [7] E. P. Rogakou, C. Boon, C. Redon, and W. M. Bonner, "Megabase chromatin domains involved in DNA double-strand breaks in vivo," *The Journal of Cell Biology*, vol. 146, no. 5, pp. 905–916, 1999.
- [8] M. Löbrich, A. Shibata, A. Beucher et al., " γ H2AX foci analysis for monitoring DNA double-strand break repair: strengths, limitations and optimization," *Cell Cycle*, vol. 9, no. 4, pp. 662–669, 2010.
- [9] O. A. Sedelnikova, E. P. Rogakou, I. G. Panyutin, and W. M. Bonner, "Quantitative detection of 125IdU-induced DNA double-strand breaks with gamma-H2AX antibody," *Radiation Research*, vol. 158, no. 4, pp. 486–492, 2002.
- [10] M. Kühne, E. Riballo, N. Rief, K. Rothkamm, P. A. Jeggo, and M. Löbrich, "A double-strand break repair defect in ATM-deficient

- cells contributes to radiosensitivity," *Cancer Research*, vol. 64, no. 2, pp. 500–508, 2004.
- [11] M. Martín, M. Terradas, G. Iliakis, L. Tusell, and A. Genescà, "Breaks invisible to the DNA damage response machinery accumulate in ATM-deficient cells," *Genes Chromosomes and Cancer*, vol. 48, no. 9, pp. 745–759, 2009.
- [12] E. Riballo, M. Kühne, N. Rief et al., "A pathway of double-strand break rejoining dependent upon ATM, Artemis, and proteins locating to γ -H2AX foci," *Molecular Cell*, vol. 16, no. 5, pp. 715–724, 2004.
- [13] J. P. Banáth, S. H. MacPhail, and P. L. Olive, "Radiation sensitivity, H2AX phosphorylation, and kinetics of repair of DNA strand breaks in irradiated cervical cancer cell lines," *Cancer Research*, vol. 64, no. 19, pp. 7144–7149, 2004.
- [14] D. Klovov, S. M. MacPhail, J. P. Banáth, J. P. Byrne, and P. L. Olive, "Phosphorylated histone H2AX in relation to cell survival in tumor cells and xenografts exposed to single and fractionated doses of X-rays," *Radiotherapy and Oncology*, vol. 80, no. 2, pp. 223–229, 2006.
- [15] H. Mahrhofer, S. Bürger, U. Oppitz, M. Flentje, and C. S. Djuzenova, "Radiation induced DNA damage and damage repair in human tumor and fibroblast cell lines assessed by histone H2AX phosphorylation," *International Journal of Radiation Oncology, Biology, Physics*, vol. 64, no. 2, pp. 573–580, 2006.
- [16] T. Yoshikawa, G. Kashino, K. Ono, and M. Watanabe, "Phosphorylated H2AX foci in tumor cells have no correlation with their radiation sensitivities," *Journal of Radiation Research*, vol. 50, no. 2, pp. 151–160, 2009.
- [17] M. Castedo, J.-L. Perfettini, T. Roumier, K. Andreau, R. Medema, and G. Kroemer, "Cell death by mitotic catastrophe: a molecular definition," *Oncogene*, vol. 23, no. 16, pp. 2825–2837, 2004.
- [18] H. Vakifahmetoglu, M. Olsson, and B. Zhivotovsky, "Death through a tragedy: mitotic catastrophe," *Cell Death and Differentiation*, vol. 15, no. 7, pp. 1153–1162, 2008.
- [19] L. Galluzzi, I. Vitale, J. M. Abrams et al., "Molecular definitions of cell death subroutines: recommendations of the Nomenclature Committee on Cell Death 2012," *Cell Death and Differentiation*, vol. 19, no. 1, pp. 107–120, 2012.
- [20] I. Vitale, L. Galluzzi, M. Castedo, and G. Kroemer, "Mitotic catastrophe: a mechanism for avoiding genomic instability," *Nature Reviews. Molecular cell biology*, vol. 12, no. 6, pp. 385–392, 2011.
- [21] R. W. Bailey, T. Nguyen, L. Robertson et al., "Sequence of physical changes to the cell membrane during glucocorticoid-induced apoptosis in S49 lymphoma cells," *Biophysical Journal*, vol. 96, no. 7, pp. 2709–2718, 2009.
- [22] A. Hochreiter-Hufford and K. S. Ravichandran, "Clearing the dead: apoptotic cell sensing, recognition, engulfment, and digestion," *Cold Spring Harbor Perspectives in Biology*, vol. 5, no. 1, Article ID a008748, 2013.
- [23] I. Vermes, C. Haanen, H. Steffens-Nakken, and C. Reutelingsperger, "A novel assay for apoptosis Flow cytometric detection of phosphatidylserine expression on early apoptotic cells using fluorescein labelled Annexin V," *Journal of Immunological Methods*, vol. 184, no. 1, pp. 39–51, 1995.
- [24] Z. Bacso and J. F. Eliason, "Measurement of DNA damage associated with apoptosis by laser scanning cytometry," *Cytometry*, vol. 45, no. 3, pp. 180–186, 2001.
- [25] J. B. P. Barber, C. M. L. West, A. E. Kiltie, S. A. Roberts, and D. Scott, "Detection of individual differences in radiation-induced apoptosis of peripheral blood lymphocytes in normal individuals, ataxia telangiectasia homozygotes and heterozygotes, and breast cancer patients after radiotherapy," *Radiation Research*, vol. 153, no. 5, pp. 570–578, 2000.
- [26] C. Barlow, K. D. Brown, C.-X. Deng, D. A. Tagle, and A. Wynshaw-Boris, "Atm selectively regulates distinct p53-dependent cell-cycle checkpoint and apoptotic pathways," *Nature Genetics*, vol. 17, no. 4, pp. 453–456, 1997.
- [27] D. G. Bebb, P. J. Warrington, G. De Jong et al., "Radiation induced apoptosis in ataxia telangiectasia homozygote, heterozygote and normal cells," *Mutation Research/Fundamental and Molecular Mechanisms of Mutagenesis*, vol. 476, no. 1-2, pp. 13–20, 2001.
- [28] M. Fernet, S. Angele, T. Dörk, and J. Hall, "Variation in radiation-induced apoptosis in ataxia telangiectasia lymphoblastoid cell lines," *International Journal of Radiation Biology*, vol. 79, no. 3, pp. 193–202, 2003.
- [29] B. Humar, H. Müller, and R. J. Scott, "Elevated frequency of p53-independent apoptosis after irradiation increases levels of DNA breaks in ataxia telangiectasia lymphoblasts," *International Journal of Radiation Biology*, vol. 72, no. 3, pp. 257–269, 1997.
- [30] A. E. Meijer, B. Zhivotovsky, and R. Lewensohn, "Epstein-Barr virus-transformed lymphoblastoid cell lines of ataxia telangiectasia patients are defective in X-ray-induced apoptosis," *International Journal of Radiation Biology*, vol. 75, no. 6, pp. 709–716, 1999.
- [31] Y.-Q. Shi, L. Li, O. Sanal et al., "High levels of delayed radiation-induced apoptosis observed in lymphoblastoid cell lines from ataxia-telangiectasia patients," *International Journal of Radiation Oncology Biology Physics*, vol. 49, no. 2, pp. 555–559, 2001.
- [32] G. R. Bicknell, R. T. Snowden, and G. M. Cohen, "Formation of high molecular mass DNA fragments is a marker of apoptosis in the human leukaemic cell line, U937," *Journal of Cell Science*, vol. 107, no. 9, pp. 2483–2489, 1994.
- [33] E. Duchaud, A. Ridet, D. Stoppa-Lyonnet, N. Janin, E. Moustacchi, and F. Rosselli, "Deregulated apoptosis in ataxia telangiectasia: association with clinical stigmata and radiosensitivity," *Cancer Research*, vol. 56, no. 6, pp. 1400–1404, 1996.
- [34] C. G. Proud, "Regulation of mammalian translation factors by nutrients," *European Journal of Biochemistry*, vol. 269, no. 22, pp. 5338–5349, 2002.
- [35] A. Strasser, "Life and death during lymphocyte development and function: evidence for two distinct killing mechanisms," *Current Opinion in Immunology*, vol. 7, no. 2, pp. 228–234, 1995.
- [36] A. E. Meijer, J. Ekedahl, B. Joseph et al., "High-LET radiation induces apoptosis in lymphoblastoid cell lines derived from ataxia-telangiectasia patients," *International Journal of Radiation Biology*, vol. 77, no. 3, pp. 309–317, 2001.
- [37] A. L. Gartel and S. K. Radhakrishnan, "Lost in transcription: p21 repression, mechanisms, and consequences," *Cancer Research*, vol. 65, no. 10, pp. 3980–3985, 2005.
- [38] A. Hirao, A. Cheung, G. Duncan et al., "Chk2 is a tumor suppressor that regulates apoptosis in both an ataxia telangiectasia mutated (ATM)-dependent and an ATM-independent manner," *Molecular and Cellular Biology*, vol. 22, no. 18, pp. 6521–6532, 2002.
- [39] S. Wang, M. Guo, H. Ouyang et al., "The catalytic subunit of DNA-dependent protein kinase selectively regulates p53-dependent apoptosis but not cell-cycle arrest," *Proceedings of the National Academy of Sciences of the United States of America*, vol. 97, no. 4, pp. 1584–1588, 2000.

- [40] B. Vogelstein and K. W. Kinzler, "Cancer genes and the pathways they control," *Nature Medicine*, vol. 10, no. 8, pp. 789–799, 2004.
- [41] K. K. Khanna, M. F. Lavin, S. P. Jackson, and T. D. Mulhern, "ATM, a central controller of cellular responses to DNA damage," *Cell Death and Differentiation*, vol. 8, no. 11, pp. 1052–1065, 2001.
- [42] D. Scott, A. R. Spreadborough, and S. A. Roberts, "Radiation-induced G2 delay and spontaneous chromosome aberrations in ataxia-telangiectasia homozygotes and heterozygotes," *International Journal of Radiation Biology*, vol. 66, no. 6, pp. S157–S163, 1994.
- [43] H. Beamish and M. F. Lavin, "Radiosensitivity in ataxia-telangiectasia: anomalies in radiation-induced cell cycle delay," *International Journal of Radiation Biology*, vol. 65, no. 2, pp. 175–184, 1994.
- [44] M. Gatei, B.-B. Zhou, K. Hobson, S. Scott, D. Young, and K. K. Khanna, "Ataxia telangiectasia mutated (ATM) kinase and ATM and Rad3 related kinase mediate phosphorylation of Brcal at distinct and overlapping sites. In vivo assessment using phospho-specific antibodies," *Journal of Biological Chemistry*, vol. 276, no. 20, pp. 17276–17280, 2001.
- [45] J. P. Banáth, D. Klovov, S. H. MacPhail, C. A. Banuelos, and P. L. Olive, "Residual γ H2AX foci as an indication of lethal DNA lesions," *BMC Cancer*, vol. 10, article 4, 2010.
- [46] E. Dikomey, I. Brammer, J. Johansen, S. M. Bentzen, and J. Overgaard, "Relationship between DNA double-strand breaks, cell killing, and fibrosis studied in confluent skin fibroblasts derived from breast cancer patients," *International Journal of Radiation Oncology Biology Physics*, vol. 46, no. 2, pp. 481–490, 2000.
- [47] H. D. Halicka, X. Huang, F. Traganos, M. A. King, W. Dai, and Z. Darzynkiewicz, "Histone H2AX phosphorylation after cell irradiation with UV-B: relationship to cell cycle phase and induction of apoptosis," *Cell Cycle*, vol. 4, no. 2, pp. 339–345, 2005.
- [48] H. Kunogi, T. Sakanishi, N. Sueyoshi, and K. Sasai, "Prediction of radiosensitivity using phosphorylation of histone H2AX and apoptosis in human tumor cell lines," *International Journal of Radiation Biology*, vol. 90, no. 7, pp. 587–593, 2014.
- [49] A. Menegakis, A. Yaromina, W. Eicheler et al., "Prediction of clonogenic cell survival curves based on the number of residual DNA double strand breaks measured by γ H2AX staining," *International Journal of Radiation Biology*, vol. 85, no. 11, pp. 1032–1041, 2009.
- [50] S. H. Macphail, J. P. Banáth, T. Y. Yu, E. H. M. Chu, H. Lambur, and P. L. Olive, "Expression of phosphorylated histone H2AX in cultured cell lines following exposure to X-rays," *International Journal of Radiation Biology*, vol. 79, no. 5, pp. 351–358, 2003.
- [51] P. L. Olive and J. P. Banáth, "Kinetics of H2AX phosphorylation after exposure to cisplatin," *Cytometry Part B: Clinical Cytometry*, vol. 76, no. 2, pp. 79–90, 2009.
- [52] E. Marková, J. Torudd, and I. Belyaev, "Long time persistence of residual 53BP1/ γ -H2AX foci in human lymphocytes in relationship to apoptosis, chromatin condensation and biological dosimetry," *International Journal of Radiation Biology*, vol. 87, no. 7, pp. 736–745, 2011.
- [53] E. P. Rogakou, W. Nieves-Neira, C. Boon, Y. Pommier, and W. M. Bonner, "Initiation of DNA fragmentation during apoptosis induces phosphorylation of H2AX histone at serine 139," *The Journal of Biological Chemistry*, vol. 275, no. 13, pp. 9390–9395, 2000.
- [54] B. Mukherjee, C. Kessinger, J. Kobayashi et al., "DNA-PK phosphorylates histone H2AX during apoptotic DNA fragmentation in mammalian cells," *DNA Repair*, vol. 5, no. 5, pp. 575–590, 2006.
- [55] F. J. Geske, A. C. Nelson, R. Lieberman, R. Strange, T. Sun, and L. E. Gerschenson, "DNA repair is activated in early stages of p53-induced apoptosis," *Cell Death and Differentiation*, vol. 7, no. 4, pp. 393–401, 2000.
- [56] A. K. Hammill, J. W. Uhr, and R. H. Scheuermann, "Annexin V staining due to loss of membrane asymmetry can be reversible and precede commitment to apoptotic death," *Experimental Cell Research*, vol. 251, no. 1, pp. 16–21, 1999.
- [57] H. L. Tang, K. L. Yuen, H. M. Tang, and M. C. Fung, "Reversibility of apoptosis in cancer cells," *British Journal of Cancer*, vol. 100, no. 1, pp. 118–122, 2009.
- [58] F. J. Geske, R. Lieberman, R. Strange, and L. E. Gerschenson, "Early stages of p53-induced apoptosis are reversible," *Cell Death and Differentiation*, vol. 8, no. 2, pp. 182–191, 2001.

Research Article

Improvement in the Detection of Cystic Metastatic Papillary Thyroid Carcinoma by Measurement of Thyroglobulin in Aspirated Fluid

Yong Wang,¹ Huan Zhao,² Yi-Xiang J. Wang,³ Min-Jie Wang,⁴ Zhi-Hui Zhang,² Li Zhang,⁵ Bin Zhang,⁶ Anil T. Ahuja,³ Chun-Wu Zhou,⁷ Yu-Xin Jiang,⁸ and Hui-Qin Guo²

¹Department of Diagnostic Ultrasound, Cancer Hospital & Institute, Peking Union Medical College and Chinese Academy of Medical Sciences, Beijing 100021, China

²Department of Pathology, Cancer Hospital & Institute, Peking Union Medical College and Chinese Academy of Medical Sciences, Beijing 100021, China

³Department of Imaging and Interventional Radiology, Prince of Wales Hospital, The Chinese University of Hong Kong, Shatin, New Territories, Hong Kong

⁴Department of Clinical Library, Cancer Hospital & Institute, Peking Union Medical College and Chinese Academy of Medical Sciences, Beijing 100021, China

⁵Department of Cancer Epidemiology, Cancer Hospital & Institute, Peking Union Medical College and Chinese Academy of Medical Sciences, Beijing 100021, China

⁶Department of Head & Neck Surgery, Cancer Hospital & Institute, Peking Union Medical College and Chinese Academy of Medical Sciences, Beijing 100021, China

⁷Department of Diagnostic Imaging, Cancer Hospital & Institute, Peking Union Medical College Hospital, Peking Union Medical College and Chinese Academy of Medical Sciences, Beijing 100021, China

⁸Department of Diagnostic Ultrasound, Peking Union Medical College Hospital, Peking Union Medical College and Chinese Academy of Medical Sciences, Beijing 100730, China

Correspondence should be addressed to Hui-Qin Guo; ghqin2006@163.com

Received 1 October 2015; Accepted 16 December 2015

Academic Editor: Kathleen Montone

Copyright © 2016 Yong Wang et al. This is an open access article distributed under the Creative Commons Attribution License, which permits unrestricted use, distribution, and reproduction in any medium, provided the original work is properly cited.

Cystic change in metastatic lymph nodes of papillary thyroid carcinoma (PTC) is a diagnostic challenge for fine needle aspiration (FNA) because of the scant cellularity. The aim of this study was to evaluate the measurement of thyroglobulin in fine needle aspirate (Tg-FNA) for detecting metastatic PTC in patients with cystic neck lesions and to validate the optimal cutoff value of Tg-FNA. A total of 75 FNA specimens of cystic lesions were identified, including 40 of metastatic PTC. Predetermined threshold levels of 0.04 (minimum detection level), 0.9, 10.0, and 77.0 ng/mL (maximum normal serum-Tg level) were used to evaluate the diagnostic accuracy of Tg-FNA for metastatic PTC detection. The areas under the receiver operating characteristic curve for diagnosing metastatic PTC of Tg-FNA values of 0.04, 0.9, 10.0, and 77.0 ng/mL were 0.5 (95% confidence interval [CI], 0.382–0.618), 0.645 (95% CI, 0.526–0.752), 0.945 (95% CI, 0.866–0.984), and 0.973 (95% CI, 0.907–0.996), respectively. With a cutoff value of 77.0 ng/mL, the combination of Tg-FNA and FNA cytology showed superior diagnostic power (97.5% sensitivity and 100% specificity) compared to FNA cytology alone (80% sensitivity and 100% specificity). We recommend a Tg-FNA cutoff of 77.0 ng/mL, the maximum normal serum-Tg level, for cystic neck lesions.

1. Introduction

Fine needle aspiration cytology (FNAC) is the most important modality for the evaluation of lymphadenopathy. It is

highly specific and sensitive in patients with solid lesions [1]. However, for cystic lesions, the lack of epithelium in cyst aspiration may lead to a false negative interpretation of FNAC results [2, 3]. Cystic lymph node metastasis has been detected

in 5.2% of malignant aspirates, and the tumor type that most frequently causes cystic change is papillary thyroid carcinoma (PTC) [4]. An ultrasonographic cystic appearance of cervical lymph nodes has been observed in 70% of metastatic PTC cases [5].

The measurement of thyroglobulin in fine needle aspirate (Tg-FNA) was initially proposed by Pacini et al. in 1992 for the detection of neck lymph node metastases in patients with PTC [6]. Several studies have reported that Tg-FNA is more sensitive than FNAC for detecting metastatic PTC and that the sensitivity of FNAC is increased when combined with Tg-FNA [3, 7–15]. However, only a few studies with a limited number of cases have focused on the utility of Tg-FNA for cystic lesions [3, 12]. The diagnostic threshold has not been well established. The wide range of suggested cutoff values for Tg-FNA in previous studies might be due to the differences in study populations. Some studies included only patients with PTC who had undergone surgery and radioiodine ablation [9–12], while others included those awaiting thyroid surgeries [13]. In addition, most studies examined Tg-FNA in selected lymph nodes, histologically proved to be either metastatic PTC or reactive hyperplasia [7–15]. The diagnostic threshold was determined based on strictly selected study populations, which may limit the general use of Tg-FNA in clinical practice.

In this study, we evaluated the value of Tg-FNA in 75 cystic lesions, the largest reported series of cystic lesions to date, and primarily examined this technique in a wider clinical context, including metastatic PTC in patients who had undergone or were yet to undergo surgery, lymph node metastases from extrathyroidal malignancies, and lesions of cervical origin. The aim of this study was to evaluate the use of Tg-FNA for detecting metastatic PTC in patients with cystic neck lesions and to validate the optimal cutoff value of Tg-FNA.

2. Materials and Methods

2.1. Case Selection. The specimens were consecutively collected from the Cancer Institute/Hospital, Chinese Academy of Medical Sciences (CAMS), between September 2012 and December 2014. Patients were selected on the basis of the following criteria: (1) having cystic neck lesions and being referred to FNA examination by their physicians and (2) the fluid aspirated from the cervical lesion being nonpurulent. FNAC and Tg-FNA measurement were performed on the enrolled patients. All patients provided informed consent before FNA. This study protocol was reviewed and approved by the ethics committee of the Cancer Institute/Hospital, CAMS.

2.2. FNAC. Palpable lesions were aspirated by cytopathologists, and nonpalpable lesions were aspirated by experienced radiologists under the real-time ultrasound guidance. FNA was performed using a 22-gauge needle attached to 10 mL syringe without the aid of a syringe holder. Several drops of aspirated fluid were first added to 0.5 mL of normal saline solution for Tg-FNA. The residual fluid in the needle was

then rinsed in CytoLyt (Hologic, Marlborough, MA, USA) to prepare a ThinPrep (Hologic) slide. Slides were fixed in alcohol and stained with Papanicolaou staining. They were then interpreted by cytologists with experience ranging from 5 to 18 years. All cases, except those diagnosed cytologically as benign, were reviewed in the daily conference among these cytopathologists.

2.3. Tg-FNA. Specimens were stored at -20°C and transferred to the clinical laboratory for thyroglobulin analysis in one month. Tg concentrations were measured using an automated electrochemiluminescence immunoassay (Cobas e 601, Roche Diagnostics, Mannheim, Germany). The minimum detectable Tg concentration was 0.04 ng/mL.

2.4. Data Analysis and Statistical Analysis. Positive final diagnoses were based on histological confirmation of metastatic PTC or cytological diagnosis of PTC. Negative final diagnoses were made for lymph nodes free of metastatic disease based on cytology and negative follow-up imaging findings for at least 12 months, histologically or cytologically confirmed lymph node metastases from extrathyroidal malignancies, and histologically or cytologically confirmed benign lesions of cervical origin.

Cytology results were grouped into two categories according to the cytology report. Cases with reports documenting metastases from PTC and those documenting suspicious metastases from PTC were considered positive. Negative diagnoses were assigned to (1) cases with reports where “atypical” was mentioned but “metastasis” was not, (2) cases of lymph node metastases from extrathyroidal malignancies, (3) cases of lymph nodes with reactive hyperplasia, and (4) cases with specific benign findings.

To interpret Tg-FNA, four threshold levels were decided according to previous reports [7–16]: 0.04 ng/mL (the Tg detection limit according to the manufacturer’s instructions in our study), 0.9 ng/mL (the Tg detection limit according to previous studies), 10.0 ng/mL, and 77.0 ng/mL (the maximum level of normal serum-Tg according to the manufacturer’s instructions and proved by evaluation of 100 healthy controls). Tg-FNA was considered positive or negative for values higher or lower than the threshold values, respectively.

Receiver operating characteristic (ROC) curve analysis was conducted to determine the most appropriate threshold value for Tg-FNA, with the areas under the ROC curve (AUC) and confidence intervals (CI) being assessed with MedCalc Version 14.10.2. Tg-FNA median values were compared using the Kruskal-Wallis test. The two-sided alpha error level of 0.05 was adjusted to 0.05/N using the Bonferroni correction for multiple comparisons. Statistical analyses were performed with SPSS 12.0 (SPSS Inc., Chicago, IL, USA).

3. Results

In total, 75 cystic aspirates were included in our study. The cervical cystic diseases were as follows: (1) 40 cases of metastatic PTC (39 diagnosed as pure metastatic PTC and one with a major squamous cell carcinoma component and a

TABLE 1: Correlations between the final diagnosis and the Tg-FNA values.

Final diagnosis	Case number	Tg-FNA values (ng/mL) range/median
Metastatic PTCs ^a	40	0.64–500+ 500+
Reactive lymphadenitis ^b	5	2.10–5.74 4.43
Metastases from extrathyroidal malignancies	15	0.10–21.15 1.38
Cervical original benign lesions	15	0.09–500+ 2.04
Branchial cleft cysts	2	0.09–0.12 0.10
Thyroglossal cysts	3	5.40–500+ 6.22
Lymphangiomas	4	0.35–3.20 1.48
Schwannomas	2	2.04–50.20 26.12
Cystic lesions of the salivary gland	4	0.10–2.54 1.29

^aOne case of metastatic PTC was diagnosed histologically as metastatic thyroid carcinoma where the tumor was mainly composed of squamous carcinoma with a small component of papillary carcinoma. The Tg-FNA value of this case was 0.64 ng/mL and was the lowest of the metastatic PTCs.

^bAll 5 cases had a history of thyroidectomy for thyroid papillary carcinoma. These negative lymph nodes were followed up by sonography for at least 12 months and showed a decrease in size.

minor papillary carcinoma component, surgically confirmed to be PTC recurrence), 5 cases of reactive lymphadenitis (all in patients with a history of thyroidectomy for PTC), 15 cases of lymph node invasion from metastatic extrathyroidal malignancies (11 squamous carcinomas and 4 adenocarcinomas), and 15 cases of benign lesions of cervical origin (2 branchial cleft cysts, 3 thyroglossal cysts, 4 lymphangiomas, 2 schwannomas, and 4 cystic lesions of the salivary glands) (Table 1).

Table 1 also shows the Tg-FNA values in the different groups of cystic lesions. Cystic metastases from PTC (median, >500 ng/mL) showed significantly higher levels on Tg-FNA than reactive lymphadenitis (median, 4.43 ng/mL, $P < 0.001$), metastases from extrathyroidal cancer (median, 1.38 ng/mL, <0.001), and benign lesions of cervical origin (median, 2.04 ng/mL, $P < 0.001$). There were two special cases. One was of a metastatic PTC, which had a very low value on Tg-FNA (0.64 ng/mL). This case was diagnosed histologically as metastatic thyroid carcinoma with the tumor mainly composed of squamous carcinoma and a small component of papillary carcinoma. The other case was of a thyroglossal cyst, which showed a Tg-FNA level as high as that for metastatic PTC (>500 ng/mL).

Based on the final diagnosis, 40 lesions were metastatic PTCs and the remaining 35 were not. We evaluated the optimal cutoff value for Tg-FNA in diagnosing metastatic PTC, and four threshold values were used: 0.04, 0.9, 10.0, and 77.0 ng/mL. The AUCs for determining metastatic PTC of Tg-FNA levels of 0.04, 0.9, 10.0, and 77.0 ng/mL were 0.5 (95% CI, 0.382–0.618), 0.645 (95% CI, 0.526–0.752), 0.945 (95% CI, 0.866–0.984), and 0.973 (95% CI, 0.907–0.996), respectively.

The AUC of the Tg-FNA cutoff of 77.0 ng/mL was the highest, significantly higher than the AUCs of the Tg-FNA cutoffs of 0.04 ng/mL ($P < 0.001$) and 0.9 ng/mL ($P < 0.001$), but not significantly higher than the AUC of the Tg-FNA cutoff of 10.0 ng/mL ($P = 0.157$) (Figure 1).

A diagnostic strategy of FNAC alone had a sensitivity of 80.0% and a specificity of 100% for determining metastatic PTC. A higher sensitivity (97.5% versus 80%, $P = 0.013$) and similar specificity (100% versus 100%, $P = 1.000$) were obtained for a diagnostic strategy of Tg-FNA combined with FNAC, compared to FNAC alone. In this strategy, a positive result was considered if the criteria for either test were met, except in one special case. In this case, the Tg level was positive (>500 ng/mL), but the definitive cytological diagnosis was thyroglossal cyst. Accordingly, a diagnosis of thyroglossal cyst with a high Tg level was a reasonable diagnosis. This case was considered negative when performing statistical analyses of the combined criteria (Table 2).

4. Discussion

Aided with FNAC, ultrasound technique is the main modality for assessing thyroid gland lesions [17–19]. A cystic appearance of lymph nodes is a characteristic of metastatic PTC [2, 3, 20, 21]. However, frequent nondiagnostic cytologic results and high false negative rates for FNA are reported in cases of cystic metastatic lymph nodes [2, 3]. In the past, we recommended thyroid examination in cases of inadequate cells in a cervical cystic aspirate, especially when the patient had a history of PTC or the fluid aspirated was brown in color. However, the results were not always as expected. It should

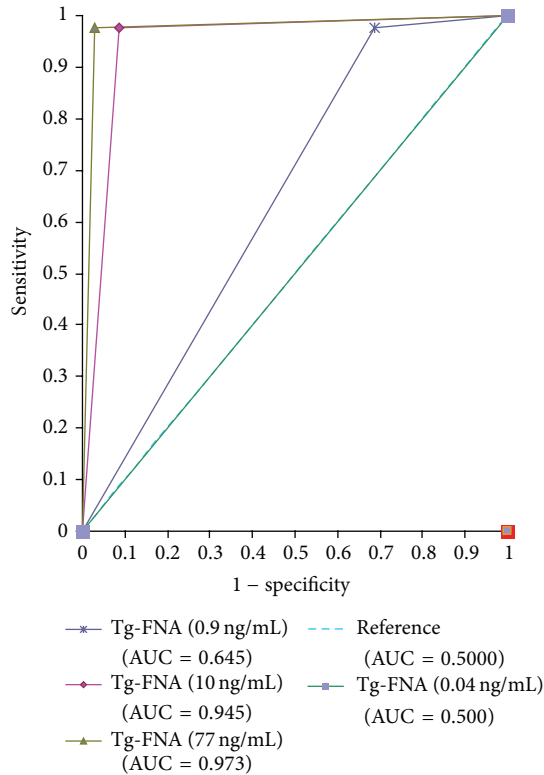


FIGURE 1: ROC curves for Tg-FNA for different cutoff values.

TABLE 2: Evaluation of metastatic PTC according to the diagnostic modality.

Modalities	SN	SP	PPV	NPV	AC
FNAC	80.0%	100%	100%	81.4%	89.3%
Tg-FNA ^a	97.5%	97.1%	97.5%	97.1%	97.3%
FNAC + Tg-FNA ^b	97.5%	100%	100%	97.1%	98.7%

^aTg-FNA refers to the optimal cutoff value of Tg-FNA at 77.0 ng/mL.

^bPositive result was determined if the positive criteria for either criterion were met except in one special case. In this case, the Tg level was positive (>500 ng/mL), but the definitive cytological diagnosis was thyroglossal cyst. Accordingly, a diagnosis of thyroglossal cyst with a high Tg level was a reasonable diagnosis. This case was considered negative when performing statistical analyses of the combined criteria. SN, sensitivity; SP, specificity; PPV, positive predictive value; NPV, negative predictive value; AC, accuracy.

be considered that many benign lesions or extrathyroidal malignancies also have a cystic appearance, as shown in Table 1. Of the 75 cystic cervical lesions included in our study, only 40 were proven to be metastatic PTC. Therefore, an objective examination for the detection of PTC in cystic lesions was needed.

Tg-FNA was initially proposed by Pacini et al. in 1992 and has been reported to increase the detection rate of metastatic PTC combined with FNAC [3, 7–16]. However, the diagnostic threshold has not been well established. In the present study, we suggested four threshold values, as in previous reports [7–15]. The functional sensitivity of Tg measurement was the most commonly used threshold values in previous studies [7, 10–12, 16]. However, the use of this threshold

value is associated with several limitations. If the aspirates are contaminated with blood containing high levels of Tg, the Tg-FNA values may be higher than the set threshold value, even if the lymph nodes are not metastatic. In patients awaiting surgery and even in patients who have undergone surgery without radioiodine ablation, serum-Tg may not be suppressed, which can confuse the diagnosis. This hypothesis was proven in our study. In the present study, Tg levels from all lymph node (both benign and malignant) aspirates were above the detectable level, which may partly be due to the high sensitivity of our detection method. According to the manufacturer's instructions, the minimum detectable Tg concentration is 0.04 ng/mL, indicating a higher sensitivity than in previous studies [7, 10–12, 16]. When 0.9 ng/mL, the reported detectable Tg level in previous studies [7, 10, 16], was used as the threshold, the AUC was only 0.645, indicating poor diagnostic ability.

The serum-Tg level has also been used as the threshold value [14, 22, 23]. A Tg-FNA/serum-Tg ratio of >1.0 is interpreted as a positive result. However, this method could not be used for patients who had not undergone serum-Tg evaluation. In addition, in cases where blood sampling for serum-Tg and Tg-FNA was not performed simultaneously but within a few days to a few weeks, hormonal variation in serum-Tg could skew the data. Therefore, we used the maximum normal serum-Tg level (77.0 ng/mL) as the threshold value, which was found to be the most valuable threshold value in our study. Another previously reported threshold value (10.0 ng/mL) was also found to be of value [14, 24]. The specificity of 10.0 ng/mL was lower than that of 77.0 ng/mL. The Tg-FNA level was higher than 10.0 ng/mL in one case of lymph node metastasis from an extrathyroidal malignancy (21.12 ng/mL) and in one case of schwannoma (50.20 ng/mL). However, none of the tested threshold values could distinguish benign from metastatic lymph nodes in patients with PTC with complete reliability. The cutoff value of 77.0 ng/mL (the normal serum-Tg level) was found to have the best diagnostic performance.

Of the cystic metastatic PTC cases, 20% (8 of 40 cases) yielded a cytologically equivocal or nondiagnostic result. This is similar to the rate reported in previous studies [7, 12] and reflects the challenge in diagnosing cystic cervical lesions with FNAC. The sensitivity for the detection of lymph node metastasis was increased greatly by combining Tg-FNA and cytology; 7 of 8 metastatic lymph nodes with negative cytology were detected using Tg-FNA. One case of metastatic PTC missed by Tg-FNA was diagnosed histologically as metastatic thyroid carcinoma, where the tumor was mainly composed of squamous carcinoma with a small component of papillary carcinoma. This phenomenon has been reported by Boi et al. [25]. In their series, 2 of the 4 metastatic lymph nodes undetectable by Tg-FNA were from anaplastic thyroid tumors, and the other 2 were from very undifferentiated PTC. Tg will not be detectable not only in lymph nodes with metastasis from anaplastic or undifferentiated PTC, but also in lymph nodes with metastasis from recurrent PTC. Because 2% to 5% of differentiated thyroid carcinomas are reported to lose their differentiated features, making monitoring by serum-Tg difficult, recurrent non-RAI-avid

18F-fluorodeoxyglucose-positron emission tomography-positive disease has been reported to develop, leading to the patient's death [26]. A similar case was encountered in our study. The patient had a history of thyroidectomy for PTC with three recurrences. Thus, we recommend combined cytology and Tg-FNA rather than either technique alone to detect any histological type of thyroid cancer metastases [25].

5. Conclusion

The results of the current study demonstrate that Tg measurement in FNA material appears to be a useful ancillary test that improves the detection of cystic PTC metastases, and the maximum normal serum-Tg level (77.0 ng/mL) is suggested as the threshold value with a good diagnostic performance for cystic lesions.

Study Limitations

There are some limitations to our study. Five (100%) reactive lymph nodes, 7 (46.7%) metastases from extrathyroidal malignancies, and 7 (46.7%) benign lesions of cervical origin were not surgically confirmed. However, all of these nonmetastatic PTC lesions had definite results on FNA and the Tg-FNA level was <77.0 ng/mL. Moreover, the 5 reactive lymph node cases were followed up for at least 12 months.

Conflict of Interests

The authors declare that there is no conflict of interests regarding the publication of this paper.

Authors' Contribution

Yong Wang and Huan Zhao contributed equally to this work as first authors.

Acknowledgment

This study was supported by Beijing Hope Run Special Fund no. LC2012A14.

References

- [1] E. Cakmakci, K. C. Caliskan, O. K. Turkoglu et al., "A modified technique for real time ultrasound guided pediatric percutaneous renal biopsy: the angled tangential approach," *Quantitative Imaging in Medicine and Surgery*, vol. 4, no. 3, pp. 190–194, 2014.
- [2] C. S. Landry, E. G. Grubbs, N. L. Busaidy et al., "Cystic lymph nodes in the lateral neck as indicators of metastatic papillary thyroid cancer," *Endocrine Practice*, vol. 17, no. 2, pp. 240–244, 2011.
- [3] M. Cignarelli, A. Ambrosi, A. Marino et al., "Diagnostic utility of thyroglobulin detection in fine-needle aspiration of cervical cystic metastatic lymph nodes from papillary thyroid cancer with negative cytology," *Thyroid*, vol. 13, no. 12, pp. 1163–1167, 2003.
- [4] M. Üstün, B. Risberg, B. Davidson, and A. Berner, "Cystic change in metastatic lymph nodes: a common diagnostic pitfall in fine-needle aspiration cytology," *Diagnostic Cytopathology*, vol. 27, no. 6, pp. 387–392, 2002.
- [5] A. Kessler, Y. Rappaport, A. Blank, S. Marmor, J. Weiss, and M. Graif, "Cystic appearance of cervical lymph nodes is characteristic of metastatic papillary thyroid carcinoma," *Journal of Clinical Ultrasound*, vol. 31, no. 1, pp. 21–25, 2003.
- [6] F. Pacini, L. Fugazzola, F. Lippi et al., "Detection of thyroglobulin in the needle aspirates of nonthyroidal neck masses: a clue to the diagnosis of metastatic differentiated thyroid cancer," *Journal of Clinical Endocrinology and Metabolism*, vol. 74, no. 6, pp. 1401–1404, 1992.
- [7] N. Cunha, F. Rodrigues, F. Curado et al., "Thyroglobulin detection in fine-needle aspirates of cervical lymph nodes: a technique for the diagnosis of metastatic differentiated thyroid cancer," *European Journal of Endocrinology*, vol. 157, no. 1, pp. 101–107, 2007.
- [8] A. Salmashoğlu, Y. Erbil, G. Çıtlak et al., "Diagnostic value of thyroglobulin measurement in fine-needle aspiration biopsy for detecting metastatic lymph nodes in patients with papillary thyroid carcinoma," *Langenbeck's Archives of Surgery*, vol. 396, no. 1, pp. 77–81, 2011.
- [9] Y. H. Lee, H. S. Seo, S.-I. Suh et al., "Cut-off value for needle washout thyroglobulin in athyrotropic patients," *Laryngoscope*, vol. 120, no. 6, pp. 1120–1124, 2009.
- [10] N. S.-J. Yap, R. Maher, and D. L. Learoyd, "Any detectable thyroglobulin in lymph node biopsy washouts suggests local recurrence in differentiated thyroid cancer," *Endocrine Connections*, vol. 3, no. 4, pp. 150–155, 2014.
- [11] Q. K. Li, S. L. Nugent, J. Straseski et al., "Thyroglobulin measurements in fine-needle aspiration cytology of lymph nodes for the detection of metastatic papillary thyroid carcinoma," *Cancer Cytopathology*, vol. 121, no. 8, pp. 440–448, 2013.
- [12] B. J. Holmes, L. J. Sokoll, and Q. K. Li, "Measurement of fine-needle aspiration thyroglobulin levels increases the detection of metastatic papillary thyroid carcinoma in cystic neck lesions," *Cancer Cytopathology*, vol. 122, no. 7, pp. 521–526, 2014.
- [13] J. Chung, E. K. Kim, H. Lim et al., "Optimal indication of thyroglobulin measurement in fine-needle aspiration for detecting lateral metastatic lymph nodes in patients with papillary thyroid carcinoma," *Head and Neck*, vol. 36, no. 6, pp. 795–801, 2014.
- [14] M. J. Kim, E.-K. Kim, B. M. Kim et al., "Thyroglobulin measurement in fine-needle aspirate washouts: the criteria for neck node dissection for patients with thyroid cancer," *Clinical Endocrinology*, vol. 70, no. 1, pp. 145–151, 2009.
- [15] J. H. Moon, Y. I. Kim, J. A. Lim et al., "Thyroglobulin in washout fluid from lymph node fine-needle aspiration biopsy in papillary thyroid cancer: large-scale validation of the cutoff value to determine malignancy and evaluation of discrepant results," *Journal of Clinical Endocrinology and Metabolism*, vol. 98, no. 3, pp. 1061–1068, 2013.
- [16] K. Pak, S. Suh, H. Hong et al., "Diagnostic values of thyroglobulin measurement in fine-needle aspiration of lymph nodes in patients with thyroid cancer," *Endocrine*, vol. 49, no. 1, pp. 70–77, 2015.
- [17] Y. Wang, L. Li, Y.-X. J. Wang et al., "Ultrasound findings of papillary thyroid microcarcinoma: a review of 113 consecutive cases with histopathologic correlation," *Ultrasound in Medicine and Biology*, vol. 38, no. 10, pp. 1681–1688, 2012.
- [18] I. Ceylan, S. Yener, F. Bayraktar, and M. Secil, "Roles of ultrasound and power Doppler ultrasound for diagnosis of

- Hashimoto thyroiditis in anti-thyroid marker-positive euthyroid subjects,” *Quantitative Imaging in Medicine and Surgery*, vol. 4, no. 4, pp. 232–238, 2014.
- [19] A. A. Tam, C. Kaya, R. Üçler, A. Dirikoç, R. Ersoy, and B. Çakır, “Correlation of normal thyroid ultrasonography with thyroid tests,” *Quantitative Imaging in Medicine and Surgery*, vol. 5, no. 4, pp. 569–574, 2015.
- [20] Y.-M. Sohn, J. Y. Kwak, E.-K. Kim, H. J. Moon, S. J. Kim, and M. J. Kim, “Diagnostic approach for evaluation of lymph node metastasis from thyroid cancer using ultrasound and fine-needle aspiration biopsy,” *American Journal of Roentgenology*, vol. 194, no. 1, pp. 38–43, 2010.
- [21] E. Mişekyte-Kaubrien, M. Trakymas, and A. Ulys, “Cystic lymph node metastasis in papillary thyroid carcinoma,” *Medicina*, vol. 44, no. 6, pp. 455–459, 2008.
- [22] T. Uruno, A. Miyauchi, K. Shimizu et al., “Usefulness of thyroglobulin measurement in fine-needle aspiration biopsy specimens for diagnosing cervical lymph node metastasis in patients with papillary thyroid cancer,” *World Journal of Surgery*, vol. 29, no. 4, pp. 483–485, 2005.
- [23] E. Sigstad, A. Heilo, E. Paus et al., “The usefulness of detecting thyroglobulin in fine-needle aspirates from patients with neck lesions using a sensitive thyroglobulin assay,” *Diagnostic Cytopathology*, vol. 35, no. 12, pp. 761–767, 2007.
- [24] M. R. D. S. Torres, S. H. Nóbrega Neto, R. J. Rosas, A. L. B. Martins, A. L. C. Ramos, and T. R. P. da Cruz, “Thyroglobulin in the washout fluid of lymph-node biopsy: what is its role in the follow-up of differentiated thyroid carcinoma?” *Thyroid*, vol. 24, no. 1, pp. 7–18, 2014.
- [25] F. Boi, G. Baghino, F. Atzeni, M. L. Lai, G. Faa, and S. Mariotti, “The diagnostic value for differentiated thyroid carcinoma metastases of thyroglobulin (Tg) measurement in washout fluid from fine-needle aspiration biopsy of neck lymph nodes is maintained in the presence of circulating anti-Tg antibodies,” *Journal of Clinical Endocrinology and Metabolism*, vol. 91, no. 4, pp. 1364–1369, 2006.
- [26] M. Braga-Basaria and M. D. Ringel, “Clinical review 158—beyond radioiodine: a review of potential new therapeutic approaches for thyroid cancer,” *Journal of Clinical Endocrinology and Metabolism*, vol. 88, no. 5, pp. 1947–1960, 2003.

Research Article

Dynamic Contrast-Enhanced CT Characterization of Xp11.2 Translocation/TFE3 Gene Fusions versus Papillary Renal Cell Carcinomas

Jian He,¹ Kefeng Zhou,¹ Bin Zhu,¹ Gutian Zhang,² Xiaogong Li,² Hongqian Guo,² Weidong Gan,² Zhengyang Zhou,¹ and Tian Liu³

¹Department of Radiology, Nanjing Drum Tower Hospital, The Affiliated Hospital of Nanjing University Medical School, Nanjing 210008, China

²Department of Urology, Nanjing Drum Tower Hospital, The Affiliated Hospital of Nanjing University Medical School, Nanjing 210008, China

³Radiation Oncology and Winship Cancer Institute, Emory University, Atlanta, GA 30322, USA

Correspondence should be addressed to Weidong Gan; ganweidong2015@126.com and Zhengyang Zhou; zyzhou@nju.edu.cn

Received 28 July 2015; Revised 15 September 2015; Accepted 20 October 2015

Academic Editor: Yi-Xiang Wang

Copyright © 2015 Jian He et al. This is an open access article distributed under the Creative Commons Attribution License, which permits unrestricted use, distribution, and reproduction in any medium, provided the original work is properly cited.

Purpose. To compare the differences of CT characteristics between renal cell carcinomas (RCCs) associated with Xp11.2 translocation/TFE3 gene fusions (Xp11.2 RCCs) and papillary cell renal cell carcinomas (PRCCs). **Methods.** CT images and clinical records of 64 patients (25 Xp11.2 RCCs, 15 type 1 and 24 type 2 PRCCs) were analyzed and compared retrospectively. **Results.** Xp11.2 RCC more frequently affected young (30.7 ± 8.7 years) women (16/25, 64%) with gross hematuria (12/25, 48%), while PRCC more frequently involved middle-aged (54.8 ± 11.1 years) men (28/39, 71.8%) asymptotically. Xp11.2 RCC tended to be heterogeneous density with some showing circular calcification. Lesion sizes of Xp11.2 RCC (5.4 ± 2.2 cm) and type 2 PRCC (5.7 ± 2.5 cm) were significantly larger than that of type 1 PRCC (3.8 ± 1.8 cm). Xp11.2 RCC contained more cystic components (22/25, 88%) than type 1 PRCC (all solid) and type 2 PRCC (9/24, 36.0%). Type 1 PRCC (13/15, 86.7%) and Xp11.2 RCC (21/25, 84.0%) showed more clear boundary than type 2 PRCC (12/24, 50.0%). **Conclusion.** CT features including diameter, boundary, attenuation, nature, and circular calcification of the tumor, combined with demographic information and symptoms, may be useful to differentiate Xp11.2 RCC from different subtypes of PRCC.

1. Introduction

Renal cell carcinoma (RCC) associated with Xp11.2 translocation/TFE3 gene fusions (Xp11.2 RCC) was introduced as a genetically distinct entity into the World Health Organization classification of renal neoplasms in 2004 [1]. Microscopically, Xp11.2 RCC shows various features, including abundant clear or eosinophilic cytoplasm, irregular nuclei with vesicular chromatin, and prominent nucleoli with papillary, nested, alveolar, or tubular architectures. Although Xp11.2 RCC is predominantly diagnosed in children and rare in adults, the disease seems more advanced and aggressive in adults than in children [2]. Moreover, based on meta-analysis, Xp11.2 RCC has a poorer prognosis than non-Xp11.2 RCC in children and young adults [3].

Previous studies with computed tomography (CT) have shown that Xp11.2 RCC appears as a large, well-defined cystic-solid renal mass with intratumoral hemorrhage and circular calcification. These features are especially evident in young females with hematuria [4–9]. In our previous study, dynamic contrast-enhanced CT (DCE-CT) showed heterogeneously moderate prolonged enhancement of Xp11.2 RCC. Different from Xp11.2 RCC, DCE-CT of clear cell RCC (CCRCC) had a typical “wash-in and wash-out” pattern, microscopically showing nests of epithelial cells with clear cytoplasm and a distinct cell membrane, separated by a delicate branching network of vascular tissue [10].

Papillary RCC (PRCC), the second most common RCC subtype, is histologically characterized by a predominantly

papillary growth pattern composed of columnar/cuboidal cells and contains two histological types with distinct behavior and prognosis [11]. Type 1 PRCC contains small cells with scanty pale cytoplasm and small ovoid nuclei that are arranged in a single layer on the basement membrane of the papillary core. Type 2 PRCC contains cells with abundant eosinophilic cytoplasm, large and spherical nuclei, prominent nucleoli, and varying degrees of nuclear pseudostratification.

There are significant challenges to distinguish Xp11.2 RCC from PRCC. Considerable similarities exist in the microscopic morphologies of Xp11.2 RCC and PRCC, causing frequent, pathology misdiagnosis [8]. It is also hard to differentiate between Xp11.2 RCC and PRCC with CT or magnetic resonance imaging (MRI) because both are hypovascular neoplasms [12, 13]. Nevertheless, identifying the correct RCC subtype is important, as Xp11.2 RCC and PRCC have different behaviors and prognosis. PRCC is usually described as a single entity that has a favorable outcome compared with CCRCC, while Xp11.2 RCC exhibits higher invasiveness and poorer prognosis than CCRCC [3]. Radical operation has served as the main treatment regimen for patients with Xp11.2 RCC, whereas patients with PRCC can be treated with partial nephrectomies.

Current radiologic literature lacks comparative studies that distinguish the RCC subtypes. For example, most radiological studies evaluated PRCC as a single subtype [12, 14, 15], and only a few studies focused on the differential diagnosis between the two histological subtypes [16]. Moreover, the difference between Xp11.2 RCC and subtypes of PRCC on DCE-CT has never been reported.

The aim of this study was to compare the difference between Xp11.2 RCC and PRCC (including type 1 and type 2) on DCE-CT.

Awareness of imaging differences between various subtypes of RCC may help promote further confirmatory diagnostic processes including immunohistochemical (IHC) staining and fluorescence in situ hybridization (FISH) assay and may help improve treatment strategy [4].

2. Materials and Methods

2.1. Ethics Statement. This retrospective study was approved by the institutional review board. The informed consent was waived due to the retrospective nature of this study.

2.2. Patients. From January 2007 to January 2015, a total of 25 consecutive adult patients (≥ 18 years old) with Xp11.2 RCC who had undergone a radical or partial nephrectomy in our institution were retrospectively identified. From 113 patients diagnosed with PRCC, based on microscopic findings, a subset of 39 PRCC-patients with a definite negative FISH assay result were selected for this comparative study. The other 74 patients failed to undergo FISH analysis due to lack of tissue specimens and as a result, therefore, were excluded from this study because a diagnosis of Xp11.2 RCC cannot be excluded solely based on microscopic findings. None of the enrolled patients had received local or systematic therapy before CT scanning and surgery.

2.3. Clinical, Treatment, and Pathological Information. A total of 25 Xp11.2 RCCs and 39 PRCCs were included in this study. Each patient had one lesion. Six Xp11.2 RCC patients were diagnosed at stage 3 and stage 4, while the majority of PRCC patients (34/39) were diagnosed at stage 1 and stage 2. Clinical, radiologic, and pathological records of the 2 RCC subtypes are shown in Table 1. No history of malignancy, chemotherapy, or toxic exposure was recorded in the enrolled patients.

Open or laparoscopic radical operation served as the main treatment for 18 patients with Xp11.2 RCC, and the remaining 7 patients underwent laparoscopic partial nephrectomy, while 23 out of 39 patients with PRCC underwent laparoscopic or open partial nephrectomies, 15 patients received radical nephrectomies, and the remaining 1 patient underwent radiofrequency ablation. Although none of the patients in both groups died during surgery, 3 patients with Xp11.2 RCC and one patient with type 2 PRCC died of distant metastasis during a follow-up between 6~78 months (mean, 36.6 months; medium, 33 months).

Gross pathological record of the specimen was reviewed by 2 pathologists to confirm the tumor's location, boundary, capsule, shape, necrotic and cystic components, hemorrhage, and tumor thrombosis observed on CT imaging. IHC staining with TFE3 antibody and FISH assay with a self-designed polyclonal break-apart probe confirmed the diagnosis of Xp11.2 RCC in 25 cases. However, both TFE3 staining and FISH assay were negative in all PRCC cases.

2.4. CT Examination. All patients underwent unenhanced and DCE-CT scans using a multidetector CT scanner (LightSpeed; GE Healthcare, Princeton, NJ) with a 5.0 mm slice thickness at 40, 70~80, and 180 seconds to obtain corticomedullary, nephrographic, and delayed phases, after injection of 1.2 mL/kg body weight of contrast media (Omnipaque 350 mg I/mL; GE Healthcare, US), at a rate of 3.0 mL/s followed by 40 mL saline solution using a power injector (Medrad Stellant, Indianola, PA). Images were obtained at a tube voltage of 120 kVp, a tube current of 240 mA, with a rotation time of 0.6 seconds, a helical pitch of 1.375, a field view of 35 to 40 cm, and a matrix of 512 \times 512.

2.5. Image Interpretation. All CT images were reviewed in consensus by 2 radiologists (Jian He and Kefeng Zhou with 5- and 10-year experience in abdominal CT diagnosis, resp.). The images were reviewed on a picture archiving and communication system workstation (GE AW4.3 workstation).

Tumor features on CT imaging were evaluated based on the following criteria:

- (i) Tumor location: the tumor was located in the left or right kidney, with cortical, cortical-medullary, or medullary involvement.
- (ii) Tumor size: the maximum diameter of the tumor was measured in centimeters.
- (iii) Tumor boundary: a clear boundary was characterized by well-defined, bulging tumor margins that displaced surrounding structures. An unclear boundary

TABLE 1: The clinical, pathological details and tumor characteristics on CT in Xp11.2 RCC and PRCC (including type 1 and type 2).

	Xp11.2 RCC (n = 25)	PRCC (n = 39)	Type 1 (n = 15)	Type 2 (n = 24)	Xp11.2 versus PRCC	Xp11.2 versus type 1	Xp11.2 versus type 2	Type 1 versus type 2
Gender (male/female)	9/16	28/11	12/3	16/8	0.005*	0.007*	0.032*	0.368
Age range (years)	19~51	32~78	35~78	32~73	—	—	—	—
Mean age (years)	30.7 ± 8.7	54.8 ± 11.1	55.9 ± 12.2	54.2 ± 10.5	<0.001*	<0.001	<0.001*	0.634
Gross hematuria	12/13	7/32	2/13	5/19	0.010*	0.026*	0.046*	0.553
Location (left/right)	7/18	23/16	8/7	15/9	0.015*	0.109	0.015*	0.571
Location (cortical/cortical-medullar/medullar)	1/23/1	8/28/3	4/11/0	4/17/3	0.131	0.089	0.159	0.311
Diameter (cm)	5.4 ± 2.2	5.0 ± 2.4	3.6 ± 1.6	5.8 ± 2.5	0.426	0.009*	0.592	0.002*
Boundary (clear/unclear)	21/4	25/14	13/2	12/12	0.084	0.819	0.011*	0.020*
Shape (regular/irregular)	14/11	25/14	12/3	13/11	0.517	0.123	1.000	0.102
Attenuation (homo-/heterogeneous)	5/20	20/19	12/3	8/16	0.012*	<0.001*	0.291	0.005*
Nature (solid/cystic-solid/cystic)	2/22/1	30/9/0	15/0/0	15/9/0	<0.001*	<0.001*	<0.001*	0.007*
Hemorrhage (with/without)	10/15	9/30	3/12	6/18	0.148	0.191	0.263	0.718
Circular calcification (with/without)	10/15	6/33	1/14	5/19	0.027*	0.022*	0.146	0.233
Fat (with/without)	0/25	0/39	0/15	0/24	1.000	1.000	1.000	1.000
Tumor thrombosis (with/without)	3/22	1/38	0/15	1/23	0.128	0.163	0.317	0.423
Lymph node metastasis (with/without)	3/22	4/35	0/15	4/20	0.827	0.163	0.641	0.095
Distant metastasis (with/without)	2/23	1/38	0/15	1/23	0.315	0.261	0.576	0.357
Treatment (OR/OP/LR/LP/RA) ^a	6/0/12/7/0	7/7/8/16/1	0/4/3/7/1	7/3/5/9/0	0.044*	0.005*	0.103	0.126
Stage (I/II/III/IV)	17/2/5/1	27/7/3/2	14/1/0/0	13/6/3/2	0.397	0.222	0.341	0.075
Median follow-up time (months)	31	32	35	30	—	—	—	—
Survival rate	88%	97.4%	100%	95.8%	0.128	0.163	0.317	0.423

Note: Xp11.2 RCC: renal cell carcinoma associated with Xp11.2 translocation/TFE3 gene fusions; PRCC: papillary renal cell carcinoma; ^aOR: open radical nephrectomy; OP: open partial nephrectomy; LR: laparoscopic radical nephrectomy; LP: laparoscopic partial nephrectomy; RA: radiofrequency ablation. * $P < 0.05$.

was defined as lacking clear borders between the tumor and surrounding structures.

- (iv) Tumor shape: a regular shape was characterized as round or oval. Irregular shapes included a roughly round or oval tumor with focal protrusions and lobulated and infiltrative growth patterns.
- (v) Tumor texture: a solid tumor had soft tissue density without obvious necrotic or cystic areas. A cystic-solid tumor had solid and cystic components. A cystic tumor was completely cystic with a capsule wall. Necrotic or cystic components were defined as the irregular unenhanced cavitation on contrast-enhanced CT images.
- (vi) Presence of intratumoral hemorrhage: intratumoral hemorrhage presented as patchy or formless hyperdense area on unenhanced CT scan (CT value 40~70 Hounsfield Unit, HU), nonenhancing on enhanced CT scan.
- (vii) Presence of intratumoral calcification: calcification presented as dense foci (>100 HU). Number, shape, and distribution of calcification were recorded.
- (viii) Presence of intratumoral fat: fat showed a hypodense area (-50 to -100 HU) on unenhanced CT scan.
- (ix) Presence of tumor thrombosis: the tumor was found in the lumen of the renal vein or the inferior vena cava.
- (x) Presence of local lymphadenopathy: retroperitoneal nodal was enlarged with a short-axis diameter at least 10 mm.
- (xi) Tumor metastasis: presence of distant metastasis in other organs, such as the liver and lung nodules, which were enlarged during follow-up.
- (xii) Tumor attenuation (HU) in unenhanced, corticomedullary, nephrographic, and delayed phases: computed tomographic attenuation values (in HU) of the tumor were measured on each phase by the 2 radiologists. The region of interest (ROI) was defined in the solid portion of the mass to avoid intratumoral calcification and cystic and necrotic components in the slice with maximum diameter of the lesion. For all images, each 100 mm² ROI was measured 3 times by both radiologists, and the mean value was used.

2.6. *Statistical Analysis.* Statistical analysis was performed using SPSS 13.0 software (SPSS Inc., Chicago, IL). Numeric data were expressed as mean ± standard deviation, and categorical data were expressed as percentages. Evaluated characteristics were compared between the RCC subtypes

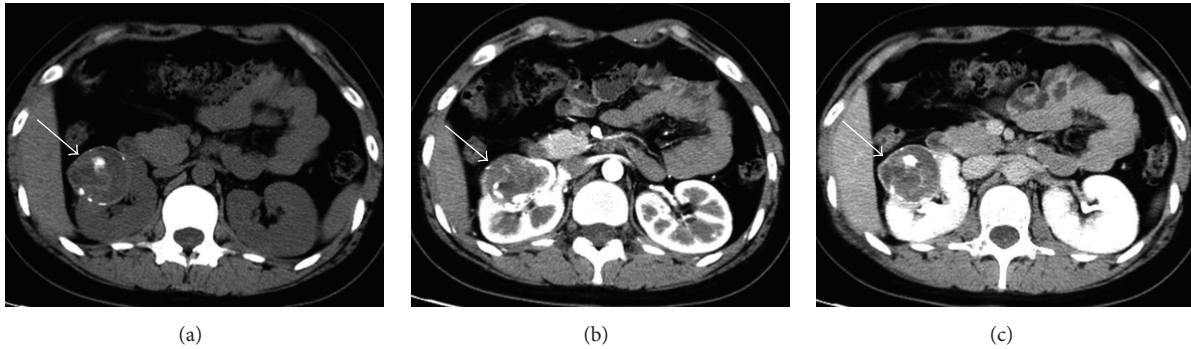


FIGURE 1: Renal cell carcinoma associated with Xp11.2 translocation/TFE3 gene fusions in a 22-year-old woman with gross hematuria. (a) Abdominal plain CT scan shows a round well-defined mass of 5.0 cm in size with mixed intensity (around 50 HU) in the right kidney. Note the punctate and circular calcification within and around the lesion. (b) The tumor, which involves both the cortex and medulla, shows heterogeneously moderate enhancement (to around 84 HU) during corticomedullary phase. (c) The tumor continues to be enhanced heterogeneously from corticomedullary phase to nephrographic phase (to around 90 HU). The unenhanced areas within the tumor indicate necrosis.

using the repeated measures analysis of variance (ANOVA) or χ^2 test. A *P* value less than 0.05 was considered statistically significant.

3. Results

3.1. Xp11.2 RCC and PRCC. The clinical, pathological details, and tumor characteristics on CT in Xp11.2 RCC and PRCC are shown in Table 1. Xp11.2 RCC more frequently affected young (30.7 ± 8.7 years) women (16/25, 64%) with gross hematuria (12/25, 48%), while PRCC more frequently involved middle-aged (54.8 ± 11.1 years) men (28/39, 71.8%) without obvious symptoms. Xp11.2 RCC was more heterogeneous (20/25, 80%) and with cysts (22/25, 88%). Circular calcification was observed in Xp11.2 RCC (15/25, 60%) more often than PRCC (6/39, 15.4%). A case of Xp11.2 RCC is shown in Figure 1.

3.2. Type 1 and 2 PRCCs. Type 2 PRCC was significantly larger (5.8 ± 2.5 cm) than type 1 PRCC (3.6 ± 1.6 cm) ($P = 0.002$). Type 2 PRCC was more likely to be heterogeneous (16/24, 66.7%) than type 1 PRCC (3/15, 20%). All type 1 PRCCs were solid, while 62.5% (15/24) of type 2 PRCC was solid. Type 1 PRCC had more clear boundaries (13/15, 86.7%) than type 2 PRCC (12/24, 50%) ($P = 0.020$).

3.3. Xp11.2 RCC and Type 1 and 2 PRCCs. Xp11.2 RCC was significantly larger (5.4 ± 2.2 cm) than type 1 PRCC (3.6 ± 1.6 cm) ($P = 0.009$). Xp11.2 RCC (20/25, 80%) was more heterogeneous than type 1 PRCC (3/15, 20%) ($P < 0.001$). Xp11.2 RCC was often cystic-solid (22/25, 88%), while type 1 PRCC was all solid. Xp11.2 RCC was more likely to have clear boundaries (21/25, 84%) than type 2 PRCC (12/24, 50%) ($P = 0.011$). Xp11.2 RCC contained more cystic components (22/25, 88%) than type 2 PRCC (9/25, 36%) ($P < 0.001$). One case of type 1 PRCC and one case of type 2 PRCC are shown with Figures 2 and 3, respectively.

3.4. DCE-CT of Xp11.2 RCC and PRCC. Both Xp11.2 RCC and PRCC showed moderately prolonged enhancement on DCE-CT and peaked at nephrographic phase (Figure 4). Tumor attenuations of Xp11.2 RCCs were significantly higher than those of PRCCs in plain and nephrographic phase scans (Table 2).

4. Discussion

4.1. Comparison between Xp11.2 RCC and PRCC. Xp11.2 RCC is characterized by various translocations involving chromosome X, all resulting in gene fusions involving the TFE3 gene [2]. Xp11.2 RCC usually affects children and young adults, with a slight female predominance (64.0% in our study) [9]. Most Xp11.2 RCCs (23/25, 92%) in this study involved both the cortex and medulla simultaneously, which were consistent with Wang et al.'s report [8] and probably responsible for the high incidence of hematuria (12/25, 48%). Most Xp11.2 RCCs (21/25; 84.0%) had clear boundaries, which were consistent with Zhu et al.'s report [6], probably due to fibrous capsules of the tumor. Based on previous studies, including our own, Xp11.2 RCC presented as a heterogeneous mass with necrotic or cystic components and intratumoral hemorrhage [4–10]. Calcification was commonly detected by CT in Xp11.2 RCC [5, 7–9], and pathological observation confirmed the formation of psammoma bodies in the tumor [2]. We reported that circular calcification around or within the tumor is a specific clue for CT diagnosis of Xp11.2 RCC [10]. On unenhanced CT scans, most Xp11.2 RCCs appear hyperdense relative to the renal parenchyma. After the injection of contrast media, Xp11.2 RCC showed heterogeneous moderately prolonged enhancement on DCE-CT [10].

PRCC also bears distinct molecular genetic and histologic characteristics [17]. Commonly seen among patients over 55 years [1], PRCC is usually a well-defined tumor containing a fibrous capsule [17]. On unenhanced CT scans, PRCC shows isoattenuation or hyperattenuation compared with that of

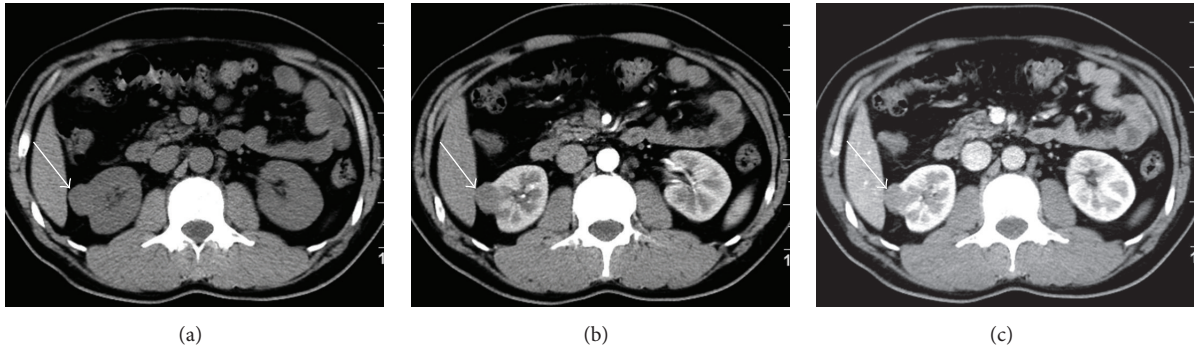


FIGURE 2: Type 1 papillary renal cell carcinoma in a 39-year-old asymptomatic man. (a) Abdominal plain CT scan shows a round well-defined isodense (40 HU) nodule of 2.5 cm in size in the cortex of right kidney. (b) The tumor is enhanced slightly and homogeneously (to around 58 HU) during corticomedullary phase without necrotic or cystic areas in the lesion. (c) The tumor continues to be enhanced homogeneously (to around 78 HU) during the nephrographic phase.

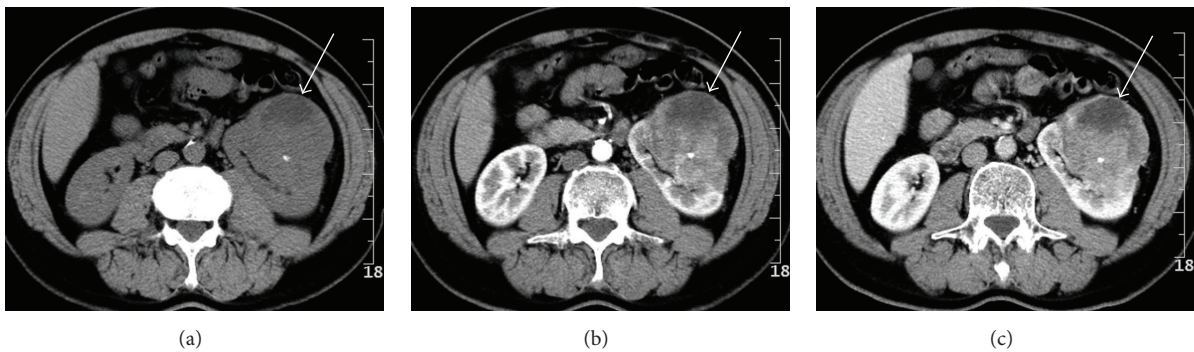


FIGURE 3: Type 2 papillary renal cell carcinoma in a 58-year-old asymptomatic man. (a) Abdominal plain CT scan shows an irregular ill-defined heterogeneous (around 44 HU) mass of 8.3 cm in size in the left kidney. Note a punctate calcification within the lesion. (b) The tumor, which involves both the cortex and medulla, shows heterogeneously moderate enhancement (to around 80 HU) during corticomedullary phase. (c) The tumor's attenuation remains around 80 HU in the nephrographic phase. The unenhanced areas within the tumor indicate necrosis.

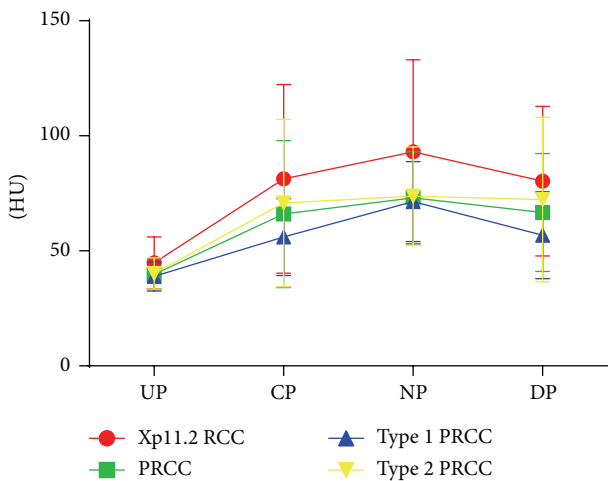


FIGURE 4: Dynamic contrast enhancement patterns of Xp11.2 RCC, type 1 and 2 PRCCs. Xp11.2 RCC: renal cell carcinoma associated with Xp11.2 translocation/TFE3 gene fusions; PRCC: papillary renal cell carcinoma; UP: unenhanced phase; CP: corticomedullary phase; NP: nephrographic phase; DP: delayed phase; HU: Hounsfield unit.

normal renal parenchyma [18]. Typically hypovascular and homogeneous [19] PRCC shows lower enhancement than CCRCC and peaks in the nephrographic phase on dynamic CT studies [20].

Clinically speaking, Xp11.2 RCC often affects young women with gross hematuria, while PRCC is more likely to occur in old men without specific symptoms. In our series, majority of patients with Xp11.2 RCC (18/25) underwent radical nephrectomy, whereas 23 patients with PRCC (79.3%) underwent partial nephrectomies in this study.

Hence, preoperative CT differentiation between those two entities is of great importance for treatment planning. There were no significant differences in diameter and location (cortical/cortical-medullar/medullar) between Xp11.2 RCC and PRCC. They shared similar boundary and shape. Both of them contained hemorrhages without fat content. Xp11.2 RCC was more heterogeneous and contained more cystic components, while PRCC was more homogenous and presented as a solid entity. Circular calcification was more often observed in Xp11.2 RCC than in PRCC. Tumor attenuation of Xp11.2 RCC (44.8 ± 11.2 HU) was significantly higher than

TABLE 2: Dynamic contrast enhanced CT attenuation (HU) of all subtypes of renal cell carcinoma.

	Xp11.2 RCC (<i>n</i> = 25)	PRCC (<i>n</i> = 37)	Type 1 PRCC (<i>n</i> = 12)	Type 2 PRCC (<i>n</i> = 25)	<i>P</i>
Unenhanced phase	44.8 ± 11.2	39.8 ± 6.6	38.9 ± 6.3	40.2 ± 6.8	0.032*
Corticomedullary phase	81.3 ± 41.0	66.0 ± 31.9	56.0 ± 16.7	70.8 ± 36.4	0.114
Nephrographic phase	93.1 ± 40.0	73.1 ± 20.0	71.4 ± 17.4	73.8 ± 21.4	0.021*
Delayed phase	80.3 ± 32.5	66.7 ± 25.6	56.8 ± 18.9	72.3 ± 35.7	0.126

Notes: Xp11.2 RCC: renal cell carcinoma associated with Xp11.2 translocation/TFE3 gene fusions; PRCC: papillary renal cell carcinoma; * *P* < 0.05 (Xp11.2 RCC versus PRCC).

that of PRCC (39.8±6.6 HU) in plain CT scans by the repeated measures of ANOVA (*P* = 0.032). Although both Xp11.2 RCC and PRCC showed moderate prolonged enhancement, the tumor attenuation of Xp11.2 RCC (93.1 ± 40.0 HU) was significantly higher than PRCC (73.1 ± 20.0 HU) (*P* = 0.021) in the nephrographic phase.

4.2. Comparison between Type 1 and 2 PRCCs. In radiology literatures, PRCC has usually been described as a single entity that has a favorable outcome [12, 14, 15]. However, in urologic studies, researchers suggested that PRCCs are a heterogeneous group of entities with different pathologic behaviors [11]. In this study all type 1 PRCCs were at stage I/II without any tumor thrombosis, lymph node, or distant metastasis, while 5 patients with type 2 PRCCs (20.8%) were at more advanced stages with more metastasis.

However, the imaging features of type 1 and 2 PRCCs were very similar. There were no significant differences of location, shape, hemorrhage, calcification, and fat between them. In this study, the mean attenuations of type 1 and 2 PRCCs were similar in unenhanced phase (38.9 ± 6.3 versus 40.2 ± 6.8 HU, *P* = 0.44), which was consistent with previous studies [16]. Both subtypes showed moderate prolonged enhancement on DCE-CT. Tumor attenuation of type 2 PRCC appeared slightly higher than that of type 1 in corticomedullary phase (70.8 ± 36.4 versus 56.0 ± 16.7 HU) without significant difference (*P* = 0.496) (Table 2), which suggested that neither enhancement pattern nor enhancement degree was helpful in discriminating them.

To our knowledge, there were no large studies that showed any specific features that can differentiate between type 1 and 2 PRCCs. We found that type 1 PRCC (3.6 ± 1.6 cm) was significantly smaller than type 2 PRCC (5.8 ± 2.5 cm) (*P* = 0.002), which is contradictory with Mydlo et al.'s report [21], but consistent with most other studies [19, 22, 23]. It was reported that type 2 PRCC grew faster than type 1 [16]. The margin of type 1 PRCCs was more distinct than type 2 PRCC, which is consistent with previous reports [19, 22, 23]. Type 1 PRCC had more homogeneous density than type 2 PRCC. All type 1 PRCCs in this study were solid, while 37.5% (9/24) of type 2 PRCCs contained cystic components, which proved clues for differential diagnosis between those two distinct types.

4.3. Comparison between Xp11.2 RCC and Type 1 and 2 PRCCs. There were no significant differences of location, hemorrhage, and fat between Xp11.2 RCC and type 1 PRCC. Both of them showed clear boundary and regular shape. However, Xp11.2

RCC was significantly larger and more heterogeneous than type 1 PRCC. Many Xp11.2 RCCs contained cysts (22/25, 88%), while type 1 PRCCs were all solid lesions (12/12, 100%) without cystic degeneration or necrosis. In addition, some Xp11.2 RCCs contained circular calcification (10/25, 40%), which was seldom detected in type 1 PRCC (1/12, 8.3%). Xp11.2 RCC enhanced heterogeneously, while type 1 PRCC enhanced homogeneously on DCE-CT.

Except for gender, age, and symptoms, Xp11.2 RCC and type 2 PRCC shared similar stage, behavior, and prognosis. Moreover, CT findings of Xp11.2 RCC and type 2 PRCC were also quite similar and difficult to differentiate between each other. Both of them were relatively large, involving both cortex and medullary of the kidney. They had similar shape and attenuation and contained hemorrhage, circular calcification without fat content. Nevertheless, Xp11.2 RCC had clearer boundaries and more cystic components than those of type 2 PRCC.

4.4. Differential Diagnosis between Other Subtypes of RCCs. We have compared Xp11.2 RCC with CCRCC and found that contrast-enhanced pattern and degree differed significantly between these two entities [10]. A tumor-to-cortex ratio in corticomedullary phase <0.62 gave a sensitivity of 90.0% and a specificity of 92.9% in differentiating Xp11.2 RCC from CCRCC (AUC = 0.957, *P* < 0.001) [10]. Zhu et al. compared the multislice CT findings of Xp11.2 RCC and collecting duct carcinoma and found that distinguishing features including density on unenhanced CT, enhancement patterns, and capsule signs may aid differential diagnosis between these two subtypes [6]. Chromophobe RCC, the third most common histologic subtype of RCC after CCRCC and PRCC, typically localizes in the periphery and presents as a well-defined and hypovascular mass, which is quite similar to Xp11.2 RCC and PRCC [24]. Further studies are required to address the differential diagnosis among these subtypes of RCC.

4.5. Limitations. There are some limitations with this study. Firstly, the sample size of Xp11.2 RCC and PRCC was relatively small [25]. Secondly, the role of other imaging methods such as MRI, positron emission tomography (PET), and more innovative imaging techniques were not referred in this study [26, 27]. For example, PRCC frequently shows a pseudocapsule and has low signal intensity on both T1- and T2-weighted MRI [19], while Xp11.2 RCC often shows hyper- or isointense on T1-weighted image and heterogeneous intensity on T2-weighted image [8].

5. Conclusion

In conclusion, Xp11.2 RCC often affects young women with gross hematuria, while PRCC affects older men without specific symptoms. Most Xp11.2 RCCs involve both the cortex and medulla simultaneously and have clear boundary, presenting as heterogeneous masses with necrotic or cystic components and intratumoral hemorrhage, circular calcification inside or around the tumor. After the injection of contrast media, Xp11.2 RCC shows moderately prolonged heterogeneous enhancement on the DCE-CT. PRCCs present as well-defined, homogeneous, and hypovascular masses on the DCE-CT. Type 1 PRCC is often smaller and more homogeneous than type 2. Type 1 PRCC has more distinct margins and less cystic components than type 2. Xp11.2 RCC is significantly larger and more heterogeneous than type 1 PRCC. Xp11.2 RCCs can be cystic and with circular calcification, while type 1 PRCCs are solid lesions without cystic degeneration or necrosis. Xp11.2 RCC enhances heterogeneously, while type 1 PRCC enhanced homogeneously on DCE-CT. Xp11.2 RCC has clearer boundary and more common cystic components than those of type 2 PRCC. Differentiating Xp11.2 RCC with different subtypes of PRCC preoperatively will be beneficial for treatment planning.

Abbreviations

ANOVA:	Analysis of variance
AUC:	Area under ROC curve
CCRCC:	Clear cell renal cell carcinoma
CT:	Computed tomography
DCE-CT:	Dynamic contrast-enhanced computed tomography
FISH:	Fluorescence in situ hybridization
HU:	Hounsfield unit
IHC:	Immunohistochemical
MRI:	Magnetic resonance imaging
PET:	Positron emission tomography
PRCC:	Papillary renal cell carcinoma
RCC:	Renal cell carcinoma
ROC:	Receiver operating characteristic
ROI:	Region of interest
TFE3:	Transcription factor E3
Xp11.2 RCC:	Renal cell carcinoma associated with Xp11.2 translocation/TFE3 gene fusions.

Conflict of Interests

All the authors have no conflict of interests to disclose.

Authors' Contribution

Jian He, Kefeng Zhou, Weidong Gan, Zhengyang Zhou, Bin Zhu, Gutian Zhang, Xiaogong Li, and Hongqian Guo participated in collection and/or assembly of data. Jian He, Kefeng Zhou, Weidong Gan, Zhengyang Zhou, Bin Zhu, Gutian Zhang, Xiaogong Li, Hongqian Guo, and Tian Liu participated in data analysis and interpretation. Jian He, Kefeng Zhou, Weidong Gan, Zhengyang Zhou, and Tian

Liu participated in paper writing. Bin Zhu, Gutian Zhang, Xiaogong Li, and Hongqian Guo participated in statistical analysis. Jian He, Kefeng Zhou, Tian Liu, Weidong Gan, and Zhengyang Zhou participated in conception and design, financial support, and final approval of the paper. All authors read and approved the paper. Jian He and Kefeng Zhou contributed equally to this work.

Acknowledgments

This work was supported by the National Natural Science Foundation of China (ID 81572512, 81501441), the Natural Science Foundation of Jiangsu Province (ID BK20131281, BK20150109), Jiangsu Province Health and Family Planning Commission Youth Scientific Research Project (ID Q201508), and Nanjing City Young Health Personnel Training Project (third level; ID: QRX11178). The opinions, results, and conclusions reported in this paper are those of the authors and are independent from the funding sources.

References

- [1] A. Lopez-Beltran, M. Scarpelli, R. Montironi, and Z. Kirkali, "2004 WHO classification of the renal tumors of the adults," *European Urology*, vol. 49, no. 5, pp. 798–805, 2006.
- [2] N. Kuroda, S. Mikami, C.-C. Pan et al., "Review of renal carcinoma associated with Xp11.2 translocations/TFE3 gene fusions with focus on pathological aspect," *Histology and Histopathology*, vol. 27, no. 2, pp. 133–140, 2012.
- [3] Q. Rao, B. Guan, and X.-J. Zhou, "Xp11.2 translocation renal cell carcinomas have a poorer prognosis than non-xp11.2 translocation carcinomas in children and young adults: a meta-analysis," *International Journal of Surgical Pathology*, vol. 18, no. 6, pp. 458–464, 2010.
- [4] T. T. Dang, E. Ziv, S. Weinstein, M. V. Meng, Z. Wang, and F. V. Coakley, "Computed tomography and magnetic resonance imaging of adult renal cell carcinoma associated with Xp11.2 translocation," *Journal of Computer Assisted Tomography*, vol. 36, no. 6, pp. 669–674, 2012.
- [5] H. J. Koo, H. J. Choi, M.-K. Kim, and K.-S. Cho, "Radiologic-pathologic correlation of renal cell carcinoma associated with xp11.2 translocation," *Acta Radiologica*, vol. 54, no. 7, pp. 827–834, 2013.
- [6] Q.-Q. Zhu, Z.-Q. Wang, W.-R. Zhu, W.-X. Chen, and J.-T. Wu, "The multislice CT findings of renal carcinoma associated with XP11.2 translocation/TFE gene fusion and collecting duct carcinoma," *Acta Radiologica*, vol. 54, no. 3, pp. 355–362, 2013.
- [7] K. Liu, P. Xie, W. Peng, and Z. Zhou, "Renal carcinomas associated with Xp11.2 translocations/TFE3 gene fusions: findings on MRI and computed tomography imaging," *Journal of Magnetic Resonance Imaging*, vol. 40, no. 2, pp. 440–447, 2014.
- [8] W. Wang, J. Ding, Y. Li et al., "Magnetic resonance imaging and computed tomography characteristics of renal cell carcinoma associated with Xp11.2 translocation/TFE3 gene fusion," *PLoS ONE*, vol. 9, no. 6, Article ID e99990, 2014.
- [9] J. He, Y. Huan, Q. Qiao, J. Zhang, and J. S. Zhang, "Renal carcinomas associated with Xp11.2 translocations: are CT findings suggestive of the diagnosis?" *Clinical Radiology*, vol. 69, no. 1, pp. 45–51, 2014.
- [10] J. He, W. Gan, S. Liu, K. Zhou, G. Zhang, and H. Guo, "Dynamic computed tomographic features of adult renal cell carcinoma

- associated with Xp11.2 translocation/TFE3 gene fusions: comparison with clear cell renal cell carcinoma," *Journal of Computer Assisted Tomography*, vol. 39, no. 5, pp. 730–736, 2015.
- [11] B. Delahunt and J. N. Eble, "Papillary renal cell carcinoma: a clinicopathologic and immunohistochemical study of 105 tumors," *Modern Pathology*, vol. 10, no. 6, pp. 537–544, 1997.
- [12] J. R. Young, D. Margolis, S. Sauk, A. J. Pantuck, J. Sayre, and S. S. Raman, "Clear cell renal cell carcinoma: discrimination from other renal cell carcinoma subtypes and oncocytoma at multiphasic multidetector CT," *Radiology*, vol. 267, no. 2, pp. 444–453, 2013.
- [13] H. Kato, M. Kanematsu, S. Yokoi et al., "Renal cell carcinoma associated with Xp11.2 translocation/TFE3 gene fusion: radiological findings mimicking papillary subtype," *Journal of Magnetic Resonance Imaging*, vol. 33, no. 1, pp. 217–220, 2011.
- [14] J. Zhang, R. A. Lefkowitz, N. M. Ishill et al., "Solid renal cortical tumors: differentiation with CT," *Radiology*, vol. 244, no. 2, pp. 494–504, 2007.
- [15] P. Bata, J. Gyebnar, D. L. Tarnoki et al., "Clear cell renal cell carcinoma and papillary renal cell carcinoma: differentiation of distinct histological types with multiphase CT," *Diagnostic and Interventional Radiology*, vol. 19, no. 5, pp. 387–392, 2013.
- [16] T. Yamada, M. Endo, M. Tsuboi et al., "Differentiation of pathologic subtypes of papillary renal cell carcinoma on CT," *American Journal of Roentgenology*, vol. 191, no. 5, pp. 1559–1563, 2008.
- [17] H. A. Alshenawy, "Immunohistochemical panel for differentiating renal cell carcinoma with clear and papillary features," *Pathology & Oncology Research*, vol. 21, no. 4, pp. 893–899, 2015.
- [18] A. Marhuenda, M. I. Martín, C. Deltoro, J. Santos, and J. Rubio Briones, "Radiologic evaluation of small renal masses (I): pretreatment management," *Advances in Urology*, vol. 2008, Article ID 415848, 16 pages, 2008.
- [19] R. Vikram, C. S. Ng, P. Tamboli et al., "Papillary renal cell carcinoma: radiologic-pathologic correlation and spectrum of disease," *Radiographics*, vol. 29, no. 3, pp. 741–757, 2009.
- [20] M. J. Leveridge, P. J. Bostrom, G. Koulouris, A. Finelli, and N. Lawrentschuk, "Imaging renal cell carcinoma with ultrasonography, CT and MRI," *Nature Reviews Urology*, vol. 7, no. 6, pp. 311–325, 2010.
- [21] J. H. Mydlo, R. Weinstein, R. Misseri, C. Axiotis, and W. Thelmo, "Radiologic, pathologic and molecular attributes of two types of papillary renal adenocarcinomas," *Scandinavian Journal of Urology and Nephrology*, vol. 35, no. 4, pp. 262–269, 2001.
- [22] K. Tsuda, T. Kinouchi, G. Tanikawa et al., "Imaging characteristics of papillary renal cell carcinoma by computed tomography scan and magnetic resonance imaging," *International Journal of Urology*, vol. 12, no. 9, pp. 795–800, 2005.
- [23] S. R. Prasad, P. A. Humphrey, J. R. Catena et al., "Common and uncommon histologic subtypes of renal cell carcinoma: imaging spectrum with pathologic correlation," *Radiographics*, vol. 26, no. 6, pp. 1795–1810, 2006.
- [24] A. B. Rosenkrantz, N. Hindman, E. F. Fitzgerald, B. E. Niver, J. Melamed, and J. S. Babb, "MRI features of renal oncocytoma and chromophobe renal cell carcinoma," *American Journal of Roentgenology*, vol. 195, no. 6, pp. W421–W427, 2010.
- [25] T. Klatte, B. Streubel, F. Wrba et al., "Renal cell carcinoma associated with transcription factor E3 expression and Xp11.2 translocation: incidence, characteristics, and prognosis," *American Journal of Clinical Pathology*, vol. 137, no. 5, pp. 761–768, 2012.
- [26] P. M. Kulkarni, N. Rey-Villamizar, A. Merouane et al., "Algorithms for improved 3-D reconstruction of live mammalian embryo vasculature from optical coherence tomography data," *Quantitative Imaging in Medicine and Surgery*, vol. 5, no. 1, pp. 125–135, 2015.
- [27] T. Ma, X. Qian, C. T. Chiu et al., "High-resolution harmonic motion imaging (HR-HMI) for tissue biomechanical property characterization," *Quantitative Imaging in Medicine and Surgery*, vol. 5, no. 1, pp. 108–117, 2015.

Review Article

Molecular Imaging with MRI: Potential Application in Pancreatic Cancer

Chen Chen, Chang Qiang Wu, Tian Wu Chen, Meng Yue Tang, and Xiao Ming Zhang

Sichuan Key Laboratory of Medical Imaging, Department of Radiology, Affiliated Hospital of North Sichuan Medical College, Wenhua Road 63, Nanchong, Sichuan 637000, China

Correspondence should be addressed to Xiao Ming Zhang; cjr.zhxm@vip.163.com

Received 24 August 2015; Revised 2 October 2015; Accepted 4 October 2015

Academic Editor: Weibo Cai

Copyright © 2015 Chen Chen et al. This is an open access article distributed under the Creative Commons Attribution License, which permits unrestricted use, distribution, and reproduction in any medium, provided the original work is properly cited.

Despite the variety of approaches that have been improved to achieve a good understanding of pancreatic cancer (PC), the prognosis of PC remains poor, and the survival rates are dismal. The lack of early detection and effective interventions is the main reason. Therefore, considerable ongoing efforts aimed at identifying early PC are currently being pursued using a variety of methods. In recent years, the development of molecular imaging has made the specific targeting of PC in the early stage possible. Molecular imaging seeks to directly visualize, characterize, and measure biological processes at the molecular and cellular levels. Among different imaging technologies, the magnetic resonance (MR) molecular imaging has potential in this regard because it facilitates noninvasive, target-specific imaging of PC. This topic is reviewed in terms of the contrast agents for MR molecular imaging, the biomarkers related to PC, targeted molecular probes for MRI, and the application of MRI in the diagnosis of PC.

1. Introduction

Pancreatic cancer (PC) is a serious threat to human health, due to malignant tumors with concealed onset, rapid development, and poor prognosis. PC is the fourth leading cause of death among all cancers in the USA, with a dismal 5-year survival rate of less than 5% [1]. These dismal outcomes can be attributed to the lack of early diagnoses and the inability to detect precancerous lesions [2]. Therefore, the detection and diagnosis of PC in the early stage are extremely urgent. At present, the methods used to diagnosis PC include tumor marker detection and imaging diagnosis. The traditional tumor markers that have been used for the early diagnosis of PC have high sensitivity in clinical use, but the specificities are not high, and these markers are thus prone to false positives [3]. Computed tomography (CT) and magnetic resonance imaging (MRI) have been used to diagnose and stage the majority of PCs with tumor detection limits of 5–8 mm, when the earliest precursor lesions are in the microscopic range [4, 5]. Nevertheless, the development of molecular imaging technology enabled the effective resolution of this difficulty. Molecular imaging is a medical imaging technique that combines molecular

biology, chemistry, material science, radiation medicine, and computer science and has created a profile for the diagnosis and treatment of this disease that exhibits wide application prospects from the bench to the clinic [6–9]. In contrast with traditional imaging techniques that are primarily based on gross anatomy structures, molecular imaging can identify pathological changes at the molecular and cellular level, determine the qualitative properties of the diseases, enable objective monitoring of the efficacy of treatment, and predict disease development. Molecular imaging research primarily includes two aspects, the first of which is the choice of imaging equipment. Molecular MR imaging has become a novel technique for assessing specific cellular or subcellular events and is becoming one of the core integrative technologies in biomedicine because many of the parameters that are used to produce contrast, such as the spin-lattice relaxation (T_1) and spin-spin relaxation (T_2) times, are dependent on the local chemical structure of the molecules being imaged [10]. In most situations, near-infrared optical fluorescence (NIRF) imaging is combined with MRI, which enables the direct visualization of the enriched area of the tumor in the visible range [11]. The second aspect is the preparation of the targeting probes of the equipment. Molecules or cells with

reporter genes or imaging agent are introduced into the body and used to observe changes at the molecular and cellular levels based on the identifying agent [12, 13]. The present study reviews the contrast agents for MR molecular imaging, related biomarkers for PC, targeted molecular probes for MRI, and their applications in the diagnosis of PC.

2. Contrast Agents for MR Molecular Imaging

At present, there are two main types of MR contrast agent. The first are Gd³⁺ + paramagnetic compounds, which can produce T_1 -weighted imaging (T_1 WI) positive contrasts. Currently, small gadolinium-containing contrast agents, such as gadopentetate dimeglumine (Gd-DTPA, Magnevist), are among the most widely used in MR molecular imaging. Because Gd-DTPA has a low molecular weight, after injection into the body, it can travel through the capillary into the intercellular space and be distributed nonspecifically. Because Gd-DTPA cannot pass through the blood-brain barrier, the contrast agent concentration achieves equilibrium rapidly in normal tissues and lesion areas [14]. The known adverse reactions to the use of DTPA include nausea, urticaria, and taste disorder. Among these reactions, the most serious is nephrogenic systemic fibrosis (NSF). This type of adverse reaction results when macrophages engulf free gadolinium and subsequently release cytokines that promote fibrosis or when gadolinium complexes are engulfed by peripheral blood mononuclear cells, which then release proinflammatory cytokines that eventually lead to tissue fibrosis [15, 16].

Another type of contrast agent is superparamagnetic iron oxide (SPIO) nanoparticles, such as Fe₂O₃ and Fe₃O₄, which mainly produce T_2 -weighted imaging (T_2 WI) with negative contrast. Compared with the Gd-DTPA, SPIO elicits lower contrast medium toxicity because the SPIO nanoparticles that are released from dying cells can be degraded in the normal iron recycling pathways [17]. Simultaneously, SPIO improves the biocompatibility and the blood retention time and increases the contrast intensity [18]. To our knowledge, the value of SPIO for targeted imaging lies in the fact that the SPIO surface can be packaged and subsequently combined with appropriate targeting ligands. In recent years, some scholars [19–23] have studied the design scheme and biological characteristics of the molecular imaging application of SPIO and believe that to ensure that SPIO has hydrophobic and certain toxic properties and is uniformly distributed in the ferrofluid the selection of the surface package material is critical. The material used for the surface coating of the magnetic particles not only must be nontoxic and biocompatible but also must allow the targetable delivery with particle localization within a specific area. In recent studies, inorganic silicon materials [24–27], polyacrylic acid [28, 29], dextran [30, 31], dopamine [32], deferoxamine [33–35], and other organic polymers have been used for the surface packaging of SPIO.

Manganese is a nonlanthanide paramagnetic metal that possesses good relaxation enhancement effects, due to the five unpaired electrons of bivalent manganese. Because manganese not only plays essential roles in cell biology but also is minimally toxic in vivo, large doses can be used in MRI.

Manganese-based contrast agents include a variety of forms, such as small organic chelates [36], macromolecule chelates [37], and oxide nanoparticles.

In general, after the contrast agent is packaged, appropriate targeting ligands need to be selected based on the research target or a specific type of cell. Pancreatic cancer is well known to express a variety of biomarkers; therefore, increasing the sensitivity and specificity of markers and their corresponding ligands is the main goal of research in pancreatic cancer-targeted imaging.

3. Related Biomarkers for PC

The increasing study of pancreatic cancer has established that pancreatic cancer is a highly heterogeneous disease involving extremely complex tumor microenvironments that express a variety of antigens and receptors within the tumor cells and surrounding stroma. These related proteins and highly expressed genes in malignant tumors are the design foundation of functionally targeted nanoparticles.

3.1. Related Serum Biomarkers for PC. Among the numerous biomarkers that have been tested for PC detection, serum CA19-9 is the most commonly used. CA19-9 is a type of carbohydrate antigen that exists at the cell surface and is associated with a variety of digestive tract tumors. However, CA19-9 lacks the sensitivity needed to detect early-stage PC [38] and to monitor responses to therapy, because of its poor sensitivity (41%–86%) and specificity (33%–100%) [39]. Furthermore, CA19-9 can also arise in some benign lesions, such as bile duct inflammation, chronic pancreatitis, and other gastrointestinal cancers [40], and tends to arise only after tumor metastasis [3]. Kim et al. [41] used CA19-9 to screen for PC in 70,940 asymptomatic patients. Among the 1,063 patients with elevated levels, only 4 had pancreas cancer, and only 2 had resectable disease. Therefore, in some special conditions, the accuracy and specificity of the use of CA19-9 as a target are also controversial views.

Muc-1 is a transmembrane mucin glycoprotein and is another biomarker that is associated with the most invasive forms of PC [42]. Muc-1 levels are elevated in the majority of patients with PC, and Muc-1 plays a key role that affects oncogenesis and the motility, metastasis, metabolism, and growth of cancer cells [43, 44]. Gold et al. [45] proved that Muc-1 is overexpressed in PC both in the cytoplasm and in the cell membrane, compared with most chronic pancreatitis tissues and normal pancreatic tissues in which Muc-1 is only expressed in the cell membrane with no cytoplasmic expression. Thus, there is a direct relationship between high invasiveness and poor PC prognosis [46, 47]. The PAM4 antibody against Muc-1 is more specific for pancreatic cancer than antibodies to the other Muc-1 antigens that are observed in other tumors. In a recent study [48], the authors found that the PAM4-reactive Muc-1 epitope was not detected in the normal pancreas but was expressed in 87% (48 of 55) of invasive pancreatic adenocarcinomas. Additionally, Muc-1 acts as a master regulator of the metabolic program that can also help tumor cells survive and proliferate in hypoxic environments [43]. Many studies [42, 49–51] have

demonstrated that Muc-1 can be used as an ideal target in the diagnosis and treatment of pancreatic cancer.

Survivin is a newly identified member of the apoptosis inhibitory protein family and has highly specific tissue distribution and powerful antiapoptotic function. Ren et al. [52] analyzed the serum levels of survivin in patients with pancreatic ductal adenocarcinoma (PDAC) ($n = 80$) and age-matched healthy volunteers ($n = 80$) and found that the serum survivin concentrations were significantly elevated in the sera of PDAC patients compared with healthy sera ($p = 0$). Dong et al. [53] performed a similar study and reached similar conclusions. Thus, the expression of the survivin protein is closely related to the biological characteristics of pancreatic tissue.

Currently, the receptors known to be related to PC mainly consist of chemokine epidermal growth factor receptor 4 (CXCR-4), vascular endothelial growth factor (VEGF), epidermal growth factor receptor (EGFR), and urokinase plasminogen activator receptor (UPAR).

CXCR-4 is the specific receptor of chemotactic factor CXCL12. Many lines of evidence indicate that the CXCL12/CXCR-4 biological axis plays an important role in the proliferation, invasion, and metastasis of PC [54–56] and is a suitable target for therapy and imaging [55, 57, 58].

EGFR is a member of the HER family, which is particularly highly expressed in malignant tumors with epithelial tissue sources. In pancreatic cancer tissue, the expressions of the differentiation of different statuses are also different.

Currently, VEGF is the most potent and specific angiogenic factor that directly affects vascular endothelial cells. In most situations, VEGFR is expressed in new vascular endothelial cells within the tumor. PC is associated with a lack of blood supply. Nonetheless, VEGFR has been found not only in blood vessels but also in blood vessel cells [59]. Furthermore, Karayiannakis et al. [60] reported that PC patients have significantly higher VEGF levels than healthy controls and that serum VEGF levels are significantly associated with disease stage and the presence of both lymph node and distant metastases.

UPAR is a versatile signaling orchestrator of cellular differentiation, proliferation, and migration [61]. Researchers recently discovered that UPAR is expressed in PC tissues at rates not less than 86%, whereas UPAR is not found in pancreatic tissues obtained from healthy subjects or patients with chronic pancreatitis [62–64]. A recent study revealed that, among the 27 genes that are commonly used in PC tissues, the level of UPAR exhibited the highest accuracy in the differential diagnosis of pancreatic ductal carcinoma and chronic pancreatitis [64]. Additionally, desmoplasia and hypovascularity are the pathological hallmarks of pancreatic tumors [65]. One study found that UPAR is highly expressed in tumor and stroma cells [66, 67]. Thus, UPAR may have very broad application prospects in PC molecular imaging research.

Additionally, some protein markers have newly been discovered. CEACAM-1 [68, 69], CEACAM-6 [70–72], CD133 [73–75], S100A4 [76–80], and midkine [81] have been shown to be biomarkers that are also expressed in PC and are significantly associated with invasion and metastasis in PC

and PC prognosis. Therefore, these markers also have the potential to become the imaging and therapy targets for PC.

3.2. Related miRNA for PC. Currently, more than 20 miRNAs have been proven to be associated with PC [82]. miRNA-21 has been considered to be the miRNA most closely related to cell proliferation, metastatic ability, and poor overall survival [83–86]. Moreover, miRNA-21 has been demonstrated to be significantly overexpressed in both PC cell lines and tissues relative to normal pancreatic tissue [87]. Additionally, some other miRNAs (130b [88, 89], 196a [90, 91], 92a [92, 93], 198 [94], 221 [95, 96], 23b [97], and 29a [98]) have also been shown to have important roles in PC. In a recent study, Nagano et al. [99] established 7 miRNA-based biomarker models (miR-20a, miR-21, miR-24, miR-25, miR-99a, miR-185, and miR-191) for PDAC diagnosis and found that these biomarkers exhibited high sensitivity and specificity in the discrimination of PC and chronic pancreatitis patients (AUC = 0.993). Therefore, the identification of the miRNAs suggests that they can also be used as potential tools for the screening of early-stage PC.

3.3. Genes Related to PC. Currently, many differentially expressed genes related to signal transduction are known to play roles in the development of PC that include the stimulation of protooncogenes, such as K-ras [100, 101], HER-2/neu [102, 103], and BRCA [104, 105], and the inactivation of tumor suppressor genes, such as SMAD4 [106], APC [107], P53 [108, 109], and CDKN2A [110, 111]. The associated genes that have been identified as being involved in these processes have potential as imaging markers for PC.

Although, at present, a wide variety of tumor markers have been associated with PC, these markers cannot fully meet the requirements of imaging targets of PC, primarily because the sensitivity, specificity, and expression quantities are not homogenous. Nonetheless, additional exploration and in-depth study are needed to select the appropriate molecular imaging targets for PC.

4. MR Target Molecular Imaging for PC

In the MR molecular imaging of PC, the key step is the preparation of the appropriate targeted molecular probes for MRI. First, an MRI molecular probe must have high specificity which can distinguish the PC from the surrounding tissues. Second, an MRI molecular probe must exhibit a high sensitivity for identifying the subtle changes in the early stage of PC (Figure 1). Additionally, an MRI molecular probe must also exhibit excellent biological compatibility that can overcome a variety of physiological barriers in the body and minimize side effects to the greatest possible extent (Figure 2). Thus, the selection of imaging probes with the above-mentioned characteristics is the primary focus and most difficult aspect of the research field of MR target molecular imaging.

4.1. Molecular Imaging Probes Targeting the Muc Protein. In 2006, Medarova et al. [112] prepared a dual-modality imaging

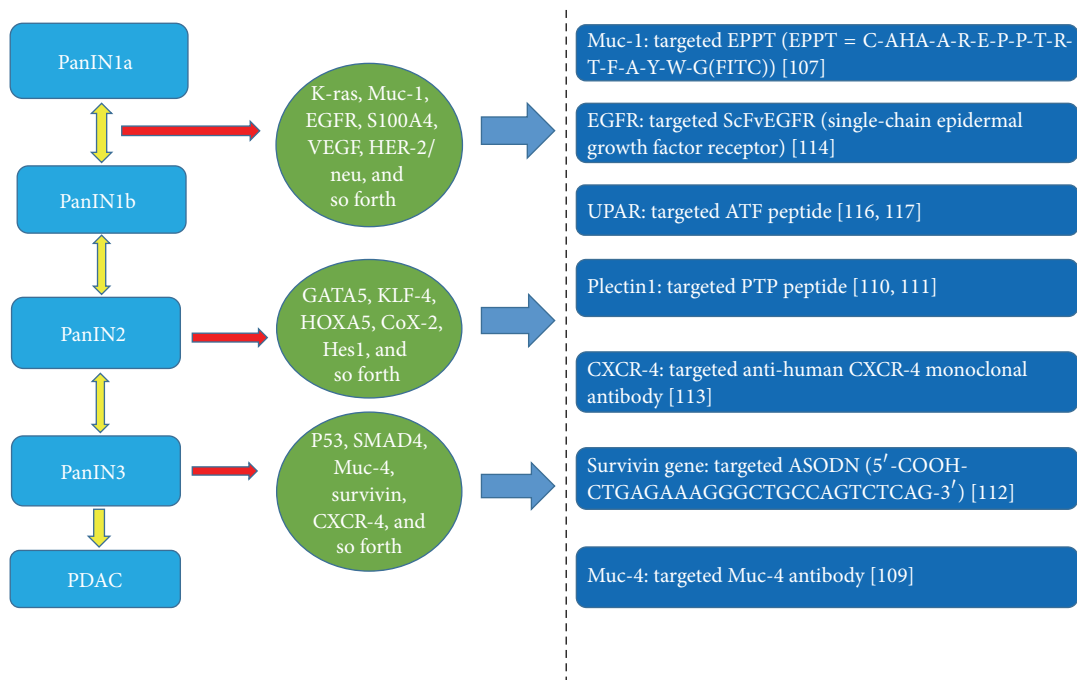


FIGURE 1: As PC progresses from PanINs to PDAC, each stage is well characterized by multiple molecular alternations. However, the identification of specific lesions using unique molecular markers as early as possible through molecular imaging will lead to the early detection of this deadly disease. The right illustrates the target materials that correspond to different PC biomarkers.

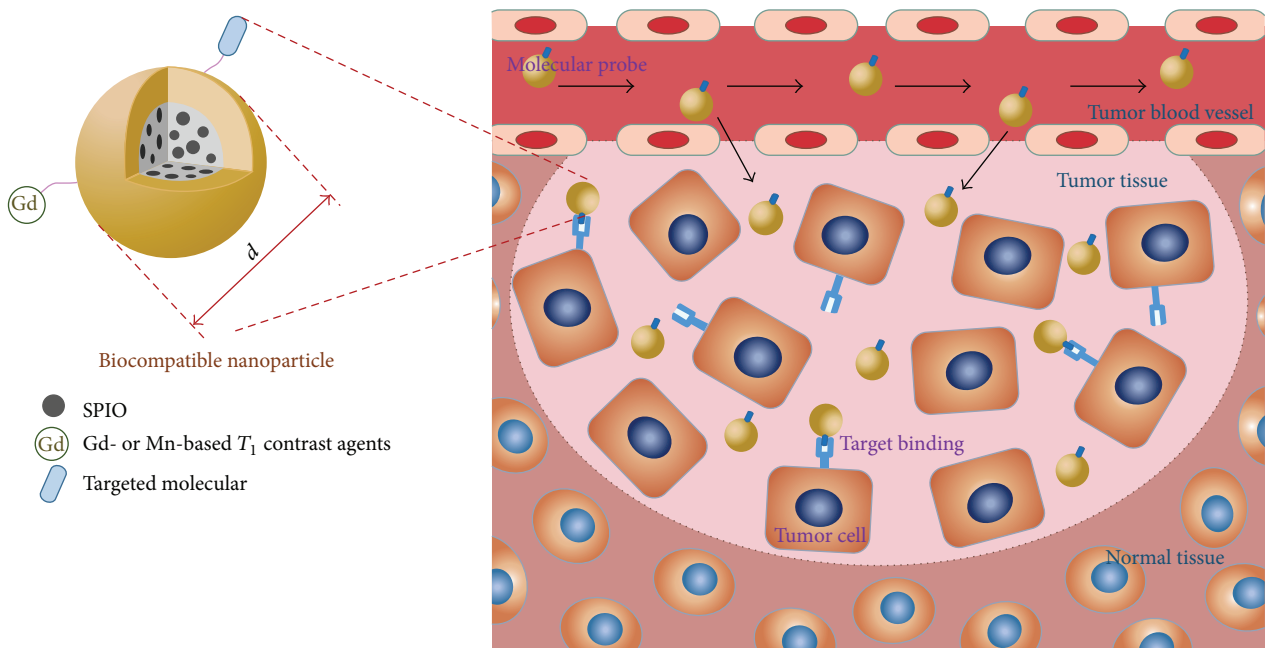


FIGURE 2: Targeted molecular MRI probes for the early diagnosis of pancreatic cancer (PC). Superparamagnetic iron oxide (SPIO) or paramagnetic metal complexes (Gd- or Mn-based T_1 contrast agents) are loaded in biocompatible nanoparticles that molecularly target the surface and are suitable at the nanoscale levels ($d = 10\sim 100$ nm). The nanocomposites can reach the tumor tissue through tumor blood vessel clearance and target and bind tumor cells to alter the signal intensity of the tumor tissue on MRI.

probe that specifically targeted the underglycosylated mucin-1 tumor-specific antigen (uMuc-1). This probe is comprised of cross-linked superparamagnetic iron oxide (CLIO) nanoparticles and peptides (EPPT) that specifically recognize uMuc-1, which is attached to the nanoparticles' dextran coats. After the injection of CLIO-EPPT in orthotopic pancreatic cancer mice, the average T_2 relaxation rate of the PC tissues significantly decreased, whereas that of the muscle tissues was unaffected. These authors concluded that the CLIO-EPPT contrast agent could be targeted to PC tissues and result in dramatic signal changes, and related iron oxides are already in clinical use [113]. In the mucin family, another membrane-bound mucin gene, Muc-4, is expressed at a high level in PC and has not yet been found in chronic pancreatitis or normal pancreatic tissues [114]. Wu et al. [115] developed the Muc-4-targeting SPIO contrast agent MnMEIO-silane- NH_2 -(Muc-4)-mPEG NPs, which exhibited better negative contrast enhancement and did not interfere with the MR images. In animal experiments, a T_2 -weighted MR study revealed that this novel contrast agent could specifically and effectively target mucin-4-expressing pancreatic tumors in nude mice. In the T_2 -weighted imaging study by these authors, they demonstrated that the intensity of negative contrast enhancement was marked in the HPAC tumor cells in which Muc-4 was expressed at a high level compared with the Panc-1 tumor cells, which exhibited significantly lower negative contrast enhancement due to lower Muc-4 expression.

4.2. The Molecular Imaging Probe Targeting Plectin1. Plectin1 exhibits distinct cytoplasmic and nuclear localization in normal fibroblasts but exhibits aberrant expression on the cell membrane in pancreatic ductal adenocarcinoma (PDAC). In one study [116], Plectin1 targeted peptides (PTP) were conjugated to the surface of magnetofluorescent nanoparticles, and the results revealed that the targeted imaging agent PTP-NP permitted imaging of PDAC against the background of normal and ductal metaplasia of the pancreas. In intravital MRI, these nanoparticles enabled the detection of small PDACs and precursor lesions in engineered mouse models that exhibited a reduction in MR signal in the PDAC regions. Furthermore, the results were confirmed by histological analysis, and fluorescence microscopy indicated that the loss of signal associated with PTP-NP uptake occurred primarily in the regions of PDAC and not in the normal regions or regions of ductal metaplasia. In another study, Wang et al. [117] developed the novel targeted imaging contrast agent dyeBSA-SPIONs-mAb. Panc-1 cell MR scanning was performed following incubation with Plectin1-targeted dyeBSA-SPIONs-mAb. This study demonstrated that a significant reduction in T_2 reduction occurred compared with the nontargeted dyeBSA-SPIONs group at the same concentration. These studies that reported the development of a specific imaging probe and the discovery of Plectin1 as a novel biomarker may have clinical utility in the diagnosis of PDAC in humans.

4.3. The Molecular Imaging Probe Targeting the Survivin Gene. More recently, the survivin gene, which is a potential

marker of PC, has been regarded as a targeting gene, and chitosan-coated magnetic iron oxide particles (MNPs) have been regarded as imaging probes for the detection of PC [19]. Chitosan-coated MNPs (cs@MNPs) and antisense oligodeoxynucleotides of the survivin gene were conjugated to MNPs to produce Sur-MNPs. The magnetic resonance signal intensities of the pancreatic cells labeled with cs@MNPs, MNPs, and Sur-MNPs were compared on T_2 -weighted images. Ultimately, these authors found that the Sur-MNPs exhibited a proper size, high stability, not cytotoxicity, and good dispersion compared with the others. More importantly, the Sur-MNPs did not accumulate in healthy lung fibroblast cells (in the control group) but were taken up by BxPC-3 cells (expressing the survivin gene) and exhibited low signal due to the T_2 -weighted effect. Thus, our research not only demonstrated that the survivin gene of PC was detectable by Sur-MNPs but also indicated that Sur-MNPs may become good negative molecular contrast agents in the diagnosis of PC. Further studies evaluating the selective uptake of Sur-MNPs in PC xenografts in vivo are extremely urgent.

4.4. The Molecular Imaging Probe Targeting CXCR-4. In 2012, He et al. [118] reported a study of the anti-CXCR-4 monoclonal antibody conjugated to ultrasmall superparamagnetic iron oxide nanoparticles (CXCR-4-USPIO) in an application of MR molecular imaging of PC cells. The results indicated that the CXCR-4-USPIO group not only exhibited lower T_2 values compared with the BSA-USPIO group but also exhibited a high affinity with the PC cells according to the MR imaging. Additionally, the T_2 enhancement ratio and ΔR^2 values of the CXCR-4-USPIO nanoparticles were useful for semiquantitatively assessing the cellular CXCR-4 expression levels. However, the defect of this study was the lack of an orthotopic human pancreatic cancer xenograft animal model to evaluate the in vivo contrast enhancement imaging efficacy of the CXCR-4-USPIO probe, and this issue will be our research direction in the future.

4.5. The Molecular Imaging Probe Targeting EGFR. EGFR is a member of the HER family. In a recent study [119], single-chain epidermal growth factor receptor antibody-(ScFvEGFR-) conjugated quantum dots (QDs) or magnetic iron oxide (IO) nanoparticles were used for tumor target imaging in vivo. This study revealed that the uptake of targeted IO nanoparticles selectively occurred in PC cells, a finding confirmed by positive Prussian blue staining results, whereas the normal pancreatic ductal epithelial cells and other normal cell types were negative for this staining. In an in vivo experiment, after the EGFR-targeted MRI of human pancreatic cancer orthotopically implanted into the pancreas of nude mice, it was shown that the ScFvEGFR-IO nanoparticles selectively accumulated within the pancreatic tumors in T_2 -weighted fast spin echo imaging, as evidenced by a decrease in the MRI signal in the area of the tumor. In a similar study [120], Yang et al. conjugated ScFvEGFR fragments with magnetic iron oxide (IO) NPs to obtain ScFvEGFR-IOs and investigated their binding and internalization by EGFR-expressing cancer cells. Using the MRI

technique, these investigators demonstrated that ScFvEGFR-IO specifically bound to and was internalized by EGFR-expressing cancer cells. Additionally, the use of ScFvEGFR-IO as a molecular imaging agent was demonstrated with MRI in an orthotopic human pancreatic cancer mouse xenografted model.

4.6. The Molecular Imaging Probe Targeting UPAR. More recently, attempts have been made to identify potential imaging probes for the active targeting of the pancreatic stroma. UPAR is a biomarker of PC that is highly expressed in tumor and stroma cells, and the active retention of these nanoparticles is increased in many target cells in tumor masses. Yang et al. [121] designed a dual mode of molecularly targeted agents that involved Fe₂O₃ nanoparticles conjugated with near-infrared dyes and uPA at the same times. The MR imaging results indicate that the systemic delivery of the UPAR-targeted nanoparticles led to their selective accumulation in the orthotopically xenografted human PC tumors in nude mice, and MRI signal reduction was detected in the UPAR-expressing cells. The probe binds to and is subsequently internalized by UPAR-expressing tumor cells and tumor-associated stroma cells. In 2013, Lee et al. [122] engineered urokinase plasminogen activator receptor- (UPAR-) targeted magnetic iron oxide nanoparticles (IONPs) that carry the chemotherapy drug gemcitabine (Gem) for targeted delivery into UPAR-expressing tumor and stroma cells in MRI. The results revealed that UPAR can act not only as the imaging probe but also as the therapy carrier for PC.

4.7. The Molecular Imaging Probe Targeting Some Antibodies and Receptors. Pirollo et al. [123] designed a tumor-targeting, liposomal nanodelivery platform to improve the early detection of tumors with MRI. These authors used Gd-DTPA in an anti-transferring receptor single-chain antibody (TfRscFv) liposomal complex and injected this complex into an animal model of PC. The results revealed that this compound significantly increased the signal of the lesion area and improved the contrast between the lesion and normal tissues, which aided the localization and qualitative diagnosis of PC. In 2006, Montet et al. [124] designed a nanoparticle-conjugate targeted to the bombesin (BN) receptors present on the normal acinar cells of the pancreas. In this study, the authors found that the BN-CLIO nanoparticles decreased the T₂ signal of the normal pancreas and enhanced the ability to visualize the tumor on MRI in a model of pancreatic cancer. Additionally, some contrast agents, such as the GO-IONP, exhibited powerful abilities for the dual-modality mapping of the regional lymphatic system by MRI [125].

5. Summary

MR molecular imaging appears to be a promising imaging modality for the early detection of PC. This imaging modality also facilitates the study of the pathological changes associated with PC at the molecular and cellular levels. Regarding this topic, we summarize the applications of MR molecular imaging in the diagnosis of PC. As a noninvasive, target-specific imaging modality, MR molecular imaging can not

only improve the early detection of PC but also be modified for the targeted selectivity of tumor cells to increase imaging resolution. At present, many studies have conducted in vivo experiments and provided evidence of the feasibility of these targeted contrast agents. However, there are still some studies that have not conducted in vivo experiments. Therefore, this issue is worthy of extensive research because these issues have great significance for targeted molecular imaging and therapy of PC. Currently, the research related to the MR molecular imaging of PC is still in its infancy phase; however, in view of the existing achievement, we believe that these studies will have a far-reaching influence on the diagnosis and treatment of PC.

Conflict of Interests

The authors declare that they have no conflict of interests related to the publication of this paper.

Acknowledgment

This work was supported by the National Nature Science Foundation of China, no. 81271643.

References

- [1] C. Y. Wu, Y. Pu, G. Liu, Y. Shao, Q. S. Ma, and X. M. Zhang, "MR imaging of human pancreatic cancer xenograft labeled with superparamagnetic iron oxide in nude mice," *Contrast Media and Molecular Imaging*, vol. 7, no. 1, pp. 51–58, 2012.
- [2] D. E. Misek, T. H. Patwa, D. M. Lubman, and D. M. Simeone, "Early detection and biomarkers in pancreatic cancer," *JNCCN Journal of the National Comprehensive Cancer Network*, vol. 5, no. 10, pp. 1034–1041, 2007.
- [3] J. L. Buxbaum and M. A. Eloubeidi, "Molecular and clinical markers of pancreas cancer," *Journal of the Pancreas*, vol. 11, no. 6, pp. 536–544, 2010.
- [4] K. Holzapfel, C. Reiser-Erkan, A. A. Fingerle et al., "Comparison of diffusion-weighted MR imaging and multidetector-row CT in the detection of liver metastases in patients operated for pancreatic cancer," *Abdominal Imaging*, vol. 36, no. 2, pp. 179–184, 2011.
- [5] M. I. Canto, R. H. Hruban, E. K. Fishman et al., "Frequent detection of pancreatic lesions in asymptomatic high-risk individuals," *Gastroenterology*, vol. 142, no. 4, pp. 796–804, 2012.
- [6] C. Piraka and J. M. Scheiman, "New diagnostic imaging modalities for pancreatic disease," *Current Opinion in Gastroenterology*, vol. 27, no. 5, pp. 475–480, 2011.
- [7] M. Miederer, M. M. Weber, and C. Fottner, "Molecular imaging of gastroenteropancreatic neuroendocrine tumors," *Gastroenterology Clinics of North America*, vol. 39, no. 4, pp. 923–935, 2010.
- [8] G. Liu, M. Swierczewska, S. Lee, and X. Chen, "Functional nanoparticles for molecular imaging guided gene delivery," *Nano Today*, vol. 5, no. 6, pp. 524–539, 2010.
- [9] Y.-X. J. Wang, Y. Choi, Z. Chen, S. Laurent, and S. L. Gibbs, "Molecular imaging: from bench to clinic," *BioMed Research International*, vol. 2014, Article ID 357258, 3 pages, 2014.
- [10] M. Hoehn, U. Himmelreich, K. Kruttwig, and D. Wiedermann, "Molecular and cellular MR imaging: potentials and challenges

- for neurological applications," *Journal of Magnetic Resonance Imaging*, vol. 27, no. 5, pp. 941–954, 2008.
- [11] C.-H. Tung, "Colorful lighting in the operating room," *Quantitative Imaging in Medicine and Surgery*, vol. 3, no. 4, pp. 186–188, 2013.
- [12] C. Zhang, M. Jugold, E. C. Woenne et al., "Specific targeting of tumor angiogenesis by RGD-conjugated ultrasmall superparamagnetic iron oxide particles using a clinical 1.5-T magnetic resonance scanner," *Cancer Research*, vol. 67, no. 4, pp. 1555–1562, 2007.
- [13] T. A. Yap, D. Olmos, L. R. Molife, and J. S. de Bono, "Targeting the insulin-like growth factor signaling pathway: figitumumab and other novel anticancer strategies," *Expert Opinion on Investigational Drugs*, vol. 20, no. 9, pp. 1293–1304, 2011.
- [14] A. Bumb, M. W. Brechbiel, and P. Choyke, "Macromolecular and dendrimer-based magnetic resonance contrast agents," *Acta Radiologica*, vol. 51, no. 7, pp. 751–767, 2010.
- [15] T. Chopra, K. Kandukurti, S. Shah, R. Ahmed, and M. Panesar, "Understanding nephrogenic systemic fibrosis," *International Journal of Nephrology*, vol. 2012, Article ID 912189, 14 pages, 2012.
- [16] T. Chopra, K. Kandukurti, S. Shah, R. Ahmed, and M. Panesar, "Understanding nephrogenic systemic fibrosis," *International Journal of Nephrology*, vol. 2012, Article ID 912189, 4 pages, 2012.
- [17] D. A. Kedziorek and D. L. Kraitchman, "Superparamagnetic iron oxide labeling of stem cells for MRI tracking and delivery in cardiovascular disease," *Methods in Molecular Biology*, vol. 660, pp. 171–183, 2010.
- [18] N. Nasongkla, E. Bey, J. Ren et al., "Multifunctional polymeric micelles as cancer-targeted, MRI-ultrasensitive drug delivery systems," *Nano Letters*, vol. 6, no. 11, pp. 2427–2430, 2006.
- [19] M. Tong, F. Xiong, Y. Shi et al., "In vitro study of SPIO-labeled human pancreatic cancer cell line BxPC-3," *Contrast Media and Molecular Imaging*, vol. 8, no. 2, pp. 101–107, 2013.
- [20] A. Figuerola, R. Di Corato, L. Manna, and T. Pellegrino, "From iron oxide nanoparticles towards advanced iron-based inorganic materials designed for biomedical applications," *Pharmaceutical Research*, vol. 62, no. 2, pp. 126–143, 2010.
- [21] A. K. Gupta, R. R. Naregalkar, V. D. Vaidya, and M. Gupta, "Recent advances on surface engineering of magnetic iron oxide nanoparticles and their biomedical applications," *Nanomedicine*, vol. 2, no. 1, pp. 23–39, 2007.
- [22] N. K. Banda, G. Mehta, Y. Chao et al., "Mechanisms of complement activation by dextran-coated superparamagnetic iron oxide (SPIO) nanoworms in mouse versus human serum," *Particle and Fibre Toxicology*, vol. 11, no. 1, article 64, 2014.
- [23] A. S. Arbab, L. B. Wilson, P. Ashari, E. K. Jordan, B. K. Lewis, and J. A. Frank, "A model of lysosomal metabolism of dextran coated superparamagnetic iron oxide (SPIO) nanoparticles: implications for cellular magnetic resonance imaging," *NMR in Biomedicine*, vol. 18, no. 6, pp. 383–389, 2005.
- [24] Y.-H. Lien and T.-M. Wu, "Preparation and characterization of thermosensitive polymers grafted onto silica-coated iron oxide nanoparticles," *Journal of Colloid and Interface Science*, vol. 326, no. 2, pp. 517–521, 2008.
- [25] F. Momenbeik and E. Yazdani, "Application of methyl silane coated iron oxide magnetic nanoparticles for solid-phase extraction and determination of fat-soluble vitamins by high performance liquid chromatography," *Journal of AOAC International*, vol. 98, no. 2, pp. 336–344, 2015.
- [26] I. Tsiapa, E. K. Efthimiadou, E. Fragozeorgi et al., "(99m)Tc-labeled aminosilane-coated iron oxide nanoparticles for molecular imaging of $\alpha_v\beta_3$ -mediated tumor expression and feasibility for hyperthermia treatment," *Journal of Colloid and Interface Science*, vol. 433, pp. 163–175, 2014.
- [27] S. Xue, Y. Wang, M. Wang et al., "Iodinated oil-loaded, fluorescent mesoporous silica-coated iron oxide nanoparticles for magnetic resonance imaging/computed tomography/fluorescence trimodal imaging," *International Journal of Nanomedicine*, vol. 9, no. 1, pp. 2527–2538, 2014.
- [28] D. Couto, M. Freitas, G. Porto et al., "Polyacrylic acid-coated and non-coated iron oxide nanoparticles induce cytokine activation in human blood cells through TAK1, p38 MAPK and JNK pro-inflammatory pathways," *Archives of Toxicology*, vol. 89, no. 10, pp. 1759–1769, 2015.
- [29] D. Couto, R. Sousa, L. Andrade et al., "Polyacrylic acid coated and non-coated iron oxide nanoparticles are not genotoxic to human T lymphocytes," *Toxicology Letters*, vol. 234, no. 2, pp. 67–73, 2015.
- [30] R. Borny, T. Lechleitner, T. Schmiedinger et al., "Nucleophilic cross-linked, dextran coated iron oxide nanoparticles as basis for molecular imaging: synthesis, characterization, visualization and comparison with previous product," *Contrast Media and Molecular Imaging*, vol. 10, no. 1, pp. 18–27, 2015.
- [31] D. Barbaro, L. Di Bari, V. Gandin et al., "Glucose-coated superparamagnetic iron oxide nanoparticles prepared by metal vapour synthesis are electively internalized in a pancreatic adenocarcinoma cell line expressing GLUT1 transporter," *PLOS ONE*, vol. 10, no. 4, Article ID e0123159, 2015.
- [32] M. Wu, D. Zhang, Y. Zeng, L. Wu, X. Liu, and J. Liu, "Nanocluster of superparamagnetic iron oxide nanoparticles coated with poly (dopamine) for magnetic field-targeting, highly sensitive MRI and photothermal cancer therapy," *Nanotechnology*, vol. 26, no. 11, Article ID 115102, 2015.
- [33] K. C.-F. Leung, C.-H. Wong, X.-M. Zhu et al., "Ternary hybrid nanocomposites for gene delivery and magnetic resonance imaging of hepatocellular carcinoma cells," *Quantitative Imaging in Medicine and Surgery*, vol. 3, no. 6, pp. 302–307, 2013.
- [34] K. C.-F. Leung, C.-P. Chak, S.-F. Lee et al., "Enhanced cellular uptake and gene delivery of glioblastoma with deferoxamine-coated nanoparticle/plasmid DNA/branched polyethylenimine composites," *Chemical Communications*, vol. 49, no. 6, pp. 549–551, 2013.
- [35] K. C.-F. Leung, C.-P. Chak, S.-F. Lee et al., "Increased efficacies in magnetofection and gene delivery to hepatocellular carcinoma cells with ternary organic-inorganic hybrid nanocomposites," *Chemistry*, vol. 8, no. 8, pp. 1760–1764, 2013.
- [36] A. Bertin, J. Steibel, A.-I. Michou-Gallani, J.-L. Gallani, and D. Felder-Flesch, "Development of a dendritic manganese-enhanced magnetic resonance imaging (MEMRI) contrast agent: synthesis, toxicity (in vitro) and relaxivity (in vitro, in vivo) studies," *Bioconjugate Chemistry*, vol. 20, no. 4, pp. 760–767, 2009.
- [37] E. Unger, T. Fritz, De Kang Shen, and G. Wu, "Manganese-based liposomes. Comparative approaches," *Investigative Radiology*, vol. 28, no. 10, pp. 933–938, 1993.
- [38] M. Goggins, "Molecular markers of early pancreatic cancer," *Journal of Clinical Oncology*, vol. 23, no. 20, pp. 4524–4531, 2005.
- [39] S. Chakraborty, M. J. Baine, A. R. Sasson, and S. K. Batra, "Current status of molecular markers for early detection of sporadic pancreatic cancer," *Biochimica et Biophysica Acta*, vol. 1815, no. 1, pp. 44–64, 2011.

- [40] M. J. Duffy, C. Sturgeon, R. Lamerz et al., "Tumor markers in pancreatic cancer: a European Group on Tumor Markers (EGTM) status report," *Annals of Oncology*, vol. 21, no. 3, pp. 441–447, 2010.
- [41] J.-E. Kim, K. T. Lee, J. K. Lee, S. W. Paik, J. C. Rhee, and K. W. Choi, "Clinical usefulness of carbohydrate antigen 19-9 as a screening test for pancreatic cancer in an asymptomatic population," *Journal of Gastroenterology and Hepatology*, vol. 19, no. 2, pp. 182–186, 2004.
- [42] L. D. Roy, M. Sahraei, D. B. Subramani et al., "MUC1 enhances invasiveness of pancreatic cancer cells by inducing epithelial to mesenchymal transition," *Oncogene*, vol. 30, no. 12, pp. 1449–1459, 2011.
- [43] N. V. Chaika, T. Gebregiorgis, M. E. Lewallen et al., "MUC1 mucin stabilizes and activates hypoxia-inducible factor 1 alpha to regulate metabolism in pancreatic cancer," *Proceedings of the National Academy of Sciences of the United States of America*, vol. 109, no. 34, pp. 13787–13792, 2012.
- [44] M. Sahraei, L. D. Roy, J. M. Curry et al., "MUC1 regulates PDGFA expression during pancreatic cancer progression," *Oncogene*, vol. 31, no. 47, pp. 4935–4945, 2012.
- [45] D. V. Gold, D. E. Modrak, Z. Ying, T. M. Cardillo, R. M. Sharkey, and D. M. Goldenberg, "New MUC1 serum immunoassay differentiates pancreatic cancer from pancreatitis," *Journal of Clinical Oncology*, vol. 24, no. 2, pp. 252–258, 2006.
- [46] T. L. Tinder, D. B. Subramani, G. D. Basu et al., "MUC1 enhances tumor progression and contributes toward immunosuppression in a mouse model of spontaneous pancreatic adenocarcinoma," *The Journal of Immunology*, vol. 181, no. 5, pp. 3116–3125, 2008.
- [47] M. Osako, S. Yonezawa, B. Siddiki et al., "Immunohistochemical study of mucin carbohydrates and core proteins in human pancreatic tumors," *Cancer*, vol. 71, no. 7, pp. 2191–2199, 1993.
- [48] D. V. Gold, Z. Karanjawala, D. E. Modrak, D. M. Goldenberg, and R. H. Hruban, "PAM4-reactive MUC1 is a biomarker for early pancreatic adenocarcinoma," *Clinical Cancer Research*, vol. 13, no. 24, pp. 7380–7387, 2007.
- [49] J. Y. Park, Y. Hiroshima, J. Y. Lee et al., "MUC1 selectively targets human pancreatic cancer in orthotopic nude mouse models," *PLoS ONE*, vol. 10, no. 3, Article ID e0122100, 2015.
- [50] J. M. Curry, K. J. Thompson, S. G. Rao et al., "The use of a novel MUC1 antibody to identify cancer stem cells and circulating MUC1 in mice and patients with pancreatic cancer," *Journal of Surgical Oncology*, vol. 107, no. 7, pp. 713–722, 2013.
- [51] P. R. Konkalmatt, D. Deng, S. Thomas et al., "Plectin-1 targeted AAV vector for the molecular imaging of pancreatic cancer," *Frontiers in Oncology*, vol. 3, article 84, 2013.
- [52] Y.-Q. Ren, H.-Y. Zhang, T. Su, X.-H. Wang, and L. Zhang, "Clinical significance of serum survivin in patients with pancreatic ductal adenocarcinoma," *European Review for Medical and Pharmacological Sciences*, vol. 18, no. 20, pp. 3063–3068, 2014.
- [53] H. Dong, D. Qian, Y. Wang et al., "Survivin expression and serum levels in pancreatic cancer," *World Journal of Surgical Oncology*, vol. 13, no. 1, article 189, 2015.
- [54] B. Shen, M.-Q. Zheng, J.-W. Lu, Q. Jiang, T.-H. Wang, and X.-E. Huang, "CXCL12-CXCR4 promotes proliferation and invasion of pancreatic cancer cells," *Asian Pacific Journal of Cancer Prevention*, vol. 14, no. 9, pp. 5403–5408, 2013.
- [55] W. Zhong, W. Chen, D. Zhang et al., "CXCL12/CXCR4 axis plays pivotal roles in the organ-specific metastasis of pancreatic adenocarcinoma: a clinical study," *Experimental and Therapeutic Medicine*, vol. 4, no. 3, pp. 363–369, 2012.
- [56] Y.-M. Jiang, G. Li, B.-C. Sun, X.-L. Zhao, and Z.-K. Zhou, "Study on the relationship between CXCR4 expression and perineural invasion in pancreatic cancer," *Asian Pacific Journal of Cancer Prevention*, vol. 15, no. 12, pp. 4893–4896, 2014.
- [57] M. Shakir, D. Tang, H. J. Zeh et al., "The chemokine receptors CXCR4/CXCR7 and their primary heterodimeric ligands CXCL12 and CXCL12/high mobility group box 1 in pancreatic cancer growth and development," *Pancreas*, vol. 44, no. 4, pp. 528–534, 2015.
- [58] Q. Xu, Z. Wang, X. Chen et al., "Stromal-derived factor-1 α /CXCL12-CXCR4 chemotactic pathway promotes perineural invasion in pancreatic cancer," *Oncotarget*, vol. 6, no. 7, pp. 4717–4732, 2015.
- [59] P. Büchler, H. A. Reber, M. W. Büchler et al., "VEGF-RII influences the prognosis of pancreatic cancer," *Annals of Surgery*, vol. 236, no. 6, pp. 738–749, 2002.
- [60] A. J. Karayiannakis, H. Bolanaki, K. N. Syrigos et al., "Serum vascular endothelial growth factor levels in pancreatic cancer patients correlate with advanced and metastatic disease and poor prognosis," *Cancer Letters*, vol. 194, no. 1, pp. 119–124, 2003.
- [61] F. Blasi and P. Carmeliet, "uPAR: a versatile signalling orchestrator," *Nature Reviews Molecular Cell Biology*, vol. 3, no. 12, pp. 932–943, 2002.
- [62] D. Cantero, H. Friess, J. DeFlorin et al., "Enhanced expression of urokinase plasminogen activator and its receptor in pancreatic carcinoma," *British Journal of Cancer*, vol. 75, no. 3, pp. 388–395, 1997.
- [63] X. Tan, H. Egami, F. Nozawa, M. Abe, and H. Baba, "Analysis of the invasion-metastasis mechanism in pancreatic cancer: involvement of plasmin(ogen) cascade proteins in the invasion of pancreatic cancer cells," *International Journal of Oncology*, vol. 28, no. 2, pp. 369–374, 2006.
- [64] Y. Chen, B. Zheng, D. H. Robbins et al., "Accurate discrimination of pancreatic ductal adenocarcinoma and chronic pancreatitis using multimarker expression data and samples obtained by minimally invasive fine needle aspiration," *International Journal of Cancer*, vol. 120, no. 7, pp. 1511–1517, 2007.
- [65] J. McCarroll, J. Teo, C. Boyer, D. Goldstein, M. Kavallaris, and P. A. Phillips, "Potential applications of nanotechnology for the diagnosis and treatment of pancreatic cancer," *Frontiers in Physiology*, vol. 5, article 2, 2014.
- [66] C. Pyke, N. Græm, E. Ralfkiær et al., "Receptor for urokinase is present in tumor-associated macrophages in ductal breast carcinoma," *Cancer Research*, vol. 53, no. 8, pp. 1911–1915, 1993.
- [67] Y. He, X.-D. Liu, Z.-Y. Chen et al., "Interaction between cancer cells and stromal fibroblasts is required for activation of the uPAR-uPA-MMP-2 cascade in pancreatic cancer metastasis," *Clinical Cancer Research*, vol. 13, no. 11, pp. 3115–3124, 2007.
- [68] D.-Y. Gong, H.-X. Fu, Y. Peng, Y.-Q. You, and Z.-P. Li, "Diagnostic value of serum CEACAM1 in patients with pancreatic cancer," *Nan Fang Yi Ke Da Xue Xue Bao*, vol. 31, no. 1, pp. 164–166, 2011.
- [69] D. M. Simeone, B. Ji, M. Banerjee et al., "CEACAM1, a novel serum biomarker for pancreatic cancer," *Pancreas*, vol. 34, no. 4, pp. 436–443, 2007.
- [70] M. S. Duxbury, E. Matros, T. Clancy et al., "CEACAM6 is a novel biomarker in pancreatic adenocarcinoma and PanIN lesions," *Annals of Surgery*, vol. 241, no. 3, pp. 491–496, 2005.
- [71] T.-M. Cheng, Y. M. Murad, C.-C. Chang et al., "Single domain antibody against carcinoembryonic antigen-related cell adhesion molecule 6 (CEACAM6) inhibits proliferation, migration,

- invasion and angiogenesis of pancreatic cancer cells," *European Journal of Cancer*, vol. 50, no. 4, pp. 713–721, 2014.
- [72] J. Chen, Q. Li, Y. An et al., "CEACAM6 induces epithelial-mesenchymal transition and mediates invasion and metastasis in pancreatic cancer," *International Journal of Oncology*, vol. 43, no. 3, pp. 877–885, 2013.
- [73] H. J. Lee, D. D. You, D. W. Choi et al., "Significance of CD133 as a cancer stem cell markers focusing on the tumorigenicity of pancreatic cancer cell lines," *Journal of the Korean Surgical Society*, vol. 81, no. 4, pp. 263–270, 2011.
- [74] H. Immervoll, D. Hoem, P. O. Sakariassen, O. J. Steffensen, and A. Molven, "Expression of the 'stem cell marker' CD133 in pancreas and pancreatic ductal adenocarcinomas," *BMC Cancer*, vol. 8, article 48, 2008.
- [75] S. Banerjee, A. Nomura, V. Sangwan et al., "CD133⁺ tumor initiating cells in a syngenic murine model of pancreatic cancer respond to minnelide," *Clinical Cancer Research*, vol. 20, no. 9, pp. 2388–2399, 2014.
- [76] P. Che, Y. Yang, X. Han et al., "S100A4 promotes pancreatic cancer progression through a dual signaling pathway mediated by Src and focal adhesion kinase," *Scientific Reports*, vol. 5, article 8453, 2015.
- [77] Y.-F. Ji, H. Huang, F. Jiang, R.-Z. Ni, and M.-B. Xiao, "S100 family signaling network and related proteins in pancreatic cancer (Review)," *International Journal of Molecular Medicine*, vol. 33, no. 4, pp. 769–776, 2014.
- [78] N. Tsukamoto, S. Egawa, M. Akada et al., "The expression of S100A4 in human pancreatic cancer is associated with invasion," *Pancreas*, vol. 42, no. 6, pp. 1027–1033, 2013.
- [79] N. Ikenaga, K. Ohuchida, K. Mizumoto et al., "S100A4 mRNA is a diagnostic and prognostic marker in pancreatic carcinoma," *Journal of Gastrointestinal Surgery*, vol. 13, no. 10, pp. 1852–1858, 2009.
- [80] K.-X. Ai, L.-Y. Lu, X.-Y. Huang, W. Chen, and H.-Z. Zhang, "Prognostic significance of S100A4 and vascular endothelial growth factor expression in pancreatic cancer," *World Journal of Gastroenterology*, vol. 14, no. 12, pp. 1931–1935, 2008.
- [81] T. Rawnaq, L. Dietrich, G. Wolters-Eisfeld et al., "The multi-functional growth factor midkine promotes proliferation and migration in pancreatic cancer," *Molecular Cancer Research*, vol. 12, no. 5, pp. 670–680, 2014.
- [82] I. G. Papaconstantinou, P. M. Lykoudis, M. Gazouli, A. Manta, G. Polymeneas, and D. Voros, "A review on the role of microRNA in biology, diagnosis, and treatment of pancreatic adenocarcinoma," *Pancreas*, vol. 41, no. 5, pp. 671–677, 2012.
- [83] M. Dillhoff, J. Liu, W. Frankel, C. Croce, and M. Bloomston, "MicroRNA-21 is overexpressed in pancreatic cancer and a potential predictor of survival," *Journal of Gastrointestinal Surgery*, vol. 12, no. 12, pp. 2171–2176, 2008.
- [84] T. Moriyama, K. Ohuchida, K. Mizumoto et al., "MicroRNA-21 modulates biological functions of pancreatic cancer cells including their proliferation, invasion, and chemoresistance," *Molecular Cancer Therapeutics*, vol. 8, no. 5, pp. 1067–1074, 2009.
- [85] E. Giovannetti, N. Funel, G. J. Peters et al., "MicroRNA-21 in pancreatic cancer: correlation with clinical outcome and pharmacologic aspects underlying its role in the modulation of gemcitabine activity," *Cancer Research*, vol. 70, no. 11, pp. 4528–4538, 2010.
- [86] B. E. Kadera, L. Li, P. A. Toste et al., "MicroRNA-21 in pancreatic ductal adenocarcinoma tumor-associated fibroblasts promotes metastasis," *PLoS ONE*, vol. 8, no. 8, Article ID e71978, 2013.
- [87] Z. Zhu, W. Gao, Z. Qian, and Y. Miao, "Genetic variation of miRNA sequence in pancreatic cancer," *Acta Biochimica et Biophysica Sinica*, vol. 41, no. 5, Article ID gmp023, pp. 407–413, 2009.
- [88] G. Zhao, J.-G. Zhang, Y. Shi et al., "MiR-130b is a prognostic marker and inhibits cell proliferation and invasion in pancreatic cancer through targeting STAT3," *PLoS ONE*, vol. 8, no. 9, Article ID e73803, 2013.
- [89] J. Yang and Y. Zeng, "Identification of miRNA-mRNA crosstalk in pancreatic cancer by integrating transcriptome analysis," *European Review for Medical and Pharmacological Sciences*, vol. 19, no. 5, pp. 825–834, 2015.
- [90] M. Liu, Y. Du, J. Gao et al., "Aberrant expression mir-196a is associated with abnormal apoptosis, invasion, and proliferation of pancreatic cancer cells," *Pancreas*, vol. 42, no. 7, pp. 1169–1181, 2013.
- [91] E. P. Slater, K. Strauch, S. Rospleszcz et al., "MicroRNA-196a and -196b as potential biomarkers for the early detection of familial pancreatic cancer," *Translational Oncology*, vol. 7, no. 4, pp. 464–471, 2014.
- [92] G. He, L. Zhang, Q. Li, and L. Yang, "MiR-92a/DUSP10/JNK signalling axis promotes human pancreatic cancer cells proliferation," *Biomedicine and Pharmacotherapy*, vol. 68, no. 1, pp. 25–30, 2014.
- [93] G. Zhang, H. Zhou, H. Xiao, Z. Liu, H. Tian, and T. Zhou, "MicroRNA-92a functions as an oncogene in colorectal cancer by targeting PTEN," *Digestive Diseases and Sciences*, vol. 59, no. 1, pp. 98–107, 2014.
- [94] C. Marin-Muller, D. Li, U. Bharadwaj et al., "A tumorigenic factor interactome connected through tumor suppressor microRNA-198 in human pancreatic cancer," *Clinical Cancer Research*, vol. 19, no. 21, pp. 5901–5913, 2013.
- [95] Y. Zhao, L. Zhao, I. Ischenko et al., "Antisense inhibition of microRNA-21 and microRNA-221 in tumor-initiating stem-like cells modulates tumorigenesis, metastasis, and chemotherapy resistance in pancreatic cancer," *Targeted Oncology*, 2015.
- [96] A. Su, S. He, B. Tian, W. Hu, and Z. Zhang, "MicroRNA-221 mediates the effects of PDGF-BB on migration, proliferation, and the epithelial-mesenchymal transition in pancreatic cancer cells," *PLoS ONE*, vol. 8, no. 8, Article ID e71309, 2013.
- [97] P. Wang, J. Zhang, L. Zhang et al., "MicroRNA 23b regulates autophagy associated with radioresistance of pancreatic cancer cells," *Gastroenterology*, vol. 145, no. 5, pp. 1133–1143.e12, 2013.
- [98] H. Nagano, Y. Tomimaru, H. Eguchi et al., "MicroRNA-29a induces resistance to gemcitabine through the Wnt/ β -catenin signaling pathway in pancreatic cancer cells," *International Journal of Oncology*, vol. 43, no. 4, pp. 1066–1072, 2013.
- [99] X.-Y. He and Y.-Z. Yuan, "Advances in pancreatic cancer research: moving towards early detection," *World Journal of Gastroenterology*, vol. 20, no. 32, pp. 11241–11248, 2014.
- [100] J. K. Lennerz and A. Stenzinger, "Allelic ratio of KRAS mutations in pancreatic cancer," *The Oncologist*, vol. 20, no. 4, pp. e8–e9, 2015.
- [101] M. A. Collins and M. P. di Magliano, "Kras as a key oncogene and therapeutic target in pancreatic cancer," *Frontiers in Physiology*, vol. 4, article 407, 2014.
- [102] S. T. Dergham, M. C. Dugan, P. Arlauskas et al., "Relationship of family cancer history to the expression of P53, P21WAF-1, HER-2/neu, and K-ras mutation in pancreatic adenocarcinoma," *International Journal of Gastrointestinal Cancer*, vol. 21, no. 3, pp. 225–234, 1997.

- [103] X. Liu, J. Li, Y. Tian et al., "Enhanced pancreatic cancer gene therapy by combination of adenoviral vector expressing c-erb-B2 (Her-2/neu)-targeted immunotoxin with a replication-competent adenovirus or etoposide," *Human Gene Therapy*, vol. 21, no. 2, pp. 157–170, 2010.
- [104] P. M. Kasi, K. S. Pedersen, and R. R. McWilliams, "BRCA2-associated pancreatic cancer and current screening guidelines," *Cancer*, vol. 121, no. 17, pp. 3046–3046, 2015.
- [105] Z. K. Stadler, E. Salo-Mullen, S. M. Patil et al., "Prevalence of BRCA1 and BRCA2 mutations in Ashkenazi Jewish families with breast and pancreatic cancer," *Cancer*, vol. 118, no. 2, pp. 493–499, 2012.
- [106] F. Liu, "SMAD4/DPC4 and pancreatic cancer survival. Commentary re: M. Tascilar et al., The SMAD4 protein and prognosis of pancreatic ductal adenocarcinoma. Clin. Cancer Res., 7: 4115–4121, 2001," *Clinical Cancer Research*, vol. 7, no. 12, pp. 3853–3856, 2001.
- [107] A. Horii, S. Nakatsuru, Y. Miyoshi et al., "Frequent somatic mutations of the APC gene in human pancreatic cancer," *Cancer Research*, vol. 52, no. 23, pp. 6696–6698, 1992.
- [108] S. Weissmueller, E. Manchado, M. Saborowski et al., "Mutant p53 drives pancreatic cancer metastasis through cell-autonomous PDGF receptor beta signaling," *Cell*, vol. 157, no. 2, pp. 382–394, 2014.
- [109] E. Hastie, M. Cataldi, N. Steuerwald, and V. Z. Grdzlishvili, "An unexpected inhibition of antiviral signaling by virus-encoded tumor suppressor p53 in pancreatic cancer cells," *Virology*, vol. 483, pp. 126–140, 2015.
- [110] D. K. Bartsch, M. Sina-Frey, S. Lang et al., "CDKN2A germline mutations in familial pancreatic cancer," *Annals of Surgery*, vol. 236, no. 6, pp. 730–737, 2002.
- [111] P. Ghiorzo, G. Fornarini, S. Sciallero et al., "CDKN2A is the main susceptibility gene in Italian pancreatic cancer families," *Journal of Medical Genetics*, vol. 49, no. 3, pp. 164–170, 2012.
- [112] Z. Medarova, W. Pham, Y. Kim, G. Dai, and A. Moore, "In vivo imaging of tumor response to therapy using a dual-modality imaging strategy," *International Journal of Cancer*, vol. 118, no. 11, pp. 2796–2802, 2006.
- [113] M. G. Harisinghani, J. Barentsz, P. F. Hahn et al., "Noninvasive detection of clinically occult lymph-node metastases in prostate cancer," *The New England Journal of Medicine*, vol. 348, no. 25, pp. 2491–2499, 2003.
- [114] M. Andrianifahanana, N. Moniaux, B. M. Schmied et al., "Mucin (MUC) gene expression in human pancreatic adenocarcinoma and chronic pancreatitis: a potential role of MUC4 as a tumormarker of diagnostic significance," *Clinical Cancer Research*, vol. 7, no. 12, pp. 4033–4040, 2001.
- [115] S.-C. Wu, Y.-J. Chen, Y.-J. Lin, T.-H. Wu, and Y.-M. Wang, "Development of a Mucin4-targeting SPIO contrast agent for effective detection of pancreatic tumor cells in vitro and in vivo," *Journal of Medicinal Chemistry*, vol. 56, no. 22, pp. 9100–9109, 2013.
- [116] K. A. Kelly, N. Bardeesy, R. Anbazhagan et al., "Targeted nanoparticles for imaging incipient pancreatic ductal adenocarcinoma," *PLoS Medicine*, vol. 5, no. 4, article e85, 2008.
- [117] X. Wang, X. Xing, B. Zhang, F. Liu, Y. Cheng, and D. Shi, "Surface engineered antifouling optomagnetic SPIONs for bimodal targeted imaging of pancreatic cancer cells," *International Journal of Nanomedicine*, vol. 9, no. 1, pp. 1601–1615, 2014.
- [118] Y. He, W. Song, J. Lei et al., "Anti-CXCR4 monoclonal antibody conjugated to ultrasmall superparamagnetic iron oxide nanoparticles in an application of MR molecular imaging of pancreatic cancer cell lines," *Acta Radiologica*, vol. 53, no. 9, pp. 1049–1058, 2012.
- [119] L. Yang, H. Mao, Y. A. Wang et al., "Single chain epidermal growth factor receptor antibody conjugated nanoparticles for in vivo tumor targeting and imaging," *Small*, vol. 5, no. 2, pp. 235–243, 2009.
- [120] A. Chopra, "Single-chain anti-epidermal growth factor receptor antibody fragment conjugated to magnetic iron oxide nanoparticles," in *BTI—Molecular Imaging and Contrast Agent Database (MICAD)*, National Center for Biotechnology Information, 2004.
- [121] L. Yang, H. Mao, Z. Cao et al., "Molecular imaging of pancreatic cancer in an animal model using targeted multifunctional nanoparticles," *Gastroenterology*, vol. 136, no. 5, pp. 1514–1525.e2, 2009.
- [122] G. Y. Lee, W. P. Qian, L. Wang et al., "Theranostic nanoparticles with controlled release of gemcitabine for targeted therapy and MRI of pancreatic cancer," *ACS Nano*, vol. 7, no. 3, pp. 2078–2089, 2013.
- [123] K. F. Pirolo, J. Dagata, P. Wang et al., "A tumor-targeted nanodelivery system to improve early MRI detection of cancer," *Molecular Imaging*, vol. 5, no. 1, pp. 41–52, 2006.
- [124] X. Montet, R. Weissleder, and L. Josephson, "Imaging pancreatic cancer with a peptide-nanoparticle conjugate targeted to normal pancreas," *Bioconjugate Chemistry*, vol. 17, no. 4, pp. 905–911, 2006.
- [125] S. Wang, Q. Zhang, X. F. Luo et al., "Magnetic graphene-based nanotheranostic agent for dual-modality mapping guided photothermal therapy in regional lymph nodal metastasis of pancreatic cancer," *Biomaterials*, vol. 35, no. 35, pp. 9473–9483, 2014.